Characterization of Steel Components Printed Using WAAM Technology

by

Zeina S. Al-Nabulsi

A thesis submitted to the University of Warwick for the degree of

Doctor of Philosophy in Engineering

School of Engineering

November 2021

Dedicated to
My Superhero Dad,

My lovely Role Model Mum,

My Backbone Zuhdi & Saad,

Abstract

This thesis presents the outcomes of research for structural engineering exploitation of 3D printed steel components produced by using Wire Arc Additive Manufacturing (WAAM) technologies. An objective of the research was to be able to apply WAAM with a Gas Metal Arc Welding (GMAW) based process to manufacture relatively large-scale components. The primary aim of the work was to study the printing process and printing strategy to produce several components for material and structural characterization work. To achieve this, several printing experiments were performed using several weld steels (in the form of 1.2 mm diameter wire), and with three external WAAM-GMAW collaborators. The largest component printed weighs 36 kg and is for a monolithic beam-to-column joint, having thin-walled beam and column sections of I-shape and different sizes. The smaller printed components (e.g., thin-walled plates and stub columns) were used to characterise the mechanical properties of the steels, which are benchmarked against Section 3 requirements in Eurocode 3 (EN 1993-1-1 or EN 1993-1-12) for the design of structural steel works. To investigate the internal structure and establish levels of porosity in the printed components, the non-destructive testing method of X-ray Computed Tomography (X-CT) analysis was employed.

From tensile coupon testing of the 3D printed steels the strains at rupture were assessed against the percentage of porosity formed during the 3D printing. A key finding was that for applications in buildings the presence of porosity has a small impact on the required material ductility and stiffness according to Eurocode 3. To satisfy the ductility requirement, the percentage of porosity should be controlled to be < 1%. Another important finding, from the X-CT evaluations, is that the printing process and its strategy both have a significant impact on the homogeneity and level of defects in the printed steels. The author therefore recommends that for quality printing it is important to consider the component's load path and functionality during the design process leading to WAAM-GMAW manufacturing. Finally, testing of the beam-to-column joint for its moment-rotation characteristics showed that it can be classified by its stiffness to be 'rigid' (in accordance with Section 5.2 of EN 1993-1-8). This proved that the WAAM printed joint has the functionality of an equivalent conventional steel rigid joint for building structures.

The new data collected from this research forms the basis for the future development of design guidelines for using WAAM manufacturing technologies in structural engineering. Outcomes presented in this thesis can also be informative for the preparation of guidelines

for safety factors, and for future applications on the potential impact on quality of steel printing of the chosen WAAM-GMAW parameters. Overall, the new contribution to knowledge and understanding is encouraging for there to be opportunities to apply 3D printing of steel to support the requirement of minimizing the mass of materials in structures for a zero-carbon economy.

Contents

Bibliography

List of Figures

vii

xi

List of Tables

Acknowledgement

Declarations

The author wishes to declare that, except for commonly understood and accepted ideas, or where specific reference is made to the work of others, the content of the thesis is her own investigation. The thesis has not been submitted previously, in part or in whole, to any university or institution for any degree, diploma or other qualification.

Publications

I. AL-NABULSI, Z., MOTTRAM, J. T., GILLIE, M., KOURRA, N. & WILLIAMS, M. A. 2020. Mechanical and X ray computed tomography characterisation of a WAAM 3D printed steel plate for structural engineering applications. Construction and Building Materials, 121700.

II. Manufacturing Printing process and strategy of a WAAM 3D printed steel join specimen for structural Engineering Application, ICAM-2020, Virtual.

III. Potential of Metal 3D Printing in Structural Engineering, European conference on structural integrity of additively manufactured material (ESIAM19), Trondheim, Norway, oral presentation.

Abbreviations

3D	Three Dimensional
a_o	dimensions of thickness
A	Amperage
AM	Additive Manufacturing
ASTM	American Society for Testing and Materials
AW	Arc Welding
b_o	gauge length
BJ	Binder Jetting
CAD	Computer Aided Design
CLDA	Curvilinear Detector Array
CiMAT	Centre for Imaging, Metrology and Additive Technologies
CNC	Computer Numerical Control
CoV	Coefficient of Variation
E	modulus of elasticiy
f_u	Tensile strength
f_y	yield strength
FEA	Finite Element Analysis
DAQ	Data Acquisition System
DED	Direct Energy Deposition
DMD	Direct Metal Deposition
DMLS	Direct Metal Laser Sintering
EBBF	Electron Beam Freeform Fabrication
EBM	Electron Beam Melting
FBP	Filtered Back Projection
FDM	Fused Deposition Modelling
GMAW	Gas Metal Arc Welding
GTAW	Gas Tungsten Arc Welding
I	Current
ISO	International Organisation for Standardisation
L_o	gauge length
L_c	parallel length
L_t	Total length
LDT	Linear Displacement Transducer
LENS	Laser Engineered Net Shaping
MAT	Medial Axis Transformation
M_e	Elastic moment
$M_{pl,Rd}$	Plastic moment of resistance
ME	Material Extrusion
MJ	Material Jetting
PAW	Plasma Arc Welding
PBF	Powder Bed Fusion
R	Resistance

R_{eH}	upper yield strength
R_{eL}	lower yield strength
R_m	tensile strength
RP	Rapid Prototyping
RHS	Rectangular Hollow Section
S_o	cross-section area
$S_{j,ini}$	stiffness of a joint
SHS	Square Hollow Sections
SL	Sheet Lamination
SLA	Stereolithography
SLS	Selective Laser Sintering
SLM	Selective Laser Melting
SoE	School of Engineering
T_w	Temperature in Water
TS	Travel Speed
UCI	University of California-Irvine
UNSW	University of New South Wales
V	Voltage
VE	Vat photopolymerisation
W_{el}	Elastic section modulus
W_{pl}	plastic section modulus
WAAM	Wire Arc Additive Manufacturing
WMG	Warwick Manufacturing Group
WFS	Wire Feed Speed
X-CT	X-ray Computed Tomography
ε_f	Elongation at failure
$\Phi_{j,Ed}$	Rotation of the joint
η	The thermal efficiency coefficient
ν	Poisson's ratio

Symbols

BD	Build Direction
DD	Deposition Direction
DT	Transducer
H	Heat Input
INC	Inclinometer
L	Longitudinal
T	Transverse
W	Weight in air
W_a	Weight in water
WSL	Wire Stick-out Length

1. Chapter one: Introduction

3D printing is an Additive Manufacturing (AM) process that creates a physical solid object from a digital model file. The technology works by adding layer upon layer of a material to build-up a complete object, which in this thesis on the 3D printing of steels is referred to as a component. Since its conception the potential of 3D printing has evolved significantly, offering efficiencies, and providing optimised engineered solutions to many products. As examples of the development, in 2010, more than 35 houses, cabins, bridges, pavilions and other structures were built using various 3D printing technologies, which can be seen as part of the Fourth Industrial Revolution (Koslow, 2017). To meet client and climate emergency needs engineers are increasingly considering the potential applications of various 3D printing technologies to manufacture their products with added value over the cost of today's products that are being routinely manufactured using conventional processes.

This thesis concerns printing with weld grades of steel as the material. Within the field of AM, metallic 3D printing is transforming many industrial sectors, but to date it has had little impact in structural engineering. This is, in part, due to the limitation on deposition rate for the material layer-by-layer build-up that were impractical until recently. However, metallic 3D printing, and by using Wire Arc Additive Manufacturing (or for short WAAM) is developing and has made significant efficiency gains in terms of rate of deposition, etc. WAAM technology uses the Direct Energy Deposition (DED) technique and for steel materials is basically a controlled welding process. For reasons given in the literature review the WAAM-Gas Metal Arc Welding printing process (or GMAW for short) was employed to print the components in the research. Within this thesis the author presents and discusses research results that can inform the foundations needed for structural engineers to use steel 3D printing with confidence.

The motivation for the PhD work comes from historical, iconic metal structures. In the past, when labour and materials were expensive, structural designs were well optimised in a high level of detail such as for the cast iron frames in the St Pancras Railway station, London, as seen in Figure 1-1.

Figure 1-1. wrought iron frames in the roof of St Pancras station

The vision today is to use AM methods, such as WAAM that has the capacity to produce large-sized components having complex geometries with the minimum time and cost, thereby to manufacture similarly optimised structural engineering solutions to that shown in Figure 1-1. To achieve this, fundamental bottom-up research is necessary to build confidence from knowing the mechanical properties of printed steels and to understand the structural behaviour of WAAM printed components of these steels.

For the PhD research, WAAM-GMAW facilities from three different collaborators were involved at separate stages. The first components were printed by Autodesk (based at the Birmingham office). The second group of components were manufactured at Steelo in London. The final group of components were from a collaboration with RAMLAB, based in Rotterdam, and involved a collaboration with a research group at Delft University of Technology. For a non-destructive evaluation the research used X-Ray Computed Tomography (X-CT) by way of a collaboration with the Centre for Imaging, Metrology and Additive Technologies (CiMAT), which is within WMG (was Warwick Manufacturing Group) at The University of Warwick. X-CT was used as a quality control technique to investigate the internal structure of the printed steels, and thereby for us to learn how effective the WAAM-GMAW processing had been, especially in producing a 'solid' homogeneous steel components with a minimal amount of porosity, which is an unwanted internal feature in 3D steel printings.

WAAM processing is today known to possess limitations that can prevent an 'ambitious' engineer from making the step-change to use this AM method to produce an optimum

complex geometrical component, say for moment-resistant joints in a steel building (where, for example, these joints are visible as an architectural feature). Therefore, having the opportunity in this PhD study to be involved in the printing processing itself (and from three facilities) enabled the author's research with WAAM-GMAW to bridge the 'gap' between using a new AM technology and the end structural engineering application. As the thesis will report we have learnt how important the printing parameters are in controlling the thickness of a thin-walled section, because it's a function of the weld bead width. Also, because the printing process will be shown to be key in controlling the quality of the required printed geometry, it is noted that the WAAM-GMAW parameters are not just key in fulfilling the required solid geometry, but also in ensuring a 'homogeneous' microstructure through proper interaction between the weld beads (as they are laid down on top and next to each other). Meteorology and welding knowledge are therefore key inputs to print a component that, for example, can possess the required mechanical properties that satisfy the minimum limitations as specified in standards (in accordance with Eurocode 3 and Clause 3 of either (EN1993-1-1:2005) or (EN1993-1-12:2007).

The overall aim of the research is to:

- develop knowledge and understanding that can enable the routine application of metal 3D printing using Wire Arc Additive Manufacturing in structural engineering.

Objectives of the research are to:

- investigate the WAAM-GMAW printing process and requirements to produce several components from weld grades of steel.
- characterize the mechanical properties of the 3D printed steels and compare results with requirements for structural grades of steel in Eurocode 3.
- to use X-ray computed tomography to characterize the internal structure of printed steel components with specific attention paid to determining both local and overall levels of porosity.
- use WAAM-GMAW to produce a full-size component of a monolithic beam-to-column joint weighing 36 kg.
- to conduct an experimental investigation to characterize the structural properties of this moment-resistant joint.

The test facilities in the Structures laboratory, within the School of Engineering at The University of Warwick, were used to carry out a strength test on the beam-to-column joint

by applying a joint moment through cantilever end loading of the beam section region to determine the moment-rotation response. The objectives of this physical testing were to investigate how the WAAM-GMAW printing strategy might have affected the overall behaviour of the joint and to classify the joint in accordance with the stiffness curve in Section 5 of EN 1993-1-8:2005 (EN1993-1-8, 2005).

Using other components from the printing programme, the mechanical properties of the printed steels were characterised using a tensile testing programme with batches of dog-bone coupons to establish whether the new test results are for grades of steel that can be used in structural engineering applications. This is achieved by choosing the requirements on strengths and strains in Eurocode 3, which are for structural grades of steel that are not necessarily acceptable for weld grades of steel employed in WAAM printings. A second evaluation is conducted to link the coupon test results for mechanical properties to the amount of porosity determined from analysis of the X-CT images.

New knowledge and understanding from this structural engineering research can be used to:

- develop standard operating procedures for WAAM;
- report the expected material properties of the WAAM-GMAW steel components;
- benchmark the WAAM-GMAW steels against what a current structural design standard requires of a grade of steel.

It is the expectation of the author that two important outcomes from the PhD studies are going to be the advancement of the WAAM-GMAW process towards producing larger-sized components and the establishment in confidence for choosing WAAM to produce structural steel components in, say, buildings and bridges.

The evolution of the five main chapters is briefly introduced next.

Chapter 2: Literature Review presents an overview on metal 3D printing with emphasis on structural engineering applications in construction, and the type of metal printers and their advantages and disadvantages from a structural engineering point of view.

Chapter 3: Manufacturing of Seven WAAM-GMAW Components and the use of X-ray as a Quality Control technique introduces and describes the steel WAAM-GMAW printing process and how the collaborative work produce the components of: a horizontal plate (by Autodesk); two vertical walls and a Rectangular Hollow Section (RHS) (by Steelo); two stub

column and the beam-to-column joint (by RAMLAB). Additionally, Chapter 3 highlights the need for having the X-ray non-destructive test method as the quality control technique.

Chapter 4: Developing the methodologies for mechanical characterisation tests presents factual information on the preparation stages for cutting-out the test specimens from the printed components, and the test methodologies for determining mechanical properties by way of series of tensile and impact coupon tests. Furthermore, this chapter introduces test methodologies for density measurement and for X-CT analysis.

Chapter 5: Characterisation of 3D printed steel presents and discusses the test results to characterise the mechanical properties of the welded steels (including for yield strengths, ultimate tensile strengths, elongations, Poisson's ratios and via impact testing for toughness). Assessment to these material properties is enhanced by knowing densities and having X-CT images and internal structural results that permit an investigation on the effect of porosity on measured mechanical properties.

Chapter 6: X-CT and test results for the monolithic beam-to-column joint is for the final chapter that presented and discusses the moment-rotation characteristics of the beam-to-column joint under monotonic static load, combined with X-CT analysis before load testing. This research is used to investigate how the WAAM-GMAW printing strategy might have affected the overall structural response. The static test results for joint response are used to classify the joint for strength and stiffness in accordance with BS EN 1993-1-8.

The thesis ends with a chapter presenting the author's conclusions from the PhD work and what further work is recommended to progress the research.

2. Chapter Two: Literature review

2.1. Introduction to Additive Manufacturing technology and its applications

Over the last three decades, the potential of 3D printing for structural components has evolved significantly, offering material efficiency, and providing several optimised solutions in many engineering sectors. The story of 3D printing started with liquid acrylate and laser processing of titanium powder, and from a base of a few interested companies there is now limitless competition amongst research centres, leading companies, and entrepreneurs (Ashley, 1991). For instance, in 2010 more than 35 houses, cabins, bridges, pavilions, etc., were built using various 3D printing technologies, which initiated the 4th industrial revolution in construction sector (Koslow, 2017). Today, more and more engineers are considering how the promising potentials of the various 3D printing methods can revolutionise the sector.

An overview of Additive Manufacturing (AM), and, in particular, metal 3D printing for application in construction is presented in this literature review. The type of metal printers and their limitations from a structural engineering point of view is examined. Combined with learning from the development of 3D printing with concrete as the feedstock (as presented in the following video,(Theguardian, 2021)), this PhD work with steel is informed in terms of current limitations and for advances in metal AM.

2.2. History of Metal Additive Manufacturing

2.2.1. Definition

In this sub-section we provide a definition to Additive Manufacturing. AM, also known as 3D printing, is a process of joining material(s) together by using a layer-by-layer build-up approach to form a solid component from powder or a wire feedstock. AM is an engineer's tool that facilities the design process, whereby a 'simple idea' can be transformed into a complex optimised solution using Computer Aided Design (CAD) software, which can then be 3D printed. Canessa (Canessa et al., 2013) explains that the 3D printing process contains the following six main steps: digital modelling; exporting; slicing; connecting; printing; finishing.

According to the American Society for Testing and Materials (ASTM) F-42 committee, who sets the industry standards for Additive Manufacturing, AM is defined in ASTM F2792-10 as "A *process of joining materials to make objects from 3D model data, usually layer upon layer, as opposed to subtractive manufacturing methodologies. Synonyms: additive fabrication,*

additive processes, additive techniques, additive layer manufacturing, layer manufacturing, and freeform fabrication." (ASTM, 2013)

2.2.2. Background of Metal Additive Manufacturing

The commencement of AM was in 1986 when (Hull, 1986) patented a system for generating 3D polymer-based objects by a stereolithographic technique. In the following years, other rapid prototyping technologies were introduced commercially, such as Selective Laser Sintering (SLS) and Fused Deposition Modelling (FDM). The main aim of the developing AM techniques was to produce a different prototype for the manufacturing sector (Wu *et al*., 2016).

The stereolithographic method uses a liquid acrylate, that hardens when it is hit by a laser beam. The object to be 3D printed is sliced into layers using a software algorithm, that then operates the stereolithographic printer to build-up the component layer-by-layer, from the bottom to the top. After the solid object is printed, it is usually placed in a curing oven to complete the solidification procedure. In 1991, at least eight companies offered stereolithographic technologies. At the time there was a lot of research activities because experts wanted to overcome its relatively slow speed and poor dimensional precision (Ashley, 1991).

In 1992, Selective Laser Sintering (SLS) was the first AM approach to appear based on the powder bed technology and was supplied by DTM Corporation (Nelson et al., 1993), which was already patented by Ross Householder in 1979 (Deckard, 1989). In the paper by (Vayre et al., 2012), we are informed that since 1992, the range of polymer material used as the feedstock started to increase. Also, during the 1990s, the company EOS developed SLS so that metallic components could be printed. This important advancement led to the introduction of Direct Metal Laser Sintering (DMLS) (Gao et al., 2015). DMLS 3D printers were capable of constructing fully dense components with an average size of 95mm x 29mm x 27mm, such as for filters and gas storage systems (Vayre et al., 2012).

In 1997, the Swedish company ARCAM started to supply a machine for Electron Beam Melting (EBM). EBM printers are similar to Selective Laser Melting (SLM) printers, which was developed by EOS (Germany), with the only difference being the source of energy (Vayre et al., 2012); (Bhavar et al., 2014); (Gao et al., 2015).

2.2.3. Development of Additive Manufacturing in different sectors

It is observed that several engineering sectors have been prominent in the 4th industrial revolution which includes exploiting AM (Karabegović, 2018) (Skilton and Hovsepian, 2018) (Moavenzadeh, 2015, Wangler et al., 2016). This highlights that the upcoming sector to adopt AM should be in construction (Fernandes et al., 2021) (Bos et al., 2016) (Berman, 2012) (Crowley, 1998). An example of how companies embrace new manufacturing technologies is Ford (Ashley, 1991), when this automotive manufacturer was motivated to develop a rocker arm that, to improve its design quality, made good use of the available prototyping technology. The results of the project showed the importance of 3D CAD and the production process, using powder printing technology, proved to be a great addition, because it was much cheaper and saved lots of time. (Ashley, 1991) reports that the automotive engineering sector learnt from Adopting Ford's approach in how rapid-prototyping technologies can be used to convert CAD (or any computer 3D design) into a real, precision model that can be held, tested, researched, and compared.

Many industries have been attracted to the benefits of 3D printing and to take advantage of the ability of AM to produce complex shaped and monolithic components. Traditionally, products require the assembly of several parts and AM is able to reduce the part number in a component. It can also simplify stages in the design process, thereby optimising the use of materials and reducing waste, which are essential to meet climate change legislation. The Canada Research Centre (Canada Research center, 2017), presented in Figure 2-1 shows the infiltration of 3D printing in several engineering sectors. With between 15 and 20% of printers supplied, the three sections of industrial machinery, aerospace and automotive are seen to be immersed in this technology. The construction sector does not appear in Figure 1 and is part of the 'Other' grouping that individually does not have 10% of the printers. It is worth highlighting that the use of 3D printing will continue to increase with time because it will become more and more economically viable (ING report, 2017).

Source: ING report, which credits responses from 61 producers of 3D printers asked what their customers use printers for

Bloomberg
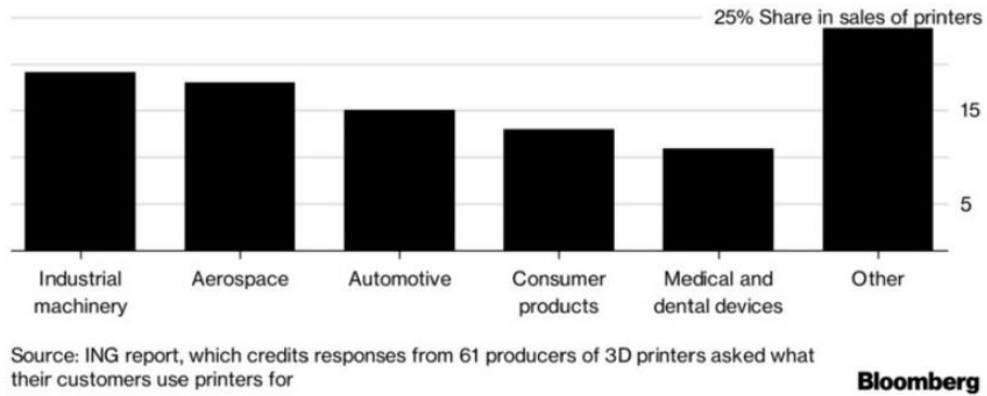
Figure 2-1. Breakdown of industries with 3D printing (Canada Research center, 2017).

In the 2000s, Rapid Prototyping (RP) technology started to be used in the construction industry, but only limited to produce architectural models using SLS, FDM and Stereolithography (SLA) types of printers. For example, Ramakrishnan *et al.* used the technology to tailor inorganic sand moulds and fit specific casting requirements for complicated shapes (Ramakrishnan et al., 2014). Gibson also managed to build both simple and complicated architectural concept models using RP technology (Gibson et al., 2002); (Ryder et al., 2002).

In 2005, (Kruth et al., 2005) studied the limitations of, and provided a benchmark for the SLS and SLM processes. This helped create a picture for the huge potential of applications. The general conditions, that need to be considered to avoid any limitations, included precision of depositing, type of feedstock material, mechanical properties of printed material, speed of deposition and reliability of the produced product. However, SLS and SLM printers were recommended to be more suitable for medical prosthesis manufacturing due to their high geometric complexity (Kruth *et al.*, 2005).

In 2011, from a business perspective, 3D printing applications and characteristics had been examined and compared with the conventional manufacturing process. As a result of the evolution in 3D printing, we find that printers are owned by the customers themselves to meet their own needs. The three phases in 3D printing can be summarized as starting with prototyping, moving on to mocking-up new designs and finally printing real products for the marketplace (Berman, 2012).

Nowadays, metal 3D printers can produce fully dense metallic parts with the manufacturing process being much simpler than traditional machining techniques. Therefore, aerospace, oil and gas, marine and automotive industries are garnering a lot of interest in 3D printing owing

to its advantages, such as freedom of part design, shape complexity and light-weighting (Duda and Raghavan, 2016); (Bhavar et al., 2014); (Camacho et al., 2017).

2.3. Development of the technology in the Construction industry

In 1997 concrete as a feedstock material was a new addition into the capacity of 3D printing. In the same year, (Pegna, 1997) proposed a new process to employ robots to position the printer head for automation. In additional to the 3D processing to fabricate large freeform concrete components, the concrete has higher strength and durability when compared to the common reinforced concrete (Wu et al., 2016). Recycled waste material could then be introduced as part of the AM process (Wu et al., 2016).

In the early 2010s, it was found that some 35 concrete buildings had been installed around the world using various 3D printing technologies and different types of concretes (Koslow, 2017). Figure 2-2 is a graphical plot of cumulative number of projects to a total 40 against years from 1996 to 2018. Results shows the slow, but steady, to 2008, and then rapid growth in 3D concrete printed projects for the construction sector. This plot for numbers of real applications of concrete as the feedstock provides further evidence to demonstrate why it is timely for having structural engineering research for AM with steel.
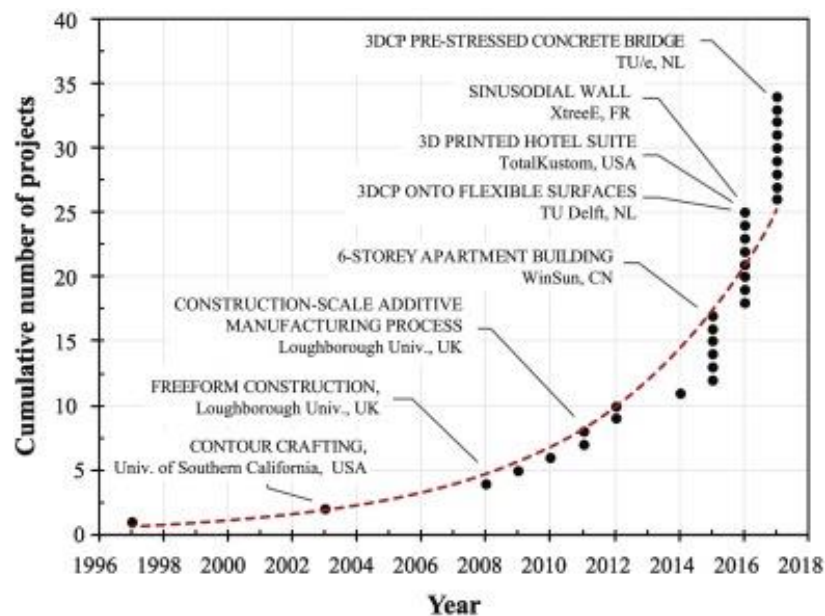
Figure 2-2. Summary of the growth in concrete printing applications in industry (Buswell et al., 2018).

(Wu et al., 2016) outlined three significant demonstrator projects using 3D printing technologies with concrete materials as important to the construction industry. These

prototypes are widely considered to be a positive turning-point for confidence in applications for civil engineering works. These key demonstrators will now be introduced:

- Firstly, in 2014, ten 200m^2 houses were printed by the Beijing company WinSun using high-grade cement, glass fibres and recycled waste material. For this demonstrator project a massive printer envelope of length 150m by a width of 10m and a height of 6.6m was used. (Bos et al., 2016) (Wu et al., 2016); (Kietzmann et al., 2015); (Feng and Yuhong, 2014).

- Secondly, in 2015, WinSun constructed a 1100m^2 five-storey apartment demonstration building and a villa using 3D printing, as seen in the photograph in Figure 2-3 (Wu et al., 2016); (Mueller, 2016); (Stampler, 2015). Although the building's concrete components were not printed on-site, the project demonstrates significant development in the capabilities of 3D printing. Not least to the extent that entire buildings of 3D printed components can be constructed.

- Thirdly, in 2014, a company called KamerMaker developed by DUS architect printed in Amsterdam a micro-house of concrete having size 2.2m by 2.2m by 3.5m (Wu *et al*., 2016) (Mueller, 2016) (Wainwright, 2014).

It is noteworthy to introduce two more demonstrator projects. In Dubai, the Office of the Future shown in Figure 2-4 was printed by Winsun in China. The Production by 3D printing could reduce the labour costs by 50% - 80%, and lessen construction waste up to 30% - 60% for similar size projects; the Office of the Future was 240m^2 (Sakin and Kiroglu, 2017) (Augur, 2016) (Koslow, 2017) (MacRae, 2016).

Moreover, Apis-Cor printed on site in Russia, and in 24 hours, a 38m^2 'habitable' house using a mobile 3D concrete printer. The outside of this building is seen in Figure 2-5 (Sakin and Kiroglu, 2017); (Koslow, 2017).

Figure 2-3. WinSun 3D Printed Mansion (~ 1100m^2), in China (Stampler, 2015)

Figure 2-4. Front view of Office of the future in Dubai, 2016 (Augur, 2016)

Figure 2-5. Apis Cor house in Russia, 2016 *(Koslow, 2017)*

These demonstrator projects highlight the advancements in size and complexity of 3D printing with concrete materials, which illustrates that there can be future possibilities in

structural engineering for metal 3D printing, providing the technology can produce monolithic components of the correct sizes and shapes, with the appropriate mechanical properties and at a cost per component that is acceptable to clients.

As a young technology, in a slowly adapting construction sector, AM is seen as an opportunity for technology enthusiasts.

Figure 2-6 is from AT(ATKearney, 2015), who in 2014 found that the 3D printing market for industrial use, including construction, was worth annually $0.8 billion. The bar chart to the left of the table with 3D printing market shows a +25% increase in the global 3D printing market for hardware, supplies and services. By the end of 2027, the AM market is predicted to have an annual revenue of $40 billion and the bar chart in Figure 2-7 (SmarTech, 2018) indicates we are to experience a very rapid growth of 12 times for the five years from 2022. It is worth highlighting the predicted annual revenue figure of $40bn for 3D printing in the construction market, which is only about 0.3% in relation to the ~$12638bn reported total global construction market in 2020 ((ConstructionMarket, 2021)

Global 3D industry market for hardware, supplies, and services $ billion

3D printing market

Sector	2014	Five-year CAGR
Aerospace (including defense)	$0.8 billion 18%	15–20%
Industrial (including construction)	$0.8 billion 18%	15–20%
Healthcare	$0.7 billion 15–17%	20–25%
Automotive	$0.5 billion 12%	15–20%
Jewelry	$0.5 billion 12%	25–30%
Energy	Less than 5%	30–35%
Other (many sectors)	Less than 20%	20–25%
Total	$4.5 billion	25%

Bar chart values: 4.5 (2014), 7.0 (2016), 11.0 (2018), 17.2 (2020), +25%

Figure 2-6. Global 3D industry market (Yusuf, 2015) (ATKearney, 2015).
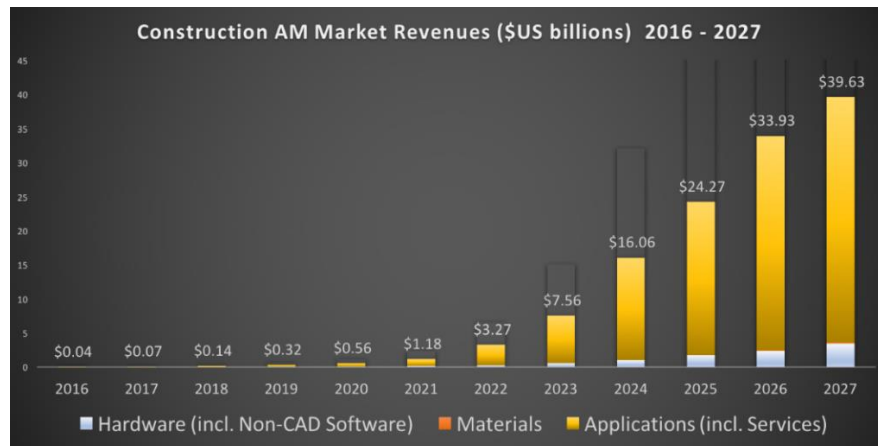
Figure 2-7. Predicted AM Market Revenue in Construction (SmarTech 2018).

Furthermore, Ramadany and Bajjou's survey (Ramadany and Bajjou, 2021) on the Moroccan construction sector marked the importance of the strategic decision at country level in integrating 3D printing concrete technology. Delaying the strategic decision will delay the implementation of concrete AM by a rate of 71.4%. Compared to the strategic decision, the Dubai Future Foundation aims to make the country of Dubai the 3D printing World hub by 2030 (Jezard, 2018). **As far as a country's strategic decision making is a key to integrating the technology in the construction sector goes, it can be seen that Dubai is working to a roadmap to have 25%** of the city-state made by 3D printers by 2025.

2.3.1. Development and current limitations of metal AM

Presented in the previous sub-section was the evolution of 3D printing, and it has been shown that large-scale components and whole buildings can be printed. However, metal 3D printing was only limited to small-sized projects by 2015, as it's development for applications is highly dependent on a mix of printing technology, material availability, printing time and cost. (Camacho et al., 2017) observed that for the construction industry it is started exploring metal 3D printing to prove that AM could be applied in order to mitigate a lot of emerging challenges. Considerations are required when dealing with metal printing as a controlled environment is required during the printing. Additionally, the printing process with metal feedstock needs to be well understood to avoid the well-known challenges against acceptable finishing quality from factors including: porosity; surface finish; density changes; shape warpage; internal cracking, etc. The quality of the finish of a 3D printed component and the mechanical structural property are a function of the chemical composition of the material, and the chosen process of printing (Seifi et al., 2016, Michael Molitch-Hou, 2017).

It is important to acknowledge that the operation of the different types of 3D printers, which will be explained in Section 2.4, lead to limitations that involve the aforementioned challenges.

2.4. Type of 3D printers

In this section the types of 3D metal printers will be introduced with attention paid to the classification of printers that will be used in this research. Seven AM methods are categorised by the International Organisation for Standardisation (ISO) and the American Society for Testing and Materials (ASTM). (ISO/ASTM 52900-15, 2015) standard establishes and defines terms used in AM technology, which applies to the additive shaping principle and thereby builds physical 3D geometries by successive addition of a feedstock material. The methods are classified by the seven different processes listed in Figure 2-8 (Camacho et al., 2017). They are from left-to-right: Material Extrusion (ME), Vat photopolymerisation (VE), Powder Bed Fusion(PBF), Material Jetting (MJ), Binder jetting (BJ), Direct Energy Deposition (DED) and Sheet Lamination (SL). Each type of printer has its own potential for different industry sectors and in this literature review there is a presentation why the DED printer is one required for the PhD work.
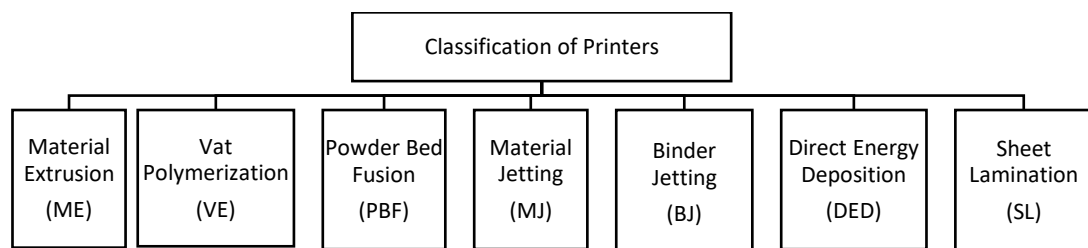
Figure 2-8. Classification of Additive Manufacturing by process.

In addition to categorising 3D printers by the technology process, it has to be understood that the printing speed and type of feedstock material are not constants. The methods can be categorised according to the type of their mounted printer head that deposits the material, and the mobility technique that moves the head during the printing process. The range of the mobility of the printer head can either depend on a temporary support, such as a gantry system, or a robotic arm that has several, up to six-degrees of freedom.

When aggregate based concrete is the material to be printed the AM methods of choice are BJ and ME (Camacho *et al.*, 2018). (D-Shape), is an example of combining BJ with a gantry system to 3D print concrete components for structural engineering applications. For AM methods that are MB based with a gantry system there is: contour crafting (Khoshnevis and Dutton, 1998); contour printing (Lim *et al*., 2012); Winsun (Feng and Yuhong, 2014);

BetAbram (Molitch-Hou, 2015); 3D concrete printing. MB methods printing with a robotic arms moving the printer head are CyBe (CyBE, 2014), Xtree (Gosselin *et al.*, 2016) and Apis-Cor (ApisCor, 2016).

We find that in metal AM the processing categories are for Powder Bed Fusion (PBF) and Directed Energy Deposition (DED). The difference between the methods in these two categories is either the source of energy used or the input form of metal feedstock, which can be, respectively, powder or wire (Duda and Raghavan, 2016, Bhavar et al., 2017). Sub-section 2.4.1 will introduce PBF and sub-section 2.4.2 is for a similar presentation on DED.

2.4.1. Powder Bed Fusion technology (PBF)

PBF technology is for a layered based process. It is classified by the degree of material melting that is required for the powder particles to bind together, which is activated either by sintering (where the material is partially melted) or by full melting. Figure 2-9 shows that there are the following four types of PBF printers: Selective Laser Sintering (SLS); Direct Metal Laser Sintering (DMLS); Selective Laser Melting (SLM); Electron Beam Melting (EBM). EBM and SLM require the powder to fully melt whilst the other types of PBF, namely SLS and DMLS, process with the powder partially melting, and therefore are less energy intensive. As their names indicate SLS, DMLS and SLM printers use a laser for the source of energy (Vayre et al., 2012). EBM has its heat source from an electron beam.
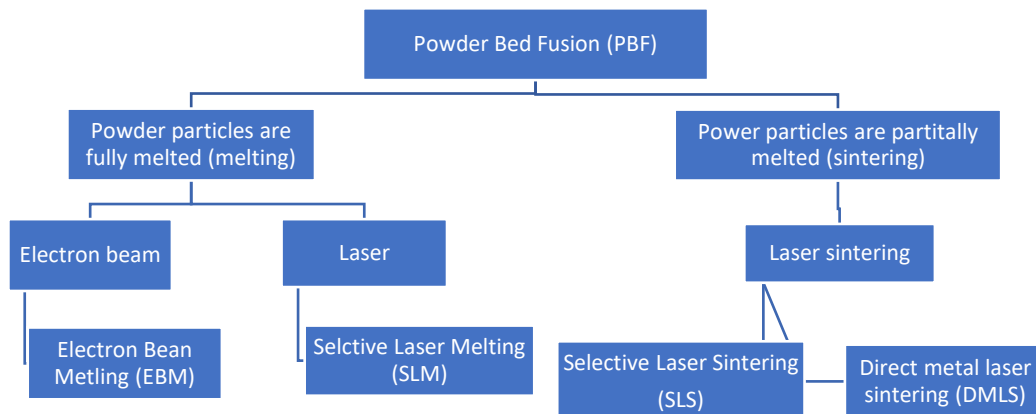
Figure 2-9. Classification of Powder Bed Fusion technology.

As shown in Figure 2-10, the powder in the PBF process will be located inside a powder chamber and is spread over the printing bed in the build chamber. The energy source (laser or electron beam) is then directed onto the printer bed and growing lay-by-lay, according to the uploaded code for the required cross-section of the part. The required material melts

down layer-by-layer in real time, all the way up to build the monolithic solid object (Bhavar et al., 2014); (Duda and Raghavan, 2016).
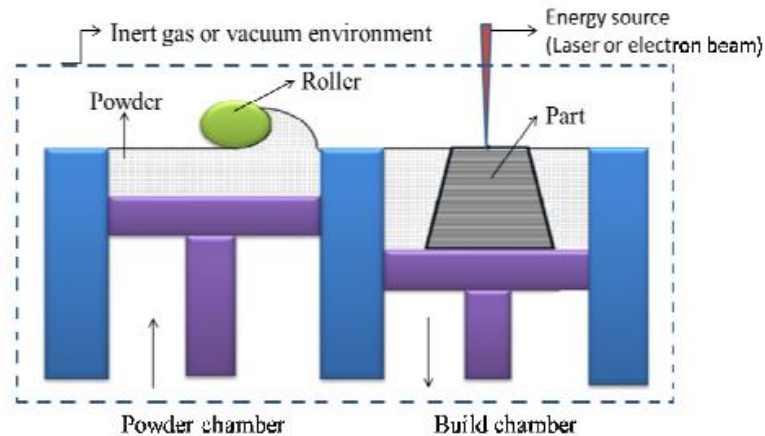
Figure 2-10. The SLM or SLS PBF process (Bhavar et al., 2014).

The SLS process is used to produce moulds and cores, using different types of polymer materials. This method requires post-processing to improve mechanical properties as the sintering process does not fully melt the polymer powder. The printed component is therefore placed in an oven to vaporise the polymer, sinter the part and molten in a different material (Vayre et al., 2012); (Ashraf et al., 2018). To use metal powders SLS was upgraded to be DMLS. This PBF process is found to be an effective technique for metal 3D printing, and almost any metal alloy in its powder form can be used (Ashraf *et al*., 2018). One weakness with DMLS metal components is that the porosity is high due to the binding mechanism and this limits the mechanical properties (Vayre et al., 2012); (Kruth et al., 2005). In 2017, DMLS accounted for the largest market share (~> 50%) of 3D printers, not least because it has the capacity to produce complex monolithic geometries needed for tooling and fixtures (MarketsandMarkets, 2019).

The SLM process has a printer that uses a more powerful laser than found in the processes of SLS and DMLS. The energy at the powder bed spot is now powerful enough to melt the powder and this removes the requirement for post-processing sintering. An additional advantage of SLM is that the printed component will have fewer or no porosities. Attention in processing is still a consideration as thermal distortion may occur owing to the high temperature required to fully melt the powder (Vayre et al., 2012). Moreover Shrinkage may take place in SLM printings due to the high energy source and a post-curing operation is not required to achieve the mechanical strength. (Vayre *et al.*, 2012).The EBM approach can be seen to be like SLM, as shown in Figure 2-11, except that the source of energy is now an electron beam.
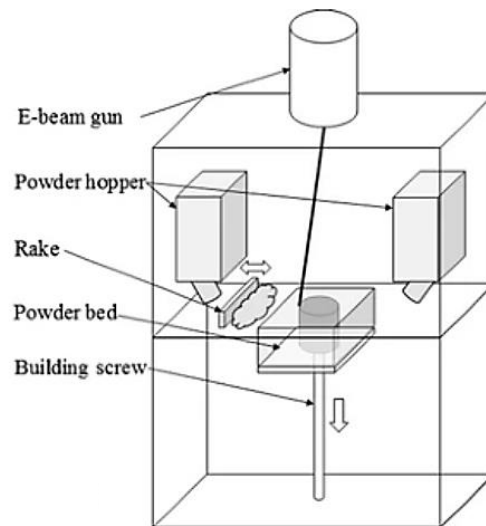
Figure 2-11. the EBM process (Zhang et al., 2018).

DMLS, SLM and EBM are PBF techniques that are used in downscaling structural applications, because now the post-processing step is not needed. Moreover, a higher resolution for complex details can be achieved, for example, the precision with deposition using the DMLS process can be as small as 20µm (MarketsandMarkets, 2019).

2.4.2. Direct Energy Deposition (DED)

In the DED process, the printer head is a mounted nozzle that fuses wire or powder feedstock to form the component that can be printed in different directions and different orientations. The deposited material is melted using a localised energy source that can be a laser, electron beam or electric arc. DED technology has several variants, such as: Direct Metal Deposition (DMD); arc additive manufacture, Laser Engineered Net Shaping (LENS); Electron Beam Freeform Fabrication (Duda and Raghavan, 2016); (Additive Manufacturing Research Group).

For the DMD approach shown in Figure 2-12, a metallic powder is sprayed directly into a laser beam to be heated. Molten droplets then collect onto the printing bed and a component is built-up over time. The thickness of the beads, formed from the molten drops, depend on the nozzle speed and the rate of material deposition (Vayre et al., 2012).
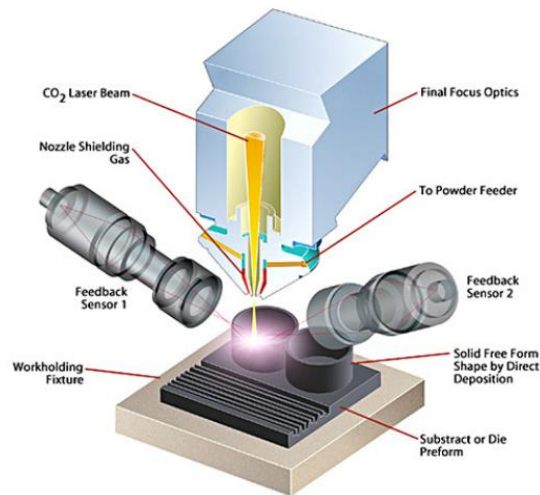
Figure 2-12. DMD's Principle by POM (Vayre et al., 2012).

In arc AM the method for depositing the metal is arc welding. The process of arc welding uses an electric arc to create heat to melt and join metals. A power supply creates an electric arc between a consumable or non-consumable electrode and the base material feedstock, using either direct or alternating electrical currents. The combination of having a metal wire, as the material feedstock, and an electric arc is known as Wire Arc Additive Manufacturing (WAAM) (Williams et al., 2016).

The types of arc welding processes are named following their different heat sources, and these can be categorized as: Gas Metal Arc Welding (GMAW); Gas Tungsten Arc Welding (GTAW) and Plasma Arc Welding (PAW). GMAW offers a higher deposition rate, reaching up to 160 g/min, which makes it an ideal to produce large-sized components in the shortest time (Martina et al., 2019); (Ding et al., 2016b). Furthermore, (Duda and Raghavan, 2016) have observed that GMAW is well-suited for adding complicated features into components larger than half a meter, for manufacturing new parts and for the repair of existing components. In arc welding the printer head is integrated with either a robotic arm or mounted on a gantry motion system.

2.5. Applications of metal 3D printing in Structural Engineering

Looking at how structural engineering applications having a metal feedstock have evolved over the last five years we can predict that 3D printed components are going to be used in construction in a more advanced way. As can be established from the published applications mentioned in this section the capabilities of AM have progressed from redesign to enhancement to onsite applications. As a premier example of a large-scale component, is the MX3D Bridge, which is a 12m span steel pedestrian bridge in The Netherlands (Yalcinkaya,

2018).. This is a world first project to demonstrate the potential of AM in the construction sector (Gardner et al., 2020). The stainless steel printed bridge weights more than 6000kgs (DutchReview, 2021).
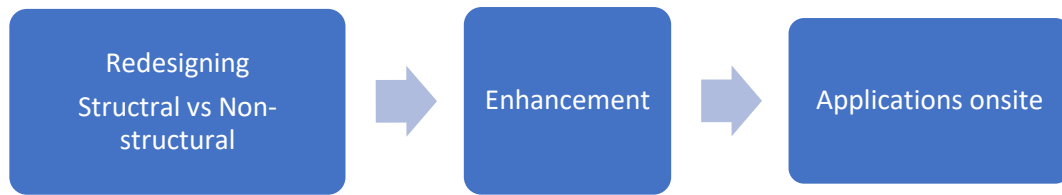
Figure 2-13. Evolution of 3D printed applications

The serial flow chart in Figure 2-13 is for the three stages in 3D printing, which are redesigning, enhancement and application onsite. For many years, conventional manufacturing processing and technologies has provided us with cost-effective engineered solutions in construction using the materials of steel, concrete, timber, etc. 3D printing gives rise to the opportunity to redesign conventional components and structures, that can lead to optimised structural shapes so that form follows force throughout a component or structure. This can provide the benefits of strong aesthetics, less material mass per component or structure and less material wasted, which inherently and positively lowers embodied energy and reduces carbon emissions to satisfy the climate emergency call.

The level of benefits is still to be quantified and is one driver for research and development work such as presented in this PhD thesis.

The redesign stage in Figure 2-13 can be for structural and non-structural components. Examples of non-structural components include a:

- SLS was used to print a 0.6m wide by 0.8m high nylon decorative joint to substitute an existing steel cladding connections (Construction, 2013);
- 1.5m by 4m by 0.1m aluminium window frame with 0.25m by 0.3m by 0.01m steel/aluminium curtain wall brackets (Mrazović et al., 2018);
- 3D printed steel WAAM offshore crane hook of approximate weight of 1000kg, as shown in Figure 2-14, which is usually manufactured by casting or forged techniques (Kanaris, 2018).

For structural elements there have been AM projects to produce scaled-down components. These demonstrators use different AM techniques to demonstrate various of the AM's capabilities. They include:

- an optimised tensegrity node structure, shown in Figure 2-15 (Galjaard *et al.*, 2015);

- the 50 by 50mm cross-section stainless steel stub columns of length 200 mm, shown in Figure 2-16 (Buchanan *et al*., 2017)

- the micro-lattice structures, shown in Figure 2-17 (Ashraf *et al*., 2018);

- a topology optimisation for stainless steel three-branch joints using SLM technology, as shown in Figure 2-18 (Wang et al., 2019a);

- a trifurcated stainless-steel joint, as shown in Figure 2-19 (He *et al*., 2020).

In 2014, the UK consultancy Arup redesigned an existing joint node to be manufactured by DMLS technology. This demonstrator project produced the first printed tensegrity node component (Ashraf et al., 2018). Structural characteristics, cost, and feedstock stainless steel material were investigated by Arup to provide results that can inspire confidence to use 3D printing technology. The node component, seen in Figure 2-15, was made from a stainless-steel alloy and constructed by printed layers of 20 to 100μm thick. Important for structural engineering applications (Galjaard et al., 2015) reports that the chemical composition and physical properties of the stainless-steel alloy satisfy the requirements in BS EN ISO 10088-1:2014 (EN10088-1, 2014).

Regarding academic studies, researchers in the Department of Civil and Environmental Engineering at Imperial College London have used the PBF technology to 3D print several stainless-steel stub columns having the Square Hollow Section (SHS) shape (Buchanan *et al*., 2017). The aim of their research was to test and compare the strength of the streel by the SHS printing with the steel in current SHSs. Micro-lattice structures were printed using EBM and SLM printers at the University of New South Wales (UNSW), shown in Figure 2-17 (Ashraf *et al*., 2018).

The enhancement stage to AM (see Figure 2-13) is illustrated by the printing of optimised dampers. Figure 2-20 show the complex shaped seismic damper from a project at the University of California-Irvine (UCI) (Guell Izard et al., 2017). By choosing AM the traditional multi-layer manufacturing processing was avoided for ease of fabrication, and to achieve the architectural pattern with the required negative stiffness. From this demonstrator project an energy dissipation technique was implemented for the low rise building, such that it had the required resilience to survive an earthquake (Bonessio et al., 2017). This University research shows that AM is capable of printing generic complex shapes that are to resist high-strain rate dynamic loadings.

Other relevant enhancements of AM and the DED processing capabilities is for large-scale components that require multi-directional printings. One example is from Yili *et al*.(Yili et al.,

2018) that is shown by one pipe joint in Figure 2-21. They produced steel pipe joints of up to 700 mm diameter with multi-directional connections for applications in buildings. By using WAAM processing they could vary the diameters of the thin-walled sections for the connecting hollow cylindrical sections.

Furthermore, to provide WAAM components for future construction applications on site, the company Autodesk has developed a mobile cabinet for the WAAM process (Scott, 2018), and because this unit is used to provide the beam-to-column joint, see Chapter 3, it will be introduced in Section 3.4.4.

Figure 2-14. Crane hooks manufactured using WAAM by Huisman (Kanaris, 2018)

Figure 2-15. Re-designed 3D node, optimised by Arup (Galjaard et al., 2015)

Figure 2-16. Stainless-steel printed SHS stub columns (Buchanan et al., 2017)
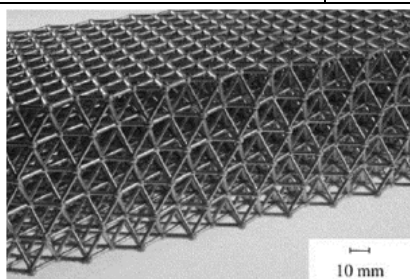
Figure 2-17. Metallic micro-lattice structures (Ashraf et al., 2018)
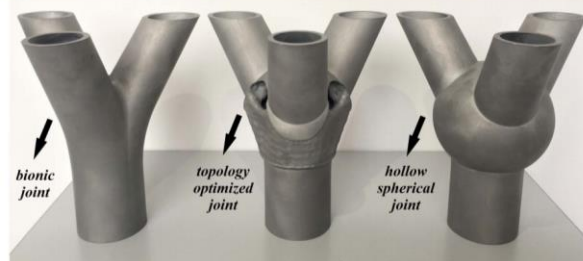
Figure 2-18. Three joint model printed using SLM 3D printer (Wang et al., 2019a)

Figure 2-19. Trifurcated stainless-steel joint (He et al., 2020)
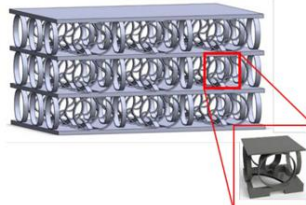
Figure 2-20. Seismic damper, with exploded view of the unit cell (Ashraf et al., 2018)

Figure 2-21. A pipe joint with varying multi-directional diameters joints. (Yili et al., 2018)

2.6. Advantages of AM

AM is an advanced manufacturing approach that is expanding nowadays, but it does not mean it will replace the conventional approaches based on subtractive and formative manufacturing. Each AM approach has its own sets of production processes, with its own set of advantages and disadvantages.

The pros for employing AM in the construction sector can be summarised, according to (Ramadany and Bajjou, 2021) is not limited to: geometrical flexibility; environmentally friendly; reducing resources in terms of time and labour; contributing to solving the housing crises that are happening due to natural disasters (such as earthquakes) or human-made ones (such as wars and their impact on the needs of refugee camps). Furthermore, Wu (Wu et al., 2016) points out that 3D printing can have significant benefits in construction by: reducing construction times (by having machines working longer hours with minimum supervision, in addition to more optimise solutions that needs less material); minimising construction costs and thereby improving affordability; reducing waste; increasing design flexibility. Because geometric flexibility and customisation opportunities are key outcomes of applying AM (Hopkinson *et al.*, 2006) these advantages can allow engineers to design and produce optimised structural components and structures.

The automation in AM processing is very advanced, and this has the positive effect of minimising the number of workers needed on construction sites. A knock-on benefit is that site accidents can be minimised, but new safety precautions will have to be considered. The positive significance of advantages is encouraging for contractors and engineering consultancies to go further with this new technology, as the overall cost will be lower in the long term.

It is likely that WAAM 3D printing will, in the short and medium term at least, complement rather than replace traditional techniques, e.g., by augmenting hot rolled steel beams with 3D printed stiffeners; rehabilitation and maintenance applications.

2.7. Challenges and limitations of AM

AM, which can be used to digitalise the construction industry, is not just limited to the current capacity of the printers. Hardware, software, feedstock material and applicational considerations are continuously being developed, as shown earlier in Figure 2-7 (SmarTech, 2018). (Keating, 2014) says that AM was in 2014 known to have three main processing concerns, and these are for: spatial dimension limitations; material dimension issues; temporal considerations. Nowadays, 3D printing has advanced to overcome these concerns

and we have mobile concrete printers that have resolved these dimensional issues (Sakin and Kiroglu, 2017), and a metal movable cabinet in the progress to be in action (Scott, 2018).

2.7.1. Spatial limitations and why WAAM is used in this research

There are a variety of AM processes, which the construction sector could implement during the early stage of the development for AM applications (Camacho et al., 2018).

Special care is needed when deciding which 3D printing process is, or processes are used with metal feedstock for future structural engineering applications. Printers using the current Powder Bed Fusion (PBF) technologies have known limitations, such as the size of the chamber, overhanging and the post-processing phase (an extra processing stage to sintering the printed metal components can be required).To prevent the PBF printed component from collapsing any overhanging surface requires a supporting element; these supports do help with the dissipation of heat energy and the avoidance of component distortion (Bhavar et al., 2014). Supports, which need to be removed during the post-processing phase, can be generated in the 3D printing using the same or different type of material feedstock (Vayre et al., 2012); (Duda and Raghavan, 2016). Because of the additional challenge of dealing with overhangings, the application of PBF printers is limited in structural engineering. Moreover, the post-processing phase makes it a harder to employ on the construction site. And to add a third reason against PBF printers for this PhD work (Ashraf et al., 2018) found that it was difficult to print horizontal struts.

Structural engineering applications require large-sized components to be printed and the current PBF printer systems are still only for relatively small-sized components. The maximum size of the component to be printed for a project is therefore an essential criterion to considered when choosing the 3D printer.

(Wu et al., 2016) has highlighted that over time that printing technology will advance to meet the needs of the construction sector. To avoid the limitation of spatial dimension, the DED process introduced in sub-section 2.4.2 is most appropriate, as the size of the printing chamber does not restrict the component's dimensions. The six-axis robotic arm used in the DED process can be readily programmed to print much larger and complex-shaped components. Moreover, the deposition rate of steel can reach 9kg/hr, which is significantly higher than that can be achieved by PBF, of 0.2 kg/hr (Zenou and Grainger, 2018). GMAW-based Wire Arc Additive Manufacturing (WAAM) has become one of the most popular processes among WAAM (Xia et al., 2020, Ding et al., 2015a, Pan et al., 2018). GMAW's low

capital investment, flexibility and basic working principle is well known in the industry, which allows its adaptation across different industrial sectors.

2.7.2. Material issues

Metal feedstock for 3D printing range from titanium alloys, nickel alloys to high-grade steel and stainless steels (Duda and Raghavan, 2016). The main printing challenges involve the technical, legal, and financial aspects. Solving the technical challenges (construction material, mechanical strength, durability, corrosion resistance, etc.) are key in building confidence in the end-product; this can be achieved through standardising the manufacturing process.

Although secondary to this PhD project with steel as the construction material, it is comforting to find that 3D printing of concretes has quickly stepped-up, and the state-of-the-art is very promising for AM being applied to produce large-sized components for buildings (Theguardian, 2021). One challenge is that for conventional buildings the design and construction processes are regulated and standardised. New regulations and standards will need to be written to involve, in the same way, building products made by 3D printing. Building houses will be similar to industrial production lines, where precision and automation are also important key elements. Furthermore, (Feng and Yuhong, 2014) highlighted the challenge that a 3D printed material should solidify quickly, to allow printing at a high speed. With recent advancements in the technology, this is not an issue as the print speed can be controlled to ensure that the time taken for the printer head to return-back to the same location for the next layer to be deposited is longer enough for the material to solidify.

Today's limitations, that routinely delay field applications from being brought to market, varies from the lack of technical information on the quality of the final product to the lack of detailed information on the printing process itself (Camacho et al., 2018).

For the design of steel structures the construction sector has the Eurocode suite of standards and for general rules and rules for buildings we have EN 1993-1-1:2005 (BSI, 2005) and for additional rules for the extension of EN 1993 up to steel grades S 700 there is part EN1993-1-12:2007 (BS, 2007). For structural steelwork there are other standards and regulations that must be adhered to. It should be noted that these standards are for grades of structural steel that satisfy standard EN 10025 for hot-rolled products of structural steels and standard EN 10149 for hot-rolled flat products made of high yield strength steels for cold forming. One significant challenge for steel 3D printing is an absence of equivalent standards and an

absence of guidance to benchmark and evaluate AM component performance over the intended design service life. It is important to note here that the types of welding steels that can be employed in the WAAM process will not necessarily give steel material properties that satisfy the Eurocodes.

A recent survey by (Ramadany and Bajjou, 2021) showed that 65.1% of construction companies agree that AM will provide technical and environmental benefits. Less positive was the survey's finding that the absence of standards are going to delay the implementation of AM to a rate of 65% (Ramadany and Bajjou, 2021).

WAAM will be the process used in this PhD work that is presented in this thesis. Not only can it be developed to produce steel components of equivalent sizes found in conventional steelwork, it also gives the potential to optimize structural shapes, so form follows forces. The main limitation with WAAM printed steels today is their unknown short-term and long-term mechanical properties. Therefore, this research aims to study the WAAM characterisation extending the existing knowledge in its structural applications and learning how the printed product will meet the current standards.

2.8. Method of non-destructive evaluation for the internal structure

Different techniques, such as radiography and liquid penetrant inspection (Lopez *et al.*, 2018), have been used in the past for the non-destructive examination of AM components. X-ray Computed Tomography (X-CT) is utilised in this research to inspect integrity and identify any internal defects, for Quality Control purposes. The main advantage of using X-CT over other non-destructive methods is its ability to give a 3D visualisation of the internal pores, which will enable the author to carry out the volumetric identification of inclusions and porosity. Also, X-CT has the capacity to locally capture varying steel densities within printed components.

X-CT is a scanning and analysis method by which it is practical to image the interior of a solid object in a non-destructive manner. It uses the principles of X-ray radiography to produce a 3D volume for the interior geometry and configuration of an object. It is popular for non-destructive testing in a range of different industries.

After X-CT revolutionised the field of medicine in its ability to provide detailed internal information, Copley recorded its non-medical applications in the late 70's in (Copley et al., 1994), such as locating and identifying the orientation of the embedded fibres in the 'carbon-fibre composite' I-beam (see Figure 2-22-a). In the casting industry, X-CT was also used as a

defect detection tool for shrinkage and porosity (as shown in Figure 2-22-b) where the pores could be found and measured by analysing the black spots.
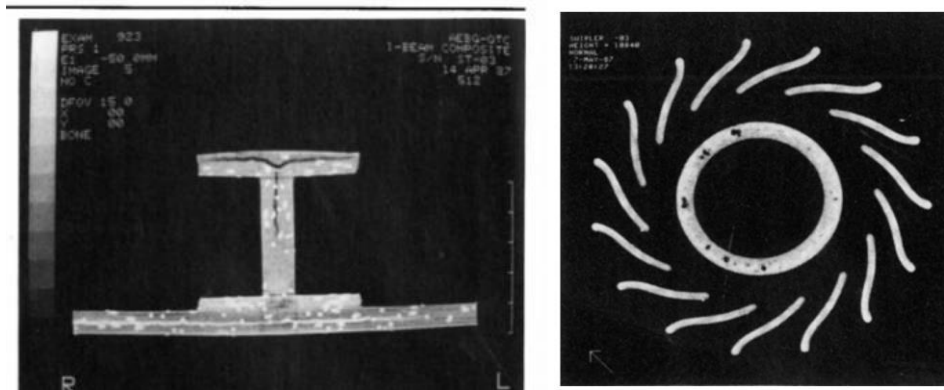
Figure 2-22. An X-CT scanned 'carbon fibre composite' I-beam section to show the orientation of the glass fibres in white and the ply separation, b - Location of pores in a steel casting (Copley et al., 1994).

Currently, many industries - including aerospace, automotive, material science and civil engineering - have adopted X-CT as a Quality Control method for AM products; so far it is the only technology for measuring the inner and outer components of an object without needing to cut it (Kruth et al., 2011). The use of X-CT in the AM industry aids the characterisation of manufacturing defects, forensic examination of fatigue and failure, as well as calculating the percentage of porosity and volume fraction (both of which are investigated in Chapter 5).

2.9. Concluding Remarks from Literature Review

In this literature review, an overview has been provided on the history of Additive Manufacturing (AM) techniques, their application in engineering sectors, and how the technology is playing its part in the fourth industrial revolution. The development of AM within the construction sector has been captured by the milestones reached with concrete materials as the 3D printing feedstock. By considering structural engineering applications of metal printed components there has been an evolution from redesign to enhancing manufacturing processes. Nowadays, the advancements are demonstrated by the potential for AM to be used to produce large-sized steel components, as shown in Figure 2-14 to Figure 2-21, that could exceed 12m, such as the MX3D bridge (Yalcinkaya, 2018).

The limitations and advantages of the different types of metal printers have been highlighted. For metal printing we can use either a Powder Bed Fusion (PFB) or Direct Energy Deposition (DED) process. DED has been chosen for this PhD work, primarily, because of its capacity to print large-sized components at a higher metal deposition rate. Had the PBF

process been chosen component size would have been limited by size of the PBF chamber and the cost higher owing to a lower deposition rate in comparison to DED.

Not only does 3D printing offer the ability to manufacture appropriate steel components, but potentially it also has the advantages of being able to produce optimize structural shapes, print bespoke components, employ automation, and reduce the need for on-site skilled welders. However, the literature review shows that there are limitations regarding knowing the material properties and having the necessary industry standards and regulations. To transfer the advantages of AM into the world of structural engineering, it is necessary to build confidence, and to do this new research and development is required to achieve this goal by filling-in the existing gaps in knowledge.

The research presented in this PhD thesis will offer knowledge and understanding for using WAAM to print 3D steel components. The non-destructive non-contact examination utilised in this study, to inspect the coupon integrity and identify internal defects, is X-ray Computed Tomography (X-CT). Results from this structural engineering research will be used to develop standard operating procedures, understand the material properties of the WAAM components and to benchmark the WAAM steels against what the current structural design codes require of structural grades of steel. It is the expectation of the author that two important outcomes are going to be the advancement of the WAAM process towards producing larger-sized components and the establishment in confidence for choosing WAAM to produce structural steel components in, say, buildings and bridges.

3. Chapter Three: Manufacturing of Seven WAAM-GMAW Components

In this chapter the author will describe the steel WAAM printing process and requirements to produce several components, in the light of what has been previously manufactured (Galjaard et al., 2015) (Mrazović et al., 2018) (Yili et al., 2018), (He et al., 2020), or with more complex 3D geometries for future applications in the construction industry. Additionally, the need for having a non-destructive test method as a quality control technique will be highlighted.

3.1. Introduction

The Wire Arc Additive Manufacturing (WAAM), which is one of the Direct Energy Deposition techniques, is the Additive Manufacturing (AM) tool chosen for this project due to its ability to produce complex and sizeable 3D printed components. WAAM technology requires multidisciplinary research teams (including a material scientist, welding specialist and machine controller) to produce end-product components. In this PhD research a quality control approach is carried out using X-ray Computed Tomography (we will use abbreviation X-CT) scanning facilities belonging to Centre for Imaging, Metrology and Additive Technologies (CiMAT) within Warwick Manufacturing Group (WMG), to investigate any internal defects in the produced components.

In this project, WAAM facilities from three different collaborators – Autodesk (based at the Birmingham office), Steelo (London) and RAMLAB (Rotterdam, and in collaboration with Delft University of Technology) - were involved at separate stages. These external contributions enriched the author's research because it enabled the study of different types of welding steel wires as a WAAM. The sizes and shapes of the printed thin-walled components (shown in Figure 3-1) comprise: a 345 by 165 by 20.5 mm horizontal flat plate (Autodesk); two walls 300 mm long having height of 30 mm and a thickness of 10 mm (Steelo); a 350 by 170 by 10 by 40 mm Rectangular Hollow Section (RHS) having a nominal wall thickness of 10 mm and a 40 mm height (Steelo); 350 mm long sections of a stub column of 200 by 200 mm with wall thickness of 11 mm (RAMLAB); a monolithic beam-to-column joint weighing 36 kg (RAMLAB). In this thesis, the author uses the single word 'joint' to refer to this unique 'steel beam-to-column joint' component. Note that the dimensions are nominal and are those specified in the CAD software used to print the components.

The manufactured components can be categorised by either the redesigning or enhancement stage as shown in Figure 2-13 in Section 2.5 of the literature review. The plates

printed horizontally or vertically belong in the enhancement category. We note that the horizontally printed plate could be the method for printing in rehabilitation applications, where an additional thickness of steel is needed critically at, for example, inaccessible locations. The vertically printed plates could be employed to produce fins attached to main beams (for example, in a composite floor structural scheme to connect to secondary beams) as an automated welding process because it minimises the necessity for the skilled welder. Components consisting of the RHS, the stub column sections and the joint, are for the redesign stage in the evolution of 3D printed applications.
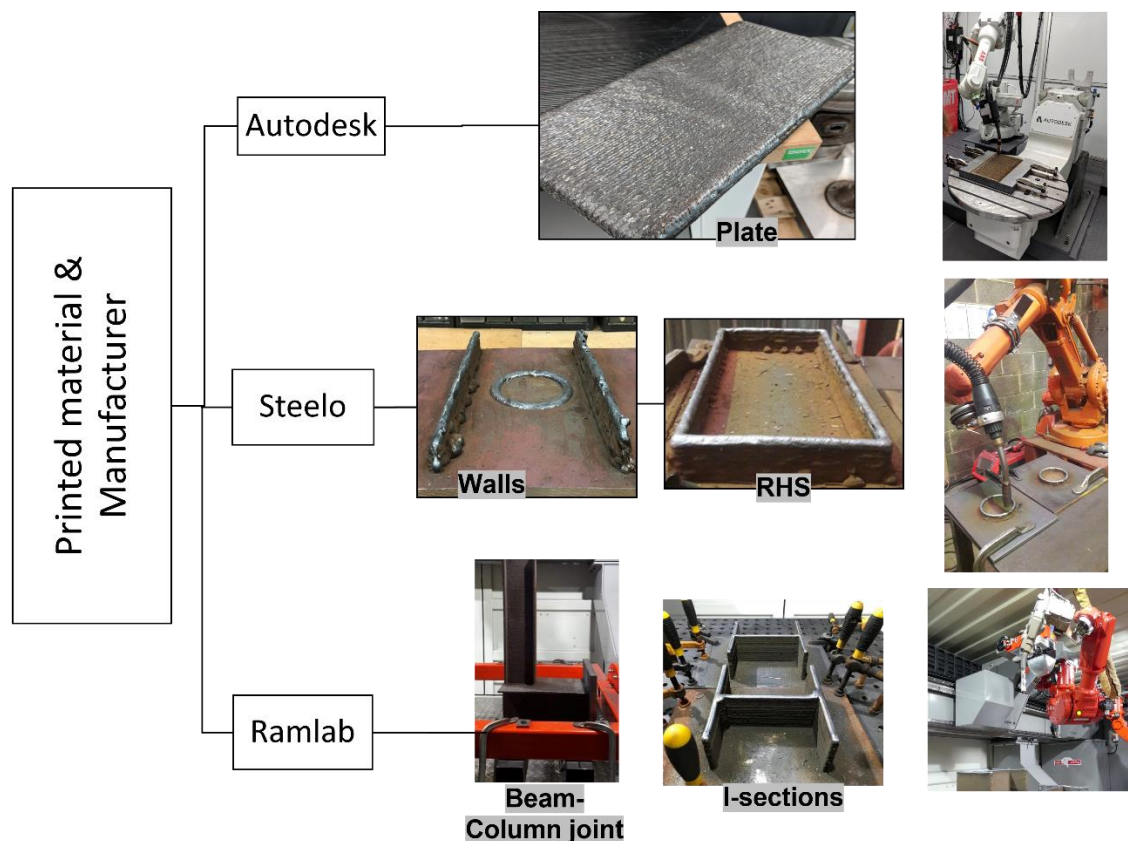
Figure 3-1. A summary of the collaborators with their printed components and used tools.

The thin-walled components will be used to extract dog bone tensile and impact test coupons for mechanical property characterization to be referenced against specification properties for structural steel in standard *Hot rolled products of structural steels* (EN10025-1, 2004), which will be explained in detail in Chapter 4. Furthermore, the joint was printed to study the rotational capacity of this moment resistance joint, with reference to 5.2 in standard *Design of steel structures–Part 1–8: Design of joints* BS EN 1993-1-8:2005. This aspect of the research is presented in Chapter 6.

X-CT scanning (see sections 2.8, 4.5 and 5.2) was also adopted in this research, to examine the internal integrity of the printed components, to ensure the reliability of the printed steels and to explore the effectiveness of the chosen printing strategy, in producing a 'solid' homogeneous material with minimal porosity. It is important for quality control in 3D printing of steel to know of the presence of pores. Result from X-CT scans will be presented in Section 5.2 and Section 6.2. Knowing what porosity is present in the components described in this chapter will permit their effect on the steel's mechanical properties, to be investigated and characterization work for this investigation is reported in Section 5.5 and Section 6.5.

Additive metal manufacturing is a sensitive multivariable process and requires carefully combining various parameters (such as heat, printing speed, type of gas and type of wire as will be discussed later) to avoid internal defects.

3.2. Hardware for WAAM-GMAW printing

WAAM is an AM technology that integrates an arc welding system with a robotic arm or gantry motion system. The heat source used in the WAAM technique is the electrical arc, used to melt the steel wire and form a welding deposition. Gas Metal Arc Welding (GMAW) has become one of the most popular welding processes amongst other WAAM techniques (Martina *et al*., 2019), as a result of its low capital investment and well-established principles in the industry. In this thesis the printing process employed will be referred to by the abbreviation WAAM-GMAW.
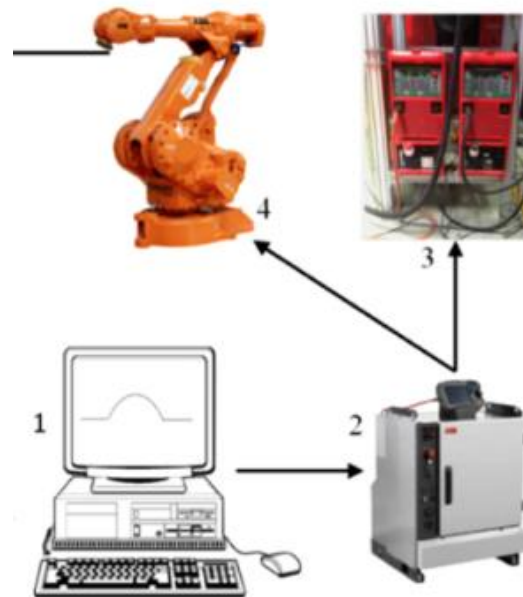
Figure 3-2. Main WAAM tools: (1) computer with operating software; (2) robot control unit; (3) GMAW welding processor; (4) robot with weld torch at end of arm (Ding *et al*., 2015a).

30

Figure 3-2 summarises the typical robotic WAAM-GMAW set-up where the welding torch contains a wire feeder and a gas inlet. Initially, a computer interface (1) is used to programme the printing path and design the printing process for the component. Then the G-code is transferred to the robot controller (2), which coordinates both the welding process and the robot motion. Also, a programmable GMAW welding processor (3) and a robot (4) combined to carry out the 3D printing with welding steel.

As seen in Figure 3-3 ABB robots at the Autodesk 3D printing cell facilities (in Birmingham) and Steelo (in London) were used for printing in this research. The 3D printing rooms consist of the main WAAM-GMAW set-up to run the printing process (shown in Figure 3-3) and the kit comprises of a robot controller, external positioner (manipulator), robot arm, wire feeding system and weld torch gas bottles.
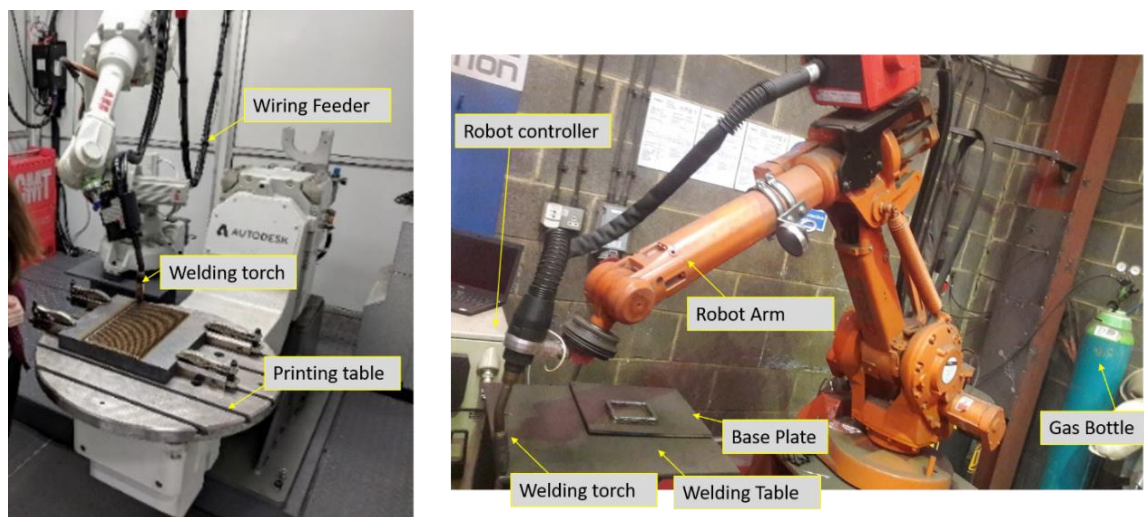
Figure 3-3. WAAM-GMAW printing set-ups: (a) at Autodesk; (b) at RAMLAB.

Printing in The Netherlands was carried out at RAMLAB facilities in Rotterdam, using the Autodesk mobile system developed to enable onsite printing for civil engineering works. The kit is shown in Figure 3-4, which has overall internal dimensions of 2.2 m wide, 2.5 m high and 5.8 m in length. The figure shows that the Autodesk container consists of two robotic arms (Panasonic TS-950 with the integrated TAWERS welding power source controller), an external manipulator with a two-axis, and a movable welding table. The six-axis robot, which is hung from a gantry system, increases the coordinate flexibility. The weld torch at the end of the robot arm is connected to a wire feeding liner (see the yellow cable) and a gas pipe. The gas flow and the speed of the fed wire can be adjusted during the printing process to keep the ignition running, and to maintain stable arc.
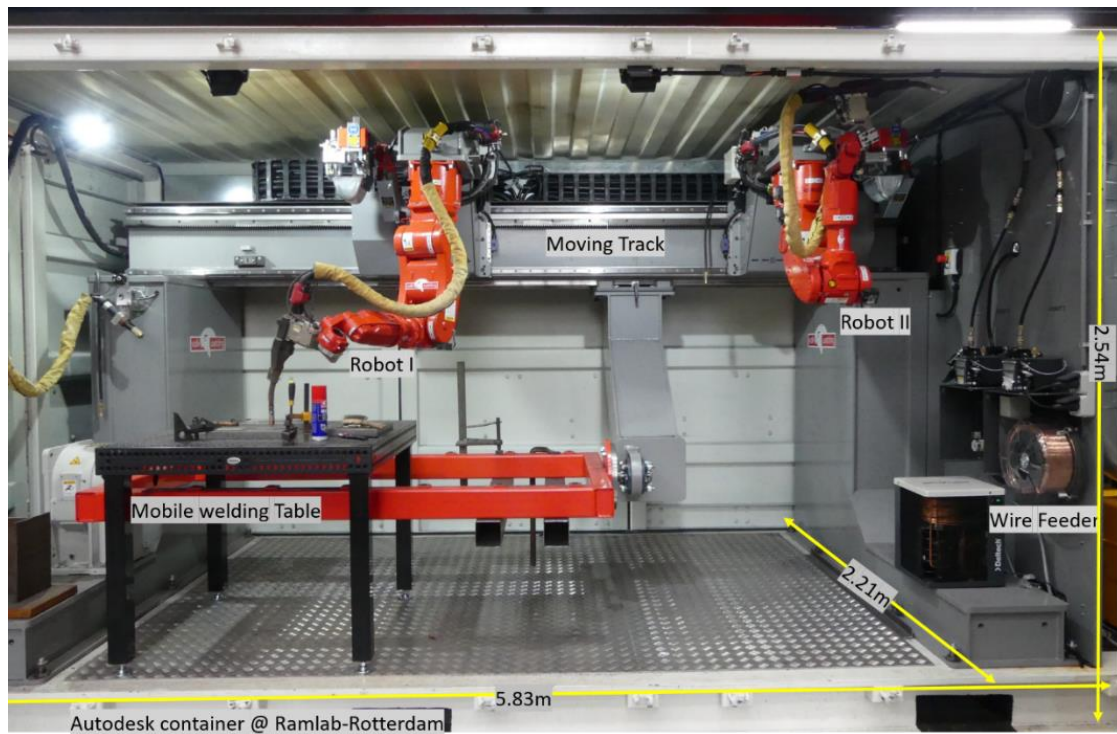
Figure 3-4. The arrangement inside the Autodesk shipping container.

3.2.1. Types of steel wire and gases used

Several types of steel welding wire were used to produce the WAAM-GMAW components, as summarised in Table 3-1. Columns 1 to 3 in the table present the main properties of the three wires used at the collaborator's facilities of Autodesk, Steelo and RAMLAB. Rows 1 and 2 give the wire's name and its designation. Rows 4 to 6 reports the mechanical properties for tensile and yield strength, and elongation after fracture. Finally, row 7 gives a summary of main application for the steel wire. Appendix 3.1, Appendix 3.2 and Appendix 3.3 provide more details on the steel wires that are of secondary importance.

With reference to standard *Welding consumables-wire electrodes and weld deposits for gas shielded metal arc welding of non-alloy and fine grain steels - Classification* (ISO 14341:2010), the deposition produced using gas shielded arc welding the letter **G** will be at the beginning of the designation, as a symbol for being used in the GMAW process (ISO14341, 2010). In row 2, the symbol **G** is highlighted in **bold** font to assure that the printing needs to be the GMAW process.

Table 3-1: Description and properties for the three steel welding wires used in the research

Manufacturer	Autodesk 1	Steelo 2	RAMLAB 3
Name	Welding grades of steel: Union K 40 steel	Copper-coated solid wire for welding C&C-Mn steels	SupraMig Ultra HD-Mild steel solid wire
Wire designation	EN ISO 14341-A **G** 35 A M23 Z2Si1	EN ISO 14341-A **G** 46 4 M21 3Si1	EN ISO 14341-A **G** 46 3 C 4Si1
Diameter (mm)	1.2	1.2	1.2
Ultimate tensile strength (MPa)	440	560	650
Yield strength (0.2%) (MPa)	360	470	500
Elongation % ($L_0=5d_0$)	25	26	26
Applications	Used primarily in vehicle and autobody fabrication	Include tanks, boilers, structural steel works, earthworks and construction works	Heavy duty and high deposition applications, e.g., in the marine industry

In the aforementioned ISO standard, the type of wire is classified based on its tensile and impact properties. The symbol (A or B) in the designation is related to the value of impact energy for the deposited welded steel. The impact energy is 47J when the symbol is A, while symbol B represents the lower impact energy of 27J. As for the tensile strength, the number after letter G is for strength and elongation properties. As an example, the RAMLAB wire has, in column 3, the designation of EN ISO 14341A **G** 46 3C 4Si1. Here the number, 46, defines that the minimum yield strength is 460 MPa, as reported in Table 3-2. Table 3-2 also specifies the ultimate tensile strength range and the minimum elongation (direct strain) at tensile rupture. The underlined symbol 'C' indicates the type of shielding gas used, where C is for a gas mixture containing Carbon dioxide, as outlined in the standard *Welding consumables – Gases and gas mixtures for fusion welding and allied processes* (ISO-14175, 2008). The suffix '4Si1' describes the chemical composition of the wire. It is noted that because the various types of steel wires have different chemical ratios, welding can require different mixture ratios in the gas composition.

Table 3-2: Strength and elongation properties of A-G46 wire, taken from (ISO14341, 2010)

Temperature (℃)	Min. yield strength (MPa)	Ultimate tensile strength (MPa)	Min. elongation (%)
20	460	530 − 680	20

As an example, the Ferromaxx® Plus shielding gas, used in the RAMLAB WAAM-GMAW process, had an average gas flow rate of 22 litres/min. At Steelo the gas was Argoshield light BOC-M21 with a flow rate of 15 litres/min. These two shielding gases have the chemical composition presented in Table 3-3, which is provided in the supplier's datasheet. For commercial reasons the author is not permitted to report the WAAM-GMAW processing parameters for the Autodesk printed flat sheet.

Table 3-3: Chemical composition of the shielding gas (% in volume)

Type of shielding gas	Ar	He	CO_2	O_2
Ferromaxx® Plus 4M (RAMLAB)	68	20	12	-
Argoshield light BOC-M21 (Steelo)	93	-	5	2

3.3. WAAM-GMAW printing parameters, path planning and printing strategy

WAAM-GMAW printing is characterised by laying down a path strategy beads to run the welding steel. To be able to print to a tight 3D geometry, that with steel is often thin walled, requires careful choice of printing parameters, and careful control of the printing strategy that includes path planning. The printing process comprises of different steps, namely: path planning; printing strategy; selection of the printing parameters. The printing process can be categorised into two main approaches, the closed and the open-looped control systems, that are summarized in Figure 3-5. The closed system of Figure 3-5(b) incorporates real-time slicing and path planning for each layer, thus being adaptive and flexible in compensating for the changes during the printing process, such as the ability to adapt to changes in the layer thickness. While the open-looped system of Figure 3-5(a) does not have feedback control, so the error could be larger. For example, in the presence of pores during the printing, if it was a closed system, the system will send feedback to highlight this. Owing to the complexity in designing the minimum path times to print each layer and thereby the component and controlling the deviations during the printing process after depositing the weld beads of steel, the open-looped system is used in this research since closed systems are not as developed.
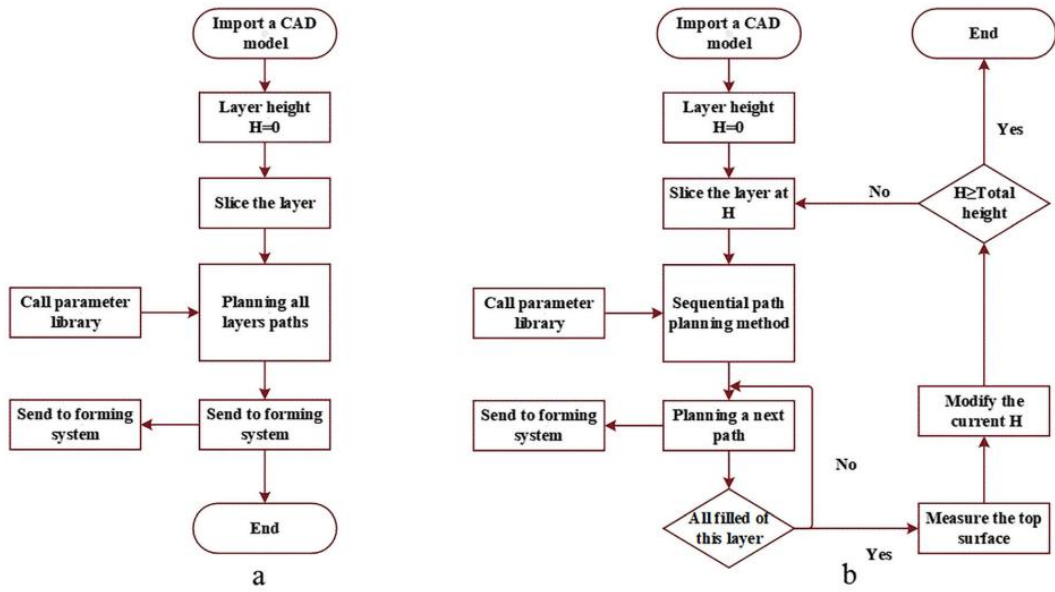
Figure 3-5. Flow chart for WAAM Printing Process: (a) opened loop; (b) closed loop (Wang et al., 2019b).

3.3.1. Printing Parameters

The process of welding is known to have essential, supplementary, and non-essential variables, as defined by the welding code (QW-251, P.76-ASME section IX). The WAAM-GMAW printing process, which follows the same principles as the conventional welding process, is set-up with a specification of the following key parameters: Travel Speed (*TS*); Wire Stick-out Length; Tip-to-work distance; Voltage (*V*); Amperage (*A*); Wire Feed Speed (WFS); Shielding gas; Filler material (ex; steel wire), etc. The interaction between these aforementioned parameters has a key impact on the geometry of steel beads after welding, and on the mechanical properties of the weld steel, comprising of a number of consolidated layers.

In the welding process we start with wire of circular cross-section and diameter 1.2 mm (see row 3 in Table 3-1). The deposited beads have a parabolic cross-section shape, which will be a function of the chosen WAAM-GMAW parameters. At Steelo, six single beads were printed of different widths and heights as seen in Figure 3-6, and the changes observed are directly linked to the set-up parameters, and in this experiment to the voltage for weld temperature and travel speed. The travel speed is the speed at which the welding torch moves along the planned path for laying down the bead.

35
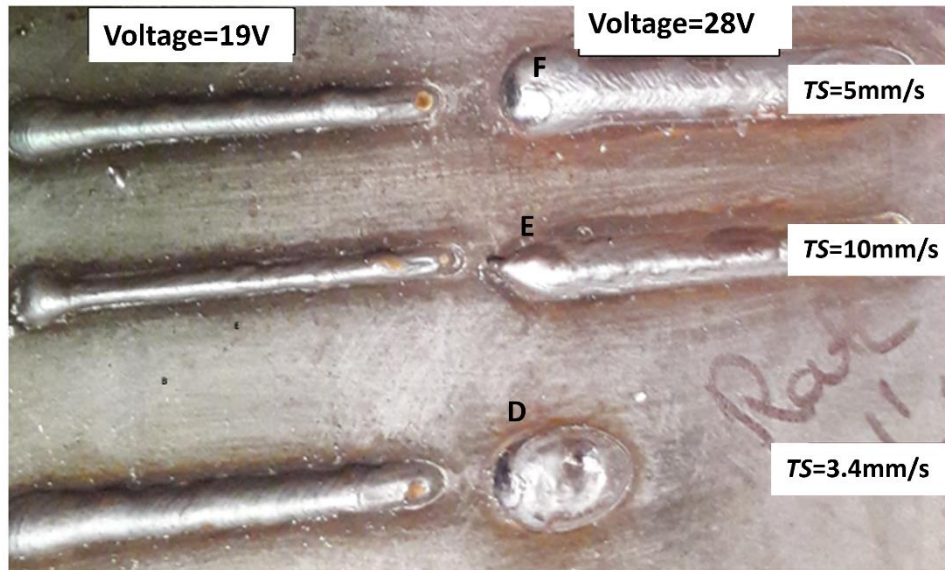
Figure 3-6. Welded beads for various Voltages (*V*s) and Travel Speeds (*TS*s); (A) 19 V and 3.4 mm/s; (B) 28 V and 10 mm/s; (C) 19 V and 5 mm/s; (D) 28 V and 3.4 mm/s; (E) 28 V and 10 mm/s; (F) 28 V and 5 mm/s.

The welder controller is calibrated to ensure that the ignition energy is sufficient to melt the steel wire, and it is able to control the WFS, which inherently changes the voltage (*V*) and amperage (*A*) values. When WFS is set to 5 m/min, the *V* and *I* is 19 V and 173 A, respectively. By doubling the WFS to 10 m/min, the printing parameters for *V* and *I* adjust to 28 V and 300 A, respectively.

Table 3-4 records the effect of changing WFS and TS on the heat input for the six deposited beads. The heat energy per millimetre of wire is reported in the last row is a function of the *I*, *V*, *TS* and η, the thermal efficiency coefficient, which is dependent on the welding process. Heat input is calculated from:

$$H = \eta \frac{I \times V}{TS} \tag{3-1}$$

Column 1 in Table 3-4 defines what information is reported in columns 2 to 7 for the six beads in Figure 3-6, which are named A to F. The three TSs investigated are 3.4, 5 and 10 mm/s and they are recorded in columns 2 to 7 and the fourth row of the table. Using Equation 3-1 the values of *H* in the last row were calculated, taking η equal to 0.8, for GMAW.

Table 3-4: Impact of changing the Wire Feed Speed and Travel Speed on the heat input per millimetre of welded bead

1	2	3	4	5	6	7
Bead	A	B	C	D	E	F
WFS m/min	5			10		
TS mm/s	3.4	10	5	3.4	10	5
Heat Input, H (kJ/mm)	0.97	0.3	0.66	2.47	0.84	1.68

After experimenting with the initial printing parameters for depositing a single bead, the WAAM-GMAW parameters were further modified until the aspect ratio for the bead width-to-height satisfied the recommendation from (Ya et al., 2013). It is preferable for the aspect ratio to be > 4, such that the shape of the beads is suitable for overlapping beads because this minimises inter-run-porosity at the weld toe and generates a smoother surface with proper overlap distance (without a deep valley). Subsequently, the following conditions were considered during the selection of the printing parameters, to ensure that:

- the arc was stable, so that the droplets of welding steel remained located in their intended positions;
- all the steel in the droplets had melted on deposition;
- each bead is continuous, well spread and has clean weld toes.

The geometry of a single bead is a key processing outcome to optimise both overlapping of beads in the horizontal plane and for the multi-layering printing in the vertically direction. Table 3-5 presents terminology that is used to explain the optimisation of WAAM-GMAW printing for multi-bead layers.

Table 3-5: Description of terminology used explain the optimisation of WAAM-GMAW printing

Parameters 1	Description 2	Figure 3
Wire Stick-out Length (WSL)	Wire length from contact tip of weld torch to surface the component, given by X mm in Figure 3-7.	
Wire Tip-to-work Distance	Distance from the end of the wire tip and the surface	Figure 3-7. Stick-out Length and Tip-to-work Distance
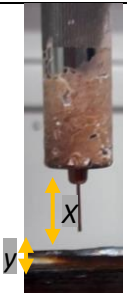
	the component, given by Y mm in Figure 3-7.	
Single bead	Deposited bead with a parabolic shape. In Figure 3-8, its variable width is w and height is h.	Figure 3-8. Single beads showing parabolic shape
Multiple beads	Overlapping of single beads; horizontally overlapping is shown in Figure 3-9 and vertical overlapping is shown in Figure 3-10.	Figure 3-9. Overlapping beads and step-over distance
Step-over distance	Lateral displacement for the overlapping of the beads, presented as distance d in Figure 3-9; it's a function of the weld bead width.	
Step-up distance	Distance the robot moves vertically (in the direction of building-up the layers), as illustrated by the vertical yellow arrowhead in Figure 3-10.	Figure 3-10. Overlapping beads and step-up distance
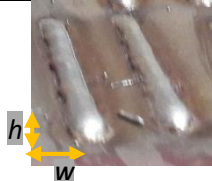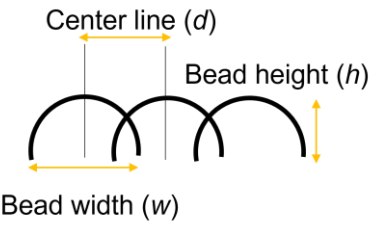
The Stick-out Length and Tip-to-work Distance is > zero and less than 1mm to ensure that the steel wire can act as a current transmitter to start the ignition. Excessive Wire Stick-out Length (WSL) of X mm > 15mm can cause the steel deposition not to fuse together properly, because melting is not fully completed. When this processing weakness is present the required homogeneous bead is not produced, and two examples are shown in Figure 3-11(a) and Figure 3-11(b). Figure 3-11 illustrates the impact of increasing the WSL, which increases the resistance. Using the equation $V = IR$ we know that if voltage is constant the current, I must decrease when the WSL increases. As a result, the total heat input per unit time, by Equation (3-1), to melt the wire and produce a continuous and well spread bead, is reduced.

(a)   (b)

Figure 3-11. Beads when there is insufficient heat energy input for the wire to completing melt, caused by excessive stick-out distance.

However, a relatively short WSF will lead to a lower resistance, allowing for higher current and consequently higher heat input per unit time. Figure 3-12(a) illustrates the impact of exposing the bead to higher temperatures that exceeds 150 °C, which is the interpass temperature for the welding recommended in BS EN ISO 14341. Overheating is known to weaken the steel and could lead to material defects such as the pores that can be seen on the surfaces of the printed layers in Figure 3-12(a) and 3-12(b).
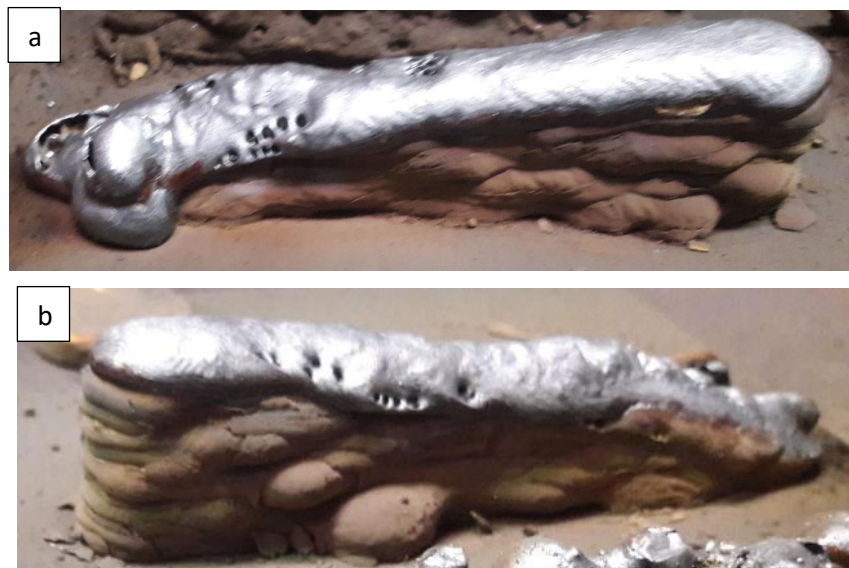
Figure 3-12. First iteration of printing at Steelo to choose the step-up distance, showing defects: (a) effect of overheating; (b) geometric inaccuracy.

In addition to setting-up the WSL, the step-up distance for a single pass bead (see Figure 3-10) was next considered. Optimising this distance between the next printed layer helps minimise the dimensional error in the vertical build direction. In Figure 3-12, the dimensional discrepancy between the layers is well observed through the fact that both vertical walls are

39

sloped, despite having a constant number of the layers in their heights. As observed from the photographs in Figure 3-12 there is molten steel overflow before the steel solidifies, owing to the WSL being too short and the heat input thereby being too high. Overflowing is largest at the ends of the bead length where the heat is highest. Section 3.4.2.1 on the Printing Parameters for the RHS explains how a wall can be printed that avoids melt overflow.

If the step-up distance is too large (~ >1.5 X layer height), there will not be sufficient bonding between the beads because of a lack of fusion in the overlap regions. Because the tip of its parabola prevents each printed layer from having a proper interaction between the subsequent layer, and therefore an interfacial layer is formed, as seen in Figure 3-13.
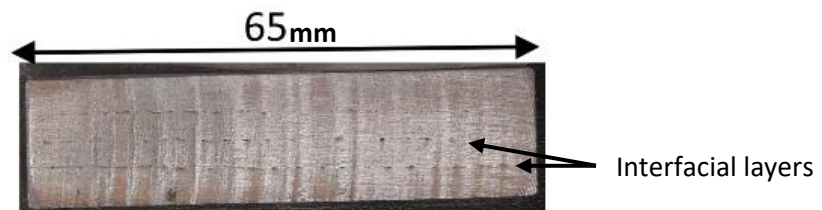
Figure 3-13. Interface between the printed layers.

Similarly, for the horizontal spacing between bead runs within a printed layer, known as the step-over distance and given by *d* in Figure 3-9, has to be optimised. Having the correct *d* of ~1.2-layer height helps in forming a smoother and homogenous welded surface.

Figure 3-14 shows how the thickness of wall, printed at Steelo, can vary giving a pronounced surface roughness over the height of the wall due to the chosen Step-up distance.

Figure 3-14. Variation in the thickness and surface roughness up the printed wall.

All the previously mentioned WAAM-GMAW processing parameters influence the built-up geometry of the printed component. If the parameters are not sufficiently optimised, the printed component can suffer from higher porosity (Figure 3-12), lack of fusion and interface between the layers (Figure 3-13), excessively rough surfaces (Figure 3-14), or overflow before solidification (see Figure 3-12(b)).

3.3.2. Path Planning

The tool path is the route that the weld torch takes so that weld steel is deposited uniformly over the area of a layer. Because there is more than one path to choose from, a key variable with WAAM printing is the tool path. Nine variations for a tool path pattern are illustrated in Figure 3-15(a) to 1-15(i). These have been developed for WAAM path planning from welding strategies and the three patterns illustrated in parts (g) to (i) of Figure 3-15 are recent developments specifically for WAAM path planning (Ding et al., 2015b, Ding et al., 2016a).
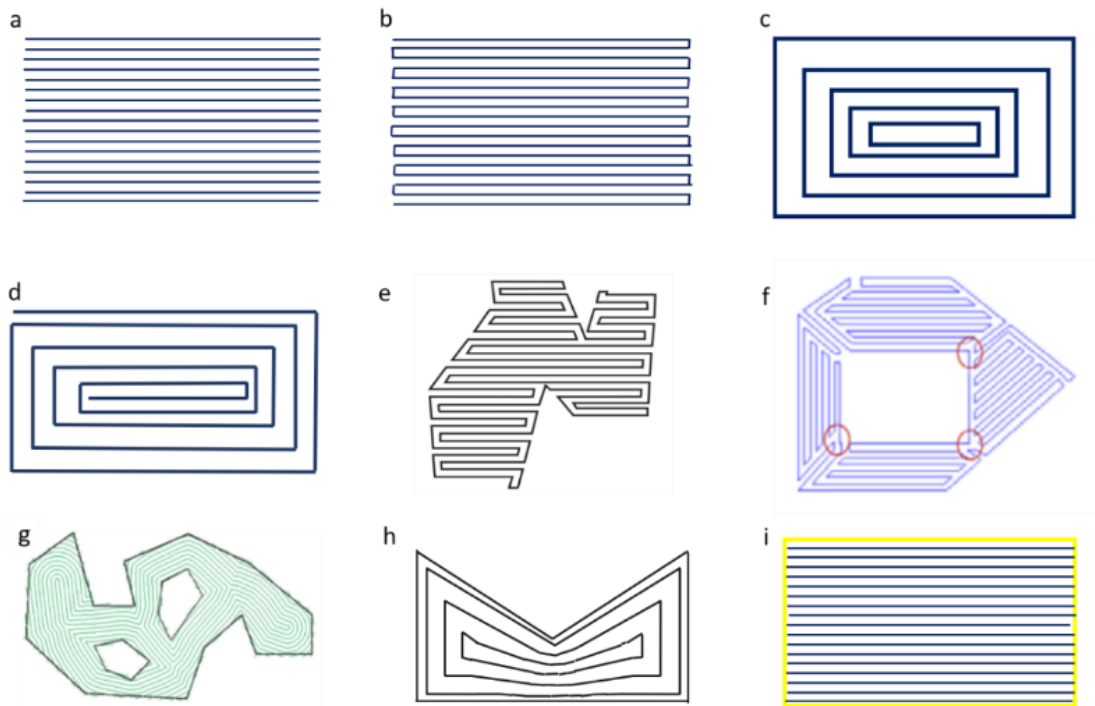
Figure 3-15. Path planning patterns: (a) Raster; (b) Zig-zag; (c) Contour; (d) Spiral; (e) Continuous line (Dwivedi and Kovacevic, 2004); (f) Convex polygon (Ding *et al*., 2014); (g) Medial axis transformation (Ding *et al*., 2015b); (h) Adaptive medial axis transformation (Ding *et al*., 2016a); (i) Hybrid.

The path planning patterns illustrated in Figure 3-15 have been categorised in three main groups.

Table 3-6 summarises these groups. The first group, for patterns (a), (b), (e) and (f), is for the linear path patterns, which originated from the raster pattern and was developed into zigzag, spiral, continuous line, and convex polygons. The second group is for contour patterns, and involves the three patterns (c), (g) and (h), showing that contouring has evolved into medial axis and adaptive axial transformations. The third group is the hybrid group, with pattern (h), which is for a combination of the patterns from the other groups in different areal regions within the layer.

Table 3-6: A brief description for nine path patterns, its development and its limitations

Category 1: Linear Path Planning		
Raster	Figure 3-15(a)	Fills in the area with equally spaced parallel lines, with the offset parallel to the printed direction as seen in Figure 3-15(a), to form a complete path based on the scanline filling algorithm from (Dunlavey, 1983). This pattern requires arc off and arc on steps for each new weld bead run with robot movement without welding. Such steps to reposition the weld torch will increase the printing time per layer.
Zigzag	Figure 3-15(b)	Fills in the area with a zigzag path, as illustrated in Figure 3-15 (b), which requires reversing the printing direction, but without any arc off/arc on steps (Rajan et al., 2001). which is for covering the area of a layer with a single continuous bead run, which, for the same layer area, will take less time to print than by the raster pattern.
Spiral	Figure 3-15(d)	Prints a rectangular shaped area using a single continuous bead run with a spiral pattern going from perimeter to centre of layer. As can be seen from a spiral in Figure 3-15(d) this pattern has no intermediate arc off/arc on steps to complete the printing of each layer.
Continuous line	Figure 3-15(e)	The approach subdivides the plane into a set of polygons, by subdividing the contour into smaller polygons (sub-polygons); to generate a continuous path for material deposition. The final torch path is obtained by connecting individual paths for all the sub-polygons and trimming along the points of intersection of the paths to form an individual sub-polygon (Dwivedi and Kovacevic, 2004).
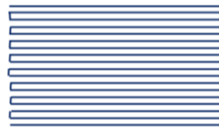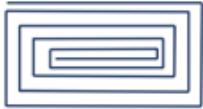
Convex polygon	Figure 3-15(f)	As shown by the example in Figure 3-15(f) the area to be printed is divided into several sub-convex, where a zigzag path for each sub-area is generated for printing a sub zone with a continuous bead run (there are no arc off/arc on steps).
Category 2: Contour Path Planning		
Contour	Figure 3-15(c)	As illustrated in Figure 3-15(c) this pattern uses the principle of plotting contours of closed bead runs that require one arc off/arc step per contour. Starts with the outer and/or inner contour, and offsets accordingly at a fixed bead width distance to print the area. Farouki *et al*. (Farouki et al., 1995) wrote a software algorithm to readily implement the contour path pattern.
Medial Axis Transformation (MAT)	Figure 3-15(g)	Instead of starting with either the outer or inner contour, the MAT pattern first calculates the central axis of the printed layer and starts printing from this reference point with bead offset for next contour.
Adaptive medial axis transformation	Figure 3-15(h)	For the adaptive medial axis transformation pattern the MAT method is further developed to consider the welding parameters and its bead width, through an algorithm developed by (Ding et al., 2016a).
Category 3: Hybrid Path Planning		
Hybrid	Figure 3-15(i)	In the example illustrated in Figure 3-15(i) the outer border of the printed area used the contour patten (yellow bead run), while a raster pattern (black lines) is used to print the interior layer area.
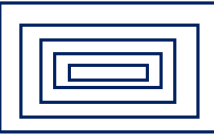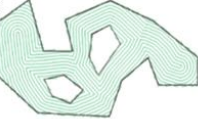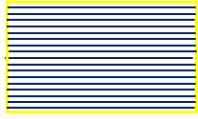
As will be presented in section 3.4 the linear path patterns of raster is used to print layers in the joint, vertical walls, I sections and horizontal plate components for this PhD work. While contour was used in manufacturing the RHS component. The choice for the raster printing paths is because this type of path planning is for multi-pass welding, which is an industry-accepted technique in the construction sector. Note that had the second grouping of contour

patterns been employed the width of the weld beads could have resulted in deficient filling of a layer. The effects on quality of printing monolithic steel from the interaction of heat input (to melt steel wire) with other WAAM-GMAW parameters will be discussed in Section 3.4.

3.3.3. Printing Strategy

The geometry of the solid object to be printed is sliced by an algorithm, that allows it to be printed layer-by-layer from the bottom to the top. There have been different models developed as slicing methods for layer segmentation such as: step wise refinement slicing (Sabourin *et al.*, 1996), adaptive slicing of Moving Least Squares surfaces (Yang and Qian, 2008) and an adaptive algorithm and data format for functional graded material (Wang et al., 2013) etc.

The slicing algorithm, to convert CAD models into accumulated layers along the height direction of the models, can be divided into simple plane, surface, and multi-directional slicing. The simplest method of slicing is the fixed direction slicing method, which performs layer slices of constant thickness, whilst the multidirectional slicing algorithm can change the printing direction but maintaining the thickness of the sliced layers. Therefore, the multidirectional slicing approach is more suitable for complex parts than the fixed direction slicing method.

The surface slicing algorithm is used to reduce the need for a supporting structure as the printed part will not have any overhanging edges. This method has the feasibility to follow the surface whether it is curved, cylindrical or non-planar. Hence, the surface slicing method has been widely used in non-metal AM and different tooling paths have already been developed such as Curved Layer Fused Deposition Modelling (Chakraborty *et al.*, 2008) and a decomposition-based curved surface slicing strategy and a transformation-based cylinder surface slicing method (Zhao et al., 2018). Although an algorithm for the surface slicing method has not yet been developed in the WAAM technology, it was used in producing the 10 multi-directional pipe joints for structural building applications (Yili *et al.*, 2018).

3.4. Component Printing Processes

This section of Chapter 3 aims to provide the background to the WAAM-GMAW printing process used to produce the following seven thin-walled (constant thickness) steel components introduced in Section 3.1: a horizontal rectangular plate, a rectangular hollow section, two vertical walls, two stud column sections, and a beam-to-column joint. Each

component has its own unique set of processing parameters, printing pattern and respective path plan to fill the area of each sliced layer with molten steel.

Figure 3-16(a) to 3-16(e) shows the slicing methodology for the components. In the five figures the gold arrows indicate the Build Direction (BD) in which the layers are printed to build-up the component. The BD is always in the vertical direction and is for the height-direction in the section when it is being printed. A single slicing approach was appropriate for six of the seven components, as depicted by the blue parallel lines in part Figure 3-16. Note that each blue line is a collection of printed layers as a single layer has a nominal thickness in the range of 1.3 to 3.3 mm. To print the joint, it was necessary to use a multi-directional layering approach as seen in Figure 3-16(a). Again, the blue parallel lines in the figure indicate the plane of the layers that are printed with the BD vertically-up. Also shown in Figure 3-16 the yellow arrow-headed lines are for Deposition Directions (DDs) of the weld-bead runs in the printing. Where the DDs are in the plane of the sliced layers and follows the tool-path profile to produce each layer.
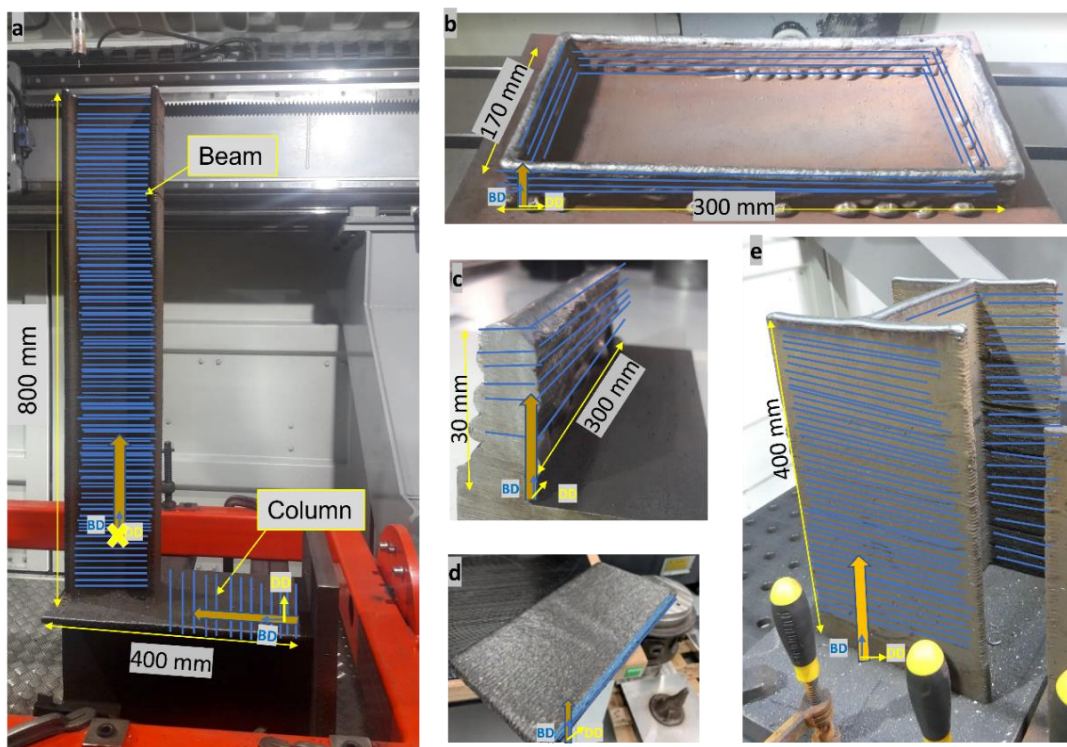
Figure 3-16. Components showing the direction of the build direction layers being printed and how the components have been sliced: (a) the beam-to-column joint; (b) the rectangular hollow section; (c) a vertical wall; (d) the horizontal plate; (e) a stud-column.

After deciding on how the component is layered, path planning was the next step in setting the 'optimum' printing process to ensure the area in a layer will be filled with weld steel. G-code was written to control the movement of the robot arm so that the weld torch will follow

the specified printing pattern, both in the horizontal plane and in the vertical direction to build-up the component.

3.4.1. Printing process for the horizontal plate

A horizontal aligned rectangular steel plate **345 x 165 x 20 mm** was printed at Autodesk (Birmingham office) using their AM facility without the author's involvement in the setting-up. As a consequence of this fact, the WAAM-GMAW processing parameters (Voltage, Amperage, etc.) were guided by their manufacturing team and the details have not been shared as this considered confidential information.

The 20 mm thickness was sliced into six main layers of 3.3 mm constant thickness, as depicted in Figure 3-16(d). The raster printing pattern for the layers was set-up using the in-house Autodesk Power Mill Ultimate software. Figure 3-17(a) and Figure 3-17(b) show the DD for the plate with blue lines for the parallel bead runs in alternative build-up layers. In Figure 3-17(c) there is a photograph of the plate semi-printed with the Cartesian *x-y* co-ordinate system for printing in the layer plane. The path of the welding torch moves Southwards for the first bead run (see blue arrow in Figure 3-17(a)), while for the next bead run the movement for depositing the weld steel is in the North direction (see blue arrow in Figure 3-17(b)), and alternates between these two printing directions until a layer is printed.
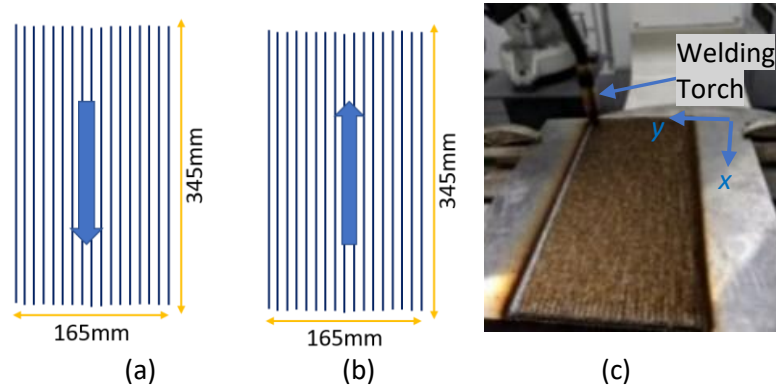
Figure 3-17. (a) 'Odd numbered' layer runs; (b) 'Even numbered' layer runs; (c) Part way through the printing of the horizontal plate, with the printing co-ordinate system.

The printing process for the Autodesk component can be summarised as having the following steps:

1. The welding torch moves in the positive *x*-direction (see Figure 3-17), as specified by the CNC code controlling the robot's movement, and the wire is melted along the designated straight path of length 345 mm to form the first weld bead for the rectangular plate.

2. The end of the weld torch moves in the positive *y*-direction (see Figure 3-17(c)) by a fixed step-over distance.

3. Steps 1 and 2 are repeated to print the bead runs across the 165 mm width of the plate.

4. After printing the area for the first layer (of nominal thickness 3.8 mm), the printhead moves vertically upwards a distance of >3.8 ~ 4mm and the wire will stick out downwards by a fixed amount~15mm.

5. Steps 1 to 3 are repeated to print the next layer. However, the beads in this next layer are printed by robot movements in the negative *x*-direction (see Figure 3-17(b))

6. Bead runs in the following layer are printed in the positive *x*-direction and the direction of printing continues to alternate until there are six layers and the plate is nominally 20 mm thick.

3.4.2. Printing process for the Rectangular Hollow Section

For details of the setup used to print the **350 x 170 x 10 x 40 mm** Rectangular Hollow Section (RHS), see Figure 3-16(b) and Table 3-7. The printing at Steelo followed the approach detailed in Figure 3-18. The figure shows the process for a singular interpass printing, where the contour of the designed component was defined by the width of a single bead.
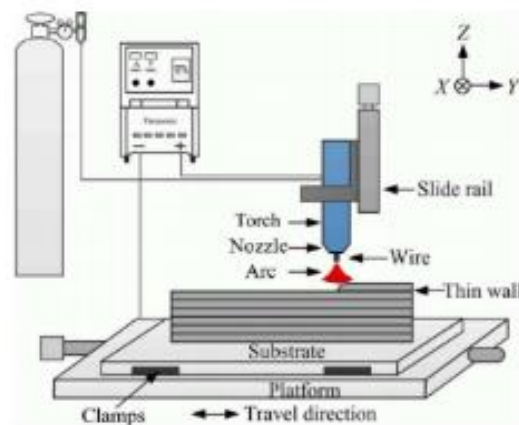
Figure 3-18. Schematic of the printing process (Xiong et al., 2018).

During printing the RHS, the nominal thickness of the walls was 10 mm, and the height of 40 mm was divided in 22 constant thickness layers, as shown in Figure 3-19. Although the chosen printing parameters (see sub-section 3.4.2.1) were for the height of each weld bead to be nominally 2 mm, due to overlayer melting the actual nominal layer thickness is 1.82 mm (note that 22 times 1.82 mm is for a nominal thickness of 40 mm). The two DD paths for printing the RHS are presented in Figure 3-19(a) and via photographs in Figure 3-19(b). It is

seen that the direction of movement is anti-clockwise and clockwise when printing alternate layers.
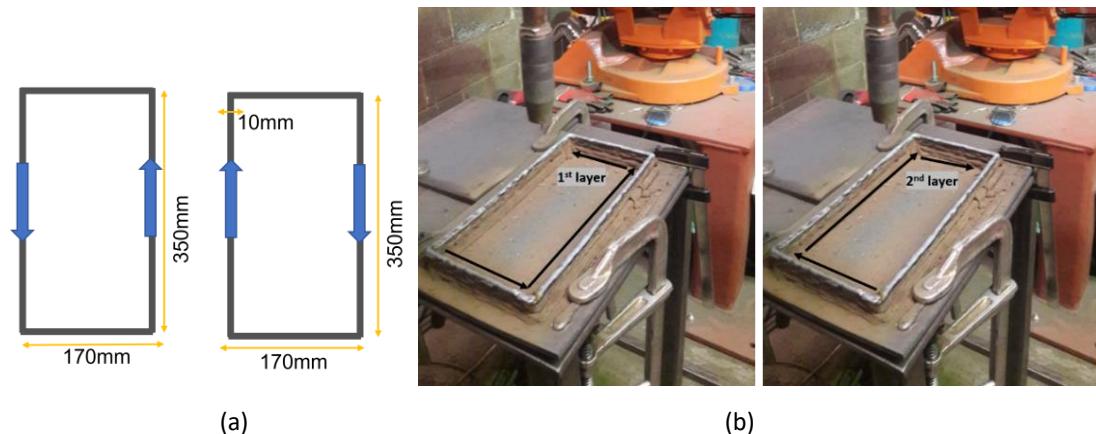
Figure 3-19. 350 x 170 x 10 x 40 mm RHS: (a) Blue arrows show the deposition direction for the odd (left) and even (right) numbered layers; (b) photographs of RHS during printing for directions of movement illustrated in (a).

The wall thickness is the same as the width of a single bead printed using the WAAM-GMAW equipment at Steelo, which is on average of 10 mm. Because the printing path, illustrated in Figure 3-19, is for a single bead the wall thickness is limited by the weld bead size. The G-code for robot movement controls the contour path profile (see Figure 3-15(c)) during printing. In addition to directing the torch head to deposit steel in alternating directions for successive layers, the robot arm moves 2 mm upwards for the step-up distance after printing each layer. Figure 3-19 (b) shows stages in the printing of the RHS component.

3.4.2.1. Printing Parameters for the RHS

Table 3-7 records the travel speeds (*TS)* for each layer and stopping times after printing 7, 10, 14 and 20 layers to cool down to the interpass temperature of 150°C. Column 1 lists the layer numbers from 1 to 11 and column 4 from number 12 to 20. In columns 2 and 5 there are the accumulative wall height as the number of printed layers increases. Presented in columns 3 and 6 is the *TS* of the weld torch, which is constant when printing a layer, yet does vary between layers.

Other processing parameters at Steelo used to produce the RHS and vertical walls (see section 3.4.3) were: Amperage is 300 A (*I*); Voltage is 28 V (*V*); *WFS* is 10 m/min; Step-up distance is 3 mm; stick out length is 15mm; shielding gas flow rate is 15 l/min; base plate thickness is 10mm.

Table 3-7: Travel speed and layer and wall height for printing the RHS components.

Number of layer	Layer height (wall height) (mm)	Travel speed (*TS*) (mm/s)	Number of layer	Layer height (wall height) (mm)	Travel speed (*TS*) (mm/s)
1	2	3	4	5	6
1	2	5	12	22	9
2	6	5	13	25	9
3	8	5	14	28	8
4	11	7	Stop 5 min		
5	13	5	15	30	10
6	14	7	16	31	10
7	15	7	17	32	10
Stop 5 min			Stop 5 min		
8	16	8	18	34	10
9	17	11	19	36	10
10	19	11	20	37	10
Stop 7 min			Stop 5 min		
11	20	11	21	39	11
			22	4	11

During the printing of the RHS component, the surface temperature was too high and exceeded the recommended interpass temperature of 150°C; this processing problem can affect the microstructure and the mechanical properties of the weld steel. In order to control the cumulative heat energy and minimise the heat input at the surface from the next layer printing, the travel speed was changed from between 3 to 11 mm/s, with a higher speed reducing the heat input with the constant wire feed speed. To support keeping the interpass temperature low enough the printing process was stopped for 5 minutes, from layer number 7, every time three layers had been deposited (see Table 3-7). It is important to understand that the printing 'optimisation', which included changing the travel speed and adding in periods of cooling time, was carried out manually using engineering experience and judgment.

3.4.3. Printing process for the two vertical walls

Using Steelo equipment two vertical walls of nominal length 300 mm and nominal height of 30 mm (shown in Figure 3-16(c)) were printed. These walls of nominally 10 mm thickness are labelled A and B and are constructed with 15 layers (each of 1.82 mm). Figure 3-20(a) shows the two final **300 x 10 x 30mm** walls that were printed using the same printing parameter as for the RHS.

Figure 3-20(b) shows the paths planning for singular interpass printing where the process alternated between the two walls because this helped reduce the stopping time (i.e., the cooling down time for the required surface temperature of 150 °C to be reached), and to support temperature control and layer thickness the printing direction was reversed for each layer.
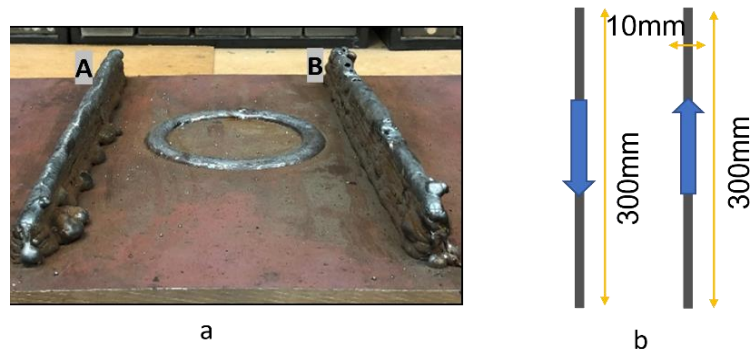
Figure 3-20. (a) Photographs of two vertical 300 x 10 x 30mm walls (b) Path planning of the walls.

3.4.4. Printing process for the I stub columns & beam-to-column joint

The Autodesk container unit, seen in Figure 3-4, was used in 3D printing the joint (as shown in Figure 3-16 (a) and Figure 3-21) and the two-stud columns (as shown in Figure 3-16(e) and Figure 3-22). Figure 3-21 shows the directions in which the beam and column sections were printed, where the orange arrows labelled BD are for the Build Direction; both the Beam (B) and Column (C) sections were printed vertically.
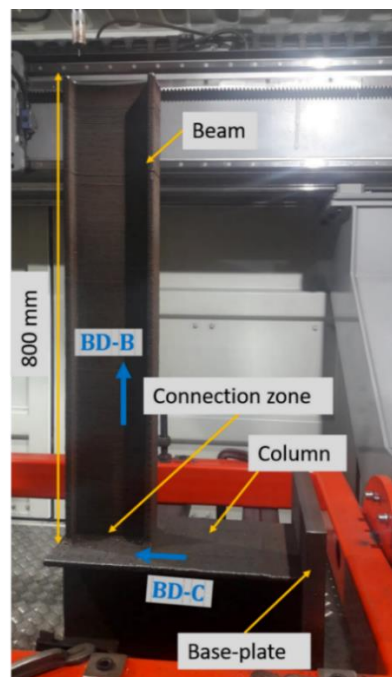
Figure 3-21. Steel beam-to-column joint after WAAM-GMAW printing.
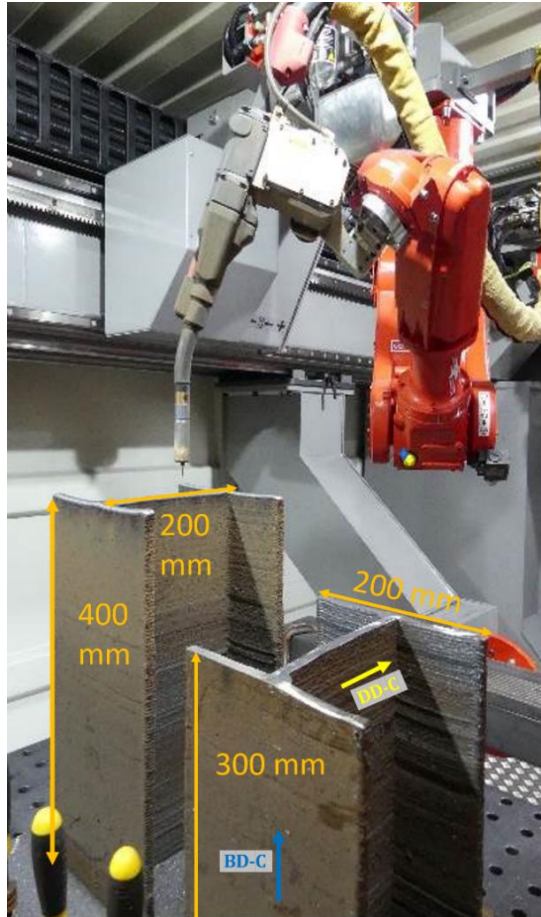
Figure 3-22. Nominal cross-section geometry of a stud-columns.

The overall printing process for the joint required the author and collaborators to design the cross-section geometries; optimise the printing parameters; choose the printing paths and the printing strategy. Instead of an optimised geometry, the I-section shape was the chosen cross-section for the beam and column sections. A reason for this was to provide a benchmark structural engineering component for the construction industry.

3.4.4.1. Sizing the I-sections

Different sizing options are to be studied before printing the final beam-to-column joint. The size of the I-stub column sections was based on the series of the tensile and impact specimens that could be extracted from the printed component. In Chapter 4, the method of extracting (minimum of three in each direction) and testing the specimens will be explained.

51
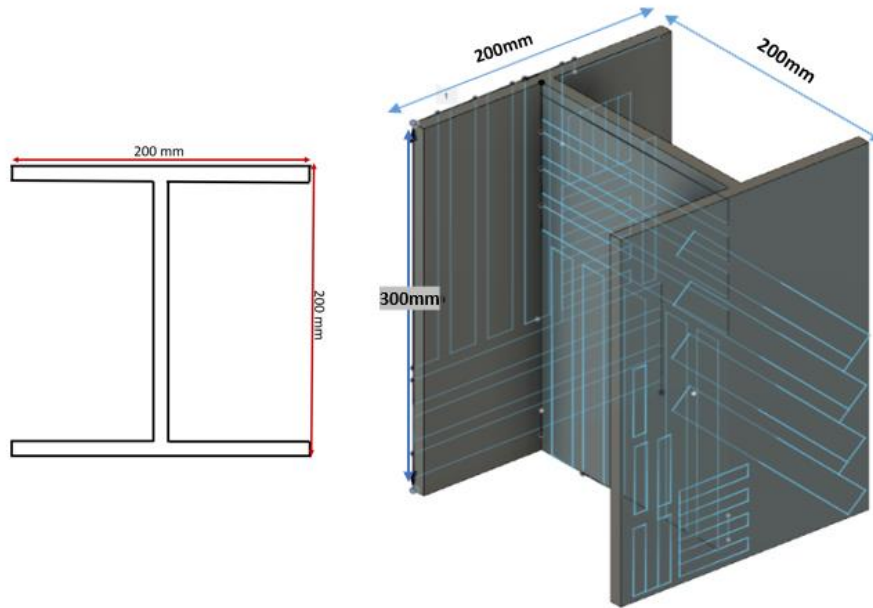
Figure 3-23. Designed dimensions of the two-3D printed I-section stub columns; one of which was part of the beam-to-column joint, and the other was used for material testing purposes.

The I-stub columns had a dimension of 200 x 200mm, as shown in Figure 3-23, whilst a decision had to be made for the size and length of the beam. The cross-sectional area of the beam was limited to the maximum loading capacity of the load cell (150 kN) and the capacity of the tensile forces in each floor socket, and its length was limited to the size of the printing room as will be presented in Figure 3-30.

Furthermore, the web and the flange thicknesses of the I-section was limited to the chosen printing parameters and the bead width (see Section 3.4.4.2). The optimised parameters for the printing strategy of the I-profiles limit the nominal thickness to 9 mm or 11 mm (for printing with 2 or 3 beads respectively). Figure 3-24 shows that both sections had an I-shape cross-section, with the cross-sectional dimension of the column (nominally 200 × 200 × 11 mm) being larger than that of the beam (nominally 140 × 60 × 9 mm).
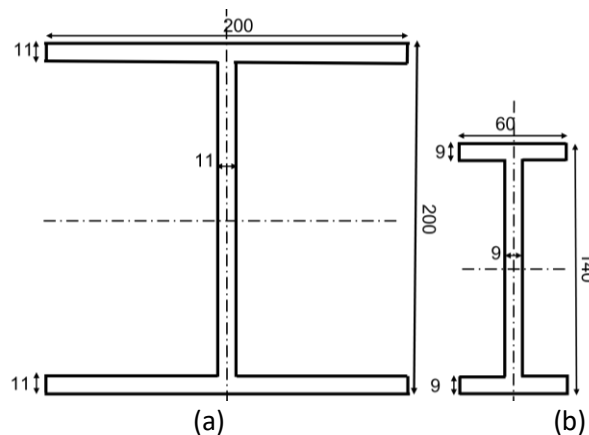
Figure 3-24. Nominal cross-sectional geometries for the sections of the beam-to-column joint: (a) column; (b) beam.

3.4.4.2. Printing Parameters for the I-sections

The WAAM-GMAW printing parameters, for the welding of the 1.2 mm diameter S460 steel wire *SupraMig Ultra HD* (see Table 3-1), utilised a 150 A current, a 14.6 V voltage, and a 900 mm/min travel speed. These values were the optimised parameters for a single pass bead weld. Table 3-8 presents additional processing parameter values used in this study. Columns 2 and 4 show the numerical values for the optimal printing parameters (highlighted in Table 3-5 in sub-section 3.3.1), which are described in columns 1 and 3.

Table 3-8: Optimal printing parameters used in printing the joint

Parameter 1	Value 2	Parameter 3	Value 4
Wire Feed Speed	4400 mm/min	Heat input	116.8 J/mm
Wire tip-to-work distance	<1 mm	Wire stick-out length	15 mm
Interpass temperature	Max 150 °C	Layer height	1.3 mm
Bead width	5.6 mm	Step-up distance	1.7 mm
Step-over distance	3.1 mm		

After setting-up the optimised parameters for the single bead the step-over and step-up distances (as discussed in section 3.3.1) were then selected. The step-over distance (between the centre of adjacent beads) of 3.1 mm was chosen to achieve a 'flat surface finish', whilst the step-up distance of 1.7 mm was selected to take into account the nominal thickness of the layer, which is 1.3 mm.

3.4.4.3. Path Planning for the I-section

The width of the single pass deposition was 5.6 mm, as recorded in Table 3-8, so multi-bead runs were necessary to achieve the designed wall thicknesses of 11 mm and 9 mm. Hence, different printing path plans were adopted with the objective to minimise the total printing time, while maintaining the acceptable interpass temperature and preserving the critical geometrical features (such as edges and corners).

The tool path for the printing pattern was designed using the Autodesk-PowerMill Ultimate 2020 software with the parameters listed in Table 3-8. For example, the centre-to-centre distance between the running arc is 3.1 mm (the step over distance) which is shown in Figure 3-25. Therefore, three beads were needed to fill the nominal 11 mm wall thickness (6.2 + 5.6

= 11.8 mm), as this consists of the distance between the paths (at 3.1 mm), the width of a bead (at 5.6 mm), and the overlapping between the beads.
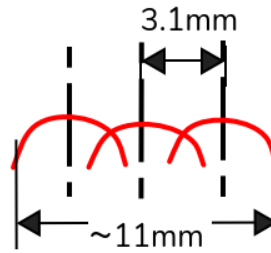
Figure 3-25. Tool path distances to print a 11 mm thick component

Two patterns, A and B, for the path planning of a I-section were followed, as shown in Figure 3-26. Pattern A contains nine discontinuous lines in the deposition path to cover the whole cross-sectional area, while pattern B contains seven lines, where the lines for linking the flange and the web (lines 6 and 7 in Figure 3-26-b) creates a more accurate continuous joint for the I-section.

A   B
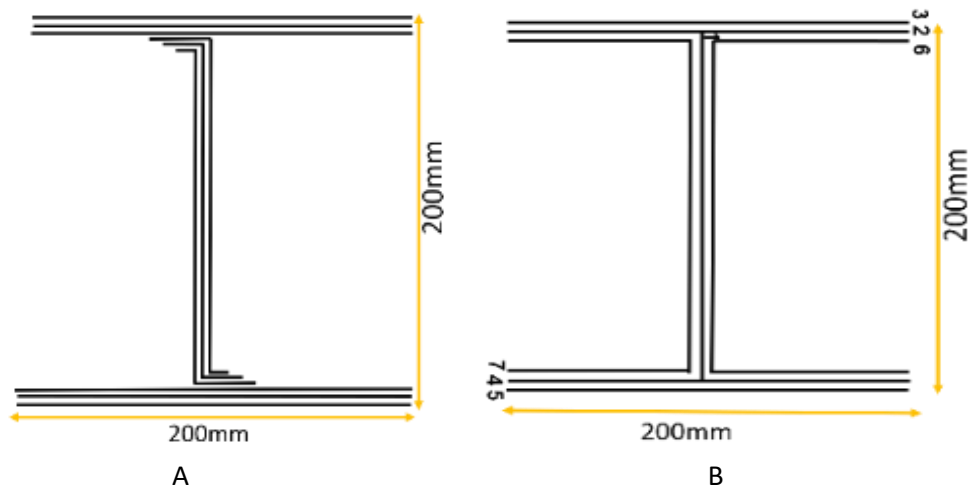
Figure 3-26. Chosen printing path patterns for the designed I-section, based on its web and flange thickness dimensions.

In pattern A, it is noted that the number of on/off points for the arc is quite high (18 arc on/off points), as there are many sub-paths. Moreover, most of the off points are at defect-sensitive regions which is at the transition zone between the flange and the web.

In pattern B, the starting points of the path lines vary from left (for sub-paths 4, 5 and 7 in Figure 3-26-b) to right (for sub-paths 3, 2 and 6 in Figure 3-26-b). The alternation in the starting points, introduced within the path planning of the I-sections, helps maintain the interpass temperature. Additionally, the middle bead in the web section (sub-path 1 in Figure 3-26-b) was optimised to be slightly longer to link together the web and the flange, such that the arc on/off region can be remelted by sub-paths 2 and 4. This remelting enables some

defects involved in the arc on/off region, including pores and unfilled interaction (see Figure 3-27), to be removed. As a result, pattern B was the adopted tool path plan for the beam-to-column joint component shown in Figure 3-21.

Figure 3-27. A printing path without the mid bead for the web and the unfilled interaction.

The overall printing time for the 200 x 200mm I-section layer was a minute. This period includes a delay robot movement time of 6 seconds before every start point for the next deposited bead. After the printing of a layer consisting of 7 beads was completed, there was a 2-minute pause for cooling in between each layer before the printing continued. Additionally, there was a 5-minute cooling time in between every set of 5 layers, to maintain the interpass temperature not to exceed 150°C.

3.4.4.4. Printing strategy for the Stub columns

The printing of the column section (see Figure 3-24 (a), commenced with two steel 400X300X30 mm baseplates clamped at their four corners. The two column sections, one for cutting out the specimens (detailed in Chapter 4) and one for the beam-to-column joint, were then printed on the plates as shown in Figure 3-28-b.
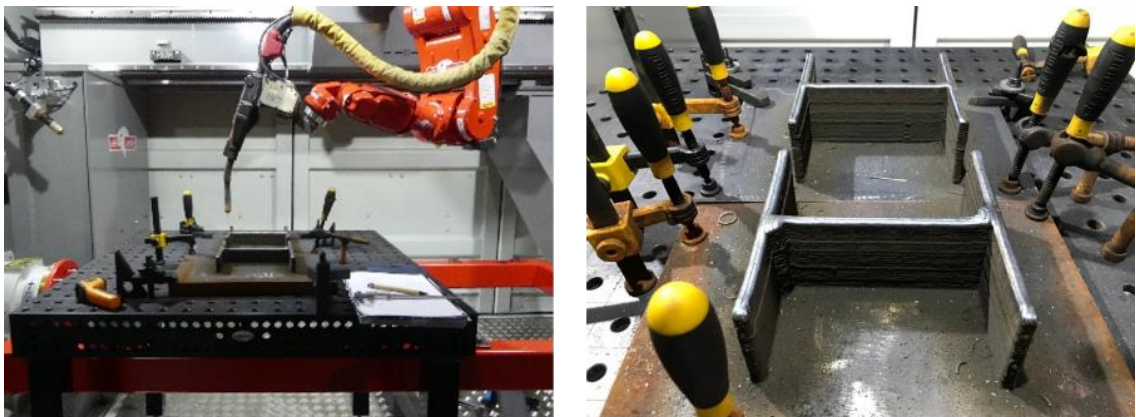
Figure 3-28. WAAM printing of the two stub columns: (a) overall set-up, (b) zoomed-in view of specimens during production.

A total printing time of 100 hours was recorded to manufacture the 36 kg monolithic component at RAMLAB facilities. It is noted that the cooling time within the total printing time is long for this part, which, in the future, can be reduced with an active cooling system in place. And this required 190 layers of printing for the 300 mm stub column, for extracting the test specimens. In comparison, the 400mm stub column (beam-to-column joint) required 240 layers of printing. Using the same parameters in this section, the beam section required 480 layers to print the full length of 800mm.

3.4.4.5. Printing Strategy for the beam-to-column joint

Prior to 3D printing the joint, two stub-column sections of heights 300 and 400 mm were manufactured to investigate different printing strategies. Their thin-walled cross-section shapes (nominally to be 200 × 200 × 11 mm) are seen in Figure 3-22. Both stub columns have a nominal wall thickness of 11 mm, with the cross-sectional shape illustrated in Figure 3-24(a). To print this section of the joint, the baseplate was horizontal so that the build direction of the column (BD-C) was vertical. After the 400mm length of the column section had been printed, the specimen was repositioned so that the beam section in Figure 3-24(b) was printed vertically, starting with the column as its 'base-plate'.

The mobile welding table in Figure 3-4 was used to print the two stub-columns and the printing strategy involving printing two different elements in different directions shown in Figure 3-21. For the columns, the printing occurred on the table of Figure 3-28-a, whilst the beam was printed on the column which was affixed to the orange frame.

Figure 3-29(a) shows the location of the secondary beam, where the printed column will be attached. In this arrangement, the lower flange of the column will be the base plate. Hence, the column will be supported by using four clamps, while the upper flange surface will act as the substrate plate for the new print (as presented in Figure 3-29(c), where the build-up of the printed layers gradually forms the beam. Before starting the printing, a clean surface was created by levelling and preparing the column, in order for the printing to be homogeneous. To ensure that the robot arm followed the designed tool path, and the beam was accurately aligned parallel to the ground level, a dry run was carried out on the marked I-section for the first layer (see Figure 3-29(b)).

<center>(a)　　　　　　　　　(b)　　　　　　　　　(c)</center>
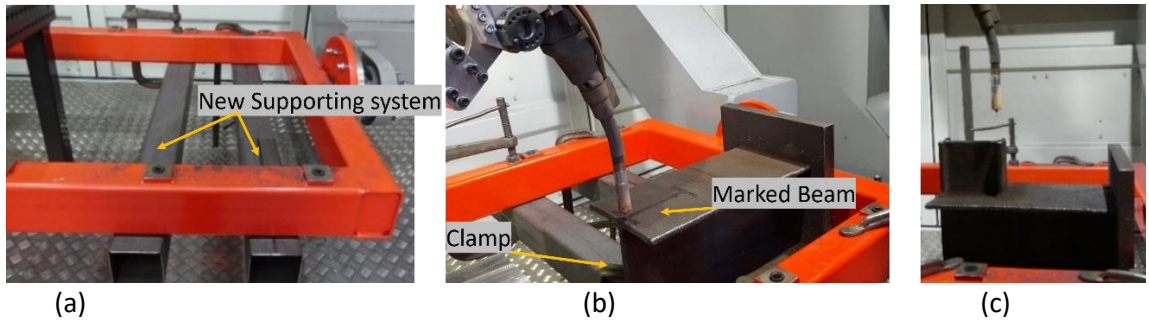
Figure 3-29. Preparation for the beam printing set up: (a) New supporting system aside to the mobile welding table; (b) positioning welding torch on the marked beam- on the column- before starting the printing process; (c) joint component with beam section partially printed.

The printing strategy for the beam-to-column joint used a multidirectional slicing approach as the manufacturing of the beam requires a different printing direction to its associated column. A new printing setup for the beam was adopted to compensate for the height limitation and the build direction for the beam section, as demonstrated in Figure 3-30.

<center>(a)　　　　　　　　　　　　(b)</center>
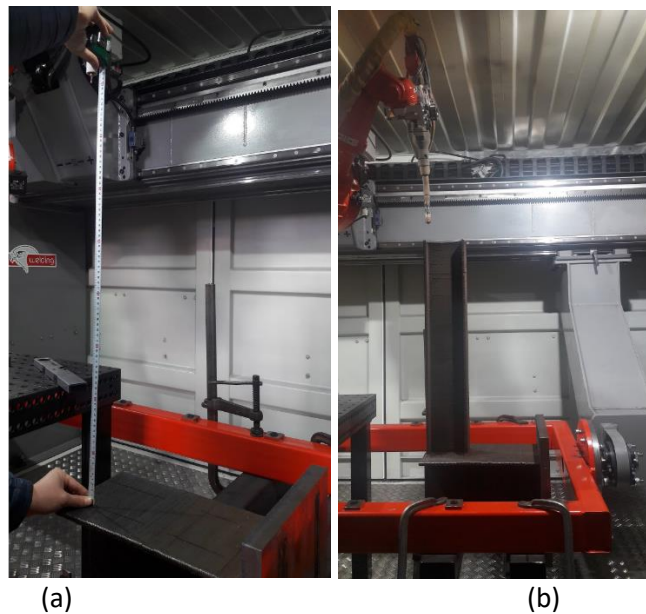
Figure 3-30. Size limitation: (a) before the beam was printed showing the maximum allowable height that can be reached; (b) After finishing the printing where the robot arm reaches the ceiling.

Transition zone

In the printing of the beam-to-column joint, the component was divided into two parts: the stub column and the beam. Due to the critical functionality of the interface zone in transferring the rotational moment to the column, the transitional zone was designed as a link between the two specimens to increase the contact surface area to transfer the load and reducing potential stress concentration conners.

<center>57</center>

Figure 3-31, shows the early steps in forming the transitional layers for this zone. The first 5 layers of the printed beam was a tapered transition zone, where the width of the flange gradually decreased (by 5mm for every successive layer) from 80mm to 60mm which is the final dimension of the beam as shown in Figure 3-24. Similarly, the depth of the beam decreased from 160mm to 140mm (see Figure 3-32). The remaining layers of the beam have the dimensions outlined in Figure 3-31.

(a) (b)
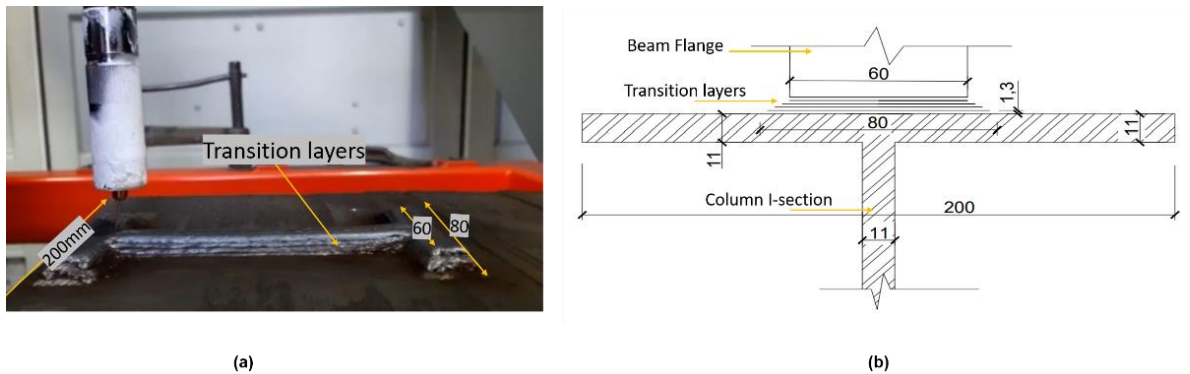
Figure 3-31. Layering up the transition zone at the interface region: (a) tapered printed layers; (b) cross-section view for the layering up transition layers.
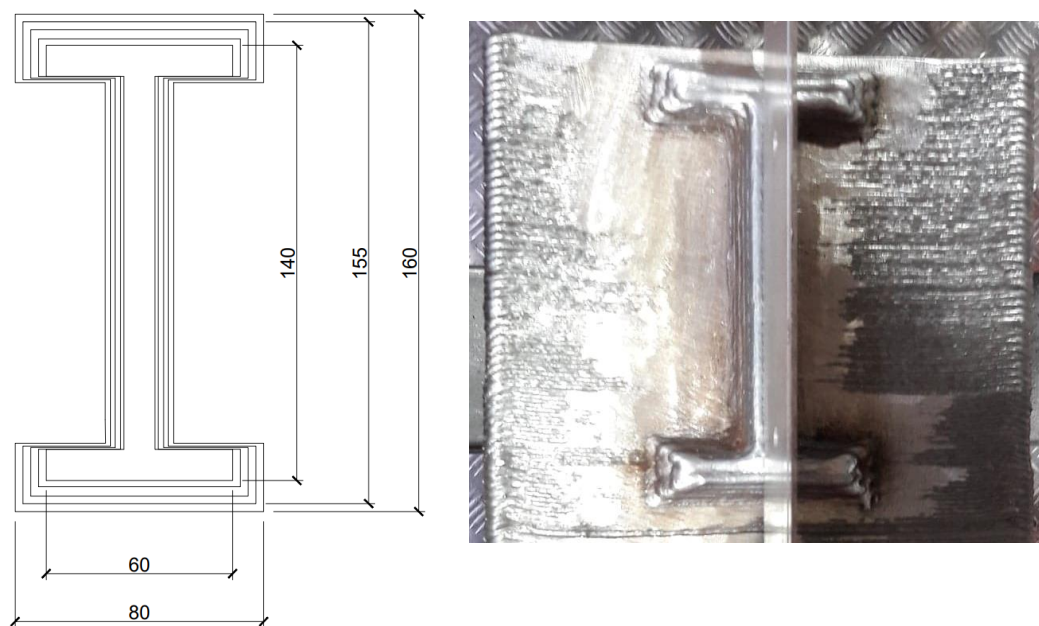
Figure 3-32. Top view for in the transition zone for: (a) the designed transition layers; (b) printed layers.

3.5. Summary

In this chapter, the development of the printing process for a steel component has been described. A background of the WAMM printing process was then presented, which highlighted the different types of steel wire and gas used, followed by the explicit details of

the printing process for the different components (horizontal plate, rectangular hollow section, two vertical walls and the beam-to-column joint).

The core stages of WAAM printing are path planning, printing strategy for slicing and the optimisation of the printing parameters. Both printing quality and efficiency is largely dependent on the parameter and conditions used, as heat accumulation is a key aspect of the whole process.

During the optimisation of the printing parameters, the following conditions were considered in this research:

- Arc stability
- Homogeneity and continuity of the printed bead
- Spreading of the welding bead (with a width-to-height ratio larger than 4)
- Cleanliness of the weld toes

The three types of path planning for filling 2D sliced planes are linear, contour and hybrid. In this research, linear path planning and the basic principle of multi-pass welding was implemented according to the welding standards.

X-ray Computed Tomography (X-CT) was the non-destructive non-contact examination method utilised in the research, to inspect the coupon integrity and identify internal defects. This was because X-CT has the ability to identify the volumetric differences in the steel material, to determine the volume fraction and to determine the size and locations of the pores.

4. Chapter Four: Developing the methodologies for mechanical characterisation tests

According to *Hot rolled products of structural steels* (EN10025-1, 2004), initial testing of structural steel is to be carried out before the material is placed in the market. The testing is to characterise the structural steel's mechanical properties, chemical composition, weldability, formability, and surface properties. This chapter presents factual information on the preparation stages for cutting-out of test specimens from the WAAM-GMAW 3D printed components, and the test methodologies for the mechanical tests for tensile and impact material properties. Non-destructive testing to characterise the welded steels involves density measurement and X-ray Computed Tomography (X-CT) analysis for investigation of internal features.

4.1. Specimen preparation: Designing, machining, and grinding

4.1.1. Design of the specimens

4.1.1.1. Dog-bone specimens:

There are two approaches for the preparation of the tensile test specimens: proportional and non-proportional. For the non-proportional test specimens, the cross section is independent of its gauge length (L_o). Whilst the cross section of the proportional test specimens is directly related to its gauge length (L_o), as shown in Figure 4-1.
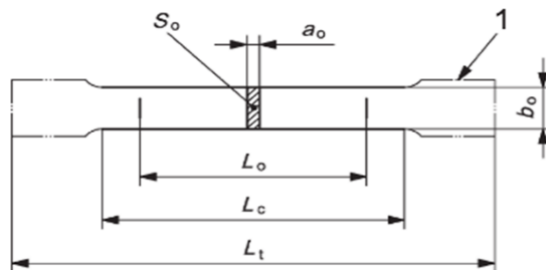
Figure 4-1. Standard tensile coupon geometry (BS/EN-ISO6892-1:2019)

In this research, the dog-bone coupons for the tensile tests were sized using the proportional test method. Figure 4-1 defines the dimensions for the designed coupons, where the gauge length (L_o) is related to the original cross-section area (S_o) by the equation $L_o = 5.65\sqrt{S_o}$; the parallel length (L_c) is defined by the equation $L_c = L_0 + 1.5\sqrt{S_o}$. The total length of the test piece (L_t) is the sum of the parallel length, twice the length of the required gripping length and twice the minimum radius between the gripped end and the parallel length, which should be not less than 12mm - as the proportional test method in Annex D of (BS/EN-ISO6892-1:2019) specifies this value for test pieces of thicknesses larger than 3mm.

In the design, the overall length of the specimens was limited to the thickness of the printed components after grinding (this process will be explained in 4.1.3.4 'Grinding') and the chosen width of the dog-bone coupons. For example, the overall length of the first specimen in Table 4-1 was limited to a thickness of 17mm after grinding. The minimum L_o for the 20 x 17 cross-section was calculated to be 104mm, and for the total coupon length of 300mm the parallel length (L_c) was 132mm.

Table 4-1: Designed coupons that was extracted from the printed material

Coupon type and labelling scheme	Thickness and width (a_o x b_o) mm	Gauge length (L_o) mm	Parallel length (L_c) mm	Length (L_t) mm
1	2	3	4	5
A_ Plate_S35 _L_T_1 to 3	17x20	$5.65\sqrt{340}$ = 104	$104.2 + 1.5\sqrt{340}$ =132	300
A_Plate_S35_ TT_T_1 to 4 (straight sided)	3.8x17	$5.65\sqrt{64.6}$ = 45	65	65
S_WALL A_S35_L_T_1 to 2 S_ WALL B_S35_ L_T_1 to 2 S_RHS_S35_ I_T_1 to 3 S_RHS _S35 _L_T_1 to 3	7x10	$5.65\sqrt{340}$ = 48	$48 + 1.5\sqrt{340}$ = 61	150
R_IA _S46 _I_T_1 to 4 R _IB _S46 _L_T_1 to 3 R_IB _S46 _T_T_1 to 5 R_IC _S46 _T_T_1 to 5	10x12.5	$5.65\sqrt{340}$=63.17	$104.2 + 1.5\sqrt{340}$ = 80	200
R_IC _S46 _L_T_1 to 3	10x10	$5.65\sqrt{340}$ = 56.5	$104.2 + 1.5\sqrt{340}$ = 71.5	150
Medium Carbon steel (EN 8)	10x20	$5.65\sqrt{200}$ = 80	$80 + 1.5\sqrt{200}$ = 101.5	300

Accompanying Figure 4-1, Table 4-1 presents the dimensions of six different coupons. Column 1 shows the labelling scheme for the coupon types, and columns 2 to 5 states the dimensions of thickness (a_o), width (b_o), gauge length (L_o), parallel length (L_c) and overall coupon length (L_t) respectively in millimetres.

The labelling of the dog-bone coupons contains 6 parts: the first stands for the material manufacturer (A: Autodesk, S: Steelo, and R: RAMLAB) and the second is for the shaped of the original components before the specimens were extracted (Plate, Wall, RHS: Rectangular Hollow Section and I: I-section). S46 or S35 categorises the strength of the wire used for printing; L (longitudinal), T (Transverse) or I (Inclined) in the fourth part reflects the direction of cut-out relative to the build-up direction. For the fifth, T stands for tensile testing and for the final subsection 1 to *X*, *X* is the number of samples extracted in the same way.

For example, specimen A_S35_Plate_L_T_1 to 3, is where A is for the Autodesk material, S35 is for the wire used, Plate is for the original type of component cut-out, L is for longitudinal direction of cut-out, T for tensile testing and 1 to 3 means that three specimens were cut-out using the same methodology. Figure 4-2 shows the second specimen that follows the same labelling scheme.
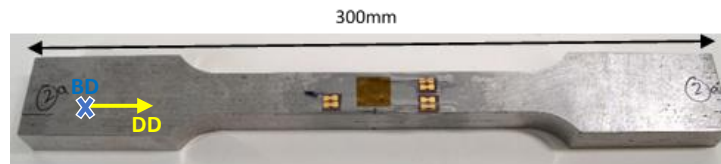
Figure 4-2. Tensile coupon specimen A_S35_Plate_L_T_2 with strain gauging

The only exception in the coupon labelling scheme was "A_S35_Plate_TT_T_1 to 4". This test specimen as shown in Figure 4-3 does not follow the dog-bone shape in Figure 4-1, and the "TT" stands for Through Thickness, as the axial strain gauging is positioned on the 'thickness' surfaces and the direction of tensile load is in the longitudinal direction.
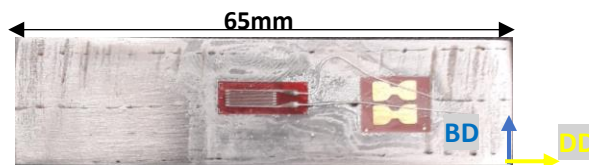
Figure 4-3. Through-thickness coupon, A_Plate_S35_ TT_T_3

For the final row in Table 4-1 the single EN 8 coupon was not extracted from a printed 3D component as it was taken from a piece of conventional EN 8 medium carbon steel. However, the dimensions were chosen in accordance with the same proportional test approach in (BS/EN-ISO6892-1:2019). This specimen was used to validate the tensile test set-up and procedure before proceeding to characterise the material properties of the printed steels.

4.1.1.2. Impact test specimens

The prepared samples for impact tests were machined with a V notch, which followed the guidance in "Metallic materials - Charpy pendulum impact test - Part 1: Test method standards" (EN/ISO148-1:2016, 2016). Table 4-2 reported the tolerances on specified test specimens. The length of the specimen was 55 mm for *L* (see Figure 4-4) with various cross-section dimensions of 10x10 mm, 10x7.5 mm and 10x5 mm. For the V-notch, only specimens with cross-sections of 10×7.5 mm and 10x5 mm were tested due to limited steel resources, as listed in Table 4-3.
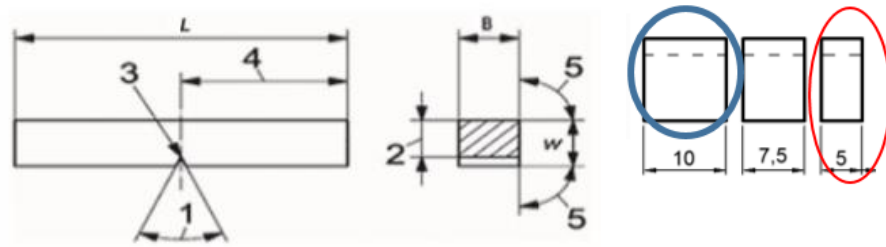
Figure 4-4. Standardised dimensions for the impact test specimens

Table 4-2: Dimension of the standardized Charpy pendulum impact specimen, Table 2 in (EN/ISO148-1:2016, 2016)

Designation	Symbol and no.	V-notch test piece			U-notch test piece		
		Nominal dimension	Machining tolerance		Nominal dimension	Machining tolerance	
				Tolerance class[a]			Tolerance class[a]
Length	L	55 mm	±0,60 mm	js15	55 mm	±0,60 mm	js15
Width	W	10 mm	±0,075 mm	js12	10 mm	±0,11 mm	js13
Thickness[c]	B	10 mm	±0,11 mm	js13	10 mm	±0,11 mm	js13
— standard test piece — subsize test piece — subsize test piece — subsize test piece		10 mm 7,5 mm 5 mm 2,5 mm	±0,11 mm ±0,11 mm ±0,06 mm ±0,05 mm	js13 js13 js12 js12	10 mm 7,5 mm 5 mm —	±0,11 mm ±0,11 mm ±0,06 mm —	js13 — — —
Angle of notch	1	45°	±2°	—	—	—	—
Ligament	2	8 mm	±0,075 mm	js12	5 mm	±0,09 mm	js13
Notch radius	3	0,25 mm	±0,025 mm	—	1 mm	±0,07 mm	js12
Notch position (centering)	4	27,5 mm	±0,42 mm [d]	js15	27,5 mm	±0,42 mm[d]	js15
Angle between plane of symmetry of notch and longitudinal axis of test piece		90°	±2°	—	90°	±2°	—
Angle between adjacent longitudinal faces of test piece	5	90°	±2°	—	90°	±2°	—
Surface roughness[b]	NA	<5 µm			<5 µm		

[a]   In accordance with ISO 286-1.

[b]   The test pieces shall have a surface roughness better than *Ra* 5 µm except for the ends.

[c]   If another thickness (2 mm or 3 mm) is specified, the corresponding tolerances shall also be specified.

[d]   For machines with automatic positioning of the test piece, it is recommended that the tolerance be taken as ±0,165 mm instead of ±0,42 mm.

Table 4-3 presents the details of the prepared specimens for the impact test. The labelling scheme will follow the same approach in sub-section 4.1.1, apart from the symbol 'I' as the fifth part, which stands for Impact, replacing 'T' for Tensile in the tensile specimens' preparation Table 4-1.

Table 4-3: Dimensions of standardized Charpy pendulum impact specimens

Coupon type and labelling scheme	Width (W) mm	Thickness (B) mm	Length (L) mm	Type of grove
1	2	3	4	5
S_WALL A_S35_L_I_1 to3 S_ WALL B_S35_ L_I_1 to 2 S_RHS_S35_ I_I_1 to 3	10	5	55	V
R_IA _S46 _L_I_1 to 5 R_IA _S46 _T_I_1 to 5 R_IA _S46 _I_I_1 to 5 R _IB _S46 _L_I_1 to 3 R_IB_S46 _T_I_1 to 4 R_IB_S46 _I_I_1 to 4 R_IC _S46 _L_I_1 to 2 R_IC _S46 _T_I_1 to 3	10	7.5	55	V

Figure 4-5 shows several test specimens with V notches for different cross-section areas. Figure 4-5(a) presents the V-notch samples S_WALL A_S35_L_I_1 to3 for specimens extracted from the Steelo (S) printed wall. Figure 4-5(b) shows samples of R_IA _S46 _L_I_1 to 2 for the specimens' cut-out from the RAMLAB (R) printed I-section.

(a)   (b)
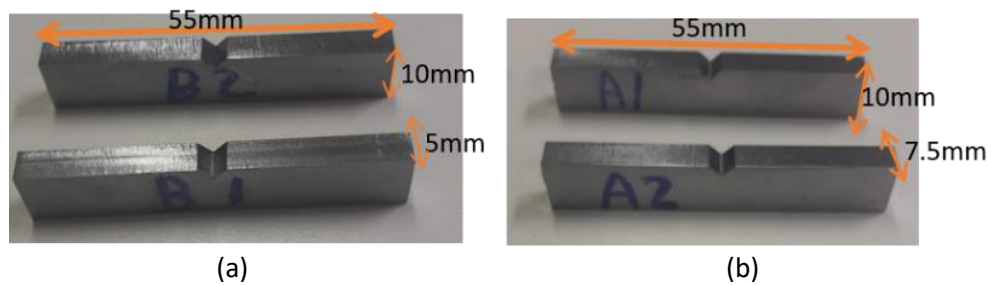
Figure 4-5. Prepared samples with V notch for the impact test: (a) S_ WALL B_S35_ L_I_1, S_ WALL B_S35_ L_I_2; (b) R_IA _S46 _L_I_1, R_IA _S46 _L_I_2

4.1.2. Positioning the cut-out of the test specimens

The positioning for cutting-out test specimens are recommended by the standards "Hot rolled products of structural steels – Part 2" (EN10025-1, 2004) and "Steel and steel products- Location and preparation of samples and test pieces for mechanical testing" (ISO377, 2013). In this research, different positioning iterations were trialled to maximize the number of specimens, taking into account the orientation for the samples. For the extraction of the impact test specimens, one edge was less than 2mm away from the edge of the printed component.

Figure 4-6 summarises the overall number of specimens and their locations within the printed components (horizontal wall, vertical wall, I-section, and the rectangular hollow section), based on the dimensions of the designed coupons summarised in Table 4-1 and Table 4-3.

Horizontal Wall — Autodesk material

- 3 horizontal dog bones
- 4 non-standardised specimens
- 5 horizontal impact specimens
- 5 Inclined impact specimens
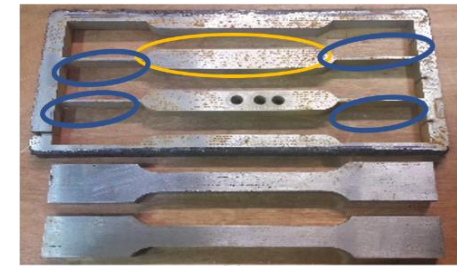
Vertical Walls & RHS — Steelo material

- 7 horizontal dog bones
- 3 inclined dog-bones
- 5 horizontal impact specimens
- 3 inclined impact specimens
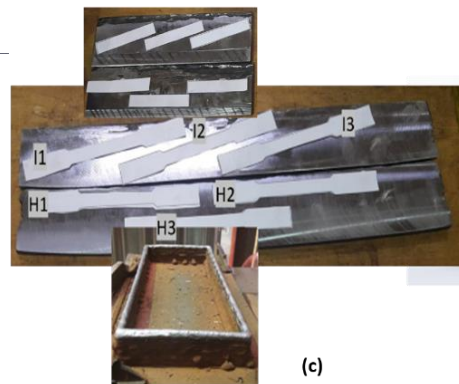
30cm stub Column I section — Ramlab material

- 6 horizontal dog bones
- 4 diagonal dog bones
- 10 vertical dog bones
- 9 horizontal impact specimens
- 9 inclined impact specimens
- 11 vertical impact specimens
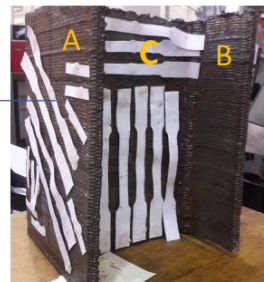
Figure 4-6. A summary of the positioning for the specimens cut-out from the printed component: (a) horizontal wall and the designed size of the dog bone coupon; (b) extracted dog bones from the plate; (c) specimens taken from the four walls split from the printed RHS component; (d)- Wall A and B with the fitted dog bone and impact specimens; (e to h): I-section with Plate A, Plate B, and Plate C and the designed location for the tensile and impact specimens.

For the horizontal wall (Autodesk), a maximum of three horizontal dog bones were cut-out, as shown in Figure 4-7. Additionally, to make good use of the leftover material, locations of four straight specimens were marked in blue (See Figure 4-7).

Figure 4-7. Autodesk plate: Location of the straight sided (circled blue) specimens extracted from the leftover material

The maximum overall number of specimens to be extracted was ten dog bones, and eight impact specimens from the vertical walls and the RHS, that was printed at Steelo. Figure 4-6(c) shows that the RHS component was separated into four walls, where the final location of the specimens following numerous iterations are marked-up, and this marking-out adhered to the dog bone dimensions in Table 4-1.

As for the I-section, which was printed at RAMLAB, the component was also split into three main plates: A, B and C, as shown in Figure 4-6 (e) to (h). Similarly, the locations of the designed dog bones and impact specimens were geometrically optimised to maximise the opportunities for material characterization.

4.1.3. Post-processing steps for extracting the specimens

Post-processing steps for the WAAM-GMAW components may include heat treatment, milling, grinding, and machining as shown in the flowchart of Figure 4-8.
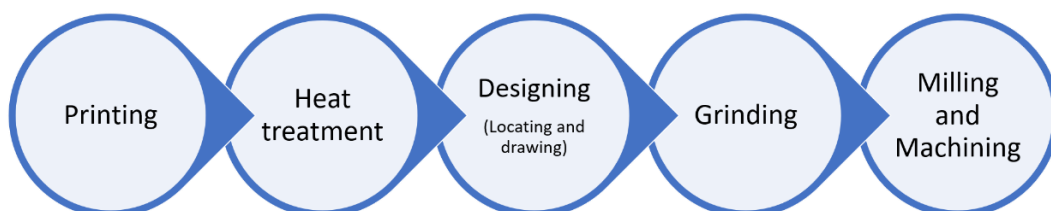
Figure 4-8. Post processing steps of steel after printing

4.1.3.1. Heat treatment

In this research, the specimens did not undergo heat treatment, to refine the grain size of the steel to improve both strength and toughness, because the process is expensive, time consuming and undesirable for construction applications. Also, the printing may be on-site where this process might not be easy to access. However, the post-3D printing heat treatment of steel may be necessary for 3D printed components in other engineering sectors, such aerospace and automotive.

4.1.3.2. CAD Drawings

After choosing the location of the samples as shown in Figure 4-6, the finalised locations of each component were drawn using CAD software before the machining and grinding processes began.

Figure 4-9 summarises the process of laying out the specimens on the plates. A 3D model of the RHS plate was drawn in SolidWorks to plan for the process of cut-out, as shown in Figure 4-9 (a). The white border lines show the locations of the plates cut-out in Figure 4-9 (b). While Figure 4-9 (c) show the designed drawing for plates 1 and 2 of the RHS section, where the spacing between the specimens took into account of the distance between the chamfering and the thickness of the cutting tool. The arrangements of the specimens in Figure 4-9 (c) matches the order in Figure 4-6(c).

(a)

(b)

(c)
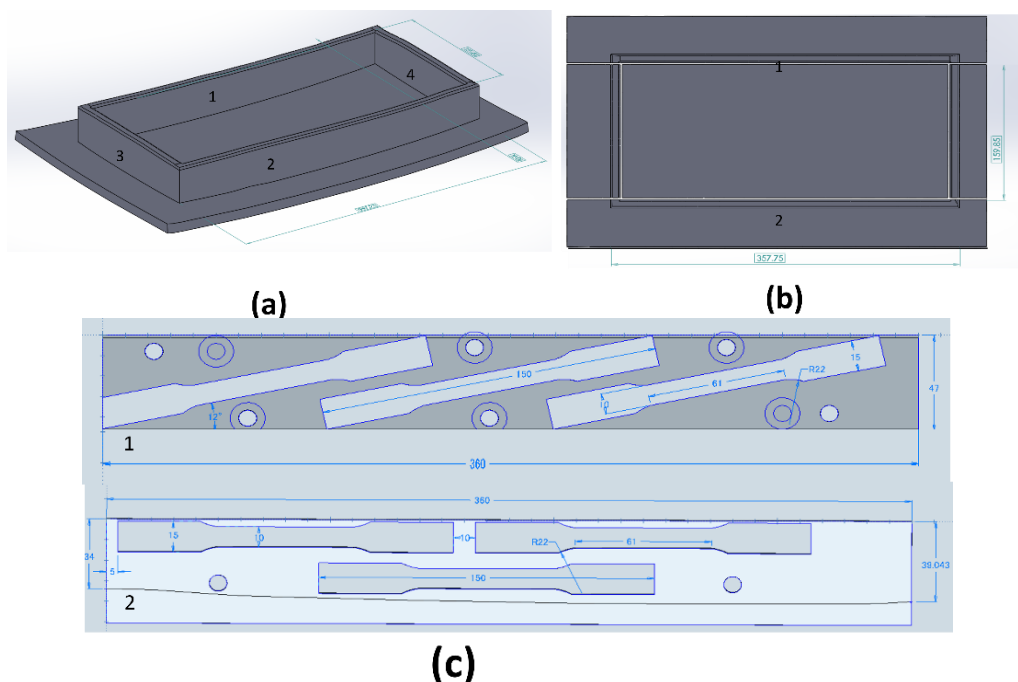
Figure 4-9. CAD drawings for Plates 1 and 2 from side walls of: (a) and(b) RHS printed at Steelo; for coupons in plates 1 and 2 to make the best use of the steel. (c) location of the coupon specimens on plate 1&2 of the RHS walls.

Similarly, for Figure 4-6(d), four dog bones and five impact specimens were designed to be extracted from the two parallel walls, as shown in Figure 4-10(a) to (c).

(a)

(b)

(c)
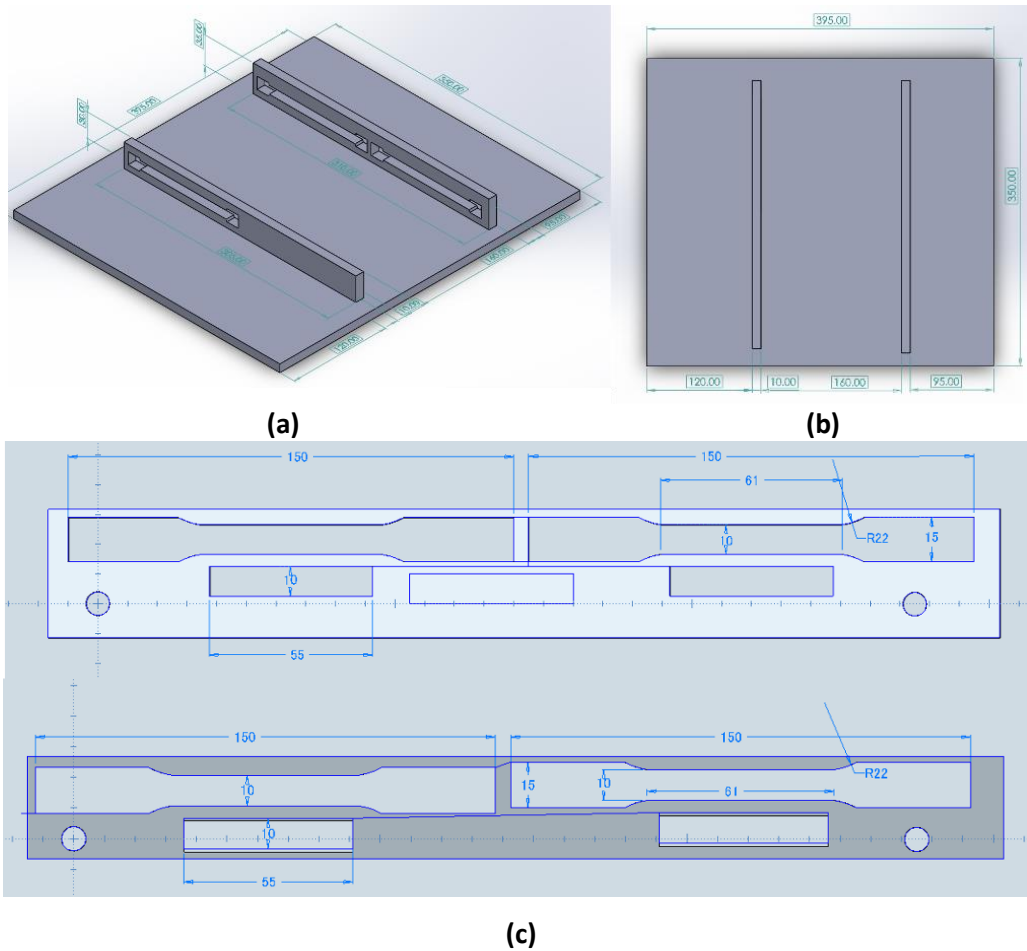
Figure 4-10. CAD drawings for: (a) and (b) the printed walls; (c) location of the coupon specimens.

In Figure 4-11, the two flanges of the RAMLAB I-section are plate A and plate B, while the web is for plate C. The layout of the coupon specimens drawn in CAD followed the chosen locations, as shown in Figure 4-6(e) to (h).
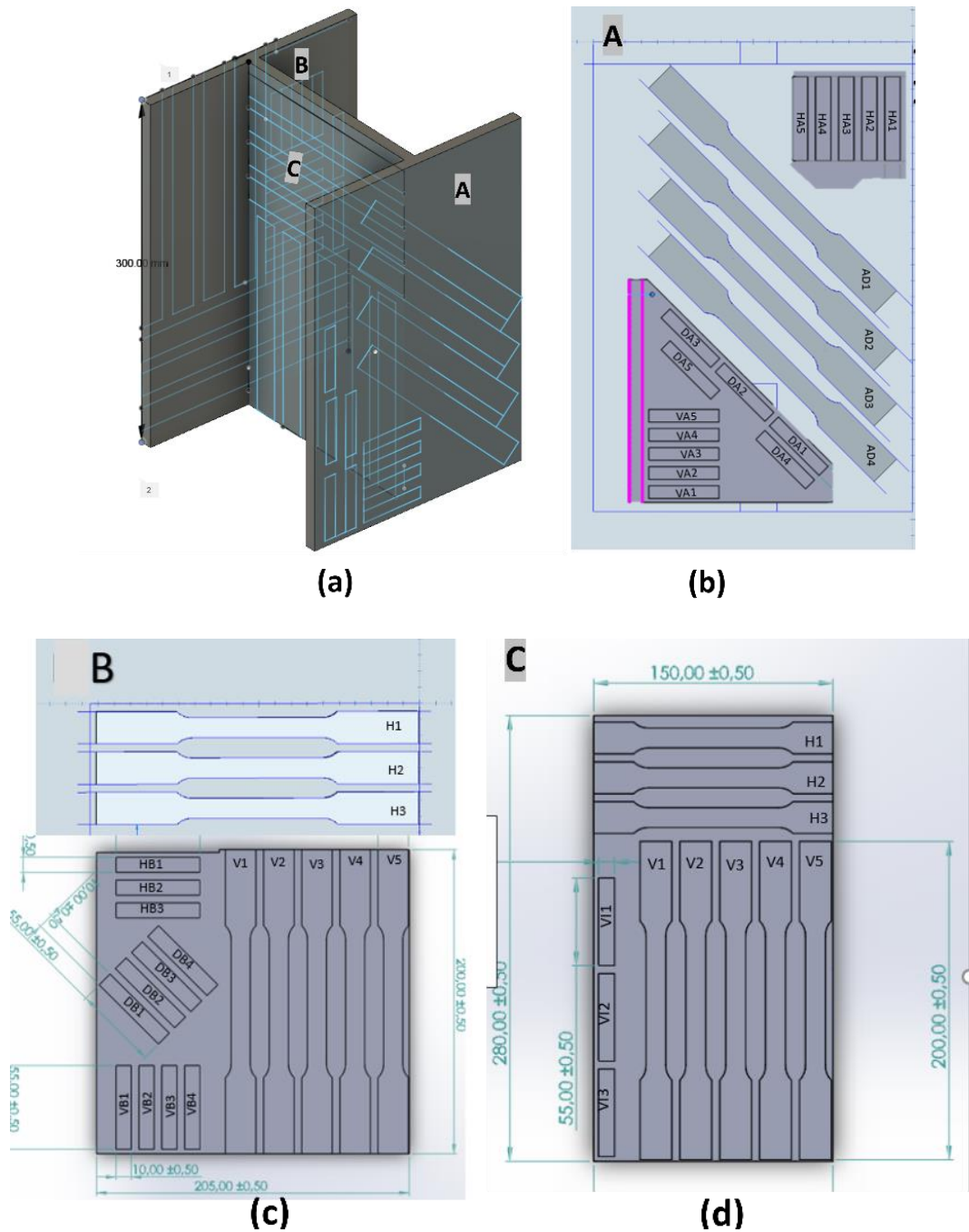
Figure 4-11. CAD drawings for: (a) printed I-section; (b) location of the coupon specimens in Plate A; (b) location of the coupon specimens in Plate B; (c) location of the coupon specimens in Plate C.

4.1.3.3. Machining and milling

Different trials to precisely locate the dog bone coupons on the printed walls are presented in section 4.1.2 "Positioning the cut-out of the test specimens". The SolidWorks 3D models (.SLDPRT files) were imported to a Haas TM-2 Computer Numerical Control (CNC) milling machine using the OneCNC XR8 software. This software post-processed the virtual cutter path into a machine code (ASCII format) part-programme, where it was directly transferred to the CNC machine's control for operation, via a linked cable. The controller then

commands the cutter path, from the part-programme, machining the required dimensions for the coupon specimens. Figure 4-12 presents the overall CNC machining process; Figure 4-12(a) shows the CNC machine, where the plate is clamped to a bed plate, using soluble oil coolant (6-8 % oil, 94-98% tap water) to minimise the friction and localised heating caused during the cutting process. The cutting tools used are a 4mm 4 Flute 4G Mill Coated Carbide Multiple Helix for Heavy Cutting End Mill - SEME71 (YG-1)) and a 4mm 4 Flute 4G Mill Coated Carbide End Mill – SEME72 (YG-1), as seen in Figure 4-12(c).

(a)   (b)   (c)
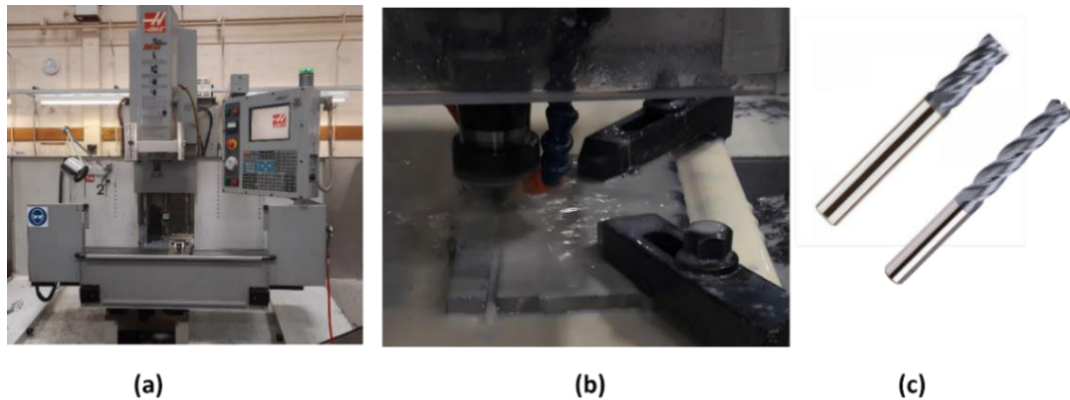
Figure 4-12. Haas TM-2 CNC milling machine for preparing coupons; (a) CNC machine; (b) machining in action; (c) cutting tools for machine tough materials such as steels.

4.1.3.4. Grinding

A 355mm diameter grinding wheel running at 2430rev/min (equivalent to a wheel surface speed of 2700m/min) was employed to grind flat the surfaces of the coupon specimens. Every time the component passed through the machines, 0.025mm of the surface was grounded away. 40 cycles of this grinding process were required to ground off 1mm of printed steel. A magnetic field (KANETSU electromagnetic chuck) created by the induction coil and the surface of the work area, kept a coupon fixed in place while, as seen in Figure 4-13(a), the wheel grinding away the rough surfaces. A similar soluble cutting fluid, as introduced in sub-section 4.1.3.3 'Machining and milling', was also used to reduce the frictional generated heat between the surface and the wheel. Specimens, such as seen in Figure 4-13(b), were set at an oblique angle to the wheel's travel to minimise surface heating, which can be relatively high because of their relatively low volume to surface area ratio.
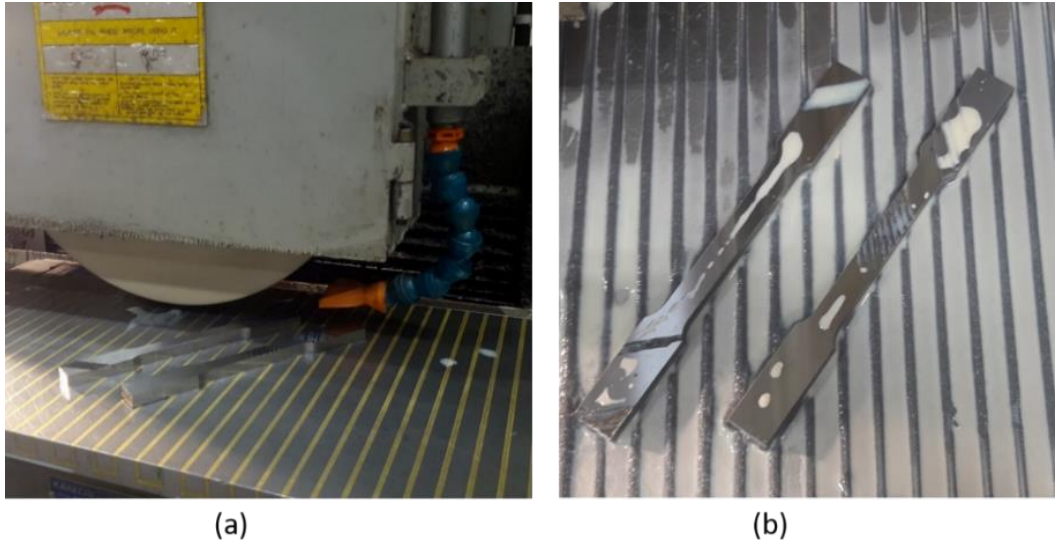
Figure 4-13. (a) Grinding process for RAMLAB dog bone coupons; (b) two specimens after grinding process.

The Autodesk component, shown in Figure 4-14(a), was cut-out using a water jetting technique, a tool capable of producing a high-pressure water jet and an abrasive substance, due to the large thickness of 20.5mm. Figure 4-14(b) to (d) show how the plate was grinded and then subsequently machines to prepare three tensile coupons.
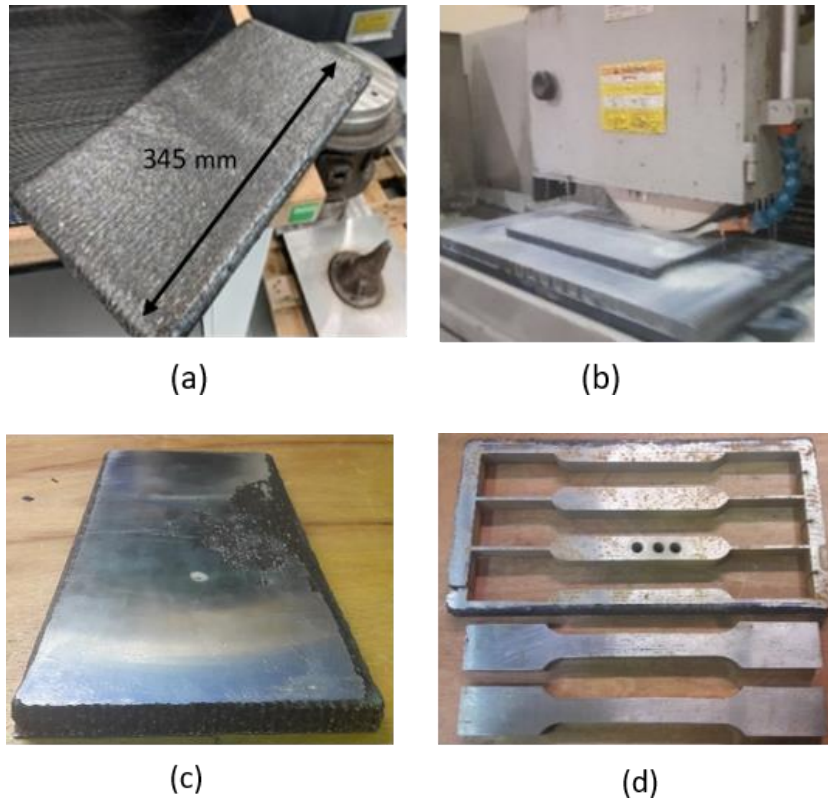
Figure 4-14. (a) 3D printed plate of thickness 20.5 mm; (b) grinding the steel sheet; (c) smooth surface as a result of the grinding; (d) extraction of the dog bones using water jetting process.

The post processing of Steelo components required grinding before milling, as shown in Figure 4-15(a) to (d).
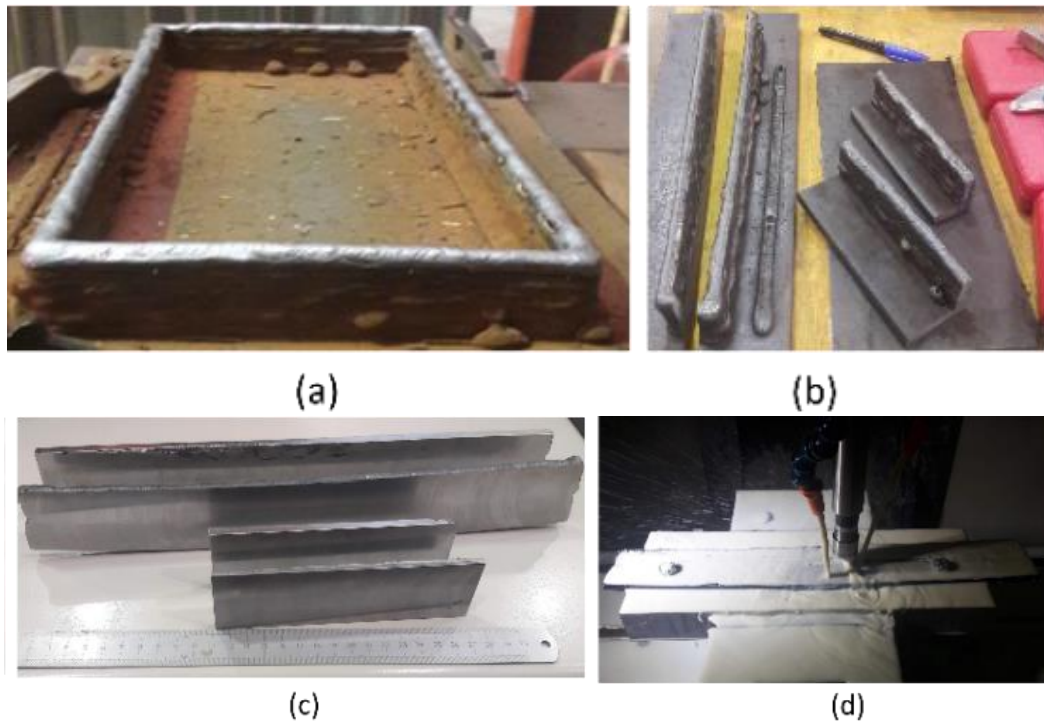
Figure 4-15. (a) 3D printed RHS component; (b) separation of the RHS into plates; (c) surfaces after grinding; (d) machining process to extract the dog bone specimens.

The following section gives a brief summary of how the I-section was machined to produce 20 dog bone and 31 impact specimens, which was done according to the technical drawings in Figure 4-11.

1. The I-section was first separated into the three plates A (flange), B (flange)and C (web), as seen in Figure 4-16(a). For each plate, Figure 4-16(b) shows the coupon outline paths for the milling tool, while Figure 4-16(c) is for the grinding process in action. Plate B was cut-out first, using the long series tool, to obtain three horizontal dog bone specimens (see Figure 4-16(d). Figure 4-16(e) shows that the dog bone coupons taken from the flange of the I-section have a short part that is for the web and connection zone; this was introduce by following pattern A for the designed I-section (see section 3.4.4.4)
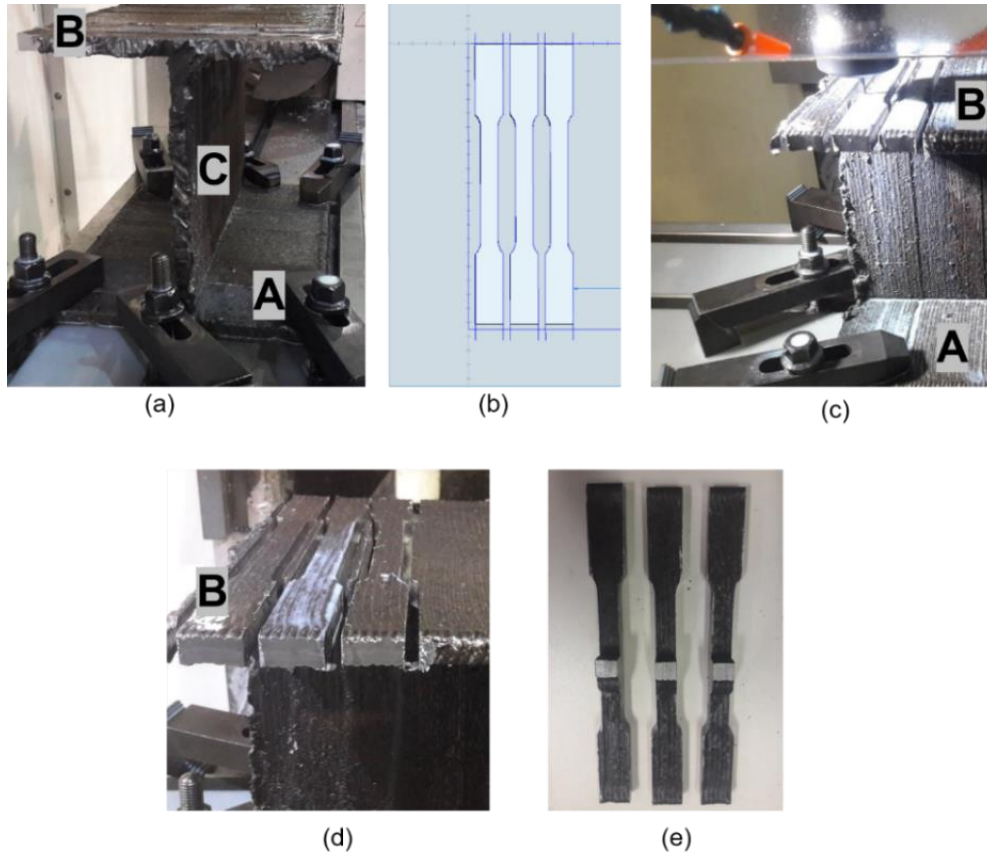
Figure 4-16. Various steps in extracting the horizontal specimens from flange plate B: (a) Separating the I-section into three plates A (flange), B (flange)and C (web); (b) Path outlines for the milling tool to extract the coupons; (c) Cutting process in action; (d) Three horizontal dog bone specimens obtained from the cutting process; (e) Dog bone coupons taken from the flange of the I-section

2. Next, the component was flipped upside down, so that, as seen in Figure 4-17(a), plate A is on the top. The cutting path for the three coupons cut from this flange followed the diagonal path shown in Figure 4-17(b).
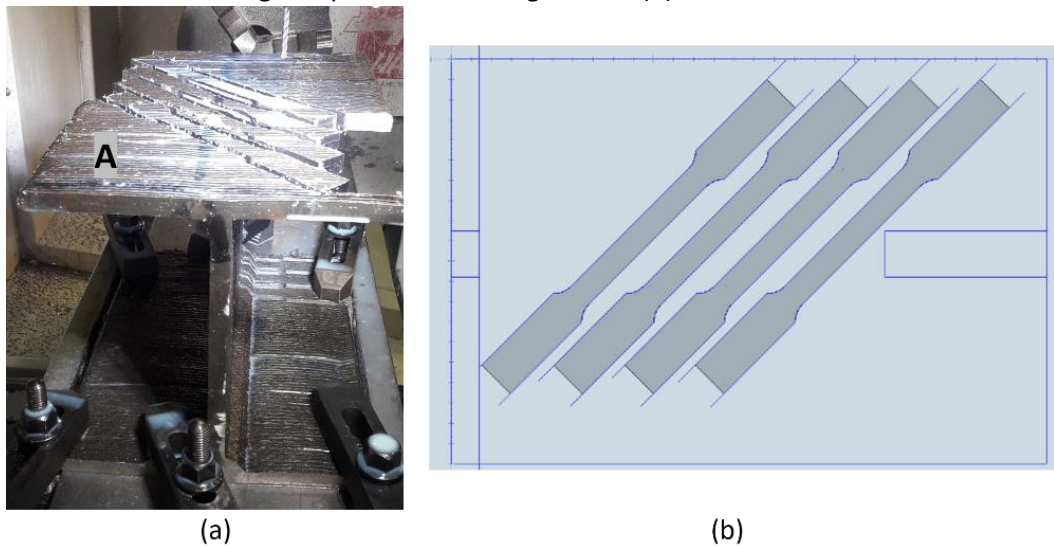
Figure 4-17. Extraction of the diagonal specimens from Plate A: (a) Diagonal specimens obtained from the milling; (b) Path outlines for the diagonal specimens

3. As shown and labelled in Figure 4-18, the leftover steel from the original I-section was separated into various plates.
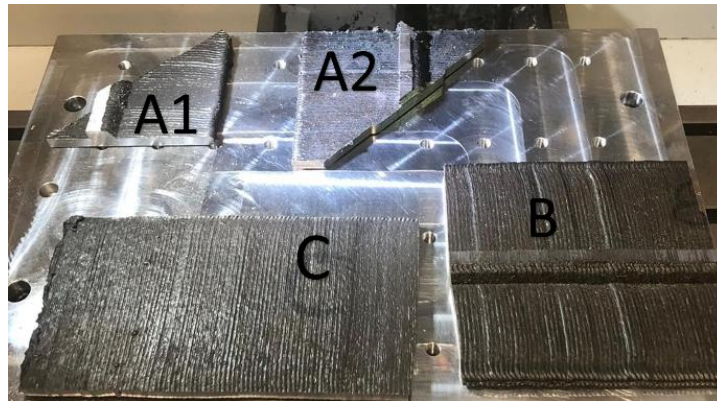
Figure 4-18. Remaining steel from I-section gave the four plates of A1, A2 and B from the flanges and C from the web.

The extraction of further coupon specimens from these plates can be seen in Figure 4-19.
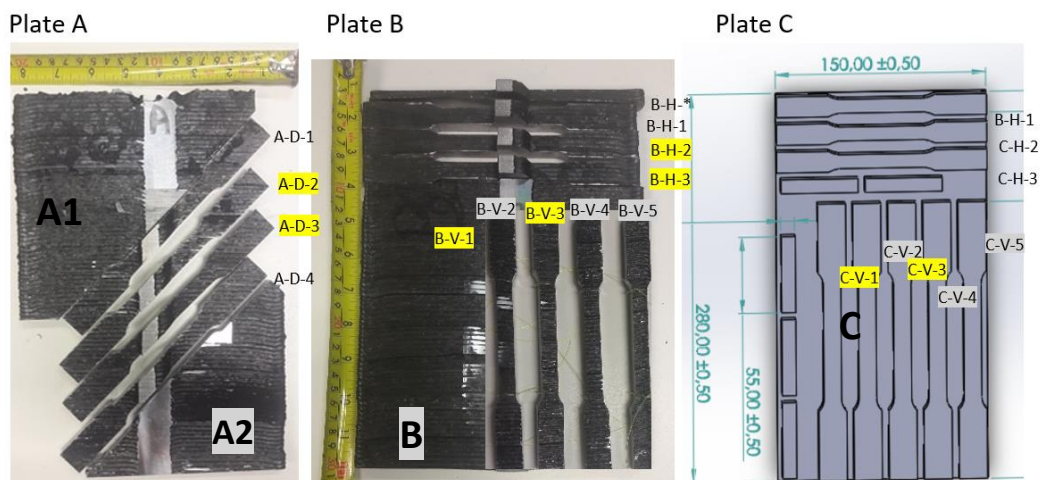
Figure 4-19. Tensile coupons extracted from plate A, B and C as outlined in Figure 4-6 and Figure 4-11

4.1.4. Setting specimens for testing

4.1.4.1. Strain gauges and wiring:

Strain gauges measure the local direct strain, due to the applied axial displacement to the material they are bonded too. They are used in this research to calculate the Poisson's ratio of the printed steel. Because the printed steel is a ductile material, YEFLA-2 post-yield (see Figure 4-20 (a)) and YEFRA-5 post-yield (see Figure 4-20 (b)) strain gauges were chosen. The individual letters in the label 'YEFRA' have their own meaning. The numbers (2 or 5) stand for the gauge length used in mm, which should be chosen based on the type of construction material. For example, the length range with reinforced concrete should be between 30 and 120mm, while the gauge length with a metal can be between 2

and 6mm. Abbreviation YE is show the gauges are post-yield (i.e. it can capture readings in the plastic region and up to a direct strain of 10 to 15%), while RA stands for a Rosette strain gauge, which captures the three principal strains at a local area as shown in Figure 4-20 (b), and finally LA means there is single gauge, as shown in Figure 4-20 (a).
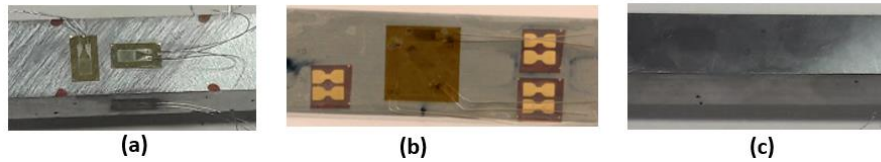
Figure 4-20. (a) Two Linear gauges for longitudinal and lateral directions; (b) Rosette strain gauges; (c) surface post preparation

Before the strain gauges were glued onto the surface it was prepared; Figure 4-20 (c) shows the surface post preparation. The required preparation to obtain a smooth clean surface included using 40 and 100 'coarse' sanding papers, followed by a soluble chemical wash (Acetone Vapor venting) to remove any grease, dust, debris, and metal particles.

After preparing a smooth and flat surface for contact between the strain gauges and steel, the strain gauges were bonded using a compatible CN-Y (cyanoacrylate) adhesive. The centre of a gauge area was positioned to be at the centre of the specimen's width. An example of strain gauging is seen in Figure 4-21 with wiring attached to the strain gauges' conductor and terminal tags.
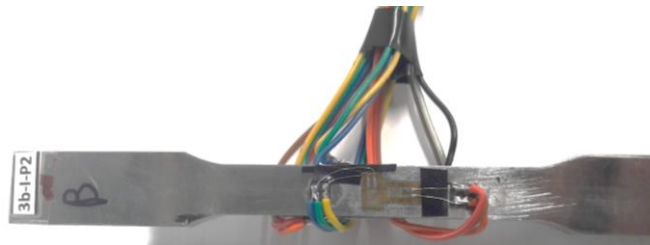
Figure 4-21. Tensile Instrumented coupon S_RHS_S35_I_T_3 with longitudinal and biaxial (Y EFLA-2 post yield) strain gauges on both outer surfaces.

4.1.4.2. Preparation of the groove:

Preparation for the impact samples required an additional step, after establishing the lay-out of specimens (for example as shown for plates A, B and C in Figure 4-22(a) to Figure 4-22(c)) and cutting-out and grinding them (as seen in Figure 4-22(d)), which is the machined impact specimens according to their exact dimensions as detailed in sub-section 4.1.1.2. Specimens with the central v grooves are shown in Figure 4-22(e).
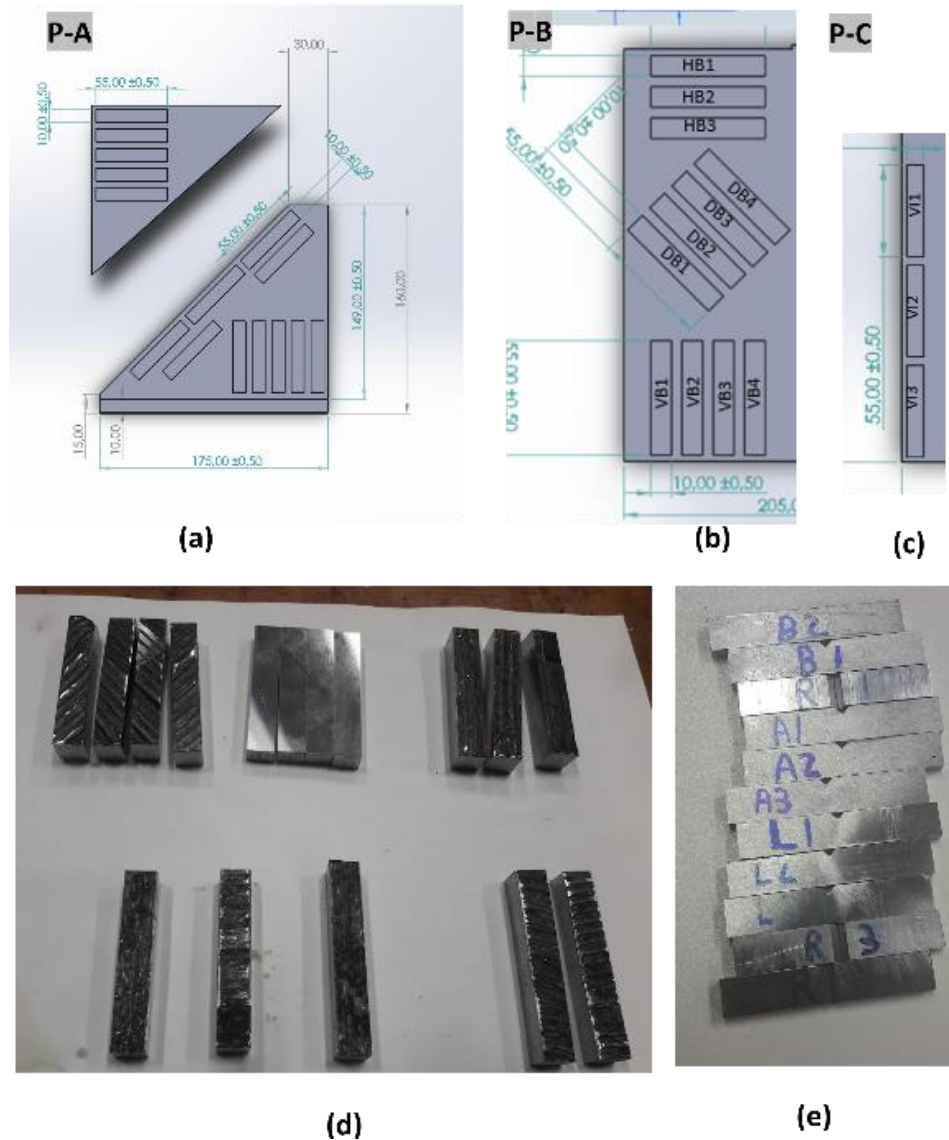
Figure 4-22. Impact test specimen preparation with the groove: (a-c) Outlined location for the impact specimens in plates A-C respectively; (d) Extracted impact samples for grinding and before the V notch was grooved; (e) Impact specimens with a V groove ready for testing

4.2. Tensile test methodology

Tensile testing was performed to determine the direct stress-direct strain relationship up to the failure of the steels. The tests were carried out using either an Instron universal testing machine with a 250kN load cell capacity (see Figure 4-23(a)) or an Instron universal testing machine with a 100kN load capacity (see Figure 4-23(b)), both located in the WMG Materials Engineering Centre.

The 250kN machine was used with specimens "A_ Plate_S35 _L_T_1 to 3" which had the largest cross-sectional area of 340 mm, as recorded in the first row of Table 4-1. Because the specified ultimate tensile strength of the printed wire used was 440N/mm^2 (Union K 40 steel) the expected ultimate tensile load for these specimens was 150kN. (Chapter 3, section 3.2.1)
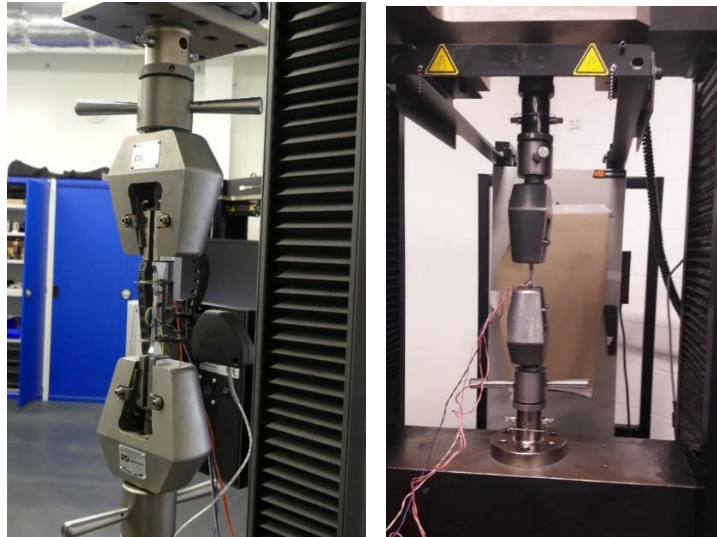
Figure 4-23. Universal testing machines with a load capacity of: (a) 250kN; (b) 100kN.

An example of the configuration for tensile testing is illustrated in Figure 4-24, which consisted of specimen A_Plate_S35_L_T_2, with longitudinal and biaxial YEFRA-5 post yield strain gauges, a 2630-118-105 extensometer ("Longitudinal Ext" in the figure) of gauge length 80mm, and an I3575-250M extensometer of gauge length 20mm ("Transverse Ext" in the figure).
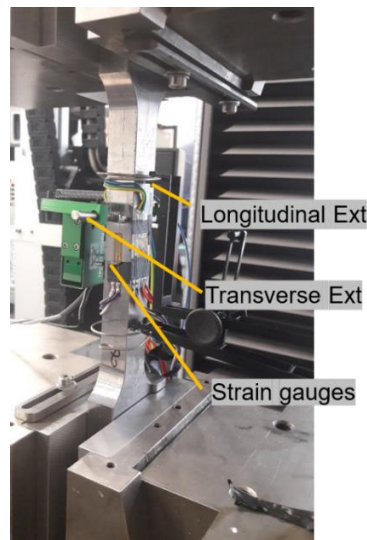
Figure 4-24. Tensile test.

Before running the uniaxial tensile strength tests, the three most important considerations were the testing rate, the Data Acquisition System (DAQ) used to synchronise the strain gauges' readings and the chosen size of the extensometer for determining direct strain.

4.2.1. Testing rate

The rate of separation of the grips (or movement of the testing machine's crosshead) is a function of the applied axial tensile load. Two approaches to choosing the testing rates,

Method A or Method B, could be carried out by following the instructions in Section 10.3 of (BS/EN-ISO6892-1:2019). Method A is based on the strain rate (controlled by the change in elongation displacement) and is divided into open and closed loop testing. On the other hand, method B is based on the stress rate (controlled by the applied load and its consistency – both of which depends on the type of the material).

The closed-loop approach in method A (A1) depends on the feedback from the extensometer to control the strain rate, whereas the open loop (A2) estimates the strain rate over the coupon's parallel length (L_c). The estimated strain rate was calculated based on the separation rate of the crosshead, which satisfies the equation $V_c = L_c \times e_{lc}$, where V_c is the crosshead separation rate and e_{lc} is the estimated strain rate over the parallel length.

A2 was the methodology used in this characterization work to change the testing rate and has the advantage of defining the points of interest, such as the upper yield strength (R_{eH}), lower yield strength (R_{eL}) and tensile strength (R_m) through a specified range of strain rates ($e_{lc}s$). For example, the calculated V_c for A_ Plate_S35 _L_T_1 to 3 specimens (with L_c = 132mm, see Table 4-1) was based on the recommended strain ranges e_{lc} in Sections 10.3.2.2-4 of ISO 6892-1 to capture R_{eH} , R_{eL} and R_m. This test information is presented in Table 4-4.

Table 4-4: Calculated crosshead separation rate

Strain rate	Chosen strain rate	Calculated V_c
1	2	3
To determine the Upper yield strength R_{eH}	Range 2: e_{lc} = 0.00025 s^{-1}	0.00025 S^{-1} x 132 = 1.98 mm/min
To determine the Lower Yield strength R_{eL}	Range 1: e_{lc} = 0.00025 s^{-1}	0.00025 S^{-1} x 132 = 1.98 mm/min
To determine the tensile strength R_m and the percentage of elongation after fracture	Range 2: e_{lc} = 0.00025 s^{-1}	0.00025 S^{-1} x 132 = 1.98 mm/min

The stroke rate was 2mm/min for the recommended 0.00025 s^{-1} strain rate over both the elastic and plastic stages, when determining the upper yield strength (R_{eh}), the proof strength (R_m), and the percentage of elongation after fracture. For the five different test coupons Table 4-5 presents the strain rate and extensometer measurements. Column 1 lists the coupon types with their labels and reported in column 2 are the strain rates.

4.2.2. Size of the Extensometer

The chosen length of the external extensometer is a function of the gauge length of the specimen, which should exceed 0.5x(L_o) and not > 0.9x(L_c), as specified in Section 8.3 of ISO 6892-1. Columns 3 to 4 in Table 4-5 present the lengths based on the minimum and maximum extensometer values and columns 5 and 6 list the lengths of the longitudinal extensometer and lateral extensometer, respectively.

Table 4-5: Strain rate and extensometer lengths for the tensile coupon specimens

Coupon type and labelling scheme	Strain rate (s^{-1})	Min Ext= 0.5x(L_o) mm	Max Ext= 0.9x(L_c) mm	Longitudinal Ext gauge length (L_e) mm	Transverse Ext length (L_e) mm	Strain gauge type
1	2	3	4	5	6	7
A_ Plate_S35 _L_T_1 to 3	1.98	0.5x104 = 52	0.9x132 = 118.8	80	20	YEFRA-5
A_Plate_S35_ TT_T_1 to 4 (straight sided)	-	0.5x45 = 22.5	0.9x65 = 58.5	25	-	-
S_WALL A_S35_L_T_1 to 2 S_ WALL B_S35_ L_T_1 to 2 S_RHS_S35_ I_T_1 to 3 S_RHS _S35 _L_T_1 to 3 R_IC_S46_L_T_1 to3	0.915	0.5x48 = 24	0.9x61 = 54.9	50	10	YEFLA-2
R_IA _S46 _I_T_1 to 4 R _IB _S46 _L_T_1 to 3 R_IB _S46 _T_T_1 to 5 R_IC _S46 _T_T_1 to 5	1.2	0.5x63.2 = 31.6	0.9x80 = 72	50	12.5	YEFLA-2
EN 8	1.52	0.5x80 = 40	0.9x101.5 = 91.35	80	-	YEFLA-2

4.2.3. DAQ and strain gauges' configuration

A Data Acquisition System (DAQ) was used in the tensile tests to record the digital load signals, the extensometer, and the strain gauge readings. The 3D printed steel stress-strain reading was to be captured directly from the testing machine using the BlueHill software. Electrical signals from, for example, a rosette gauges were transmitted and proceeded into filtered data to be analysed using the Micro-Measurement System 8000 DAQ system and its software.

The DAQ system had the capacity for eight channels to input signals from strain gauges, in parallel with the main machine controller, as shown in Figure 4-25. With specimens A_ Plate_S35 _L_T_1 to 3, channels 1 to 6 were configured to input signals from the rosette strain gauges, while channels 7 and 8 were linked to the load transducer (the load cell on the Instron testing machine) and longitudinal extensometer, respectively. The DAQ system and the load controller with the Instron were set-up to ensure that the readings were taken in real time and concurrent.

Thereby, the strain gauge readings could be synchronised with the stress (tensile load) applied to a specimen and synchronised with the recorded displacement from the longitudinal extensometer.

1-6 Strain gauges   7- Load   8- Longitudinal EXT
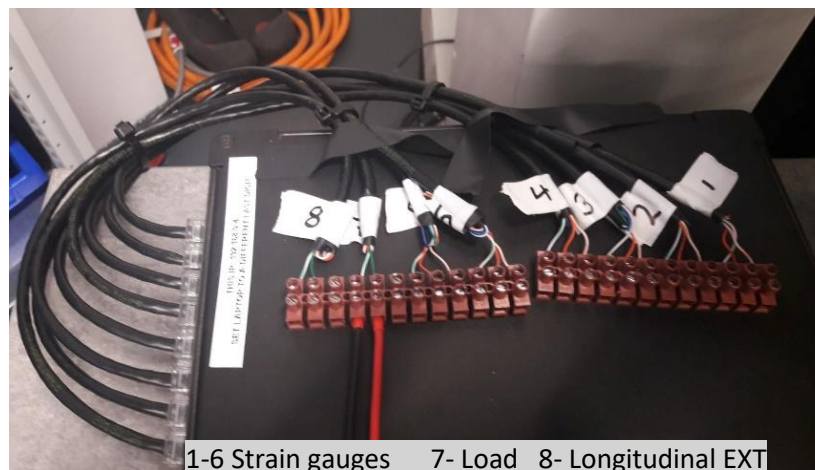
Figure 4-25. DAQ system with the eight channels labelled 1-8.

In the following sub-section, the details of the load and strain gauge configuration will be presented for the DAQ and load controller system.

4.2.3.1. Configuration of the strain gauges

A strain gauge converts the material's displacement over its length, under the applied forces, into a change in electrical resistance, which is then converted into a digital value of strain.

Figure 4-26 shows the gauge configuration profile with Channel 6 of the DAQ having a strain gauge. The type of gauge is YEFLA-2, and values for the profile were taken from the supplier's data sheet. The gauge factor is 2.16 (for the YEFLA-2 strain gauges), whilst the gauge resistance is 120 Ω for a quarter bridge connection.
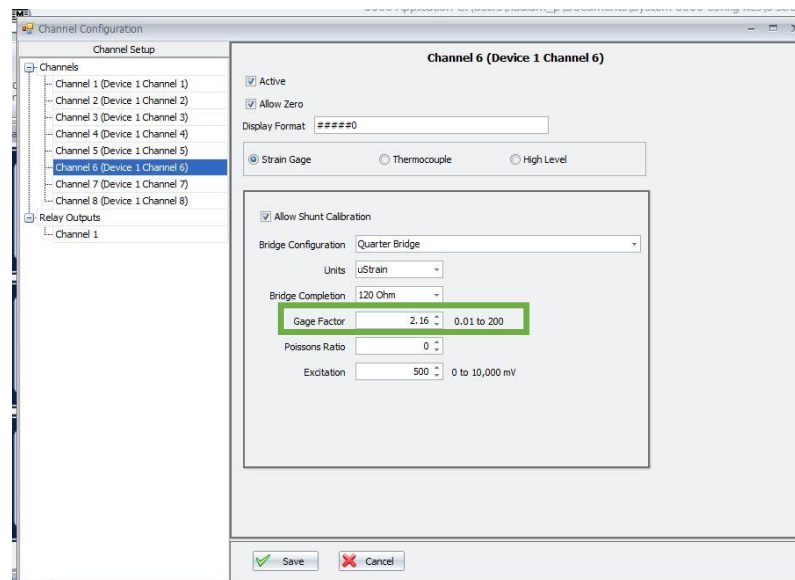
Figure 4-26. Configuration profile for the strain gauge linked with channel 6 (see Figure 4-25)and the excitation value.

The excitation voltage (V) is the voltage across the strain gauge, which induces a current (I) through the foil wire, enabling the resistance (R) to be measured. The current, however, generates heat i.e., increasing the gauge's temperature; the rate of energy transfer follows the equation for power: $P = IV = I^2 R = \dfrac{V^2}{R}$. A balanced excitation voltage was considered to minimise the heat generated. The lower the voltage, the lower the heat energy. A 500mV excitation voltage was applied across a strain gauge. Hence, the calculated heat dissipation, in J/s, is equal to $\dfrac{V^2}{R} = \dfrac{0.5^2}{120}$ = 0.00208J/s which is insignificant for the used strain gauge. By having a lower excitation voltage, the post yield gauges were able to record strains as high as 15%.

4.2.3.2. Load configuration

The analogue reading for tensile load, from the controller of the Instron testing machine, was connected to the DAQ software. This reading was converted into a digital format so that load readings could be synchronised with the strain gauge measurements. The proportional conversion factor between the load and voltage is shown in Figure 4-27, which is an example set-up of the input channels to give an output signal of 1 volt per 25 kN load increment.
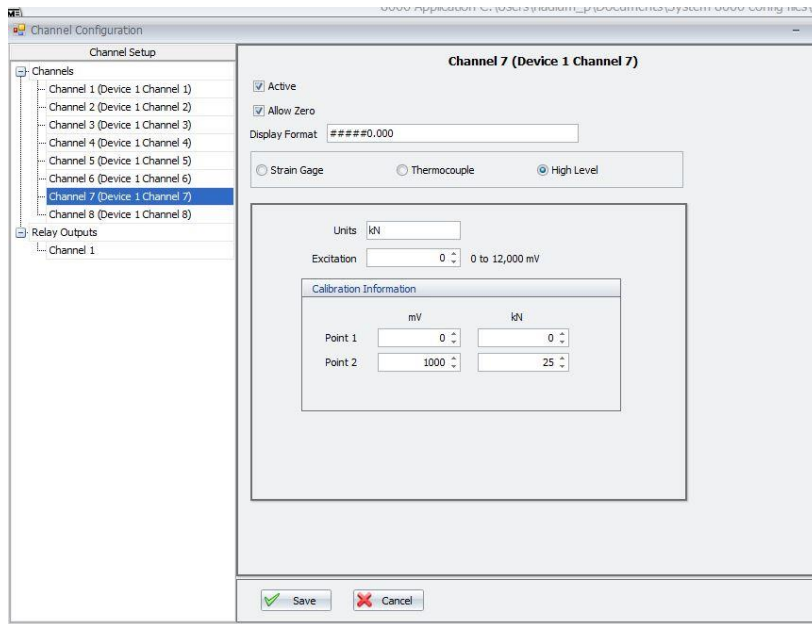
Figure 4-27. Configuration of the load channel with the DAQ system for readings from the load cell.

4.2.3.3. Extensometer configuration:

Similar to sub-section 4.2.3.2 the channels for the two extensometers were set-up such that the DAQ system transforms 1V into a direct strain of 2% as seen in Figure 4-28.
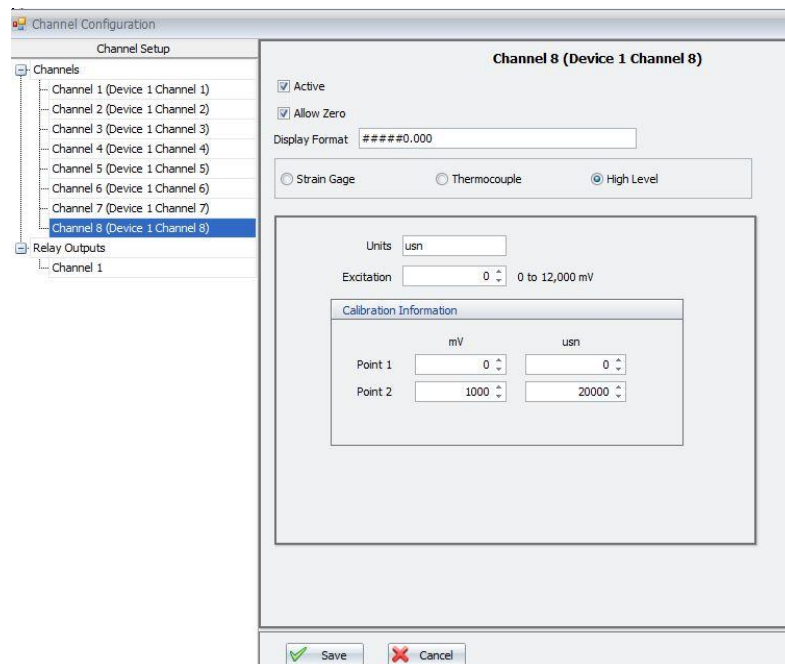
Figure 4-28. Configuration of the extensometer channel with the DAQ system and the strain.

4.2.4. Tensile machine and extensometer

The interaction between the tensile testing machine, strain gauges, and extensometers is summarised in Figure 4-29.
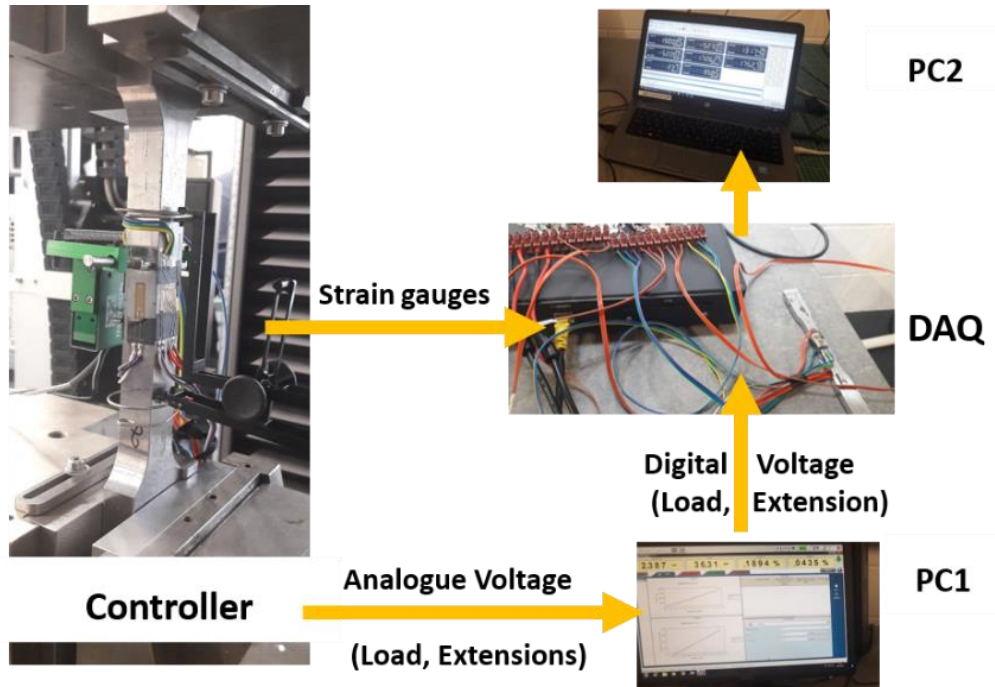
Figure 4-29. Interaction diagram between DAQ system, Instron testing machine and PCs to synchronise the readings of load, strains, and displacements.

The DAQ system was linked to the test machine controller (to capture the load and extensometer displacements), in-sync with the strain gauges (record the current flow due to the applied load). Specimen data were recorded in real time by the Instron's controller using BlueHill software (V 3.76.4926 (kN)) for the A_ Plate_S35 _L_T_1 to 3 and EN 8 steel coupons (see Table 1-1). The readings from a 2630-118-105 extensometer measuring longitudinal displacement, with a gauge length of 80mm, and an I3575-250M extensometer measuring transverse displacement, with a gauge length of 20mm, were recorded by both the DAQ and BlueHill software. The 6 strain gauge links were recorded in real time using a Micro-Measurements System 8000 DAQ that filtered, and record strains synchronised with the tensile load signal impulses from the tensile machine.

4.3. Impact test methodology

To measure the absorbed energy for the printed steels, standardised specimens (see sub-section 4.1.1.2 and Table 4-3) were designed to measure the toughness and the impact loading in accordance with *Metallic materials — Charpy pendulum impact test Part 1: Test method* (EN/ISO148-1:2016, 2016). In Figure 4-30, the pendulum impact MTS Exceed E22

testing machine, in the materials lab at the Delft University of Technology, was used at room temperature of 20 ± 1°C with V-notched samples, of size 55mm x 10mm x 7.5 or 5mm.

Figure 4-30. MTS Exceed E22 pendulum impact testing machine in the TU-Delft lab

As shown in Figure 4-31(a) a specimen was placed in the lower part of the machine on two supports for a span length of 42.5 mm. The specimen was positioned such that its centre was aligned to the centre of the pendulum strike with an accepted tolerance of 0.5mm, as marked in Figure 4-31(b). A pendulum was then released with a hammer moving downwards to hit the specimen.

1	Anvil
2	test piece
3	Supports
4	Shroud
5	Width, W
6	Length, L
7	Thickness, B
8	Centre of strike
9	Direction of pendulum swing

(a) **(b)**
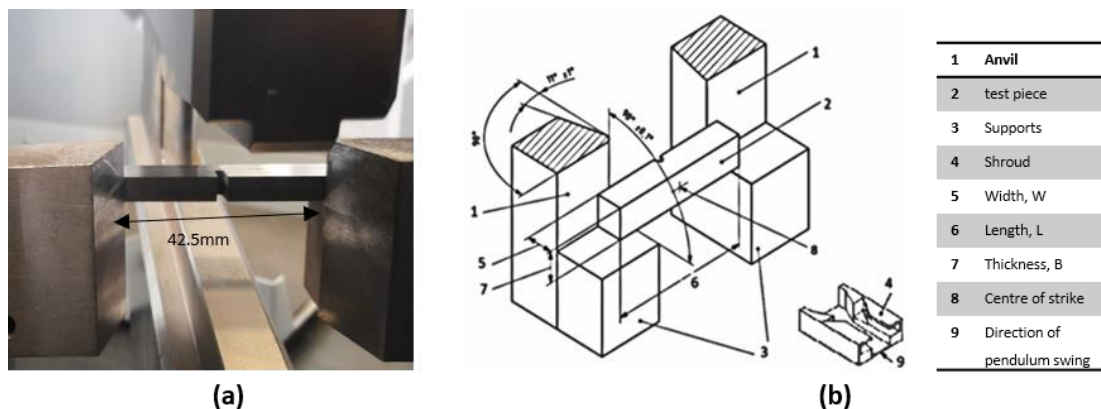
Figure 4-31. (a) specimen with a standardised notch centred; (b) pendulum impact test machine standardised terminology according to BS EN ISO 148-1:2016.

4.4. Density measurement technique

To measure the density of steel, the precision electronic balance shown in Figure 4-32 was used. As seen in Figure 4-32 (a) it has a built-in underhook from which a coupon is hung to

measure the weight in air (W). Next, the balance was zeroed before submerging the coupon in water, as seen in Figure 4-32 (b). Changes in weight of specimen ($W - W_a$) and the temperature of the water were recorded.
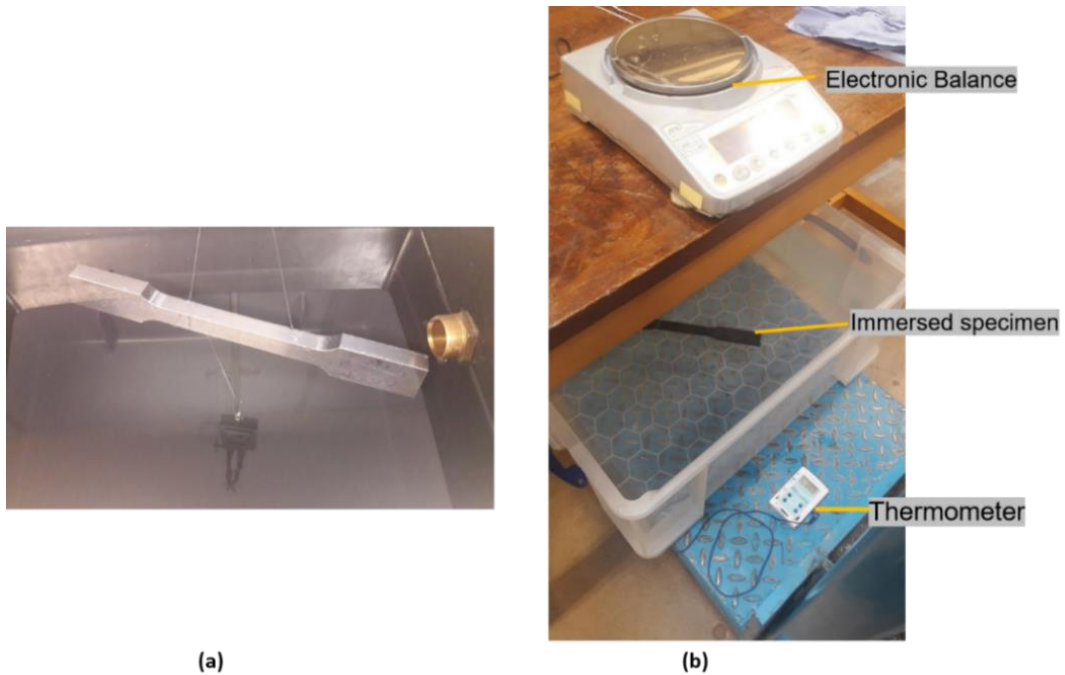
Figure 4-32. (a) Hanging specimen; (b) Specimen submerged in water.

4.5. X-CT scan scanning

X-ray Computed Tomography (X-CT) is a process by which it is practical to create images of the interior of solid components in a non-destructive manner. In this research, X-CT scanners at the Centre for Imaging, Metrology and Additive Technologies (CiMAT), a centre in WMG at The University of Warwick were used to investigate the interior of the printed component as a testing method for Quality Control. X-CT was employed to establish the sizes, amount (volume fractions), and distributions of porosity for using the coupon specimens listed in Table 4-6. In this table column 1 details the name of the scanned components using the labelling system from Table 4-1, while column 2 summarises the size and shape of the scanned coupon components.

Table 4-6: A summary of all the 3D printed specimens that were X-rayed

Name of the samples	Type and size of the components
1	2
A_ Plate_S35 _L_T_3 (dog-bone) A_Plate_S35_ TT_T_2 (straight sided) A_Plate_S35_ TT_T_1 (straight sided)	 (a) (b) Figure 4-33. (a) 300x20x17mm dog-bone coupon; (b) 65x3.8x17mm straight-sided coupon
S_WALL A_S35_L_T_1 S_WALL A_S35_L_T_2 S_ WALL B_S35_ L_T_1 S_ WALL B_S35_ L_T_2 S_RHS_S35_ I_T_1 S_RHS_S35_ I_T_3	 Figure 4-34. 150x10x7mm dog-bone coupon
R_IA _S46 _I_T_2 R_IA _S46 _I_T_3 R _IB _S46 _L_T_2 R _IB _S46 _L_T_3 R_IB _S46 _T_T_1 R_IB _S46 _T_T_3 R_IC _S46 _T_T_1 R_IC _S46 _T_T_3	 Figure 4-35. 200x20x11mm dog bone coupon
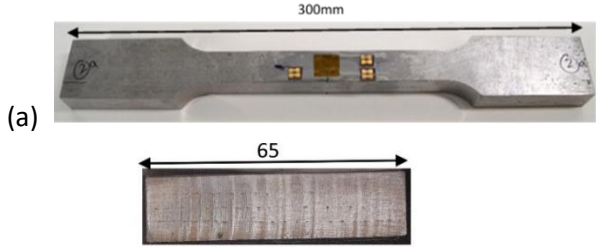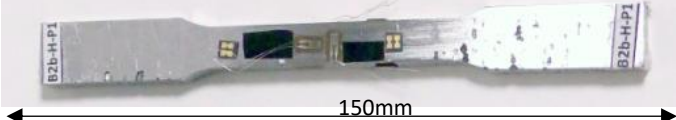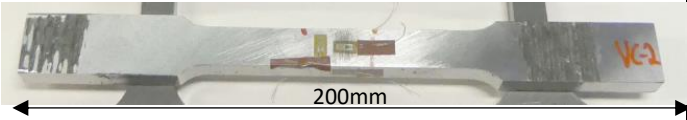
Another part of the X-CT characterisation work was to scan the connection zone in the 36 kg beam-to-column joint, which is shown in Figure 4-36. The imaging of this relatively large component is for regions of interest identified by the blue ellipsoidal borderline in the figure.
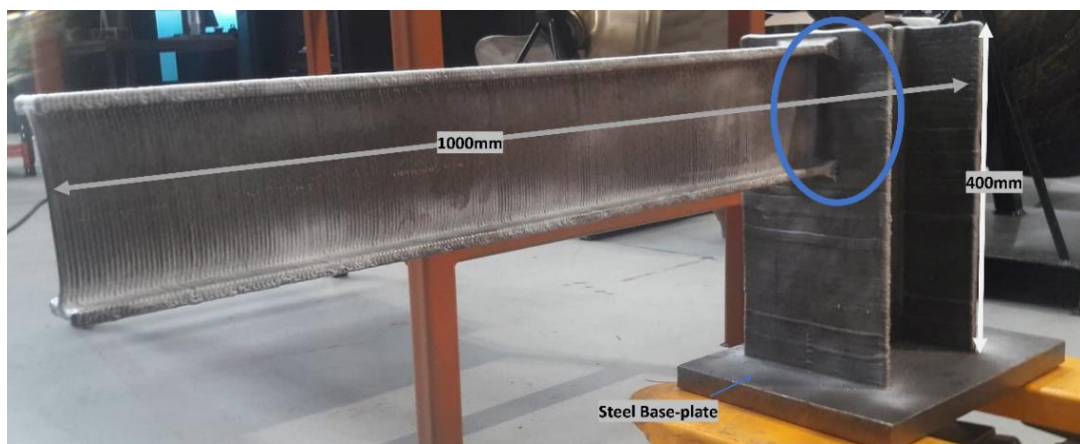
Figure 4-36. Monolithic beam-to-column joint formed by printing an 800mm beam on top of 400mm stub column (photo also shows steel base-plate).

The X-CT results aim to build a base understanding of how porosity, internal fusion and the interacted layers can affect the overall homogeneity and mechanical properties of the welded steels.

4.5.1. X-CT methodology

The scanner consists of an X-ray source and a detector, between which the object of interest is placed, as shown in Figure 4-37. To scan the object, continuous X-rays are fired from the source towards the detector, through the object. As the X-rays travel through the object, they are attenuated, with the degree of attenuation being proportional to the thickness of the material it travels through, its material composition, and its density.
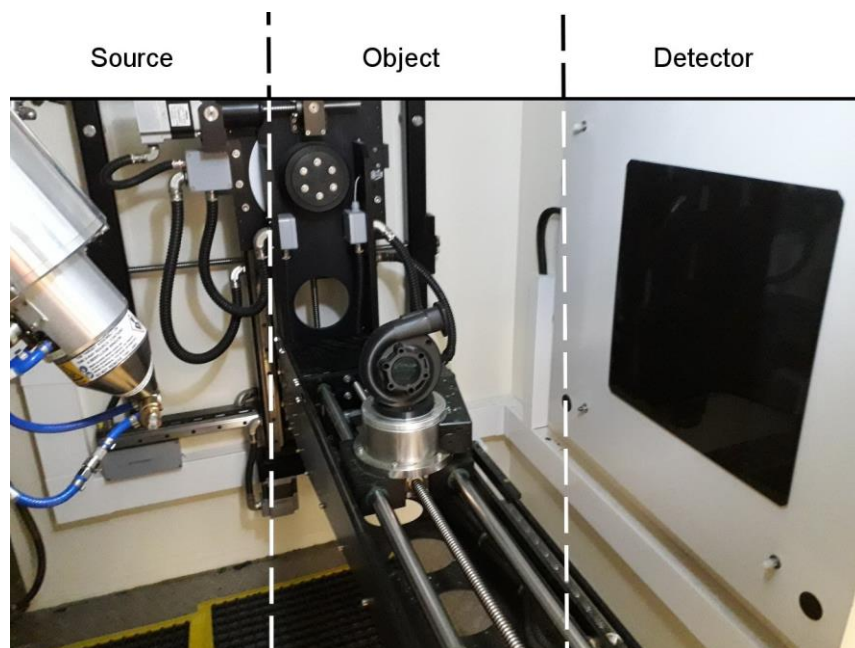
Figure 4-37. Main parts of the Nikon XT H 225 LC X-CT scanner consisting of the source, object, and flat panel detector.

The attenuated X-rays and its energy value recorded are then registered by the detector, where the attenuated X-rays are recorded by the detector panel, each of its pixels registering incoming X-rays. This creates a radiograph image of the object, as shown in Figure 4-38, much like in conventional radiography.
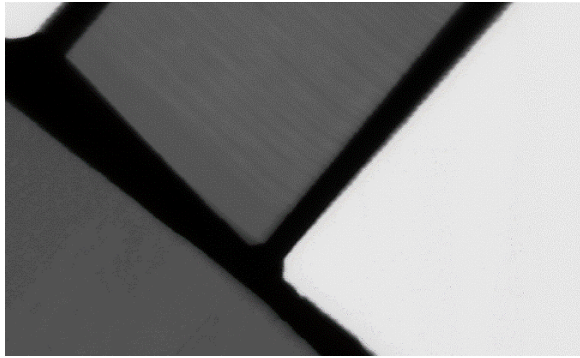
Figure 4-38. A radiographic image for one of the beam-to-column joint.

The object in the X-CT scanner is then rotated in small increments ('six' per degree of rotation) and at each increment a new radiograph is acquired. This process is repeated through 360° in order to obtain a full set of radiographs of every orientation around the object. By using this testing procedure an X-CT experiment provides radiographs that can be reconstructed using tomography software to construct 3D images of the scanned objects that provides for an internal investigation of the material's internal structure (analysis).

4.5.2. X-ray specimen preparation

Mounting an object in the scanning chamber is dependent on a few key parameters, such as the size of the chamber, the dimensions of the chamber access door, and the size of the object so that a full rotation of the object does not strike either the walls of the scanning chamber or the source or detector.

The tilting angle of the object is key to minimise streak artefacts, which is a known phenomenon in X-CT. Scanning artefacts can be identified as scanning issues with certain shapes and properties, as there are many categories with their own causes. For example, beam-hardening occurs in dense samples where lower energy X-rays are completely attenuated at the surface of the object, causing the edges to be brighter than the centre. Also, ring artefacts happen when flat surfaces are parallel to the main axis of the cone beam, which could cause the boundaries of the image to blur, and ring-shaped shadows to appear.

For the beam-to-column joint, different orientations were considered to ensure sufficient X-ray penetration in the regions of interest. These regions are marked-out by the blue rectangular boundary seen in Figure 4-39. The figure shows three practical configurations for positioning the beam section of the joint on the scanning table. In Figure 4-39(a), the joint is self-stabilising, but the base plate is now obstructing the X-ray beam from reaching the marked-out regions during the full rotation of the joint. Similarly, for the configuration option seen in Figure 4-39(b), the volume of steel in the base plate that the X-rays would need to

pass through will lead to under-penetration in the regions of interest, and thereby a poor scan. In Figure 4-39(c) the X-ray path line is shown as a black dotted line. This figure shows the optimal configuration, where the regions of interest can be sufficiently penetrated by X-rays from all orientation angles. Because this was also the only feasible scan configuration set-up it was chosen.
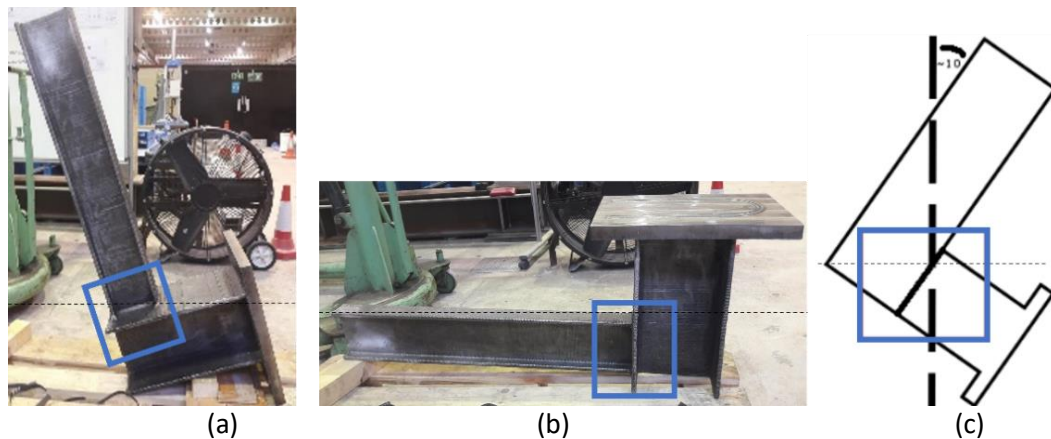
Figure 4-39. Three configurations for the positioning of the joint in the X-ray machine where the X-ray path lines (black dotted line) penetrate the marked blue area: (a-b) Self-stabilising joint; (c) Schematic for the optimal configuration.

The length of the beam section was 800mm (see Figure 4-36), and the maximum allowable distance before the end of the arm would hit the wall was 600mm. This limitation meant that a tilting angle was necessary to avoid collision with all scanning elements and minimise image noise and artefacts. Figure 4-40(a) to (c) illustrates the three proposed titling angles to the vertical of 10°, 30° and 40°. The optimum angle is 40°.
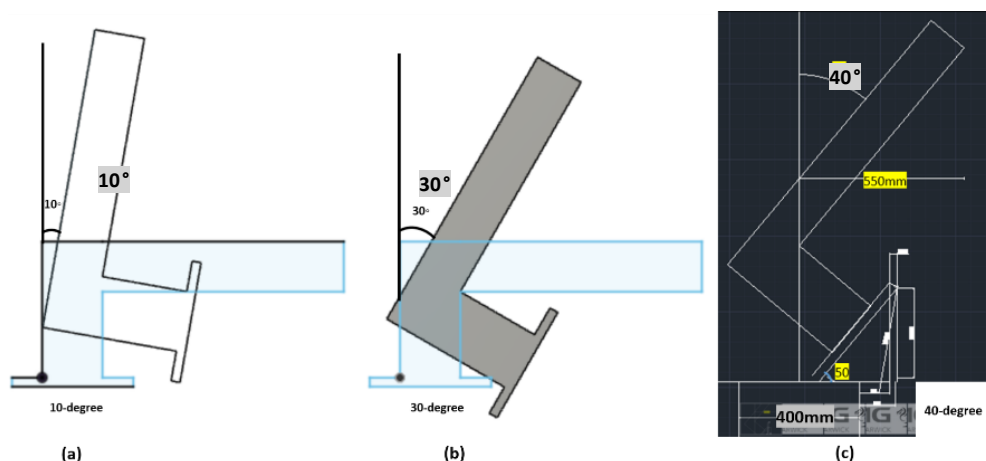
Figure 4-40. Joint component set-up and proposed tilting angles to the vertical: (a) 10°; (b) 30°; (c) 40°.

To support the joint on the 40cm diameter rotational table seen in Figure 4-41(a), the timber supporting platform seen in Figure 4-41(b) was fabricated by the School of Engineering carpenter to provide the required tilting angle of 40°. The timber platform has a base plate

of 500mm wide. As shown in Figure 4-41(c) a block of Plastazote foam was used to hold dog bone coupons in place at the required inclination during the X-ray scanning process.
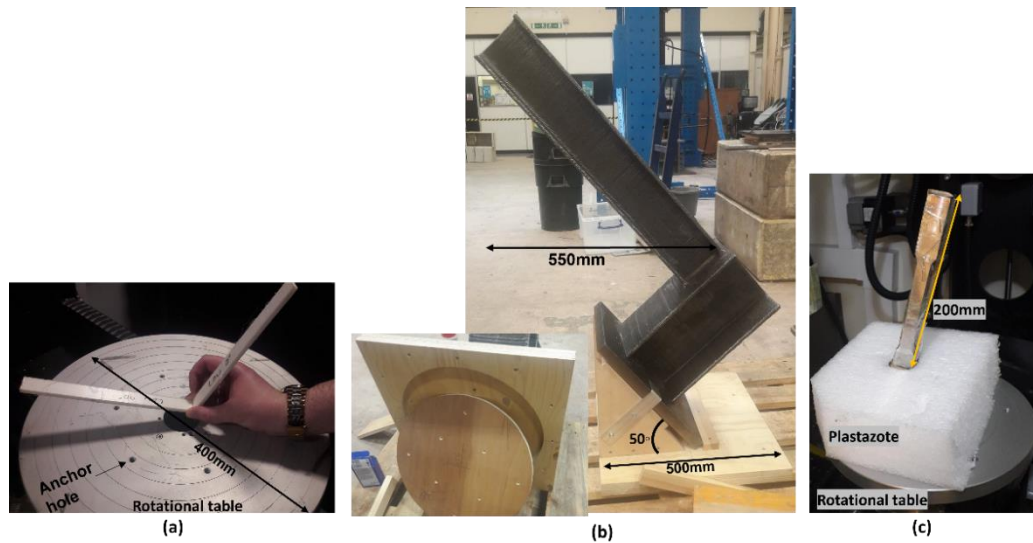
Figure 4-41. (a) X-CT scanning rotational table; (b) timber support platform for joint; (c) dog bone coupon supported with inclination in a block of Plastazote foam.

4.5.3. X-CT scanning process and parameters

The joint was scanned using a Curvilinear Detector Array (CLDA) and a collimator system. The dog bone specimens were scanned using the same approach as the flat detector panel, as demonstrated in Figure 4-37. The primary difference between a CLDA with a collimator and a flat panel is illustrated in Figure 4-42, where the collimator restricts the standard X-ray cone beam into a fan beam to CLDA device.
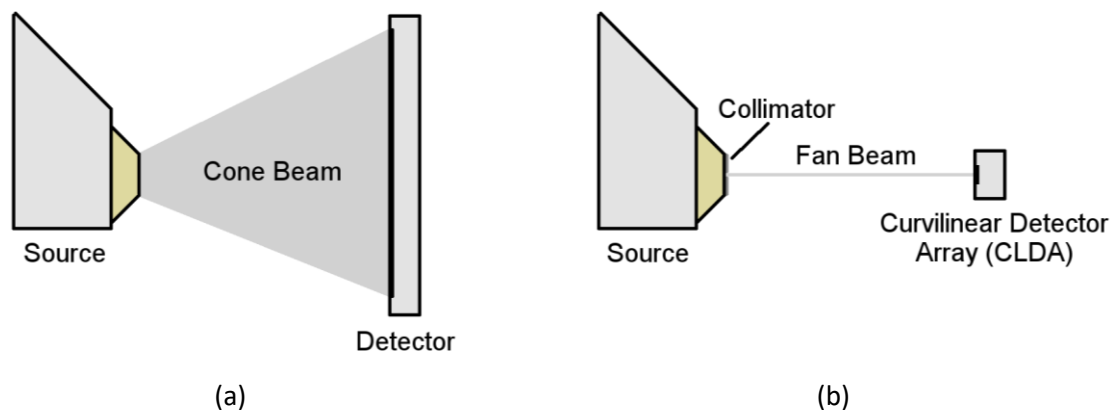
Figure 4-42. Comparison between; (a) flat panel, and (b) CLDA with a collimator

The X-CT scanning parameters were chosen in collaboration with the CiMAT collaborators. The beam-to-column joint, see Figure 4-43, was scanned using a Nikon X-TEK XTH 450 system. This X-CT equipment has a CLDA and a collimator in lieu of a regular flat panel detector because this reduces X-ray scattering within the scanning chamber, leading to

reduced signal noise in the resulting dataset. The trade-off is a longer scanning duration, which is 76 hours for the regions of interest in the joint.
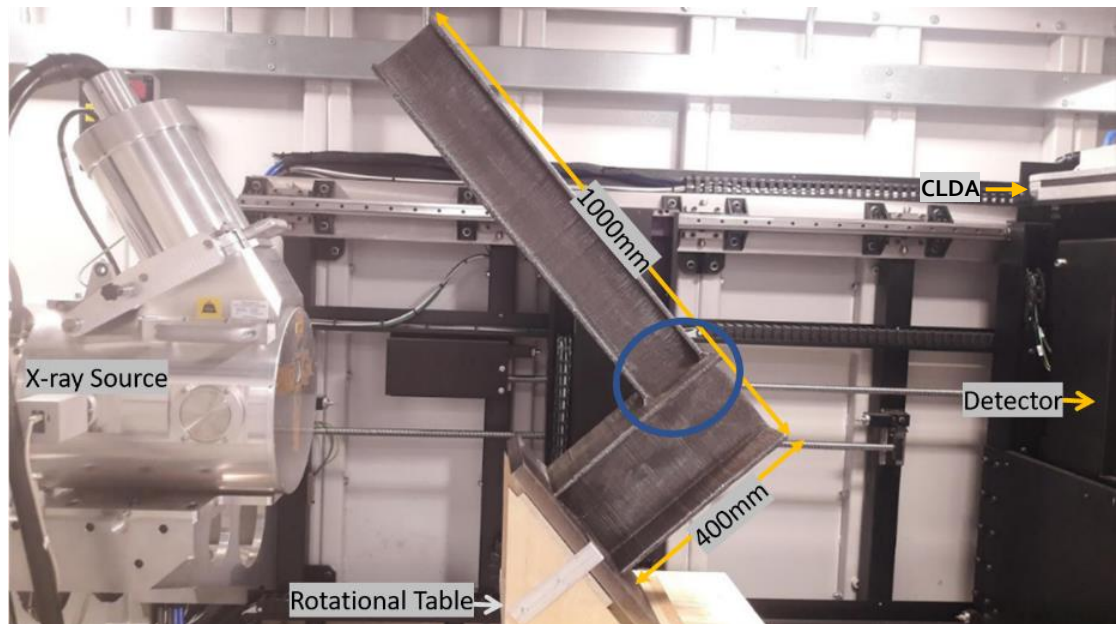
Figure 4-43. Nikon X-TEK XTH 450 system with an X-ray source, CLDA and a detector for the beam-to-column joint positions on its timber support platform on top of the scanning table

Figure 4-43 shows the joint with the regions of interest marked in blue, and it has average volume dimensions of 200 by 20 by 186 mm. The chosen parameters for the X-ray scanning of 2100 projections are: a voltage of 410kV; an amperage of 488µA; a Tin filter of 5mm; an exposure of 120ms. This produced a series of radiographs through a full rotation, which was reconstructed using the Filtered Back Projection (FBP) algorithm (Feldkamp et al., 1984). The scanning process took 76 hours and produced a final 3D model of the joint interface, with a voxel resolution of 217µm (or 0.22 mm). The voxel is the same as a pixel (2-D grid) but in three-dimensional space; it is a cubic that could have different dimensions in the X, Y and Z axes.

As for the dog-bone coupons and the straight-sided specimens introduced in Table 4-6, X-ray scanning employed a Nikon 225 LC (N-225) and a Tescan Uniform XL (TU-XL) system shown in Figure 4-44(a). The gauge length was the scanned region of interest as marked in black in Figure 4-44(b) and had an average dimension of 60x20x11mm for each sample. The process required about 50 minutes to penetrate the focused area.

Figure 4-44. (a) Dog-bone coupon; (b) volume of interest marked on surface with black pen marks

To provide a benchmark for the X-CT scanning quality and the chosen parameters in Table 4-7, Figure 4-45 presents an image of EN 8 steel; this benchmarking image can be used to establish a reliable contrast and to eliminate the uncertainty regarding the known X-CT limitations, such as signal noise.

Figure 4-45. X-CT image of an EN 8 steel specimen used as a benchmark.

Table 4-7 summarises the used parameters for the X-CT scanning for the dog bone coupons, which are listed in column 1 of table. The scanner used is stated in column 2, whilst the voxel resolution (in μm) and the thickness of the Tin filter are reported in columns 3 and 4. The chosen Voltage, Amperage and Exposure time are listed in columns 5 to 7, respectively. The voltage is defined as the maximum energy of emitted X-Ray radiation from the source to the detector. The amperage measures the strength of the current of the electron beam during X-ray generation, and the quantity of X-rays produced. The settings were varied across the

specimen types, the thickness of the part, its composition, and its shape to produce optimum grey value ranges for higher resolution images. The greyscale value is simply an arbitrary representation of the proportion of X-rays attenuated at a particular voxel point, where high values equate to no attenuation and small values equate to complete attenuation.

Table 4-7: Summary of X-CT system variable for scanning tensile coupons.

Coupon type	Machine	Voxel (μm)	Tin filter (mm)	Voltage (kV)	Amperage (μA)	Exposure (ms)
1	2	3	4	5	6	7
R_IA _S46 _I_T_2 R_IA _S46 _I_T_3	N-225	37	1.5	210	171	2000
R_IB _S46 _T_T_1 R_IB _S46 _T_T_3	N-225	33	1.5	215	153	2000
R _IB _S46 _L_T_2	TU-XL	35	4.0	180	308	1850
R _IB _S46 _L_T_3	TU-XL	35	4.0	180	228	2450
EN 8 steel	N-225	10	0.5	200	40	2829
A_Plate_S35_TT_T_1 (Straight sided)	N-225	30	1.5	200	75	4000
S_WALLB_S35_L_T_1 S_WALLB_S35_ L_T_2	N-225	145	1	200	75	2829
S_RHS_S35_ I_T_1 S_RHS_S35_ I_T_3	N-225	145	1	200	75	2829
S_WALL A_S35_L_T_1 S_WALL A_S35_L_T_2	N-225	145	1	200	75	2829
S_RHS_S35_L_T_1 After testing	N-225	11	1	210	50	4000
S_WALL A_S35_L_T_1 After testing	N-225	11	1	210	50	2829
S_WALLB_S35_L_T_1 After testing	N-225	11	1	210	50	4000

4.5.4. X-ray scanning analysis

The acquired radiographs generated through CT scanning are processed to create a voxelised 3D volume of the region of interest, a grid of grey values which represent the proportion of x-rays attenuated in that particular region. This process is known as reconstruction, most commonly using the FDK algorithm (Feldkamp et al., 1984). In effect, each of the radiographs has a known position when acquired during scanning. These radiographs are effectively 'blurred' across the circular volume, each radiograph averaging together across the 3D space to produce a 3D representation of the interior of the sample

This process is the fastest among reconstruction algorithms but is generally more susceptible to scanning issues based on shape and physical properties, which manifest themselves in the form of 'artefacts'. These are then typically exported as a set of .tif images, an image stack or volume, which can be imported into evaluation software for analysis.

The Avizo 2020 software (from Thermo Fisher Scientific) was used to analyse the volume and to calculate the volume fractions of features of interest in the beam-to-column joint and within the gauge length volume in the dog-bone specimens. Avizo 2020 was used to store, process and segment the raw image data. It uses mathematical functions in the Avizo library in order to carry out the volumetric analysis. For example, for the joint (see Figure 4-46), the raw data stored includes its lattice details (total number of slices), data info, memory size, physical size, and voxel size. The dimensions of each cubic voxel are 0.216623 by 0.216623 by 0.216624mm, i.e., the depth of each slice is roughly 216 microns in the x, y, z directions.

The overall number of slices in the lattice, Is 1043 x 1071 x 1265; refer to first entry in the screen shot shown on Figure 4-46. Multiplying the total number of slices having a thickness of 216 microns in each of the x, y, z directions gave the physical size of the imaged volume as 226 x 23 x 274mm, which corresponds to the fourth row in the screen shot in the figure.
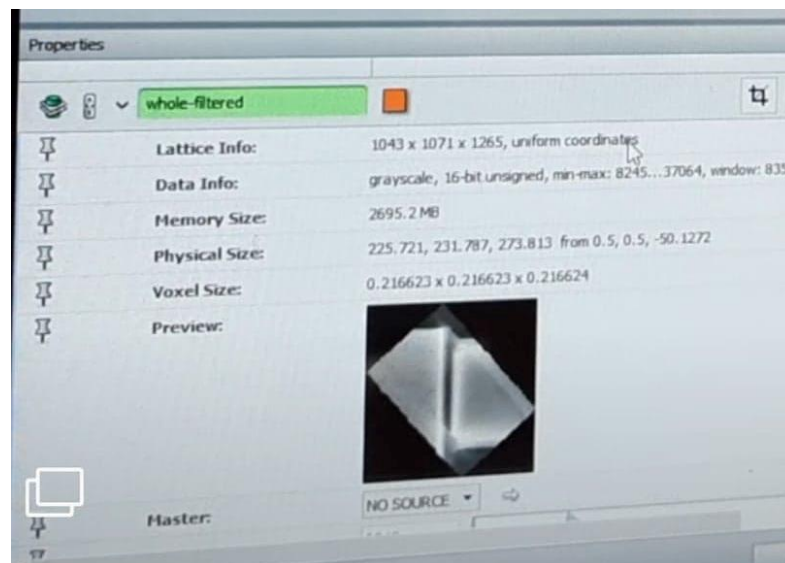
Figure 4-46. Properties for the captured raw data with the beam-to-column joint

Avizo 2020 was used to threshold out the presence of pores within the weld steel. However, owing to the differential grey scale values in the processed volume caused by the attenuation artefact in the centre of the studied region of the joint, pores could not be automatically extracted. Instead, manual segmentation was used, a process which involves manually marking pores on each slice in the volume. This process was necessary but time-consuming.

Before the pores could be segmented, the threshold, which is the range of values between two different selected grey values must be defined. This threshold needed to be regularly adjusted due to variations in the grey values of pores and metal throughout the volume. Figure 4-47 demonstrates this, where the grey images represent the grey-values and the blue the pores, currently selected within the threshold. A magic wand tool was used to select the isolated pores in 3D, the selected voxels being saved in various groups according to their location in the scanned component. Three groups were used: the beam, the column, and the transition zone.
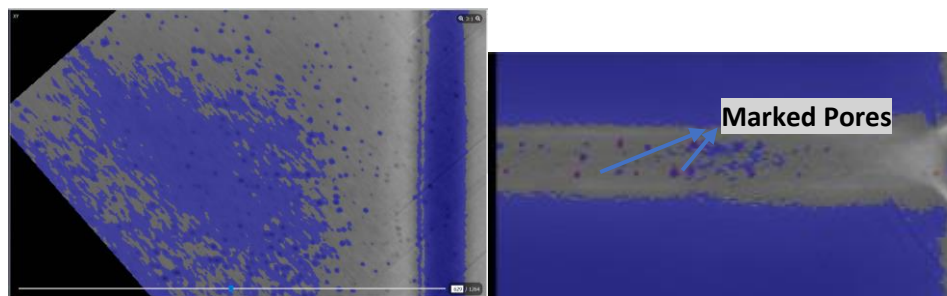
Figure 4-47. Image from one of the slices that has been adjusted in order to mark the pores

This process of pore extraction was repeated on all slices through the volume. Additionally, in places where contrast was insufficient, pores had to be individually selected on each slice using a paintbrush tool.

The manual work to capture all visible pores in three regions of interest for the connection zone of the beam-to-column joint took approximately 300 hours to complete. Due to the coarse resolution of the scan, any porosity features smaller than 500µm were unlikely to be visible within the scan data.

For the dog-bone samples, segmentation could be completed automatically due to considerably more uniform grey value distribution. Watershed segmentation was used in Avizo, where seeded grey values are selected and then automatically grown until they reach a defined boundary, at the interface between the 'air' in pores and the surrounding welded steel.

4.6. Summary

This chapter provides factual information on how the dog bone coupons were prepared from the WAMM-GMAW steel components. The process required designing the specimen sizes, planning their locations within the printed components, drawing them in CAD to prepare the CNC machine coding, preparing the surfaces to affix the strain gauges on the tensile specimens and the machining of the groove for the impact specimens. Both the design of the

geometry and the test methodologies followed (BS/EN-ISO6892-1:2019) for the tensile testing and (EN/ISO148-1:2016, 2016) for the impact testing.

In this chapter the author introduced the Instron universal testing machines for the series of tensile tests in Section 4.2. The loading machine was linked to a DAQ system to capture in real time the readings from external extensometers and strain gauges, in parallel with the tensile load. Details are given for the chosen loading rate and the lengths of the extensometers, and these test parameters are to be found in Table 4-4 and Table 4-5, respectively.

The impact test method is introduced in Section 4.3 for how the toughness of the welded steels was determined.

In Section 4.4 the method used to determine density of steel was introduced, it involved weighing of the specimen of known volume, in air and under water.

Sections 4.5 is for introducing and explaining the non-destructive test method of X-ray Computed Tomography (X-CT). Important information was presented on the preparation requirements (e.g., the tilt angle of the scanned object and defining the scanning parameters) and experimental set-up to run the X-CT scan. Moreover, using as an example the beam-to-column joint in sub-Section 4.5.4 introduced the implementation of the Aviso software (both by automatic and manual and methods) for data reduction to extract internal features (e.g., to establish the volume fraction of porosity) within a volume of the steel.

5. Chapter Five: Characterisation of 3D printed steel

In Chapter 4 the author presented the methodologies for X-ray Computed Tomography (X-CT) imaging, tensile and impact testing carried out, at room temperature, to characterise the WAAM-GMAW steels introduced in Chapter 3. The focus of this chapter is on the test results and their discussion to characterise the mechanical properties (including the yield strength, ultimate tensile strength, elongations, Poisson's ratio, and toughness) of the welded steels for structural engineering applications. These test results are enhanced with further characterization work for density and X-CT evaluation as Quality Control testing of 3D printed steel components and to permit an investigation on the effect of porosity on mechanical properties.

5.1. Introduction

Mechanical tensile testing was used to assess whether or not the tensile properties of the welded steels satisfied the material properties of structural grades of steel as defined in Section 3 of *Eurocode 3: Design of Steel Structures - Part 1-1: General rules and rules for buildings* (NA to, and BS EN 1993-1-1:2005), and hence can be classified as a structural steel according to this design code. Impact test results are used to establish whether or not the steels satisfy the minimum toughness requirement at room temperature.

The new test results have the objective to widen the use of printed steel in the construction industry. This will be achieved through building confidence by expanding the foundation of knowledge and understanding by knowing how the steels perform in terms of material properties against the requirements of the structural Eurocodes.

Test standards *Metallic materials - Tensile testing - Part 1: Method of test at a room temperature (BS/EN-ISO6892-1:2019)* and *Metallic materials- Charpy pendulum impact test. Test method* (BS EN ISO 148-1:2016) were used to determine the tensile properties and impact energies, respectively. The new test results will be compared against the tensile properties reported in Section 3 Materials in BS EN 1993-1-1:2005, and additional notes in Parts 1 and 12 of Section 3 *Additional rules or the extension of EN 1993 up to steel grades S700* (EN1993-1-12:2007). Similarly, for toughness, the test results will be compared against the required impact energies at room temperature (20°C) taken from Table 2.1 for steel grade S355 in BS EN 1993-1-10:2005 and from Table 8 in BS EN 10025-2:2009 for steel grade S235-S500.

5.2. X-ray Computed Tomography (X-CT)

X-ray Computed Tomography (X-CT) is described in Section 4.5 and was essential in providing valuable information on the internal structure of the printed components, which can be linked to measured material properties and the WAAM-GMAW printing described in Chapter 3.

Archimedes' Principle was used to determine the porosity by measuring the overall density of each specimen and comparing this value with the known density value of steel (EN 8-coupon), which is 7.70 g/cm^3 (the **upper** value of 7850 kN/m^{3}taken from Table A.4 Construction materials-metals in *Eurocode 1: Actions on structures — Part 1-1: General actions — Densities, self-weight, imposed loads for buildings* (BS/EN1991-1-1:2002). Density measurements help evaluate the quality of the X-CT readings because of discrepancies in X-CT readings can be justified by the low resolution in identifying the pores in the highly dense material.

Scanned were undertaken for three different steel wires printed by the three WAAM-GMAW processes with Autodesk, Steelo and RAMLAB; these are introduced in Sections 3.4. X-CT imagining provides the information needed to understand and comment on the outcomes of the different printing processes. Scanning tensile coupons before and after the testing had the objective to investigate the interfacial surfaces between weld beads and to determine the amount and distributions of pores. The percentages of porosity in these dog-bone and straight sided coupons, as summarised in Table 4-6 and Table 4-7, will be linked to the steel's material properties in Section 5.4.

5.2.1. X-CT results for the Horizontal Plate Component

X-CT imaging is uniquely able to segment the different internal regions in 3D printed steels according to the achieved attenuation of the X-rays and to providing a volumetric analysis, as explained in Section 4.5. Figure 5-1(a) shows the X-CT image of the WAAM-GMAW steel in the Autodesk horizontal plate described in Section 3.4.1, after the sheet had been ground (see Section 4.1.3.4) to provide a smooth and flat surface and to study the characterisation of the internal material without considering the impact of its roughness. In the figure we can see five weld layers of approximately 3.8mm thickness and four-layer interfaces. The variations in the grayscale (see Section 4.5.3) present regions in the steel with a higher density (because of higher atomic number) being bright grey and regions having a lower density being dark grey.

3.8mm

(a)   (b)
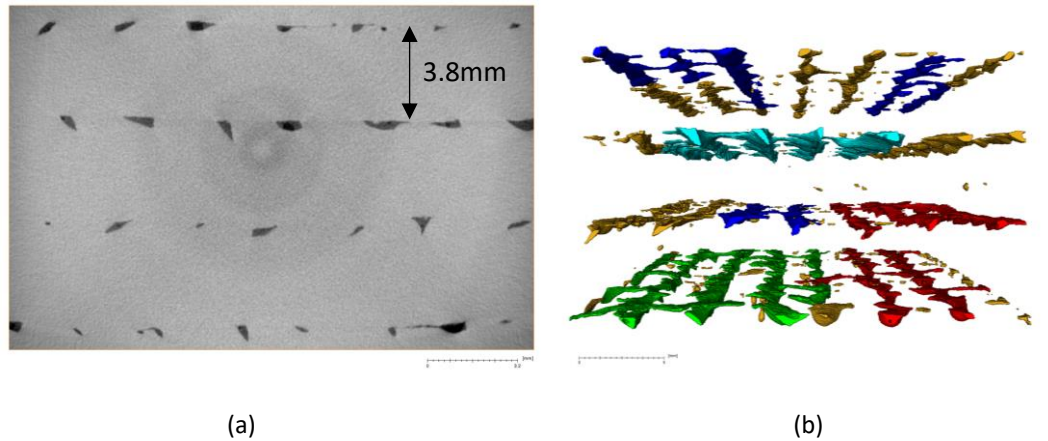
Figure 5-1. X-CT image before testing: (a) 2D view; (b) 3D view of the interfacial regions alone.

In Figure 5-1(a) the interfaces between five layers are clearly identified by the four rows of 'black dots. As the step-over distance (see Table 3-5) was not sufficient for the weld beads to fuse together, so the molten steel has not fully coalesced and thereby created the interfacial region between the printed layers seen in Figure 5-1(a) and Figure 5-1(b). As a result, the 'black dots' in Figure 5-1(a) are identified as internal voids. As can be observed the grey image in Figure 5-1(a) is affected by common ring artefacts (see section 4.5.2) that do not limit the segmentation of the different regions. In Figure 5-1(b) there is a 3D view from a X-CT scan that shows the amount and distribution of porosity at the layer interfaces in the Autodesk steel printing. The five different colours in part (b) have no technical meaning and are introduced to improve the clarify of the information presented.

Three types of samples were involved in the non-destructive evaluation, namely the dog-bone coupon A_Plate_S35 _L_T_3 before and after tensile testing, and after testing the through-thickness coupons A_Plate_S35_ TT_T_1 & 2. The level of importance of the X-CT results is discussed after the tensile coupon test results are reported and discussed in Section 5.5.

From the X-CT scan displayed in Figure 5-2 it is seen that the layered structure comprises three constituents having different volume fractions. The grey coloured region is for the bulk of the volume and is the homogeneous Union-40K steel constituent, after WAAM-GMAW processing. The brown, green, greenish blue and blue coloured volumes in the figure are for interfacial regions between the five layers, where there is a change in steel density. The final constituent, displayed with blue regions, is for the low volume faction of porosity that lies within the interfacial layers.

99
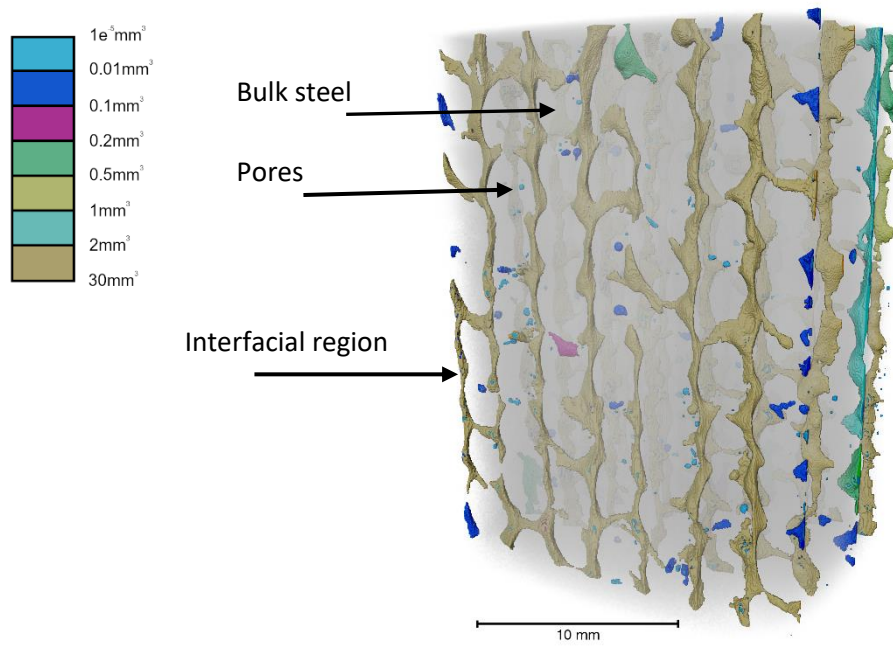
Figure 5-2. 3D X-CT scan showing the internal composition of steel taken from the A_ Plate_S35 _L_T_3 dog bone from the horizontal plate.

The seven different colours in the Figure 5-2 legend represent the volume range of the identified pores and interfacial regions. Light blue is the colour chosen for individual voids of volumes up to 0.01 mm^3; blue for range 0.01 to 0.01 mm^3; purple for volumes range 0.1 to 0.2 mm^3; green for range 0.2 to 0.5 mm^3; brownish yellow for range 0.5 to 1 mm^3; greenish blue (turquoise) for range 1 to 2 mm^3. And to complete the seven-volume ranges, interfacial having a volume from 2 to 30 mm^3 are coloured brown. These colour ranges have been unified in all the X-CT images for section 5.2.

Figure 5-3 shows the internal structure before tensile testing, and from these results the volume fraction of porosity can be calculated. From the extent of the different interfacial steel seen in Figure 5-3 the author finds that the printing parameters used by Autodesk (refer to Section 3.4.1) did not allow the molten steel to fully coalesce, and this printing deficiency could be due to both the wire tip-to-work distance and the step-over distance (see Figure 3-7 and Figure 3-10) being larger than their 'optimised' values, which were not known *a priori*. These X-CT results highlight that if processing is not optimised the steel in the interfacial regions can have a slightly lower density than that of the bulk. Figure 5-4 further shows that there are, at the layer interfaces, pockets of porosity, which clearly for steel performance in structural engineering applications needs to be minimised, if not eliminated.
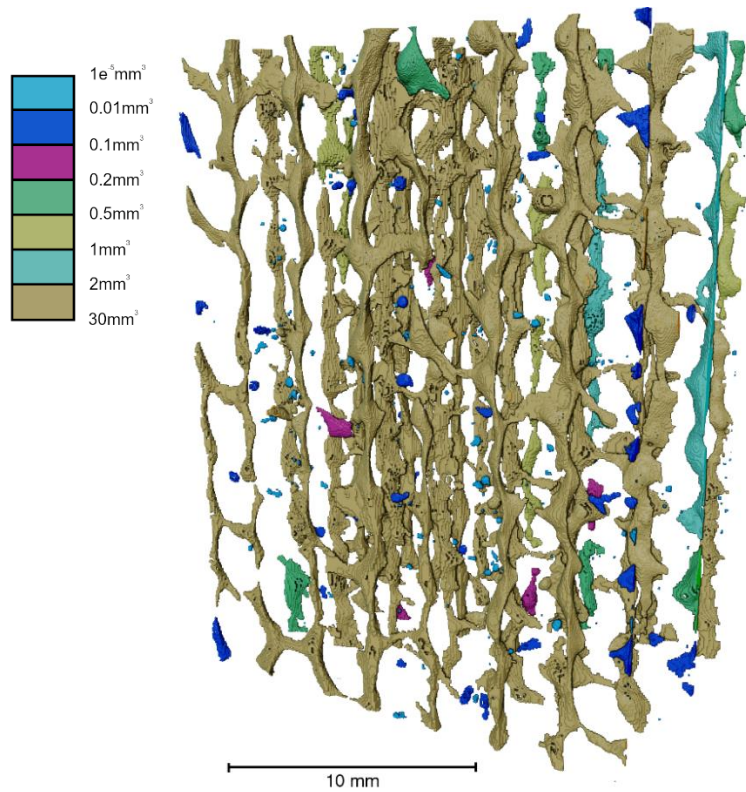
Figure 5-3. 3D structure of the interfacial regions, which have a lower steel density than the bulk of the component; the different colours show the range of volume sizes.
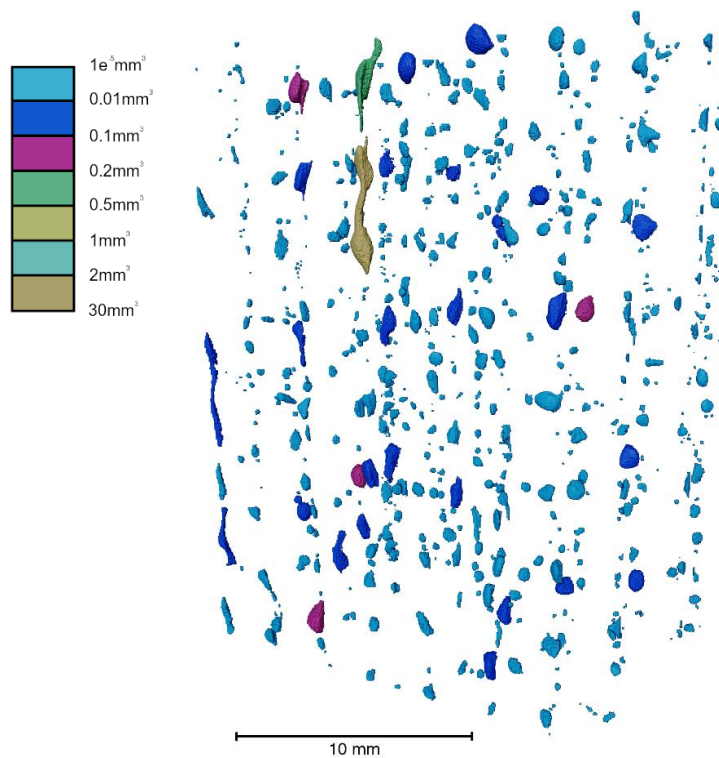
Figure 5-4. Distribution of pores where the different colours show the range of pore volume sizes.

A volumetric analysis of steel before tensile testing finds that the mean volume fraction of porosity is 0.1% (see Figure 5-4), while the volume fraction of the regions of steel having the

lower density is 1.68% (see Figure 5-3). The calculated average density for the A_ Plate_S35 _L_T_1 to 3 specimens extracted from the horizontal plate (Autodesk) is 7.77 g/cm^3. with a 0.9% difference from the recognised density of EN 8 used as the benchmark grade of structural steel (See Section 4.4).

5.2.2. X-CT Results for the RHS and the Vertical Walls

From the Rectangular Hollow Section (RHS) and the wall components printed by Steelo (see Section 3.4.2 and 3.4.2.1) six tensile specimens were involved in the non-destructive evaluation, namely S_WALL A_S35_L_T_1 & 2, S_ WALL B_S35_ L_T_1 & 2, and S_RHS_S35_ I_T_1 & 3. Their X-CT images are illustrated in Figure 5-5(a) to Figure 5-5(f). The six parts in the figure present representations of the internal structure, which comprise two constituents, with the grey coloured regions for the weld steel of a single homogeneous phase (see Table 3-1), and the purple, blue and green regions for the pores, where the different colours show the range of pore sizes as described earlier in Figure 5-2's legend.
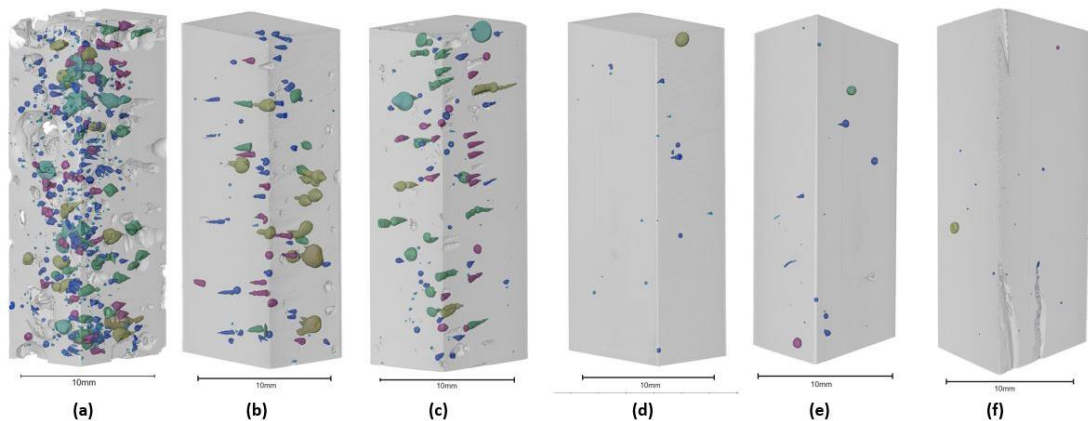
Figure 5-5. Internal pore sizes and distribution for Steelo printed steel, specimen: (a) WALL A_L_2; (b) WALL B_L_2; (c) WALL A_L_1; (d) WALL B_L_1; I RHS_I_1; (f) RHS_I_3.

In Figure 5-6 there are two images for S_WALL A_S35_L_T_2, showing in part (a) the external surfaces and in part (b) the internal pore sizes and distribution. Figure 5-5 and Figure 5-6 are for scan images for volumes of steel before tensile testing, which provided X-CT results to calculate the volume fraction of porosity. The six specimens in Figure 5-5 (a) to Figure 5-5 (f) are ordered in descending percentage of porosity, from 4.4% (S_WALL A_S35_L_T_1) to 0.91% (S_RHS_S35_ I_T_3), as recorded in Table 5-1. Table 5-1 tabulates the main X-CT test values and the calculation of the steel's density. Column 1 defines the specimens (corresponding to the naming system in Table 4-1), while columns 2 to 6 list the results per specimen from the X-CT analysis: label volume (which is the total volume of the scanned

element) , total volume of pores ($\sum V$), number of individual pores counted, percentage of porosity, and maximum volume of a pore. The percentage of porosity (column 4) is equal to the total volume of pores (column 3) divided by the label volume (column 2).

WALL A and WALL B specimens seen in Figure 5-5 (a) to (d) and Figure 5-6 have a relatively high porosity level, and as discussed in Section 5.4.2 this has a detrimental impact on limiting the elongation at failure, ε_f, in addition to reducing the yield strength and the tensile strength values. Figure 5-6 shows a high porosity level in S_35_WALL A_L_T_2, associated with the chosen printing parameters that meant the stopping time before depositing the next weld bead (as presented in Section 3.4.2) was insufficient to maintain the inter-pass temperature at 150°C. This deficiency in printing at Steelo would have been limited by increasing the cooling time.

(a)   (b)
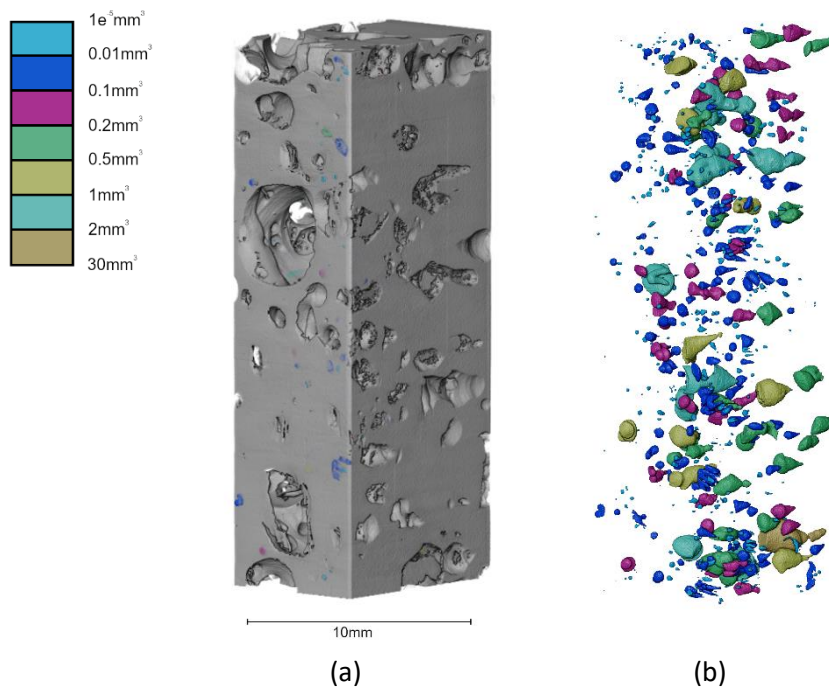
Figure 5-6. X-CT results for S_WALL A_S35_L_T_2 showing the: (a) external surfaces; (b) internal pore sizes and distribution, where the different colours show the range of pore size.

These X-CT images highlight the homogeneity of the Steelo printed steel as the interfacial regions found with the Autodesk-printed steel do not exist; this is because the chosen step-over distance was optimised. Also, S_RHS_S35_ I_T_1 & 3 in Figure 5-5(e) Figure 5-5 (f) show the improvement in minimising pore creation when maintaining the interpass temperature at 150°C during printing of the RHS. As can be seen the amount of porosity is now relatively very low.

The calculated density of the specimens (the test method is summarised in Section 4.4) is recorded in column 10, while columns 7 to 9 record the interim readings: the weight of the specimen in air (W), the changes in weight after immersing the specimen in water ($W - W_a$) and the temperature of the water (T_w), respectively. The recorded change in weight ($W - W_a$) gives the volume of the specimen (V) as stated in Archimedes' principle, which is then used to determine the relative steel density. The formula to calculate the density, ρ, is

$$\rho = \frac{W}{W - W_a}\, \rho_w, \qquad\qquad 5\text{-}1$$

where ρ_w is the density of water, equal to 1 g/cm^3 at 4°C. To adjust ρ_w for the recorded temperature (T_w) in column 9, Appendix 5.1 was used to adjust the changes of temperature (Weast, 1972).

Using Equation 5-1, most of densities for RHS components in Table 5-1 are in the range 7.6 to 7.7 g/cm^3, which seems appropriate. The average calculated density for the longitudinal specimen's cut-out is 7.65 g/cm^3, whilst it is 7.68 g/cm^3 when determined using the inclined specimens. All in all, the average density for the steel in the RHS component is 7.66 g/cm^3 and it has an average porosity of 0.085 %.

The two parallel wall components (WALL A and WALL B) have a large deviation in the percentage of porosity, with one sample taken from WALL A having 4% and another from Wall B 0.78%. As a result, the density is lower. The average density of WALL A is 6.72 g/cm^3, which is a 12.7% difference from EN 8 steel, and WALL B has an average density of 7.5 g/cm^3, which is a 2.2% difference from the benchmark specimen. If non-porous steel has a density of 7.7 g/cm^3, then 4% is for corresponds to a density of 7.39 g/cm^3 and 1% to 7.6 g/cm^3. Specimens S_WALL A_S35_L_T_2, S_WALL A_S35_L_T_1 and S_ WALL B_S35_ L_T_2 is giving a density that is not matching porosity volume fraction. This is because the porosity level is higher at the end of the coupons, outside the studied X-CT scope, as highlighted earlier in Figure 4-44 (see the black box). Also, this can be seen visually in the figures below in column 1 in Table 5-1.

Table 5-1. X-CT and density test results for the specimens extracted from the RHS, Wall A and Wall B images shown in the first row and column)

Name of the specimens	X-CT results					Density calculation			
	Label volume [mm³]	$\sum V$ of pores [mm³]	Number of pores	% of porosity	Max V of pore [mm³]	W [g]	$W - W_a$ [g]	T_w [°C]	ρ [g/cm³]
1	2	3	4	5	6	7	8	9	10
S_WALL A_S35_L_T_2	1426	62.8	787	4.4	13	86.51	12.86	16.1	6.72
S_WALL A_S35_L_T_1	1783	14.0	330	0.78	1.6	97.77	13.3	15.9	7.35
S_ WALL B_S35_ L_T_1	1796	0.85	22	0.048	0.64	104.2	13.61	16.3	7.64
S_ WALL B_S35_ L_T_2	1783	16.3	109	0.91	2.33	99.71	13.50	16.3	7.37
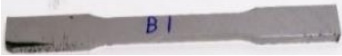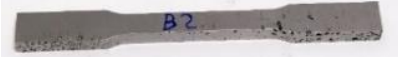
S_RHS_S35_ I_T_1	1788	0.75	27	0.042	0.21	101.76	13.22	18.5	7.69
S_RHS_S35_ I_T_3	1784	0.62	28	0.035	0.19	103.69	13.48	18.5	7.65
S_RHS_S35_ I_T_2	No X-CT scan	-	-	-	-	102.17	13.25	18.5	7.70
S_RHS_S35_ L_T_1	No X-CT scan	-	-	-	-	103.26	13.50	18.4	7.63
S_RHS_S35_ L_T_2	No X-CT scan	-	-	-	-	104.74	13.67	18.4	7.65
S_RHS_S35_ L_T_3	No X-CT scan	-	-	-	-	104.35	13.60	18.4	7.66

5.2.3. X-CT results for Stud Column steel

Eight tensile coupons, extracted from one of the two stub columns printed by RAMLAB (refer to Section 3.4.4), were X-ray scanned before tensile testing was carried out. Figure 5-7(a) to Figure 5-7(h) show 2D or 3D images for the eight specimens of R-IA-S46_I_T_2 and 3, R-IB-S46_T_T_1 and 3, R-IB-S46_L_T_2 and 3, R-IC-S46_T_T_1 and 3. Note that when the image is 2D the porosity distributed throughout the volume appear on one surface (see Figure 5-7(c) to Figure 5-7(h), which, of course, is not the physical reality. For the four coupons seen in Figure 5-7(e) to Figure 5-7(h) there is material for the web-flange junction. This steel was removed from the coupon to have it ready for the tensile testing.
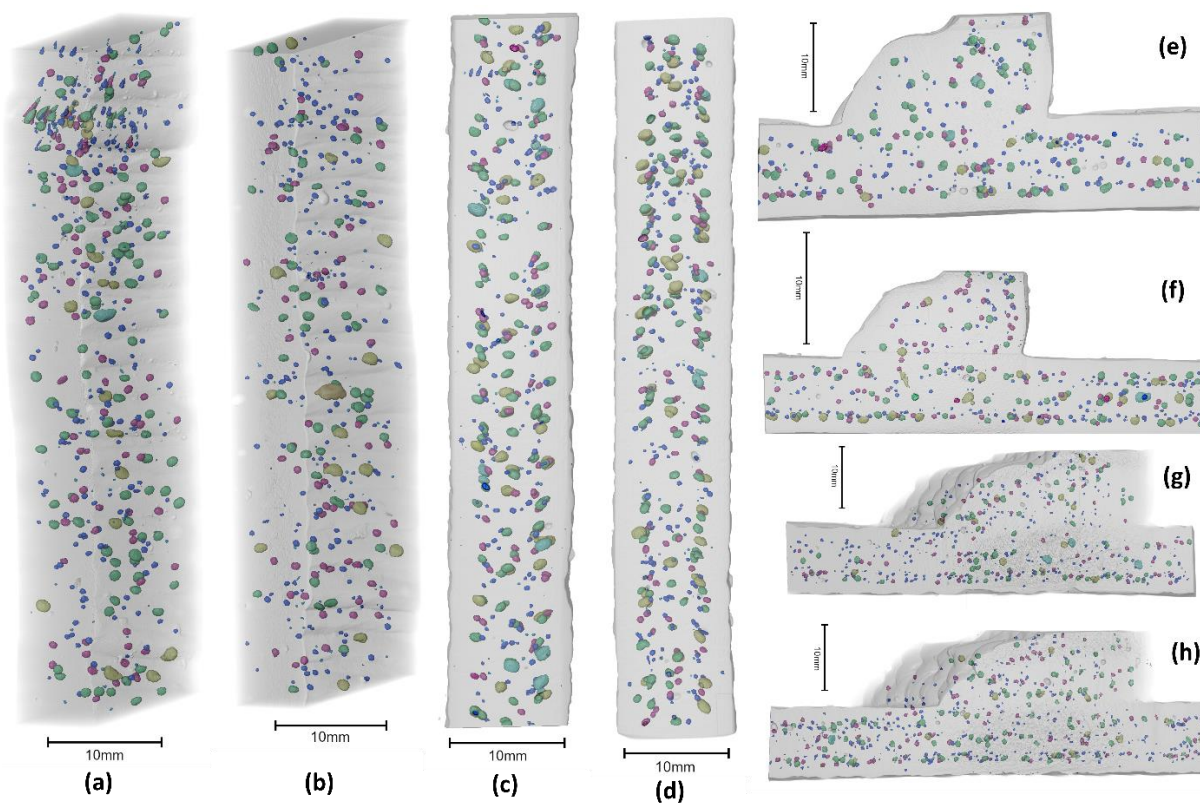
Figure 5-7. Pore sizes and distribution of RAMLAB printed steel, where the specimen naming system has been shortened e.g., R-I**A**-S46_**I**_T_**3** is A_I_3: (a) B_V_3; (b) B_V_1; (c) C_V_1; (d) C_V_3; (e) B_L_2; (f) B_L_3; (g) A_I_2; (h) A_I_3, where the different colours show the range of pore size.

Table 5-2 follows the same presentation as in Table 5-1 that is introduced in sub-section 5.2.2. Of the eight specimens, the two labelled C_V_1 and C_V_3 were extracted from the web and the remaining six were cut-out, in three directions of diagonal (inclined at 45°), longitudinal and transverse, from flange material. The percentage range of porosity was found to be from 0.45 to 1.05%, as reported in column 5 in Table 5-2. The volume of the steel in the coupons reported in column 2 of Table 5-2 is used to calculate the percentage of porosity; refer to data and results in columns 7 to 10.

As seen in Figure 5-7 there is a reasonable scatter in the distribution of pores, with no observable localisations. This means that the presence of pores is not a systematic error, as they are not associated with the deposition process (i.e., the printing path, the printing process, and the printing strategy). The technical reason for the presence of pores can be explained using the information presented in Figure 5-8, which was the root cause for the splattering and vapour condensation observed during the WAAM-GMAW printing.

| (a) | (b) | (c) |
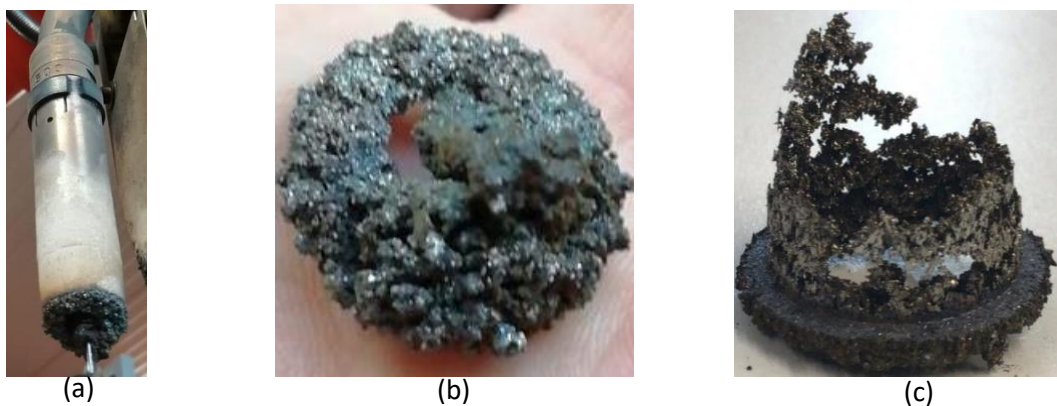
Figure 5-8. Typical splatter and vapour condensation: (a) on the shielding gas cap; (b)&(c) solidified splatter of steel after being removed from the gas cap.

During the printing of a stub-column section, a GMAW processing problem was identified, which affected the shielding gas flow and resulted in pores. Its manifestation is shown in Figure 5-8(a) to Figure 5-8 (c). Figure 5-8 (a) shows the spattering of metal at the end of the weld torch, and the vapour condensation of weld steel on the shielding gas cap. Particles of the splatter (a form of metallic oxide) was dropping into the weld melt pool during the melting. This led to a turbulent flow for the weld gas which resulted in the pores and impurities in the printed component. Figure 5-8 (b) and Figure 5-8 (c) show a conglomerate of oxidised steel removed from the torch. This GMAW processing problem was resolved by the addition of inter-layer cleaning protocols when the beam-to-column joint was printed (will be explain later in Section 6.2).

Extracted from the density results listed in column 10, the average density for the:

- web material is 7.71 g/cm^3.
- flange material is also 7.71 g/cm^3 (inclined and transverse coupons)
- flange material is 7.73 g/cm^3 (longitudinal coupons).

It is noteworthy that the volume fraction of porosity is always < 1%. The average density of the welded steel in the stud column is 7.72 g/cm^3 with a 0.25% difference when compared to the reported density of EN 8 structural steel.

X-CT analysis from the eight scans finds that the percentages of porosity in the 45° inclined, transverse (both extracted from the web) and longitudinal coupons (extracted from the flange) are 0.82%, 0.85% and 0.49%, respectively. The variation can be justified by the known printing problem as bead runs are deposited, as shown in Figure 5-8. A reason for the transverse and inclined coupons having the higher percentages of porosity is because their material composes of X-printed layers (See Figure 3-22 where the printing direction are defined), whereas the longitudinal material with lower volume fraction of porosity consists of only Y-printed layers. The average percentage of porosity within the stud column from the material samples scanned is 0.79%, and the volume fraction of porosity being less than < 1% with regard the quality of the printing.

Table 5-2. X-CT and density test results for the dog-bone coupons extracted from a RAMLAB stub column (image shown in the first row).

Name of the specimens	Label volume [mm³]	$\sum V$ [mm³]	Number of Pores	% of porosity	Max V of pore [mm³]	W [g]	$(W - W_a)$ [g]	T_w [°C]	P [g/cm³]
			X-CT results				Density calculation		
1	2	3	4	5	6	7	8	9	10
R_IA_S46_I_T_1	-	-	-	-	-	299.8	38.92	21.6	7.69
R_IA_S46_I_T_2	12959	100.95	711	0.78	1.5	303.64	39.28	22.1	7.72
R_IA_S46_I_3	12360	105.22	783	0.85	1.9	296.9	38.37	22.2	7.73
R_IA_S46_I_T_4	-	-	-	-	-	298.35	38.65	22.2	7.71
R_IB_S46_L_T_1	-	-	-	-	-	292.3	37.87	21.6	7.71
R_IB_S46_L_T_2	9373	41.93	353	0.45	1.2	293.5	37.86	22.3	7.74
R_IB_S46_L_T_3	10151	53.76	431	0.53	1.3	284.5	37.87	22.3	7.74
R_IB_S46_T_T_1	8149	63.83	525	0.78	3.1	292.3	35.02	22.1	7.71

R_IB _S46 _T_T_2	-	-	-	-	-	270.9	35.02	22.1	7.72
R_IB _S46 _T_T_3	7923	73.32	653	0.93	1.6	272.6	35.30	22.1	7.71
R_IB _S46 _T_T_4	-	-	-	-	-	270.54	35.04	19.4	7.71
R_IB _S46 _T_T_5	-	-	-	-	-	269.91	34.89	19.3	7.72
R_IC _S46 _T_T_1	7734	81.34	490	1.05	1.5	227.31	197.88	22.5	7.71
R_IC _S46 _T_T_3	8194	77.94	469	0.95	1.4	229.04	199.42	22.5	7.72
R_IC _S46 _T_T_4	-	-	-	-	-	267.25	232.6	19.2	7.70
R_IC _S46 _T_T_5	-	-	-	-	-	268.2	233.45	19.1	7.70
R_IC _S46 _L_T_1	-	-	-	-	-	136.21	118.5	22.4	7.69
R_IC _S46 _L_T_2	-	-	-	-	-	143.12	124.66	22.5	7.74
R_IC _S46 _L_T_3	-	-	-	-	-	128.7	112	22.5	7.70
EN 8					-	488.28	62.28	19.9	7.83

5.3. Analysis of Impact Test Results

Toughness is defined as the ability of materials to deform plastically and to absorb energy under the action of loading before fractures (IOWA_S_U). Measurement of toughness can be used in "quality control" through comparison of impact energies between different engineering materials.

The following points were considered for the impact testing (refer to Section 4.1 and 4.3) of the printed steels:

- The impact testing is to be carried out in accordance with test standard (EN/ISO148-1:2016, 2016).
- According to 9.2.3.3 in EN 10025 part 2 and 6, for nominal thicknesses ≤ 12 mm, test pieces with reduced widths can be used, and the largest width practical is to be chosen. As explained in Sub-Section 4.1.1.2) impact specimens with reduced width had to be used and always the largest possible width was taken. (EN10025-1, 2004)
- According to 10.2.2 in EN 10025 part 2 and 6, each specimen impact energy from the V-notch Charpy test cannot be lower than 70% of the average value from the batch of results after testing nominally three identical V-notch Charpy specimens.
- According to 1.3.4 in EN 1993-1-10:2005 for the use of various grade of structural steel in the design of steel structures, the impact energy will not be less than 27 J (at a specified test temperature) in the V-notch Charpy test.

The test procedure for impact testing (Section 4.3), was carried out at room temperature of 22°C. As a result of having printed steel with a nominal thickness ≤ 12 mm, the V-notch impact specimens varied in thickness with overall dimensions of either 55 x 10 x 7.5 mm or 55 x 10 x 5 mm, and also varied in terms of their cut-out directions relative to the direction of WAAM-GMAW printing.

Table 5-3 records the absorbed energies for the V-notch (55 x 10 x 5 mm) specimens of steel printed by Steelo (see Sections 3.4.2 and 3.4.4 3), which were extracted in the longitudinal and 45° inclined directions to the direction of printing (see Figure 4-6- c/d and Figure 4-10). In the table there are the labels for the coupons from which the impact specimens were machined as per standard (EN/ISO148-1:2016, 2016). Five was the maximum number of specimens in a batch. The symbol – is entered in a cell when there is no specimen tested. Impact energy in Joules for the specimens and their batch average is given to three significant figures.

Table 5-4 to Table 5-6 have the same presentation as Table 5-3 to record the absorbed energies for the V-notch specimens extracted from RAMLAB printed steel stud column - see Figure 4-11 and Section 4.1.4.2. The average dimensions of the nominally identical specimens of 55 x 10 x 7.5 mm, were extracted from three different directions-longitudinal, transverse and 45° inclined to the direction of printing.

Table 5-3. V-notch Charpy impact test results using specimens of Steelo steel.

Coupon source of steel and impact specimen number	1	2	3	4	5	Average (J)
S_WALL A_S35_L_I_1 to3 S_ WALL B_S35_ L_I_1 to 2	85.5	75.4	78.7	78.2	80.2	79.6
S_RHS_S35_ I_I_1 to 3	76.8	88.3	77.7	-	-	80.9

Table 5-4. V-notch Charpy impact test results for the transverse specimens' cut-out from the web and the flanges of the RAMLAB stud column.

Coupon source of steel and impact specimen number	1	2	3	4	5	Average (J)
R_IA _S46 _T_I_1 to 5	117	138	107	104	120	117
R_IB _S46 _T_I_1 to 4	119	97	123	127	-	116
R_IC _S46 _T_I_1 to 3	117	124	129	-	-	123

Table 5-5. V-notch Charpy impact test results for the longitudinal specimens' cut-out from the web and the flanges of the RAMLAB stud column.

Coupon source of steel and impact specimen number	1	2	3	4	5	Average (J)
R_IA _S46 _L_I_1 to 5	157	146	149	137	127	143
R _IB _S46 _L_I_1 to 3	124	93	107	-	-	108
R_IC _S46 _L_I_1 to 2	109	108	-	-	-	109

Table 5-6. V-notch Charpy impact test results for the inclined specimens extracted from the flanges of the RAMLAB stud column.

Coupon source of steel and impact specimen number	1	2	3	4	5	Average (J)
R_IA _S46 _I_I_1 to 5	115	134	135	140	-	131
R_IB_S46 _I_I_1 to 4	112	109	109	101	-	108

Table 5-3 shows that the Steelo printed steel (Copper-coated solid wire- EN ISO 14341-A **G** 46 4 M21 3Si1) has an average toughness of about 80 J, where the RAMLAB printed steel (SupraMig Ultra HD- Mild steel solid wire - EN ISO 14341-A **G** 46 3 C 4Si1) has an average impact energy more than 110 J, at 20°C. These Charpy V-notch toughness results show that the two WAAM-GMAW steels satisfy the EN 1993-1-10:2005 standards for the steel materials that can be used in the design of steel structures. The reported readings in Tables 5-3 to 5-6 are for three times higher than the minimum requirement of 27J. Moreover, it is found that the impact energies of both Steelo and RAMLAB materials vary by < 1% with the printing orientation, which the author concludes has a minimal effect on the steel's toughness.

5.4. Tensile Test Results

Understanding the material properties of the WAAM-GMAW steels is vital to ascertain the potential for 3D printed steel in structural engineering applications. Tensile testing leads to the determination of the key material properties in structural steel design, which will include: elastic stiffness or modulus of elasticity (E), ductility, Poisson's ratio (v), yield strength (f_y), and ultimate tensile or tensile strength (f_u). To provide a benchmark material, a single tensile dog-bone coupon, with the same dimensions, introduced in the proportional test approach of Sub-Section 4.1.1.1, was prepared using EN 8 (a medium carbon steel). The final row in Table 4-1 (refer to Section 4.1.1) states that cross-sectional dimensions of the EN 8 coupon are 10 x 20mm. The benchmark testing had the aim to validate the tensile test set-up and procedure before proceeding to characterise the material properties of the printed steels.

Testing was performed at room temperature of 20-25°C with humidity of 30-50%, and at a constant crosshead separation rate (reported in Table 4-5). The recommended strain rate of 0.00025 s^{-1} was followed to determine the upper yield strength (R_{eh}) and the proof strength (R_m). R_{eh} is the first peak for the force in the elastic zone before the decrease in the stress strain graph and R_m is the stress corresponding to the maximum force in the plot. With respect to the structural design standard (BSI, 2005), known as Eurocode 3, R_{eh} and R_m is equivalent to yield strength, f_y, and ultimate tensile strength, f_u, respectively.

Prior to presenting and discussing the test results, the material properties of structural steel for the design of steel structures will be presented next. The standard BS EN 10025 for hot-rolled products of structural steels lists the specific steel grades that has been satisfied (EN10025-1, 2004). The properties for hot-rolled steels with a thickness ≤ 40mm, have a

range of characteristic yield strengths (from 235 to 460 N/mm^2) and a range of characteristic ultimate tensile strengths (from 360 to 570 N/mm^2).

The tensile properties for the different grades of high yield strength, hot-rolled structural steels (with a thickness > 3mm and < 50mm) at room temperature have the following ranges, taken from Table 1 in EN 1993-1-12:2007: the characteristic f_y are from 500 to 690 N/mm^2 and the characteristic f_u are from 590 to 770 N/mm^2. It is noted that the higher the yield strength, the higher ultimate tensile strength.

Section 3.2.2(1) of (BSI, 2005) provides the ductility requirements, which are expressed as follows:

A minimum ductility of steel is required, and it should be expressed in terms of limits for:
  – the ratio f_u/f_y of the specified minimum ultimate tensile strength (f_u) to the specified minimum yield strength (f_y).
  – the elongation at failure for a gauge length of 5.65 S_o (where S_o is the original cross-sectional area highlighted in Figure 4-1).
  – the ultimate strain ε_u, where ε_u corresponds to the ultimate tensile strength (f_u).

Note that for the limiting values of the ratio f_u/f_y, elongation at failure, ε_f, and ε_u for buildings are defined in the British Standard (BS) Annex to EN 1993-1-1:2005, where the following is recommended:

  – Elastic global analysis: $f_u/f_y \geq 1.10$; Elongation at failure is not less than 15%; $\varepsilon_u \geq 15\varepsilon_y$.
  – Plastic global analysis: $f_u/f_y \geq 1.15$; Elongation at failure is not less than 15%; $\varepsilon_u \geq 20\varepsilon_y$.

Plastic global analysis cannot be used for bridges. For bridges, the limiting value for elastic global analysis is given as:

  – Elastic global analysis: $f_u/f_y \geq 1.20$;
  – Elongation at failure is not less than 15%;
  – $\varepsilon_u \geq 15\varepsilon_y$.

The limiting values for the ratio f_u / f_y, at ε_f and ε_u for steel grades greater than S460 and up to S700 are given next for bridges, buildings and other (highway) structures. The following values are taken from the additional rules to EN 1993-1-1 in Section 3.2.2 of the *Eurocode 3: Design of steel structures Part 1-12* (EN1993-1-12:2007) for the extension of EN 1993 up to steel grades S700:

- Elastic global analysis: $f_u/f_y \geq 1.05$;

- Elongation at failure is not less than 10%;

- $\varepsilon_u \geq 15f_y/E$.

For the purpose of carrying-out structural design calculations the steel's stiffness is taken as the (mean) modulus of elasticity at 210 kN/mm² and Poisson's ratio is 0.3; see paragraph 3.2.6 in BS EN 1993-1-1:2005.

When reporting stress values, they will be reported to the nearest N/mm², strains to the nearest 0.1% and modulus of elasticity to the nearest kN/mm² (which is also GPa).

5.4.1. Horizontal Plate Tensile Test Results

This sub-section reports the characterisation of the material properties of Autodesk printed steel, using coupons extracted from the horizontal plate component.
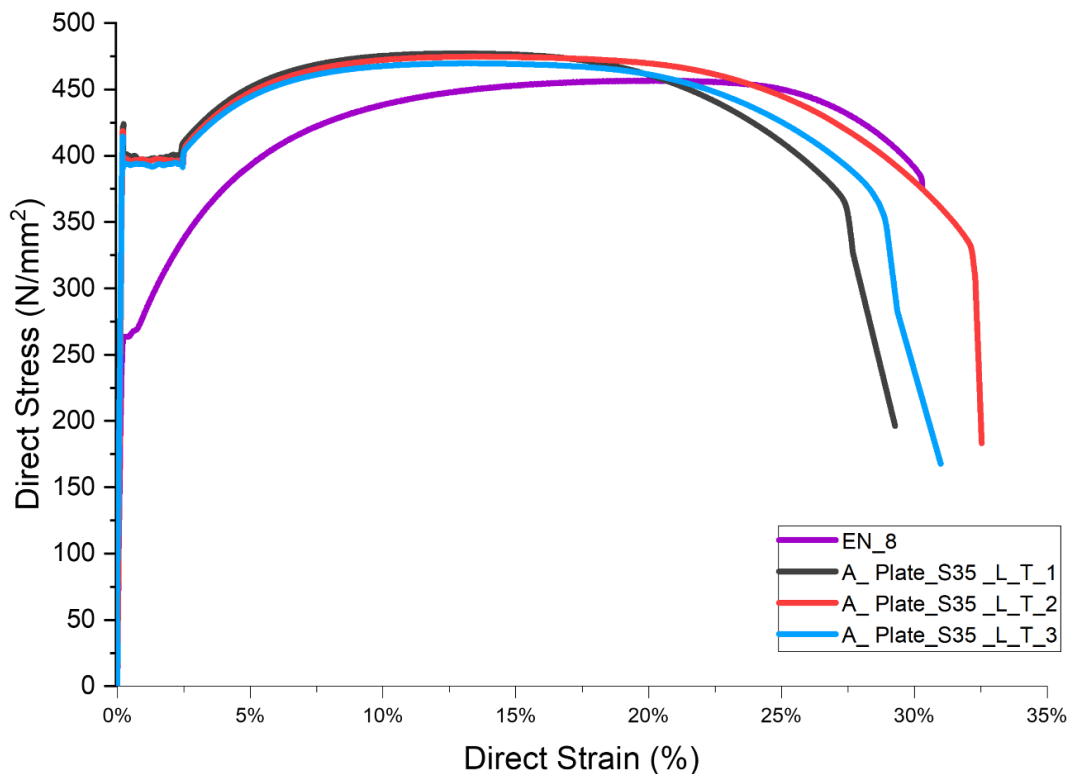
Figure 5-9. Plot showing the direct stress against direct strain for the dog-bone coupons A_Plate_S35 _L_T_1 to 3 and EN 8.

Figure 5-9 presents the direct stress-direct strain curves for the three coupons A_ Plate_S35 _L_T_1 to A_ Plate_S35 _L_T_3 (coloured blue, red and black) until ultimate failure has been reached. For comparison, the figure also plots a purple-coloured curve for the single coupon of EN 8 steel. Inspection of the plotted test results show that the three curves, for the A_

Plate_S35 _L_T_1 to 3 steel coupons, have similar, but not identical, ductile-steel characteristics to the benchmark EN 8 steel.

Table 5-7 reports the material property results from testing coupons A_ Plate_S35 _L_T_1 to 3. Column 1 in the table gives the coupon labels and statistical terminology. Column 2 gives *E*, which was calculated using the least squares fit method up to 65% of the linear (elastic) slope, in the direct stress-direct strain curves plotted in Figure 5-9. Column 3 tabulates the values of yield strength, f_y. Columns 4 and 5 list the ultimate strength, f_u, and its corresponding tensile strain, ε_u, respectively. And finally, column 6 is for the elongation at failure, ε_f.

Table 5-7. Material properties for Autodesk steel determined using coupons A_ Plate_S35 _L_T_1 to 3 and test method in BS EN 10002.

	Material property				
	E	f_y	f_u	ε_u	ε_f
	[kN/mm^2]	[N/mm^2]	[N/mm^2]	[%]	[%]
1	2	3	4	5	6
A_ Plate_S35 _L_T_1	219	424	477	13.0	27.5
A_ Plate_S35 _L_T_2	216	419	475	13.7	30.9
A_ Plate_S35 _L_T_3	189	415	470	13.5	28.7
Mean	208	419	474	13.4	29.0
Standard deviation		4.51	3.61	0.36	1.72
Coefficient of variation (%)		1.1	0.8	2.8	6.7
Characteristic value		411	467	12.7	25.8

The last four rows in Table 5-7 list the results of the statistical analysis on the coupons, which are: mean, standard deviation for a normal Gaussian distribution, Coefficient of Variation (CoV) and characteristic value. Note that the mean value of the modulus of elasticity is also its characteristic value. For strengths the coefficient of variations is close to 1% showing that for a coupon having cross-section size 20 x 17 mm there is low strength variation. For strength and strain properties, the characteristic values are obtained in accordance with paragraphs in Annex D of EN 1990:2002 by using a characteristic value equal to the mean minus *n* times SD, where SD is the standard deviation. For three coupons in the batch *n* is equal to 1.89 referring to Table D1 in EN 1990:2002. Because in practice it is preferable to use the coefficient of variation "V$_x$ known", in addition to the fact the coefficient of variation

was < 10% for properties reported in columns 3 to 6. Thus, there is justification to calculate the characteristic value with the assumption that the coefficient of variation is known *a priori*. If a coefficient of variation had been > 10% then *n* could be taken as 3.37 and the calculated of characteristic values will be lower.

From the tabulated statistical results, the mean f_y is 419 N/mm². Also, the mean ε_y is 0.21%, which has not been reported in Table 5-7 as it is a constant value. The mean f_u is 474 N/mm² at a mean ε_u of 13.4%, with the mean ε_f at 29%. The mean values for the f_y and ε_f in Table 5-7 are 14% higher than that reported by the supplier for the Union K 90 wire (see Table 3-1).

It is observed that the mean *E* is 208 kN/mm², which is 1.4% lower than the corresponding value in Eurocode 3. A reason for this is the relatively low *E* of 189 kN/mm² measured with coupon A_ Plate_S35 _L_T_3, whereas a mean *E* is 218 kN/mm² is acceptable (based on the linear elastic response of the two other coupons).

Poisson's ratio, *v*, was determined by combining the readings from the axial and transverse extensometers and the bi-axial strain rosettes. From the strains plotted in Figure 5-10, *v* is determined from the gradient of linear portion of the transverse-longitudinal strain curves.
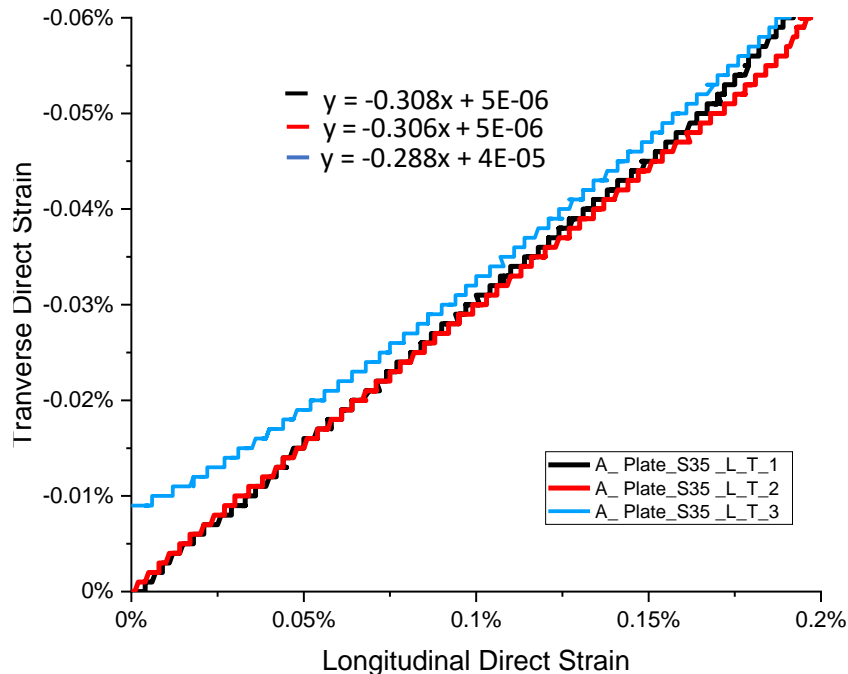
Figure 5-10. Plots of transverse against longitudinal direct strains for the determination of Poisson's ratio.

Coupons A_ Plate_S35 _L_T_1 to 3 gave vs of 0.308, 0.306 and 0.288 for a giving mean of 0.3, which matches the value specified in 3.2.6 of Eurocode 3 (BSI, 2005).

Four stress-strain curves for the tensile tests, on the non-standard straight-sided coupons A_Plate_S35_ TT_T_1 to 4, are plotted in Figure 5-11. Note that comparing to the A_ Plate_S35 _L_T_1 to the 3 dog-bone coupons of cross-section 17 x 20 mm (see Table 4-1), these four coupons had a smaller cross-section area of 3.8 x 17 mm. The four plotted curves coloured in yellow, green, blue, and mauve, are compared against the curve from the EN 8 coupon, which is coloured in purple. From the smaller four coupons, the mean f_y is 375 N/mm^2, at mean strain of 0.2%. The mean f_u is 454 N/mm^2 at a mean ε_u of 12.7%. Although the mean strain of these non-dog-bone shaped coupons at yield is the same, f_y is 44 N/mm^2 lower than determined from testing the three A_ Plate_S35 _L_T_1 to three dog-bone coupons. It is also seen that the mean f_u is 20 N/mm^2 lower. Because these coupons are straight-sided and non-standard their test results are not used to determine characteristic values for comparison with material properties in Eurocode 3.
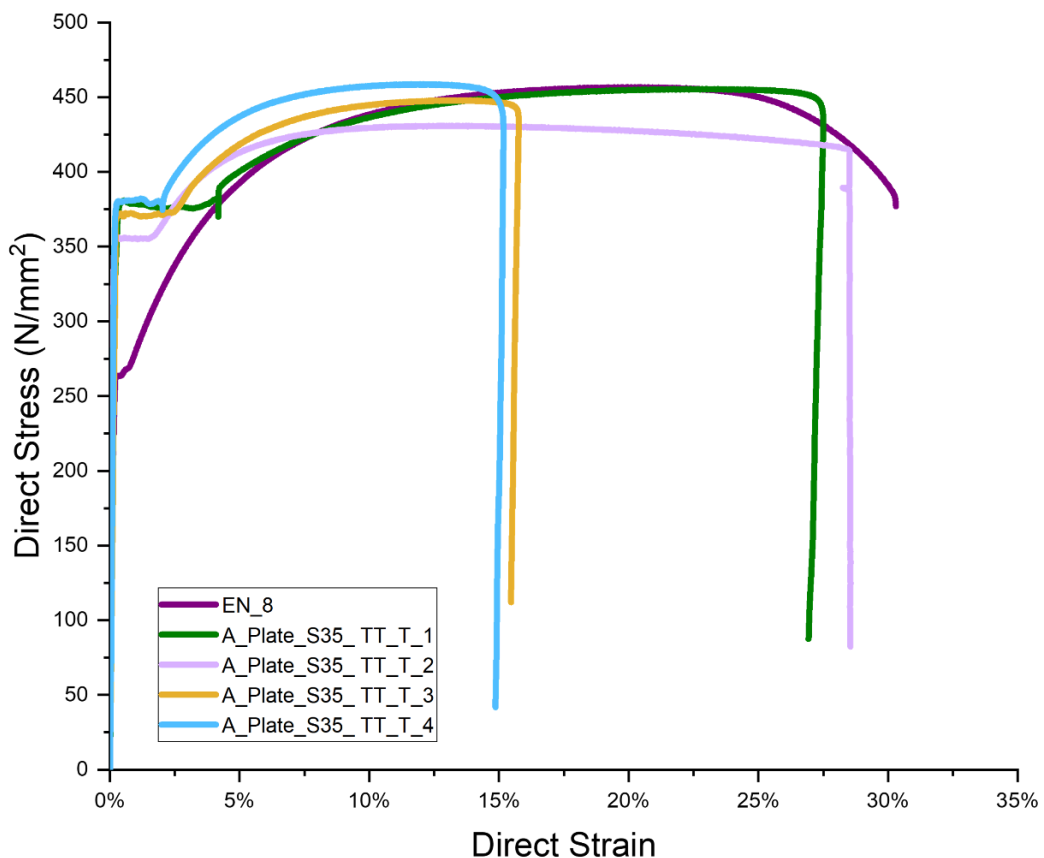
Figure 5-11. Plots of direct stress against direct strain for non-standard straight-sided coupons A_Plate_S35_ TT_T_1 to 4.

The plotting of test results in Figure 5-11 further show that the steel's response for coupons A_Plate_S35_ TT_T_1 to 4 is consistent to a tensile strain of about 14.6%. Though a drop off for WAAM_L_TT_3 and 4 is reported, the ε_f, measured after connecting together the two fractured parts were 18% and 21%, respectively. This indicates that the ε_f, matches the 25% of elongation reported in Table 3-1.

Figure 5-12 plots the test results for the seven coupons extracted from the Autodesk printed horizontal plate, to highlight the differences in ε_f, the elongation at failure. The fracture strains for coupons A_Plate_S35_TT_T_3 and 4 have not been included, which will be explained in section 5.5 and Figure 5-23. Stress-strain curves can be divided into the following three main stages: linear elastic, strain hardening and steel fracture. The stress-strain curves for coupons A_Plate_S35_L_1 to 3 (coloured in black, red and blue respectively) show similarities in the first two stages, while a divergence starts with the onset of the falling branch and recorded fracture strain, ε_f.
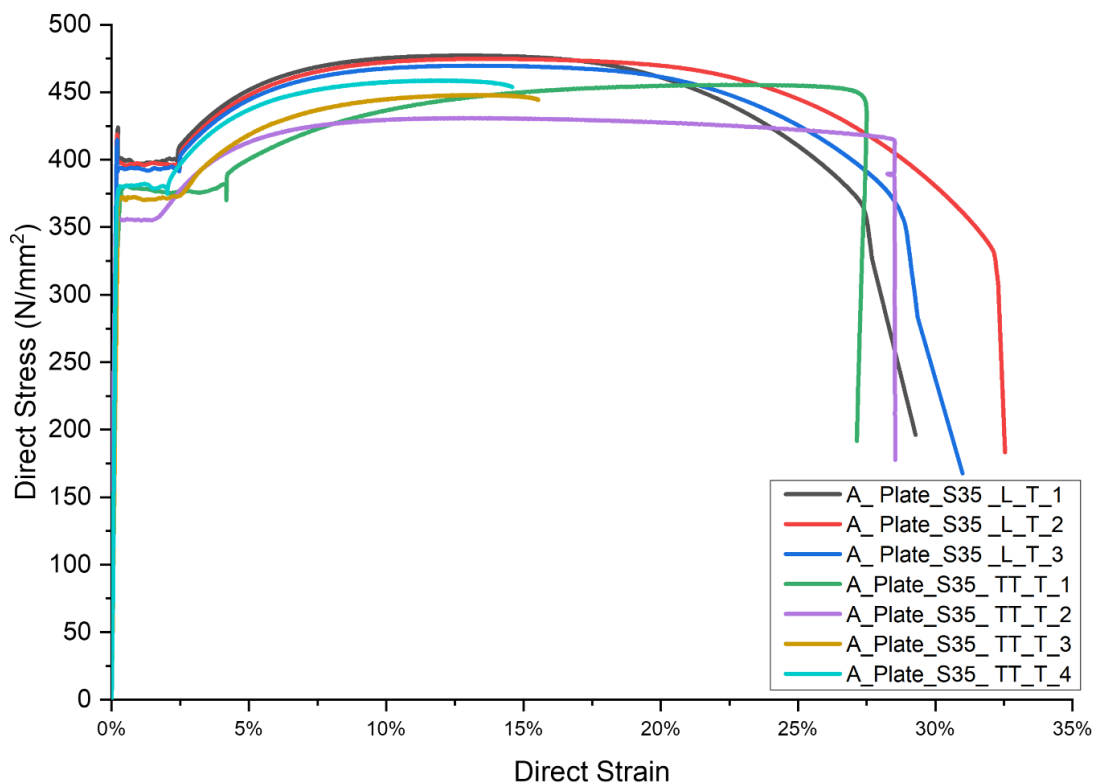
Figure 5-12. Stress-strain curves combining all the tensile test results from Figure 5-10 and Figure 5-11.

5.4.2. RHS and vertical wall (A and B) results

Figure 5-13 shows the plots of the direct tensile stress-direct strain curves until ultimate failure, coloured blue, red and black, from testing the Steelo printed coupons S_RHS _S35 _L_T_1 to S_RHS _S35 _L_T_3. Also plotted in the figure is a purple-coloured curve for the

benchmarking curve from testing the EN 8 steel (see Table 4-1). Testing of these RHS and Steelo printed vertical wall (A and B) coupons were performed at room temperature of 23.5°C and 34% humidity and at a constant stroke rate of 1 mm/min following the recommended $0.00025S^{-1}$ strain rate (see Table 4-5). A 2630-112-125140 axial extensometer with a 50 mm gauge length and a I3575-250M-ST-E97330 transverse extensometer with a 10 mm gauge was used to measure the elongations of the coupons, which was used to calculate the direct strain. A detailed summary for the extensometer and the strain gauges used is reported in Table 4-5.
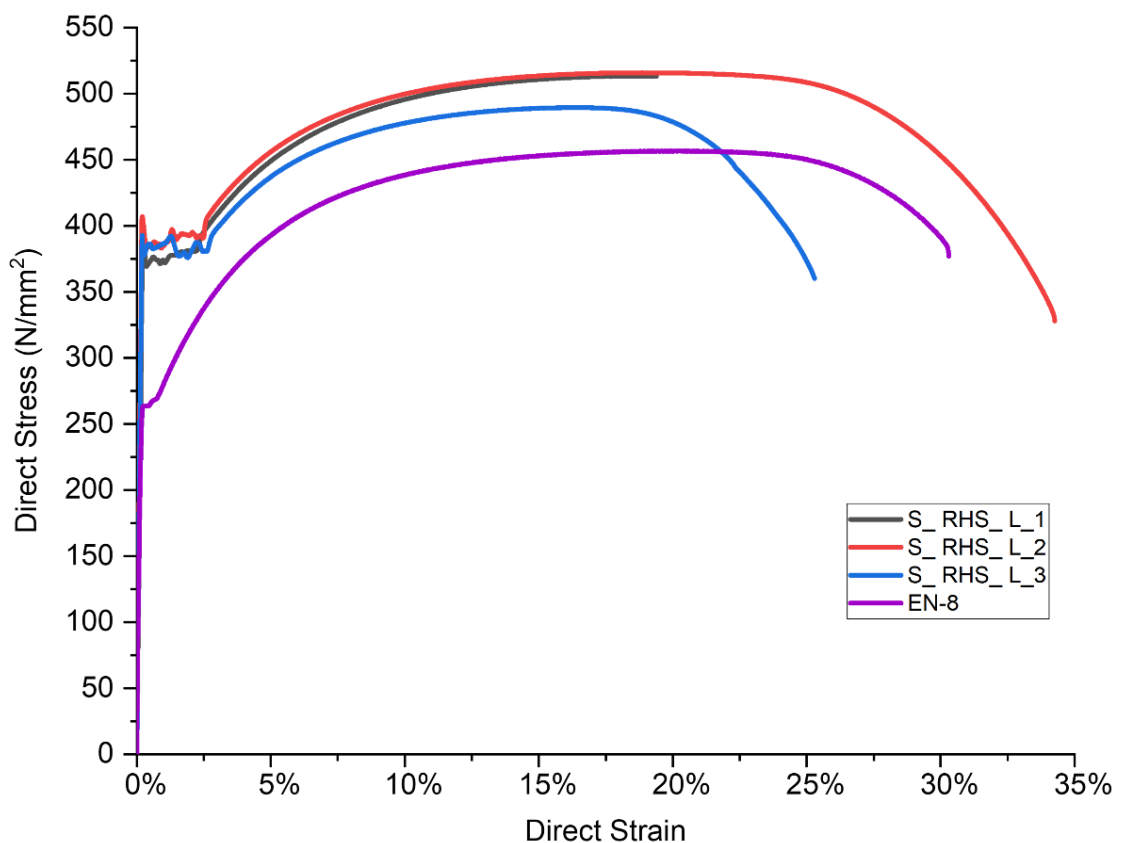
Figure 5-13. Tensile test results for the horizontal specimens extracted from the RHS component.

Table 5-8 reports the individual test results for the longitudinal coupons S_RHS_S35_ L_T_1 to 3. This table has the same format as Table 5-7. The mean f_y is 397 N/mm^2 at a mean ε_y of 0.21%. The mean f_u is 506 N/mm^2 at a mean ε_u of 18%, with ε_f higher than 24%. Figure 5-13 shows that the steel's response for coupons S_RHS_L_T_1 and 2 coincide to a strain of about 20%. Although the linear elastic stage of the dog-bone coupons is similar, f_u from coupon S_RHS_L_T_3 is 25 N/mm^2 lower than measured with coupons S_RHS_L_T_1 and 2. Also, the mean f_u closely matches the reported value of 510 N/mm^2 (see Table 3-1) from the supplier for the wire used in printing the Steelo components, as shown in Figure 3-19.

Table 5-8. Mechanical properties for the longitudinal coupons cut out from the RHS component.

	Material property				
	E [kN/mm^2]	f_y [N/mm^2]	f_u [N/mm^2]	ε_u [%]	ε_f [%]
1	2	3	5	6	7
S_RHS_S35_ L_T_1	186	392	513	18.7	24.3
S_RHS_S35_ L_T_2	217	407	515	18.9	35
S_RHS_S35_ L_T_3	220	393	490	16.3	27
Mean	208	397	506	18.0	28.8
Standard deviation		8.4	13.9	1.5	5.6
Coefficient of variation (%)		2.1	2.8	8.1	19.3
Characteristic value		381	480	15.2	18.3

Plotted in Figure 5-14 are four tensile stress-strain curves from testing longitudinal coupons cut-out from WALL A and WALL B (for S_WALL A_L_T_1 to 2 and S_WALL B_L_T_1 to 2). The modulus of elasticity of the four coupons is consistent, giving a mean of 210 kN/mm^2, as reported in Table 5-9. Table 5-9 has same presentation as Table 5-7 and Table 5-8, except the only statistical data presented is the mean values.
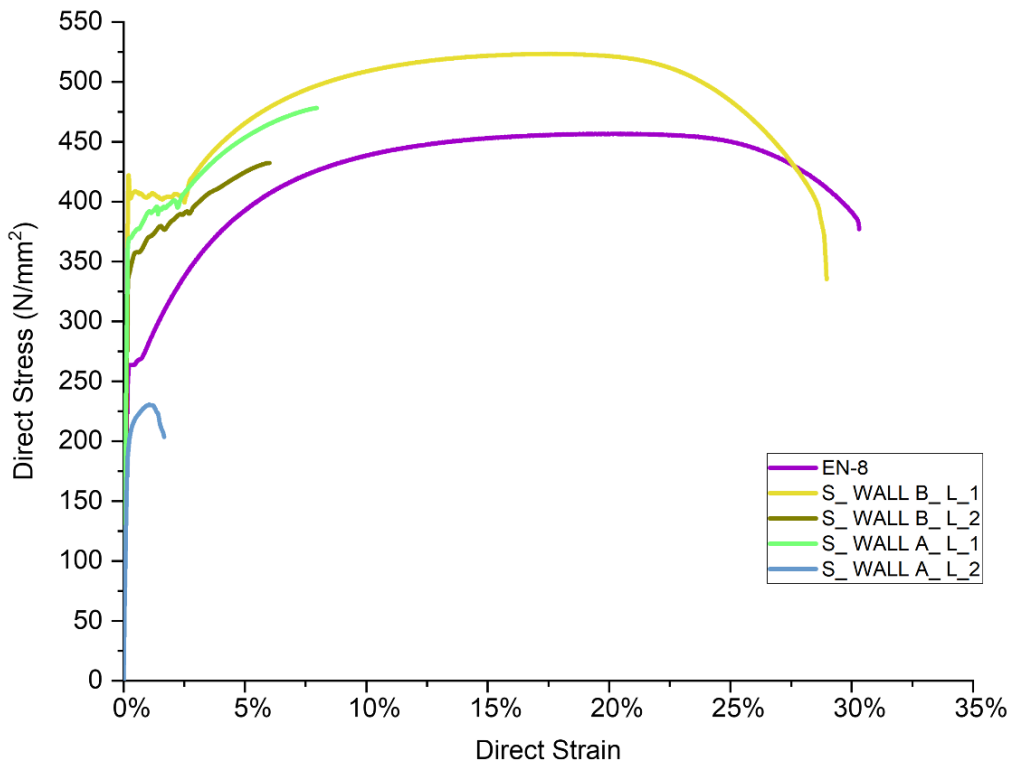
Figure 5-14. Tensile test results for the longitudinal specimens extracted from WALL A and WALL B.

It is known (Eudier, 1962) that the higher the percentage of porosity the lower will be the strength and strain at rupture. From column 6 of Table 5-9 coupons S_WALL A_L_T_1 and S_WALL B_L_T_2 ruptured with a tensile strain, ε_f, of about 6%, and their values of f_y in column 3 of Table 5-9 are 90 and 114 N/mm^2 below the minimum of 470 N/mm^2 for the as-supplied weld steel wire (see Table 3-1 and Appendix 3.2). More striking is an ε_f, of 3.5 % with coupon S_WALL A_L_T_2 that has a yield strength of only 206 N/mm^2 (the author notes this f_y is 48% less than the mean f_y from the three RHS coupons). Owing to the poor quality of the printed steel in WALL_A and WALL_B components the coupon test results in Table 5-9 are not used to determine the characteristic values, which could be used to compare against the material properties in Eurocode 3, which is a study made in Section 5.5.

Table 5-9. Mechanical properties for longitudinal cut out specimens from WALL A and WALL B.

	Material property				
	E	f_y	f_u	ε_u	ε_f
	[kN/mm^2]	[N/mm^2]	[N/mm^2]	[%]	[%]
1	2	3	4	5	6
S_WALL A_S35_L_T_1	207	370	479	8.2	5.9
S_WALL A_S35_L_T_2	216	206	230	1.05	3.5
S_ WALL B_S35_ L_T_1	220	422	523	17.6	29.5
S_ WALL B_S35_ L_T_2	195	346	432	6	6
Mean	210	336	416	8.2	11.2
Standard deviation		113.0	158.5	8.5	15
Coefficient of variation (%)		33.6	38.1	103.4	133.5

Figure 5-15 presents the plots of the tensile stress-strain curves to ultimate failure from the testing of the 12° inclined coupons (see Figure 4-9) S_RHS_S35_ I_T_1 to 3 (coloured in blue, green and golden respectively) and the benchmarked coupon of EN 8 grade steel (coloured in purple). Inspection confirms that the three curves indicate that the Steelo printed steel has overall stress-strain characteristics similar to the benchmark EN 8 steel curve. This finding indicates that there is no perceived change in material properties with inclination of coupon cut-out with respective to the longitudinal (0°) direction.
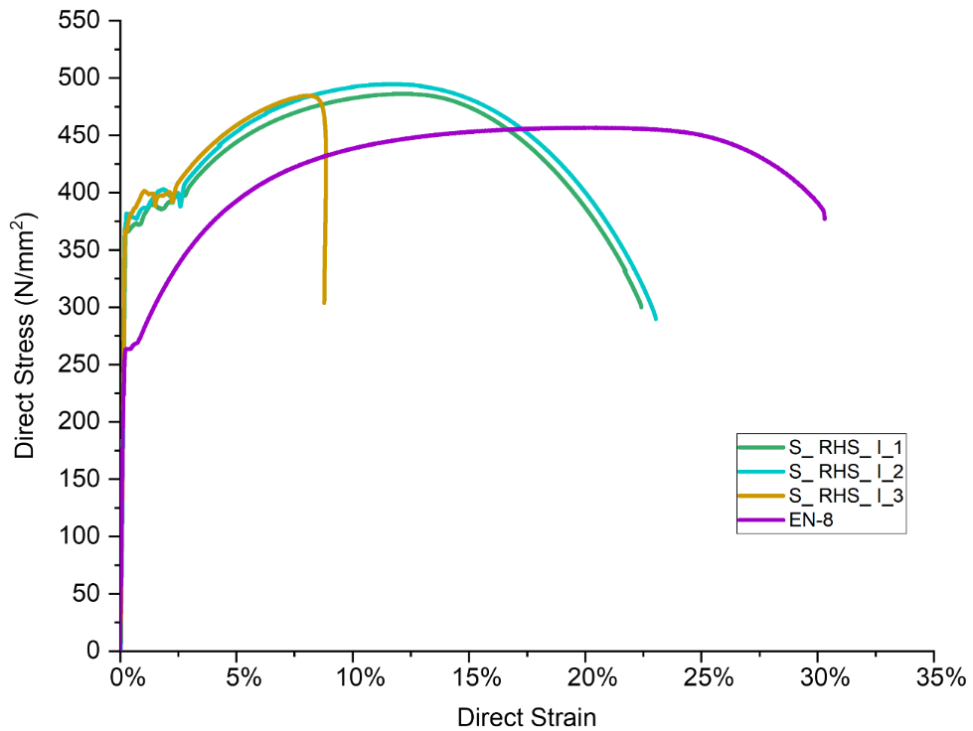
Figure 5-15. Tensile test results for the 12° inclined coupons extracted from the RHS component.

Table 5-10 reports the individual test results for the 12° inclined coupons using the same reporting format as in previous tables that have the full statistical data.

Table 5-10. Mechanical properties for the inclined cut out specimens from the RHS component.

	Material property				
	E	f_y	f_u	ε_u	ε_f
	[kN/mm^2]	[N/mm^2]	[N/mm^2]	[%]	[%]
1	2	3	4	5	6
S_RHS_S35_ I_T_1	220	393	490	16.3	22.4
S_RHS_S35_ I_T_2	1900	378	495	17	23.0
S_RHS_S35_ I_T_3	191	366	485	8.1	14.6
Mean	200	379	490	17.1	20.0
Standard deviation		13.5	5.0	4.1	4.7
Coefficient of variation (%)		3.6	1.0	34.4	23.5
Characteristic value		353	481	4.2	11.1

From the table the mean f_y is found to be 379 N/mm^2 at a mean ε_y of 0.21%. The mean f_u is 485 N/mm^2 at a mean ε_u of 8%, with mean ε_f at 15%. Coupon S_RHS_S35_ I_T_3 ruptured at a recorded strain of only 8%; the actual ultimate strain was 15%, which was not recorded by

the extensometer as the value of ε_f was outside the measuring range of the extensometer. Therefore, a manual measurement for the change of length was made by taking the two broken pieces and measuring the overall new length.

Figure 5-16 plots the results from testing the six coupons, extracted in the longitudinal and 12° inclined directions from the Steelo printed RHS components. As expected, there is an observed similarity in the stress-strain relationship for all the coupons in the linear elastic stage and the early part of the strain hardening stage. Significant deviations in the relationships are observed to start when the strain exceeds 12%. The justification for plotting the two groups of coupons is to highlight the differences in ε_f. Note that because it was not measured the elongation at failure for coupon S_RHS_S35_I_T_3 is not shown.
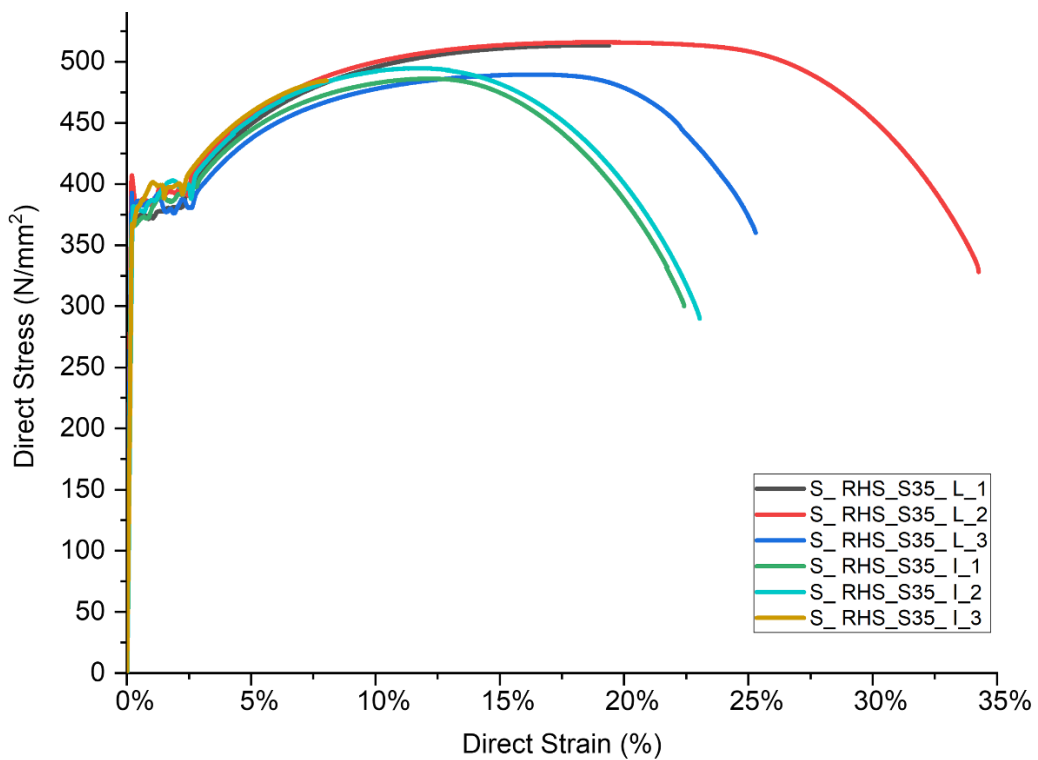
Figure 5-16. Tensile test results combining all the results from Figure 5-13 and Figure 5-15.

5.4.3. Stub Column Test Results

This sub-section reports on the characterisation of the material properties for the coupons extracted from one of the two RAMLAB printed stud column sections, as introduced in Section 4.1.3.2. Tensile testing was performed as detailed in Section 4.2 at a room temperature of 22.6°C and with 40% humidity. Direct strain readings were recorded during

testing using an Instron 2630-112 series strain gauge extensometer, as explained in Section 4.2.2.

Figure 5-17 presents plots for the stress-strain curves of six transverse coupons (R_ I**B**_S46 _T_T_1 to 3 and R_ I**C**_S46 _T_T_1 to 3) cut-out from the flange (plate **B**) and the web (plate **C**) of the stud-column. For the lay-out of coupons see Figure 4-11. For these RAMLAB printed coupons the linear elastic stage and the early part of the strain hardening stage are seen to be similar. As previously found, these new test results with tension loading now applied transversely to the direction of printing highlights the large range in ε_f, which is from 9% to 14%.
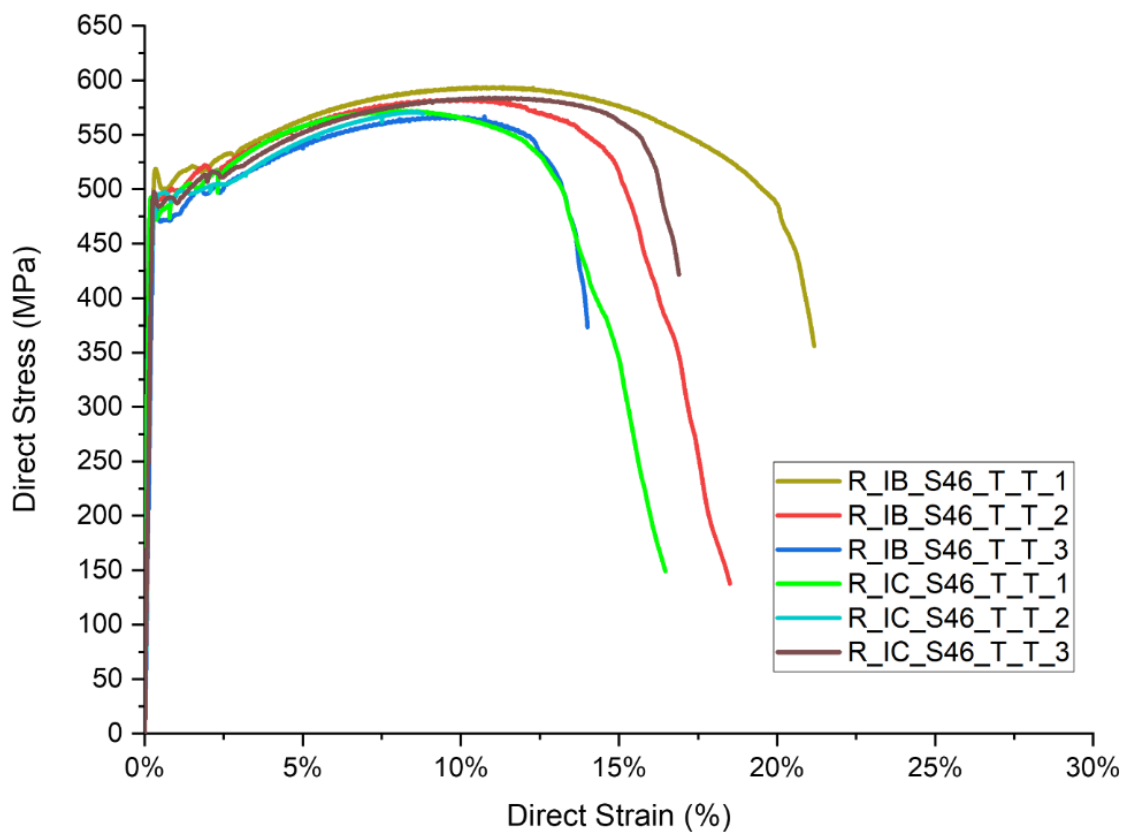
Figure 5-17. Plots of direct stress against direct strain for the transverse cut out specimens.

For the six coupons R_ I**B**_S46 _T_T_1 to 3 and R_ I**C**_S46 _T_T_1 to 3, Table 5-11 reports the mean f_y to be 470 N/mm^2, the mean f_u to be 567 N/mm^2 and a mean ε_u of 9.8%, with the fracture strain higher than 14%. The yield and ultimate tensile strengths in Table 5-11 are higher than reported by the supplier for the SupraMig Ultra HD- Mild steel solid wire (see column 3 in Table 3-1 and Figure 3-3) used to 3D print the steel sheet. From the tabulated results the mean E is 208 kN/mm^2.

Table 5-11. Mechanical properties for transverse material in a RAMLAB stud column component.

	Material property				
	E	f_y	f_u	ε_u	ε_f
	[kN/mm²]	[N/mm²]	[N/mm²]	[%]	[%]
1	2	3	4	5	6
R_ IC_S46 _T_T_1	221	492	572	8.0	16.5
R_ IC_S46 _T_T_2	207	491	570	8.2	24.9
R_ IC_S46 _T_T_3	210	497	584	10.7	16.9
R_ IB_S46 _T_T_1	202	519	594	11.3	21.2
R_ IB_S46 _T_T_2	213	491	582	9.8	18.5
R_ IB_S46 _T_T_3	188	470	567	10.7	14
Mean	208	493	578	9.8	18.7
Standard deviation		15.3	10.3	1.4	3.9
Coefficient of variation (%)		3.1	1.8	13.4	20.8
Characteristic value		466	560	6.7	10.1

Using the standard format, Table 5-12 presents the individual test results for the three 45° inclined coupons. From the tabulated values the mean f_y is 520 N/mm² for a mean ε_y of 0.21%. The mean f_u is 605 N/mm² at an ε_u of 8%, with ε_f higher than 15%.

Table 5-12. Mechanical properties for the 45° inclined material from the RAMLAB stud column component.

	Material property				
	E	f_y	f_u	ε_u	ε_f
	[kN/mm²]	[N/mm²]	[N/mm²]	[%]	[%]
1	2	3	4	5	6
R_ IA_S46 _I_T_1	215	501	596	4.9	15
R_ IA_S46 _I_T_2	221	548	631	12.9	27
R_ IA_S46 _I_T_3	199	513	587	6.3	21
Mean	212	520	605	8.0	20
Standard deviation		24.7	23.1	4.3	5.5
Coefficient of variation (%)		4.7	3.8	53.5	27
Characteristic value		474	561	0.07	10

Figure 5-18 shows the tensile plots of the direct stress-direct strain curves to ultimate failure for the test results of the 45° inclined coupons R_IA_S46_ I_T_1 to 3 (coloured in pink, green and black respectively).

Inspection of the test results show that the three curves, for the coupons R_IA_S46_ I_T_1 to 3, have similar yielding and initial strain hardening characteristics. Although for the two coupons R_IA_S46_ I_T_1 and 3 ε_f is displayed at only 5% and 8%, respectively, the actual tensile strain at failure was 15% and 20% (as reported in Table 5-12). Because these rupture strains could not be recorded by the extensometer (elongation was outside of the measuring range) a value (nearest percentage) was determined using a millimetre ruler to measure the final of the gauge length by holding the two halves of a ruptured coupon together.
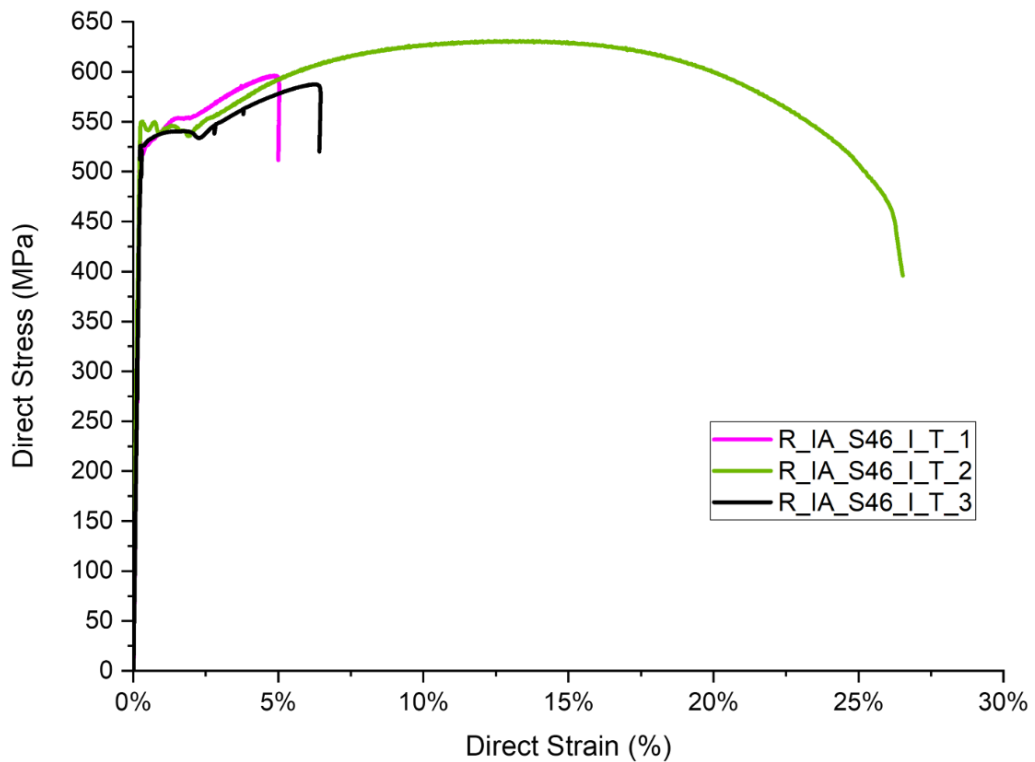
Figure 5-18. Plots of direct stress against direct strain for the 45° inclined cut out specimens.

To highlight the differences in ε_f Figure 5-19 plots together the test results for the nine coupons, extracted in the transverse and 45° inclined directions from the RAMLAB stub column. For the reason given, the 'true' fracture strains for coupons R_IA_S46_I_T_1 and 3 are not displayed.
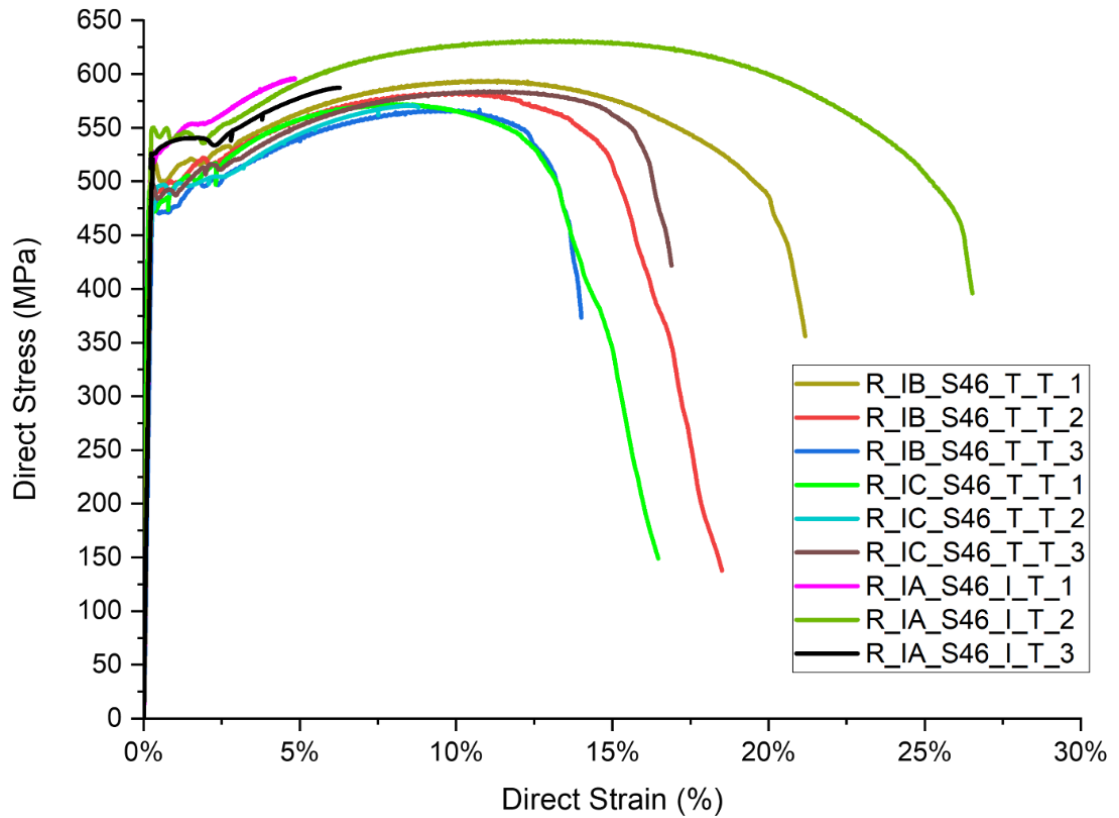
Figure 5-19. Tensile test results combining all the results from Figure 5-17 and Figure 5-18.

The linear elastic, yielding to commencement of the strain hardening stage in the tensile response of the coupons is seen to be similar. However, in the Figure 5-19, it is observed that the mean f_y for the 45° inclined coupons is 27 N/mm^2 higher than the mean value for the transverse coupons.

Additionally, Figure 5-20 to Figure 5-22 present the test results for the longitudinal coupons R_IB_S46_ L_T_1 to 3 and R_IC_S46_ L_T_1 to 3, first independently and then in Figure 5-22 combined. Figure 5-20 is for the three longitudinal coupons, extracted from flange B in the stub column (refer to Figure 4-11), with curves for the three coupons R_IB_S46_ L_T_1 to 3 having colours of blue, green and purple, respectively. The shape of the curves for these longitudinal coupons is similar until the steel has strain hardened. The material properties of f_y, f_u, ε_u and ε_f show variations, as seen by the test results reported in Table 5-13
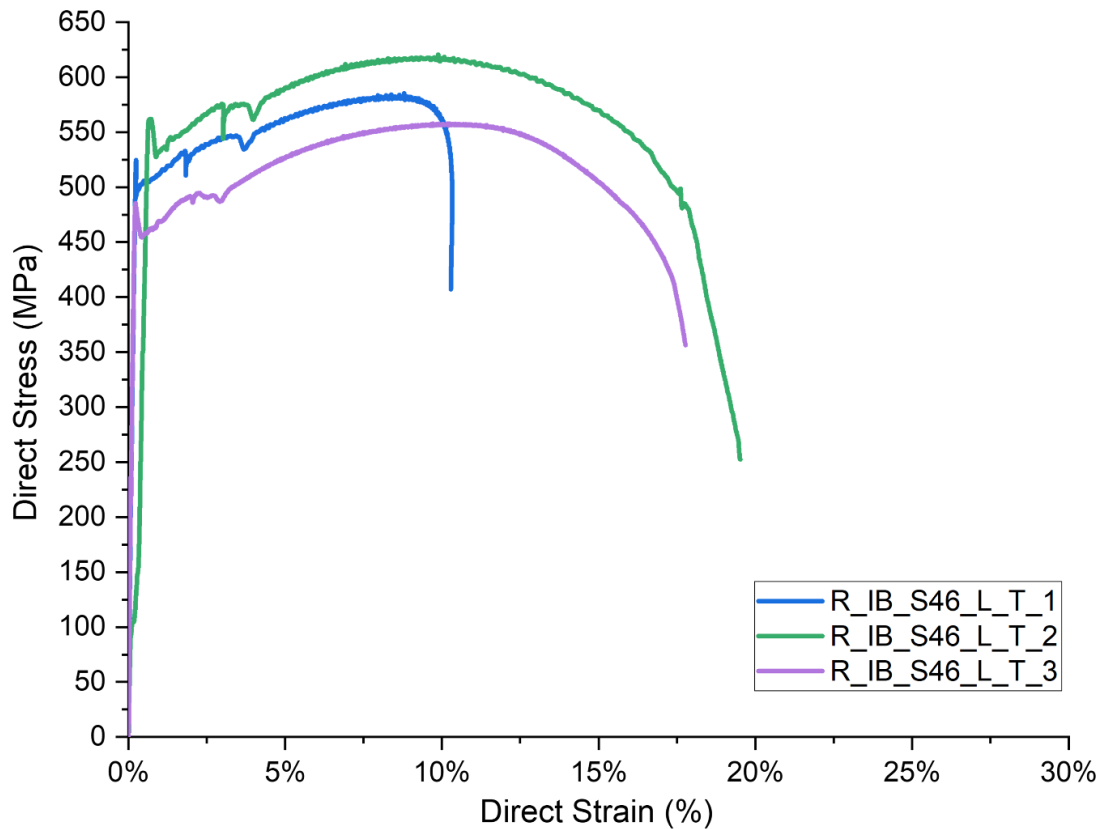
Figure 5-20. Plots of stress against strain for the longitudinal specimens extracted from Flange B.

Table 5-13. Mechanical properties for the longitudinal cut out specimens from Flange B.

	Material property				
	E	f_y	f_u	ε_u	ε_f
	[kN/mm^2]	[N/mm^2]	[N/mm^2]	[%]	[%]
1	2	3	4	5	6
R_IB_S46_ L_T_1	201	524	585	13.8	15.3
R_IB_S46_ L_T_2	195	562	621	9.90	19.5
R_IB_S46_ L_T_3	214	483	558	10.2	17.8
Mean	206	523	588	11.3	17.5
Standard deviation		39.5	31.5	2.2	2.1
Coefficient of variation (%)		7.6	5.4	19.3	12.1
Characteristic value		449	528	7.2	13.5

Figure 5-21 plots the stress-strain curves for three longitudinal coupons of R_IC_S46_L_T_1 to 3 for Web C of the RAMLAB stud column. The stiffness of this batch of coupons is consistent and the mean modulus of elasticity is 208 kN/mm², which is reported in Table 5-14.
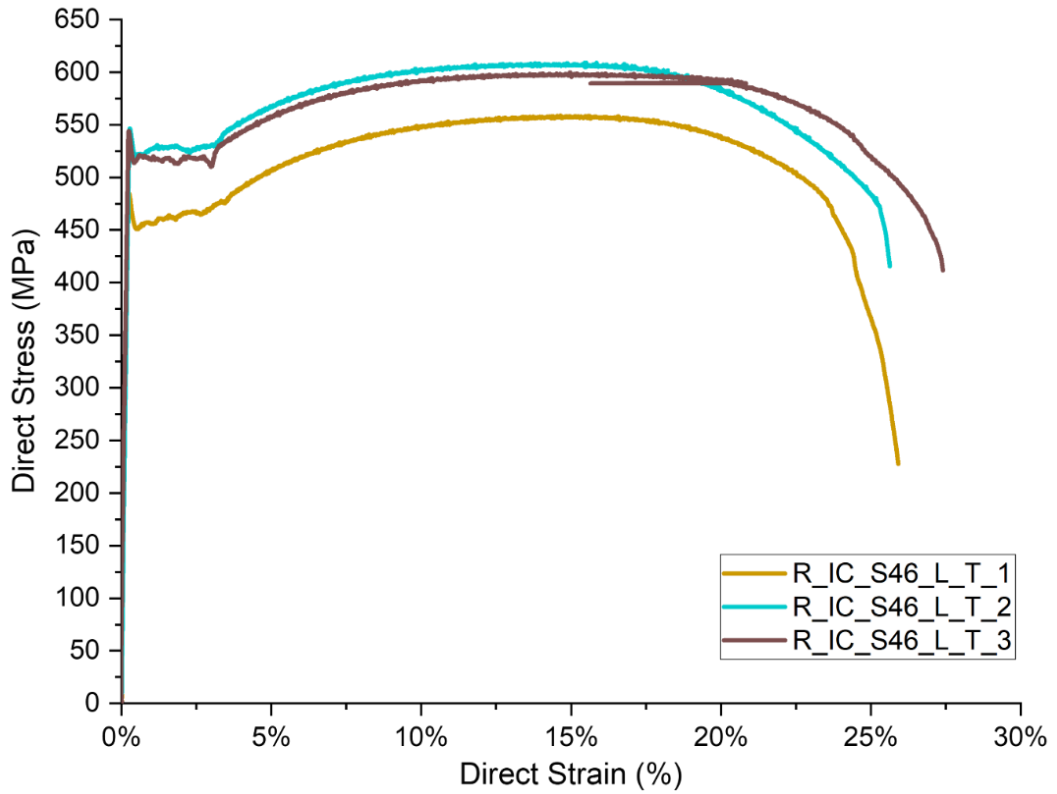
Figure 5-21. Direct stress-direct strain curves for the longitudinal specimens cut out from Web C.

Table 5-14. Mechanical properties for the longitudinal specimens cut out from Web C.

	Material property				
	E	f_y	f_u	ε_u	ε_f
	[kN/mm^2]	[N/mm^2]	[N/mm^2]	[%]	[%]
1	2	3	4	5	6
R_IC_S46_ L_T_1	207	484	559	14.6	25.9
R_IC_S46_ L_T_2	203	546	609	15.5	25.6
R_IC_S46_ L_T_3	213	544	600	15.0	27.4
Mean	208	525	589	15.0	26.3
Standard deviation		35.0	26.7	0.4	1.0
Coefficient of variation (%)		6.7	4.5	2.7	3.7
Characteristic value		459	539	14.3	24.5

Plotted in Figure 5-22 are test results for five longitudinal coupons, apart from R_IB_S46_L_T_2. As previously has been observed, there are similarities in the stress-strain relationships until strain hardening becomes developed. The significant difference in the five curves lies with the strain at rupture ε_f.

131
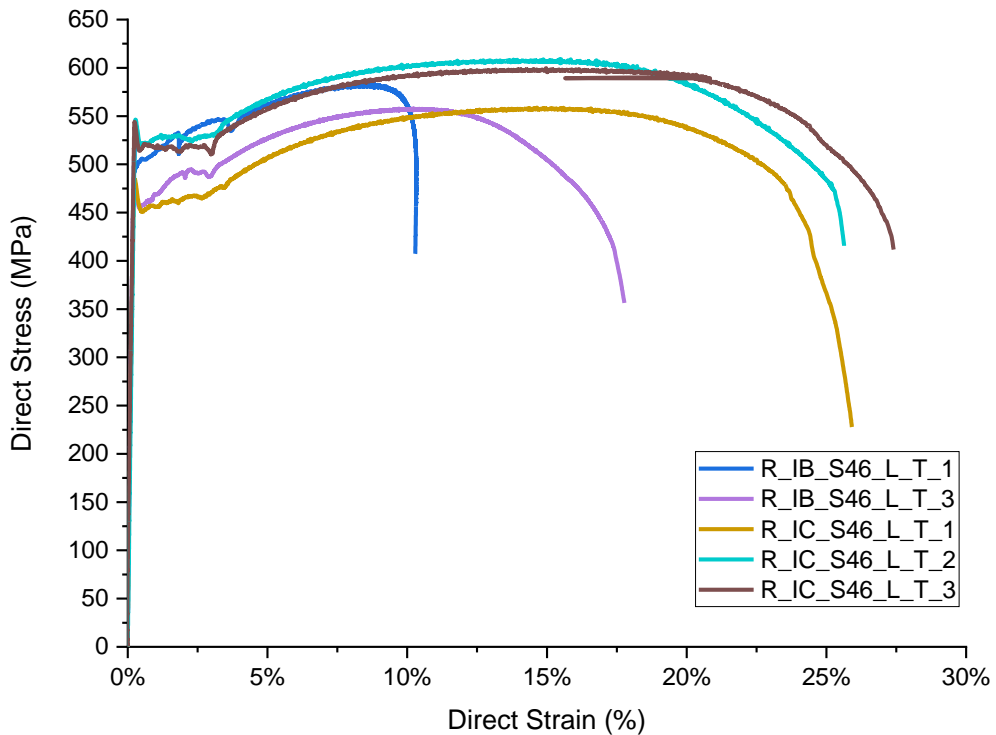
Figure 5-22. Tensile test results combining the five results from Figure 5-20 and
Figure 5-21.

5.5. Discussion of the tensile results

In this section the authors will give a discussion from an evaluation of the characterization work presented in Chapter 5 and the previous sections. In particular, Section 5.4 reports on the tensile test results, and the stress-strain curves are presented in Figure 5-10 to Figure 5-23, with important material properties listed in Table 5-7 to Table 5-14.

We will first consider how the tension coupons failed. Figure 5-23 (a) to Figure 5-23 (e) present photographs showing ruptured coupons of Autodesk (Figure 5-23 (a), Figure 5-23 (b), and Figure 5-23(c)) and Steelo (Figure 5-23 (d)) and RAMLAB (Figure 5-23(e)) printed steels. All five failed test specimens show steel with extensive plastic deformation and with the failure mode due to the conventional ductile 'cup and cone' failure mechanism. As observed, the type of failure in dog bones (Figure 5-23 (a, d and e)) and non-standard straight-sided coupons (Figure 5-23 (b) and (c)) is ductile fracture, as the tensile stress-strain relationship goes beyond the elastic limit, eventually forming localised extensive plastic deformation.
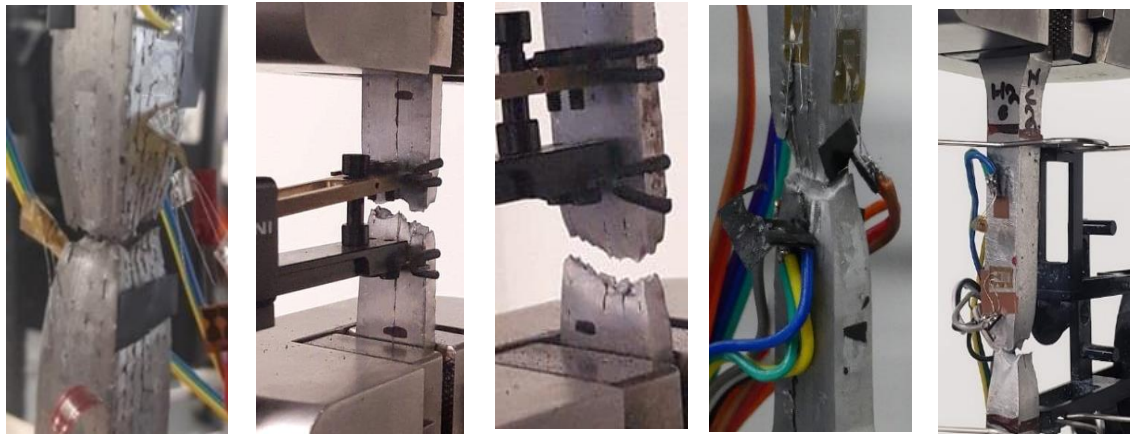
(a)   (b)   (c)   (d)   (e)

Figure 5-23. Ductile cup-and-cone failure for coupon: (a) A_Plate_S35_L_T_3, (b) A_Plate_S35_L_TT_1, (c) WAAM_L_TT_3, (d) S_RHS_S35_ I_T_2, (e) R_IC_L_T_2

The author determined that the average reduction in cross-sectional area of Autodesk printed steel is 53% for coupons A_Plate_S35_L_T_1 to 3 (see Figure 5-9), 40% for coupons A_ Plate_S35 _TT_T_1 and 2 (see Figure 5-11) and 30% for coupons A_ Plate_S35 _TT_T_3 and 4 (see Figure 5-11). The lower the reduction in cross-sectional area, the lower is the elongation at failure, ε_f, which can be seen from the ultimate strains plotted in Figure 5-11, or in Figure 5-14. The explanation for why ε_f with the two coupons WAAM_L_TT_3 and 4 has not exceeded 15% is that the 'cup and cone' failure did not occur in the 12.5 mm gauge length of the extensometer. This short gauge length can be seen in Figure 5-23 (c), with rupture site above it. In other words, ε_f has not been established with these two coupons; only for deformations leading-up to commencement of the 'cup and cone' failure, when the plastic strain is about 12%.

It has been found that for steel cut-out of the Steelo RHS component the reduction in cross-sectional area for the longitudinal coupon S_RHS _S35 _L_T_1 is 35%, and higher, at 51% for both S_RHS _S35 _L_T_2 and 3. In comparison, the average reduction in cross-sectional area for the 45° inclined coupons S_RHS_S35_I_T_1 to 3, with a percentage of porosity of 0.048%, is > 50%.

From the green-brown and blue coloured curves in Figure 5-14 it is seen that ε_f is 6% or lower for coupons S_WALL A_S35_L_T_1 and S_WALL B_S35_L_T_2. This extremely low elongation at failure of the Steelo printed steel is linked to the effect of weld heat history on the formation of the steel's microstructure. As expected, their mean reduction in cross-sectional area at 11% is significantly lower than for RHS coupons at 35%, and test results from WALL A and WALL B coupons have been excluded from the characteristic value calculations, as

mentioned earlier in Sub-Section 5.2.2. With coupon S_WALL A_S35_L_T_2 (blue coloured curve in Figure 5-14) having 4.4% volume fraction of porosity the strain at brittle rupture just exceeded 3%.

For the RAMLAB printed stud column component (refer to sub-section 5.4.3), the average reduction in cross-sectional area for the longitudinal coupons R_IC _S46 _L_T_1 to 3 and R_IB _S46 _L_T_1 to 3 (see Figure 5-22, Table 5-13 and Table 5-14) is 55%. This steel has a volume fraction of porosity of 0.5% (see Table 5-16). To make a comparison, the average reduction in cross-sectional area of the 45° inclined coupons R_IA_S46_I_T_1 to 3 (see Figure 5-18 and Table 5-12) is 43% (with porosity of 0.82%), and the average reduction for the transverse coupons R_IB_S46_T_T_1 to 3 and R_IC_S46_T_T_1 to 3 (see Figure 5-17 and Table 5-11) is 35% (with average porosity of 0.93%).

X-CT imagining and evaluation is key in this research work to provide a link between the internal structure of printed steels and the test results for tensile mechanical properties, introduced in Section 5.4. The X-CT results of scanning the coupons before (see Figure 5-2, Figure 5-3, Figure 5-4, Figure 5-5 and Figure 5-7) and after (see Figure 5-24 , Figure 5-25 and Figure 5-26) tensile testing, shows the change in internal structure (owing to failure deformations) and its impact on the type of failure; especially at the interfaces where the porosity exists in the Autodesk material and at the location of the pores in the Steelo and RAMLAB materials. This highlights how the WAAM steel response to tension is related to the material's short-term properties.

From X-CT evaluation in sub-section 5.2.1 it is known that for the Autodesk printed steel that there are three main constituents. Table 5-15 reports the post-testing volume fractions of the three constituents in coupons A_Plate_S35_ L_T_1, A_Plate_S35_ TT_T_1 and A_Plate_S35_ TT_T_2. Column 1 outlines the three constituents (see Figure 5-2) as bulk steel, interfacial regions and porosity. Columns 2 to 4 presents the volume fractions for the three constituents in percentages. From the first row in the table, it is found that bulk steel is for 99.2 to 99.5% of the printed steel. It is observed that the mean percentage for the interfacial regions is 0.48%, with specimen values ranging from 0.38 to 0.64%. Furthermore, the porosity is found to be lying in the range from 0.05 to 0.21%, and this is within the same range of porosity for the specimen before testing, which was 0.1%, their porosity suggests a localised difference in the amount of porosity at the interfacial regions. This finding might be

reflected in localised differences in material properties. As required when 3D printing of steel, the lowest volume fraction of the three constituents was the porosity.

Table 5-15. Volume fractions of the three constituents in coupons of Autodesk horizontal plate.

	Volume fraction (%)		
	A_Plate_S35_ L_T_1	A_Plate_S35_ TT_T_1	A_Plate_S35_ TT_T_2
1	2	3	4
Bulk steel	99.52	99.42	99.24
Interfacial regions	0.43	0.38	0.64
Porosity	0.05	0.21	0.12

Figure 5-24 and Figure 5-25 give a visual representation for the X-CT volumes of the A_Plate_S35_ TT_T_1 and A_Plate_S35_ TT_T_2 coupons after fracture.

(a) (b) (c) (d)
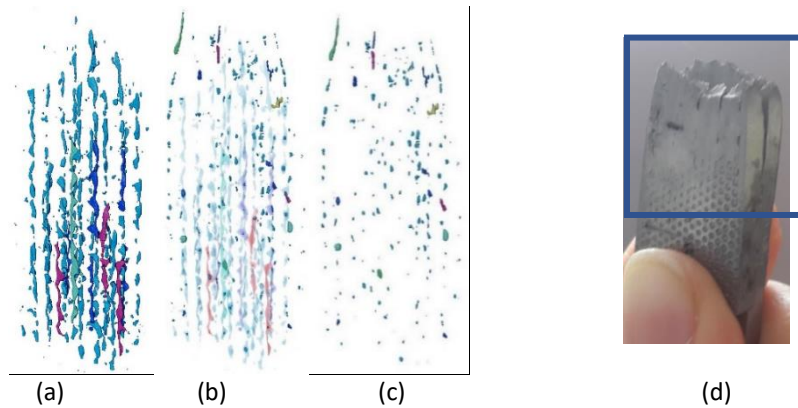
Figure 5-24. Internal structure of the coupon A_Plate_S35_ TT_T_1: (a) interfacial regions; (b) interfacial regions and porosity; (c) porosity distribution; (d) X-CT scanning region of the coupon shown by the blue box.

(a) (b) (c) (d)
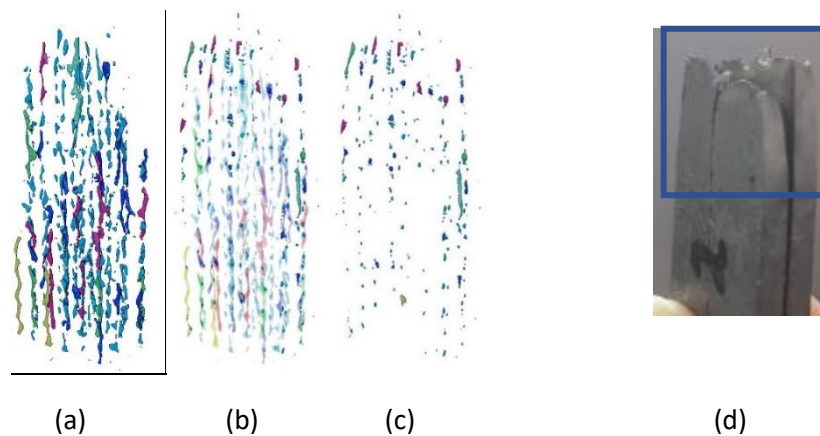
Figure 5-25. Internal structure of the coupon A_Plate_S35_ TT_T_2: (a) interfacial regions; (b) interfacial regions and porosity; (c) porosity distribution; (d) X-CT scanned region of the coupon shown by the blue box.

The interfacial regions are displayed in Figure 5-24(a) and Figure 5-25(b) and shows a homogenous deformation throughout the cross section of the coupons. In Figure 5-24(b) and Figure 5-25(b), the interfacial regions with associated porosity are known to have a lower density than that of the bulk steel. From the images for the porosity alone, seen in Figure 5-24(c) and Figure 5-25(c), it can be observed that the 'cup and cone' failure occurs at the top of the volume or where prominent voids are elongated and rupture takes place. Photographs of the two coupons in Figure 5-24(d) and Figure 5-25(d) show the regions scanned by X-CT.

Similarly, in Figure 5-26(a) to Figure 5-26 (d) the scanned coupons for Autodesk, Steelo and RAMLAB printed steels show that fracturing occurred at the pores (as highlighted by the red coloured elongated pores in the images in parts (c) and (d)). It is feasible that one of more of these voids (in addition to the overheating interpass) may have led to the premature fracture, which is signalled by the low elongation at failure of 6% (from the measured ε_us are reported in Tables Table 5-9) than the expected minimum of 20% as specified in Table 1A-section 4.2 in EN (ISO14341, 2010) or the mean ε_f values of 26% for the Steelo copper-coated solid wire for welding C&C-Mn steels and for the RAMLAB SupraMig® Ultra HD- Mild steel solid wire.
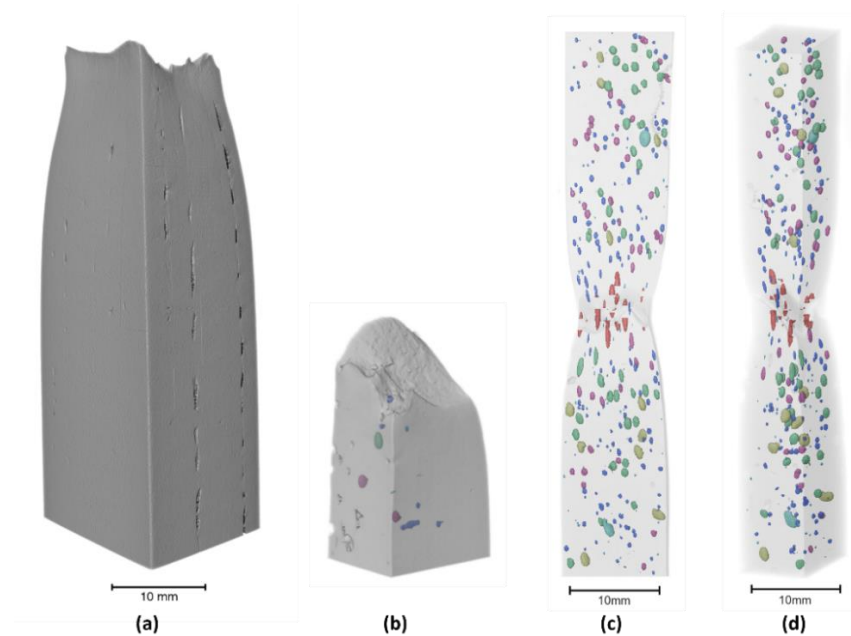
Figure 5-26. X-CT images for failed coupons: (a) Autodesk A_Plate_S35_ T_T_1; (b) Steelo S_RHS_S35_ I_T_2; (c) RAMLAB R_ IA_S46 _I_T_1- 3D; (d) RAMLAB R_ IA_S46 _I_T_1- side view

After calculating the volume fraction of porosity and inspecting the internal structure of the coupons (see Section 5.2), the amount of porosity is observed to affect the tensile results (see the direct stress-direct strain curves for the specimens presented in Section 5.4, Figure 5-14). This is not the situation for the 'elastic slope' (used to calculate the modulus of elasticity) in the linear elasticity stage prior to yielding. All the tensile coupon test results followed the same stress-strain relationship, with an average variation of around 1-3% in the measured yield strength, f_y, yield strain, ε_y, strain hardening to ultimate tensile strength, f_u, and elongation at failure, ε_f. The understanding gained from the test results presented in this thesis raises the question: How are the material properties of f_y, ε_y, f_u and ε_f affected by the presence and distribution of voids, and a possible greater localised non-homogeneity in WAAM-GMAW printed steels?

Casting of steels is a manufacturing method, widely used in the construction industry, that can be taken as a reference for 3D printed steels. Both methods have porosity issues in the end products, in addition to other limitations such as shrinkage, surface roughness and tolerance (Baddoo, 1996). Casting has been used in the construction industry with these limitations for many years and was used initially for non-key elements and structures carrying lower stresses.

Eudier(Eudier, 1962) found that the existence of porosity has a large effect on the fracture strain and the yield strength of cast steel; these values decrease significantly for higher percentages of porosity. The internal molecular equilibriums of the printed component under uniaxial load is also related to the plastic flow balance between the stages of the tensile stress-strain curves (Roylance, 2001). During the ductile fracture stage, where there was a large observed variation in the stress-strain relationship, Hardin and Beckermann showed that the fracture mechanism is affected by the size and distribution of voids and porosity (Hardin and Beckermann, 2007) (Hardin and Beckermann, 2013).

Table 5-16 reports characteristic and other results from the series of coupon tests, which are identified by their labels in Column 1. Column 2 in the table gives the mean modulus of elasticity, E, calculated for each batch of coupons; columns 3 to 5 list the characteristic values for yield strength, f_y, ultimate tensile strength, f_u and strain at failure, ε_f (or elongation at failure). Column 6 tabulates the ratios for f_u/f_y, which can be directly compared to the ductility requirements in BS EN 1993-1-1, as explained in Section 5.5. In column 7 representative values for the volume fraction of porosity in the coupon steels, which have

been determined using X-CT imagining, are reported in Table 5-1 and Table 5-2 of this chapter.

Table 5-16. Summary of characteristic values, mean elongations at failure and representative volume fractions of porosity.

	E [kN/mm^2]	f_y [N/mm^2]	f_u [N/mm^2]	ε_f [%]	f_u/f_y	Volume fraction of porosity %
1	2	*3*	4	5	6	7
Autodesk (Table 5-7)						
Union K 40 steel wire (mean)	-	360	440	25	1.22	N/A
A_ Plate_S35 _L_T_1-3	208	411	467	25.8	1.14	≤ 0.21
Steelo (Table 5-8 and Table 5-10)						
Copper-coated solid wire (mean)	-	470	560	26	1.2	N/A
S_RHS_S35_ L_T_1-3	208	381	480	18.3	1.26	≅ 0.2
S_RHS_S35_ I_T_1-3	200	353	481	22.1	1.36	≅ 0.2
RAMLAB (Table 5-11 to Table 5-13)						
SupraMig® Ultra HD- Mild steel solid wire (mean)	-	500	650	26	1.3	N/A
R_ IB_S46 _T_T_1-3	203	448	555	10.9	1.24	≤ 0.86
R_ IC_S46 _T_T_1-3	217	488	561	10.5	1.15	≤ 1.0
R_ IA_S46 _I_T_1-3	212	474	561	10.3	1.18	≤ 0.82
R_IB_S46_ L_T_1-3	206	449	528	13.5	1.18	≤ 0.5
R_IC_S46_ L_T_1-3	208	459	539	24.5	1.17	-

From the results presented in Table 5-16 it is found that the characteristic strengths are for:

Autodesk printed steel f_y = 411 N/mm^2 and f_u = 467N/mm^2;

Steelo printed steel mean f_y = 366 N/mm^2 and mean f_u = 480 N/mm^2;

RAMLAB printed steel batches give range f_y from 449 N/mm^2 to 488 and f_u from 528 to 561 N/mm^2.

Except for the RAMLAB steel the strengths for Autodesk and Steelo steels are found to lie within the Eurocode 3 (EN1993-1-1:2005) ranges of 235 < f_y < 460 N/mm^2 and 360 < f_u < 560 N/mm^2, which is for nominal values presented in Table 3.1 for steel grades S235 to S460 of

hot rolled structural steel. For the RAMLAB steel, its characteristic strengths are towards the upper limit and slightly above this for yield strength and ultimate tensile strength. The RAMLAB printed steel has therefore been shown to possess characteristic strengths that are within the scope of hot-rolled structural steel grades in *Eurocode 3 – Design for steel structures - Part 1-12 Additional rules for the extension of EN 1993 up to steel grades S 70*0 (BS, 2007). From Table 1 in this standard the nominal values for four steel grades are 500 < f_y < 690 N/mm^2 and 590 < f_u < 770 N/mm^2.

It is noteworthy that characteristic values of f_y and f_u in the transverse direction compared to those in the longitudinal directions are higher, at 473 and 550 N/mm^2 for plate C (which is the web) vs 448 and 541 N/mm^2 for plate B (which is the flange). The differences can be due to localised printing parameters and the temperature history during the printing, and for cooling down of the printed steel.

Next the discussion will consider the ductility requirements as laid out in Section 3.2.2(1) of (BSI, 2005) and NA to BS 1-1:2005 for structural grades of steel, recognising that they are for hot-rolled steel sections. It is also to be understood that for this study on ductility requirements that minimum specified values (see 3.2.2 in EN 1993-1-1:2005) are taken to be characteristic values determined using test results with relatively small batch sizes (3 coupons). The objective of this study is to establish if weld steels used in the WAAM-GMAW printing can provide material properties that satisfy ductility requirements. If they do, then the case can be made that the design rules in Eurocode 3 Part 1-1 are valid for steel sections produced by this AM method. There follows a brief assessment of each of the three printed steels.

From Table 5-16 the ratio of f_u/f_y = 1.14 for the Autodesk printed steel is acceptable as a S355 steel grade, because, accounting for the level of uncertainty in the test results, it can be said to satisfy the ductility requirement of f_u/f_y = 1.15 in BS EN 1993-1-1 for plastic global analysis for the design of buildings or bridges. Elastic global analysis is only feasible for buildings (and not for bridges) because f_u/f_y < 1.20; although the elongation at failure, ε_f, at 26% is > 15%. The elastic global analysis ductility requirement of $\varepsilon_u \geq 15\varepsilon_y$ is also satisfied, since ε_u, at 12.7% (as reported in Table 5-7), is > 15 times ε_y =0.21%= 3.15%.

Again, taken from Table 5-16 the mean of two f_u/f_y ratios for Steelo printed steel is > 2, and so this WAAM-GMAW material satisfies the ductility requirements of S355 grade steel. Moreover, the ε_f of this steel is > 15% and ε_u at 8% is > 15 times ε_y =0.21% = 3.15%, thereby

satisfying the ductility requirements in BS EN 1993-1-1 for elastic global analysis for design of buildings or bridges. It is also found that the Steelo steel has material properties that satisfy the plastic global analysis for buildings, because ε_u at 8% is > 20 times ε_y =0.21% = 4.2%.

The RAMLAB printed steel is to be treated differently because its material properties presented in Table 5-16 indicate that it is for a steel with a higher grade than S460 (the upper limit in EN 1993-1-1:2005), and as such the ductility requirements are scoped by standard EN 1993-1-12:2007, which permits the extension of EN 1993 up to the steel grade of S700. The five f_u / f_y ratios reported in column 6 of Table 5-16 are > 1.05 (having range 1.15 to 1.24 and for a mean of 1.18). Moreover, the five ε_fs in listed column 5 are all > 10% and required $\varepsilon_u \geq 15f_y/E$ = 15x564/20900 = 0.04 or 4% is satisfied (see Figure 5-17 to Figure 5-22). The ductility requirements in EN 1993-1-12:2007 for steel grades from S460 to S700, that can be used in steel structures, for elastic global analysis, are therefore satisfised.

Bardin and Beckermann (Hardin and Beckermann, 2013) suggest that when the volume fraction of porosity is less than a few percent, there is no measurable loss of stiffness, large stress concentrations or stress redistribution, but it will significantly reduce the steel's fatigue strength. The percentage of porosity in the printed steels is: 0.2% for Autodesk; 0.05% for Steelo; 1% for RAMLAB. Such a range from 0.05 to about 1% does not seem to have a significant impact on material properties determined under static loading. It has been found that the three WAAM-GMAW steels have material properties as determined by standard coupon testing to satisfy the ductility requirements in Eurocode-3.

5.6. Concluding remarks

This chapter presented the impact, tensile, density and X-CT results for the prepared specimens. The aim of the experiments carried out herein was to compare the mechanical properties of the printed steel with conventional structural steel, to learn whether the printed steel can be considered as a 'structural steel' material and whether design code Eurocode-3 can be used for future reference in 3D printing structural applications. A detailed description of the characterisation test (also known as the tensile test for determining the direct stress - direct strain relationship and Poisson's ratio of the steel), impact test, density measurements and the analysis of the X-CT scan was presented.

A non-destructive examination (X-CT) of the extracted specimens was used to identify any internal defects, which can be linked to the described printing process in Chapter 3, as summarised below:

- In the horizontal plate, the existence of the interfaces between the five layers are clearly shown by the X-CT images (see Figure 5-1) as a result of the step-over distance during the printing process, which was insufficient for the beads to fuse together.

- In the Wall A and WALL B components (printed at Steelo), the printing error was due to the high interpass temperature between the beads which was not maintained. Cooling time for the printing of the RHS component was increased and this was directly reflected by the percentage of porosity which fell drastically from 4.4% (in the S_WALL A_S35_L_T_2 coupon from Wall A) to 0.04% (in the S_RHS_S35_ L_T_1-3 coupons from the RHS component).

- The X-ray reading of the RAMLAB material showed a scattered distribution of pores, in comparison to the systematic printing error in the Autodesk material regarding the interfacial regions, which is not associated with the deposition process (printing path, printing process and printing strategy).

- The porosity level reaches 1% for the specimens cut out in the transverse direction and an average of 0.5% for the longitudinal and inclined directions. The justification for the presence of the scattered pores was explained by Figure 5-8, where splattering and vapour condensation was observed during the printing.

A lesson learnt from highlighting the internal defects via X-CT analysis (e.g. calculating the volume fraction), was how to eliminate the defects by establishing the optimum WAAM printing parameters.

In this research the percentage of porosity was linked with the material properties to investigate how localised discontinuities (voiding) may affect the mechanical properties. Tensile tests are reported together with a discussion of X-CT examination of the steel before and after testing, to provide data towards a fuller understanding of the mechanical properties, and to account for factors for orientation and the effect of porosity and the interfacial surface between the printed layers.

- To investigate further the quality of a WAAM steel, a comparison has been made between newly tested mechanical properties and those listed for structural steels in

Section 3 Materials of EN1993-1-1:2005 for normal steel, EN1993-1-12:2005 for high yield steel.

- Modulus of elasticity is a good indication of stiffness; the higher the value the stiffer the material which is the slop in the elastic region. The mean value of the tested specimens satisfied the design Eurocode 3.

- The stress caused by the applied forces will cause the material to deform, where it is important to understand the type of failure mode for this material. Figure 5-23 shows a typical dog-bone failure of specimens within the different cut out configuration and type of used wire.

For the impact test, the room temperature was chosen as a starting point for using the material in structural engineering internally and not as a key element in a building. The material satisfies BS EN 1993-1-10:2005/AC for toughness requirements of 27 J. Moreover, it is found that the impact energies of both Steelo and RAMLAB materials vary by < 1% with the printing orientation, which the suggests that this has a minimal effect on the steel's toughness.

6. Chapter Six: X-CT and test results for the monolithic beam-to-column joint

This chapter reports the rotational behaviour of the printed beam-to-column joint under monotonic static load and the X-CT analysis before load testing; to investigate how the printing strategy has affected the overall structural response. The testing programme was undertaken using the facilities of the Structures laboratory in the School of Engineering (SoE), University of Warwick. The experimental set-up includes designing and preparing the test rig, calibrating the instrumentation, and setting the loading profile. The results will be used to classify the beam-to-column joint in accordance with BS EN 1993-1-8:2005.

6.1. Introduction, Philosophy and Vision

Although WAAM-GMAW printed components are to have exotic or topologically optimised geometries for form following forces, a conventional monolithic beam-to-column joint with thin-walled I-sections was printed in this PhD study. This approach offers comparable test results with known, conventional steel joints and its vision is to advance the understanding of applying WAAM-GMAW processing for large-sized steel components in structural engineering.

The moment-rotation experiment links the moment-rotational response of the beam-to-column joint, under a monotonic static load, with the X-CT analysis in section 6.2 and printing process in Section 3.4.4. Establishing data on how the internal structure of the printed transition zone interacts is key in this research, to learn how it will influence the overall moment-rotation behaviour in the beam to column joint test.

The results will be used to investigate how the printing strategy has affected the overall structural response and the classification of the beam-to-column joint in accordance with BS EN 1993-1-8:2005.

6.2. X-CT results

X-CT scanning of the transition zone was analysed for the printed joint (there was no X-CT scanning of the conventional joint), where failure is designed to happen during the load test. X-CT analysis captured the sizes and quantity of the local internal structural features in the key zone of the joint. The technology utilises a series of radiographs, as presented in section 4.5, to construct a 3D model that includes the internal and external geometries of the examined object, as shown in Figure 6-1.
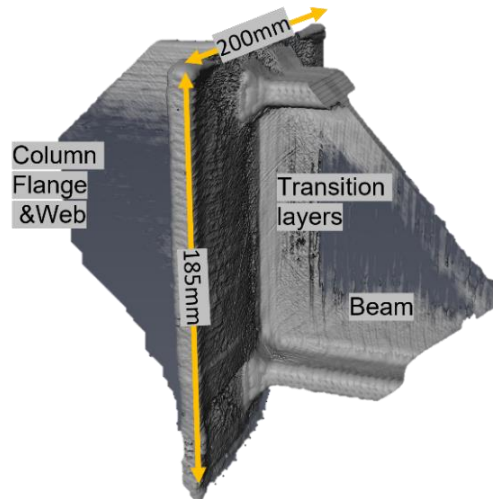
Figure 6-1. 3D volume of the interior of the joint zone from the X-CT imagining of the WAAM-GMAW joint

The reconstructed radiography data presents the steel with a higher atomic number in brighter grey, steel with a lower atomic number in darker grey and volumes of air identified as black regions. Figure 6-2 shows the level of absorbed energy in the different parts of the monolithic element (beam, column, and transition zone). This reading is a function of the atomic number and the density of each printed part.
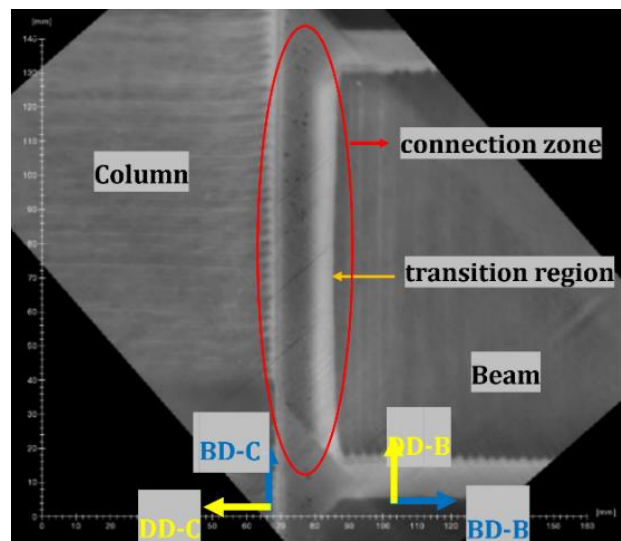
Figure 6-2. X-CT image for the beam-to-column, highlighting the different absorption levels along the different sections of the beam

The aim of using X-CT is to explore how effective the WAAM manufacturing process is and how confident we can be in producing 'solid' homogeneous steel components with minimum porosity, especially in the regions of the steel where failure by plasticity will occur.

144

It is observed that the absorption level is high at the transition zone and the flanges. The lighter the colour, the higher the energy absorbed and the denser the material. The white colour in the transition region (the five tapered layers) shows the impact of the chosen printing process, as detailed in section 3.4.4, which is reflected by the denser and porosity-free zone. For the location of the flanges, this is predictable as the plates are thicker and wider.

A coloured scheme was followed to categorise the X-CT analysis process according to its location, as shown in Figure 6-3, for easier segmentation. The location of pores in the web of the column is represented in red; green is used for the flange of the column while the beam is shown in blue, and the transition region is coloured in purple.
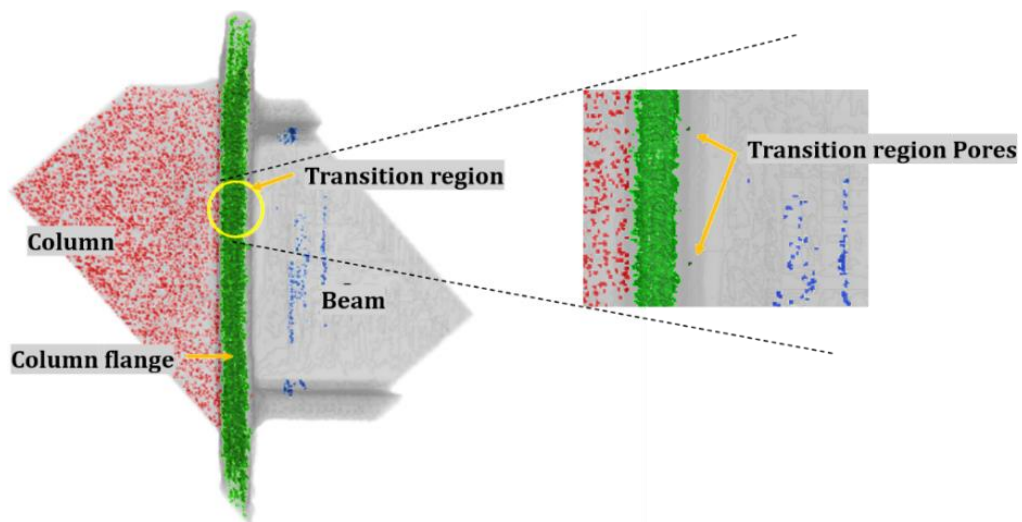
Figure 6-3. Segmentation of the pores and its respective colouring scheme

The importance of monitoring the printing process can be reflected by the column, where there is an abundance of pores as cleaning protocols were not followed. The details of the encountered problems have been explained in Section 5.2.3, which includes the turbulent and trapped gas within the head of the printing tool and the accumulation of grounding wires.

Figure 6-4 shows the exact locations of the pores in the two different orientations for the component. A system printing error can be highlighted in one half of the beam section, as the pores occurred within specific layers (in the centre of the web and at the periphery of the flanges). Note that this occurred 20mm from the surface of the transition zone and was a result of insufficient gas flow, which was corrected when printing of the rest of the beam. Reasons for the existing pores in the column were discussed in Section 5.2.3.
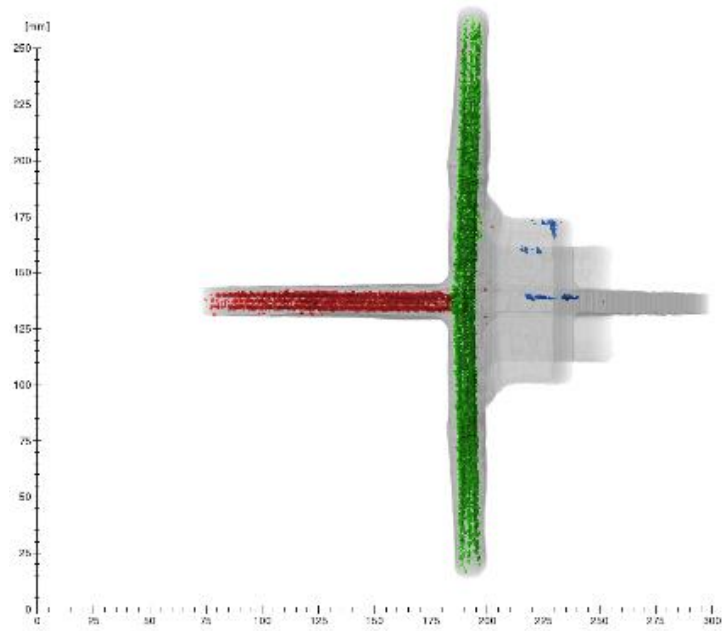
(a)
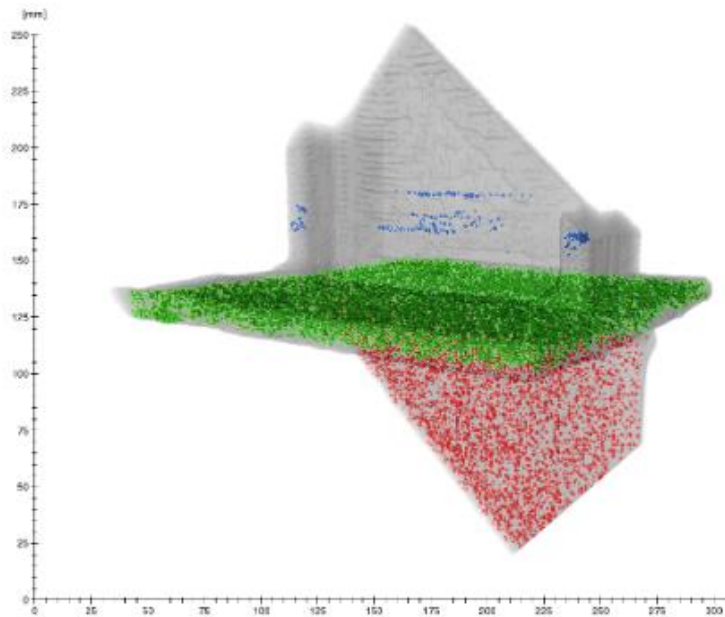
(b)

Figure 6-4. Location of pores in the transition zone of the specimens: (a) Top view; (b) 3D view

After the number and sizes of the voids were digitally identified, the mass of the beam section was automatically segmented and refined manually, from which porosity volume fractions were determined. However, the column and the transition zone were manually segmented as explained in Section 4.5.4. Table 6-1 lists the percentage volume fractions of porosity in the three regions of interest, namely: the column section, the beam section, and the transition region between the two sections.

Table 6-1. Distribution and percentage of porosity in the zones of interest.

Zones of interest	Column	Beam	Transition region
Volume fraction (%)	1.55	0.07	0.002

Although the same printing strategy and printing parameters were employed to manufacture the monolithic joint, the results in Table 6-1 indicates that the column section (adjacent to the connection zone) has the higher porosity volume fraction at 1.55%, whereas it is significantly lower at 0.07% in the beam section.

To minimize formation of porosity, the modification made during processing was to adjust the inter-layer cleaning protocol. After every 5 layers of printing, cleaning both the welding torch and the weld surface was introduced during the stopping time. The stopping times were around 5 minutes to maintain the inter pass temperature. The cleaning protocol ensured the removal of accumulated metallic condensation on the gas cap, which was explained in Section 5.2.3. The dramatic improvement this made in reducing the porosity level by 95% in the X-CT results for the beam section, can be seen in Figure 6-3 and Figure 6-4.

6.3. Numerical analysis for the dimensions of the beam-to-column joint

The schematic diagram for the experimental set-up used for testing the joint is shown in Figure 6-5. The two key considerations while sizing the dimensions of the joint were the maximum capacity of the hydraulic-load actuator and the maximum allowable uplift force transferred to the floor socket in the structural lab. The maximum capacity of the load cell is 150 kN and the capacity of the forces per socket is 105 kN. Therefore, the geometrical dimensions were chosen (see Figure 3-24) so that failure by a plastic section moment at the beam-to-column interface would happen without these force capacities being exceeded during the static test.
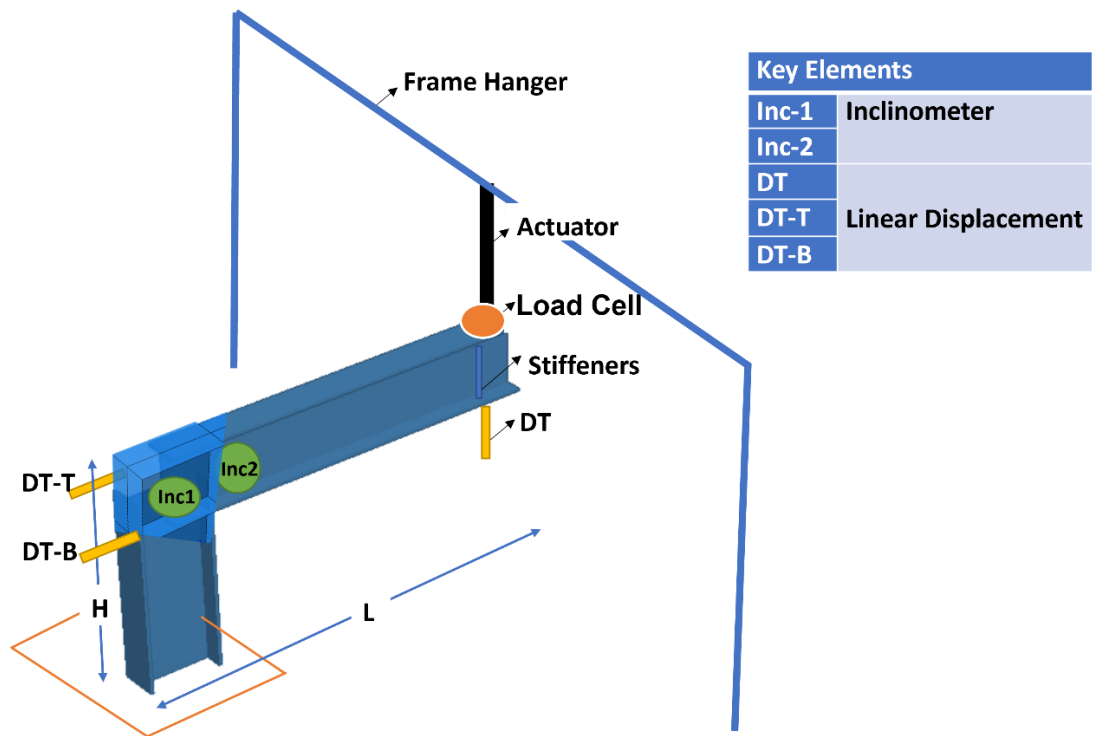
Figure 6-5. 3D schematic of the experimental set-up for testing the beam-to-column joint.

Figure 6-6 shows the beam-to-column joint which was printed at RAMLAB-Netherlands (see Section 3.4), using Autodesk mobile-cabins designed for onsite construction printing.
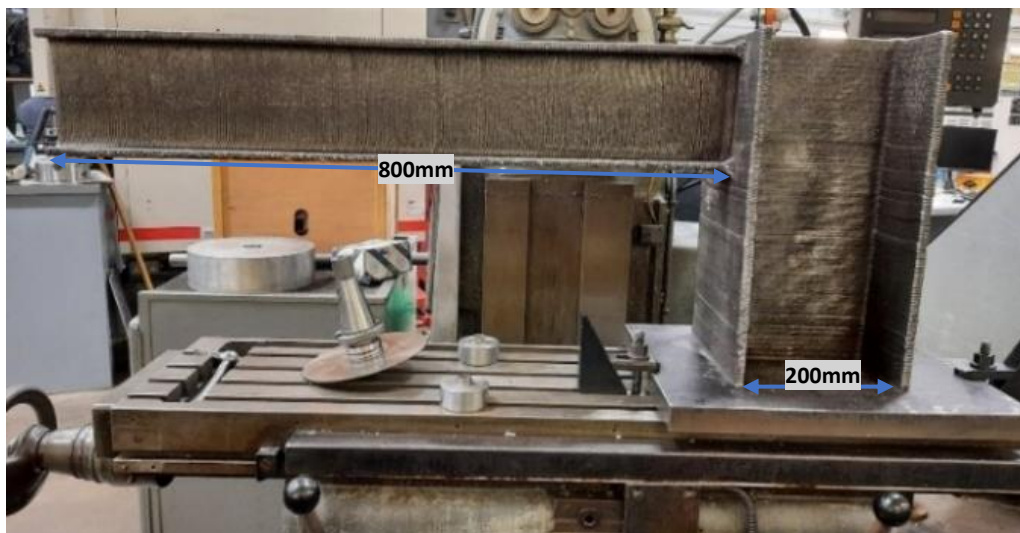
Figure 6-6. WAAM 3D-printed beam-to-column joint.

Abaqus Finite Element Analysis (FEA) was employed to ensure that the applied load during the test, where the beam-to-column joint reached its plastic limit, was below the load actuator capacity. The results from the FEA model demonstrated that the joint would yield within the capacity of the load actuator, and the results are not presented, as there is no other benefit.

As found from Chapter 5, the 3D printed steel is idealised as an elastic-plastic material i.e., it follows Hooke's Law until the yield stress and then deforms plastically under constant stress, as represented by the plots in Section 5.4. The graphs also show a sharp peak at the yield point, after which the strain satisfies the requirements in Eurocode 3.

The beam was designed to fail in bending so additional stiffeners were added to avoid local buckling, following paragraph 6.2.8 considerations in Eurocode 3. The stiffeners were welded in the lab to save time and avoid any complexity in the printing process (see section 6.4.2).

6.4. Experimental set-up

It was decided that before the moment-rotation testing of the WAAM-GMAW printed joint could take place a similar beam-to-column joint test would be used to check the instrumentation and the test methodology. This second beam-to-column specimen was fabricated using standard steel welding and conventional structural steel sections. For convenience this is hereafter referred to as "the conventional joint". The photograph in Figure 6-7 (a) shows this conventional joint when set-up in the loading rig, prior to testing.

Table 6-2 summaries the two joint specimens in terms of their section sizes for the column and beam parts and the method of fabricating the connection between the horizontal beam section and the vertical column section. Shown in Figure 6-7(b) is the WAAM-GMAW joint with the same experimental set-up (before load testing) as for the conventional joint in Figure 6-7(a). Column 1 in the table is for the joint descriptor, with column 2 for the type of steel in the column and beam sections, followed by columns 3 and 4 presenting their section sizes. For the conventional joint the column is an 450mm length of the standard section UKC 203x203x46 and the beam is an 850mm length of the standard section UKB 152x89x16. Column 5 in Table 6-2 shows that for the conventional joint welding, a full penetration butt weld was used to fabricate the connection between the standard steel sections. In accordance with section 4 of EN1993-1-8:2005, KEN-weld steel of a 0.8mm diameter with a feed rate of 5.75m/min was used. For the WAAM-GMAW joint the connection was printed with the beam section and so is of the same steel as the rest of the monolithic component.

(a)   (b)

Figure 6-7. Test set-up before load testing for: (a) Conventional joint; (b) WAAM-GMAW joint.

Table 6-2. Summary of steel and sizes of the two joint specimens.

Joint	Steel	Section for column	Section for beam	Type of connection
1	2	3	4	5
Conventional	S355	UKC 203x203x46	UKB 152x89x16	Welded
WAAM-GMAW	SupraMig Ultra HD-Mild steel solid wire	Web: 178x11 mm Flanges: 200x11 mm	Web: 122x9 mm Flanges: 60x9 mm	Printed, with transition zone (see sub-section 3.4.4.3.1 and Figures 3.28 and 3.29)

A Full moment welding connection was employed to connect the stiffeners to the beam and column of the two components, as presented in Figure 6-8.
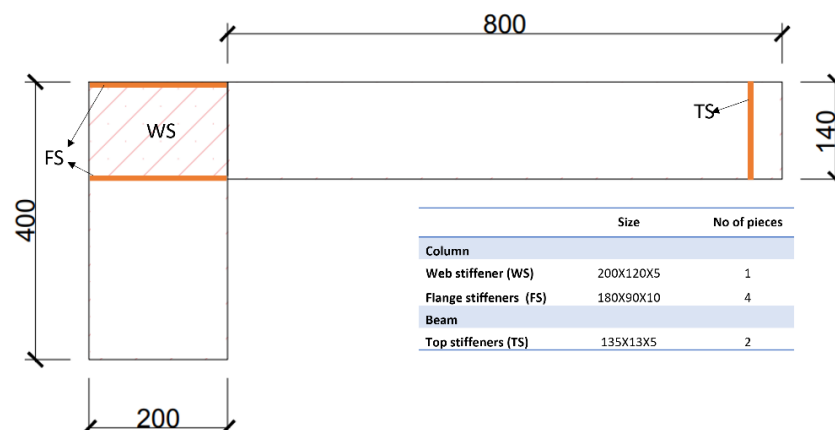
Figure 6-8. A side view for an engineering drawing showing the location of the stiffeners on the WAAM-GMAW joint.

150

The grade of steel used for the beam and the column was S355, whereas S275 was used for the stiffeners. The average characteristics yield strength values obtained from testing the transverse cut-out coupons was 466 N/mm^2 and the average characteristics ultimate strength of the printed material was 560 N/mm^2. The steel grade for the printed joint will be marked as S466. Table 6-3 presents details of the instrumentation used in the experiments, as presented in Figure 6-5. Column 1 in the table is for the type of transducer, with column 2 for the sensor label as seen in Figure 6-9, followed by columns 3 and 4 presenting the type of measurement and the full- scale range of the sensors. Column 5 in Table 6-3 shows the unit used for each sensor.

Table 6-3. Summary of senor instrumentation

Type of transducer	Sensor label	Variable measured	Full scale	Units
1	2	3	4	5
Strain gauges	SG-Top	Strain	10000	Microstrain
	SG-Bottom		10000	
Displacement Transducer	DT	Displacement	101	Mm
	DT-T		50	
	DT-B			
Inclinometer	Inc-1	Angle of rotation	120	Degree
	Inc-2			

Figure 6-9 shows the two inclinometers attached to the joint. INC1 is at the centre of the column section with a top and bottom web stiffener to monitor its verticality by way of rotation INC1. INC2 is positioned on the beam's web, at the same horizontal centreline of the beam section and 10 mm away from the start of the transition zone, to measure the beam rotation. The strain gauges SG1 and SG2 shown in Figure 6-9(a) are position on the top and bottom flanges of the beam and recorded direct strains for the elastic response before development of the plastic hinge in the connection and transitional zones. The ball-joint was used to maintain the verticality of the actuator on the tip of the beam and also to accommodate the expected rotation in the connection, as shown in Figure 6-9(b). Furthermore, an additional external transducer (DT) was attached to the nearest point to the tip of the cantilever beam, as shown in Figure 6-9 (b).
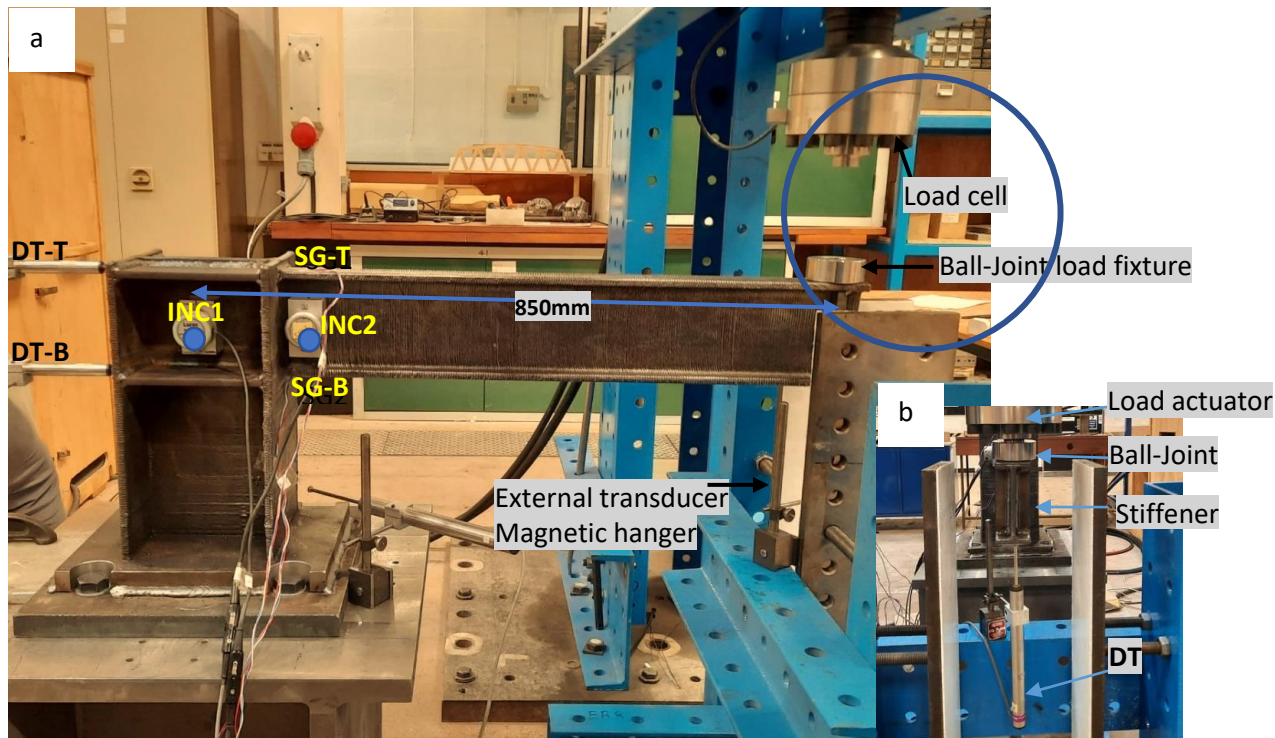
Figure 6-9. (a) Side view of joint before testing; (b) Front view for a ball-joint load transfer fixture and the load actuator.

Preparation for the moment-rotation test required the following steps:

- Designing the testing rig to carry the hydraulic-load actuator.
- Positioning the beam such that the compressive downward load, from the hydraulic jack, was applied close to the tip of the cantilever.
- Calibrating and validating the sensors.
- Attaching the rotation and displacement sensors to record the changes in deformations, the former sensor for rotation and latter sensor for translation displacement
- Attaching the strain gauges to record the strain in sync with the applied load, which can be multiplied by the modulus of elasticity to indicate the stress.
- Creating loading profiles for the sensors and synchronising the readings with the load controller.

6.4.1. Preparation of the test rig

A test rig was designed to safely transfer the loads from the actuator to the strong floor in the laboratory. The test rig is depicted in Figure 6-10(a) shows the main frame constructed of "Meccano" with 4 inch spaced 22 mm diameter holes bolted together using M20 steel

bolts that supports the hydraulic actuator, and which has the two braced frames seen in Figure 6-10(b) to provide out of plane stability to the test rig.

| (a) | (b) |
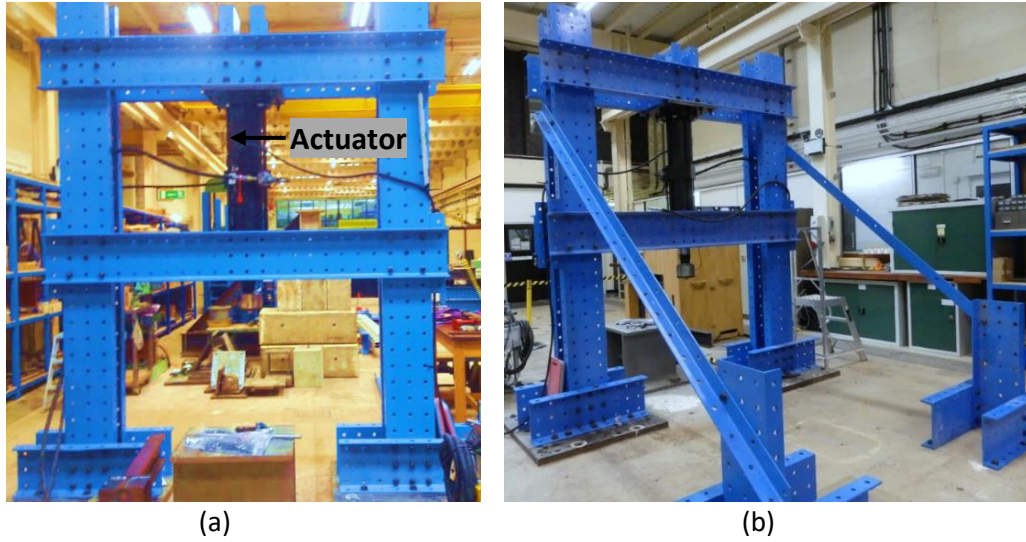
Figure 6-10. (a) Front view of the test rig mainframe; (b) Isometric view of test rig to show bracing.

After setting-up the frame to carry the actuator a steel base block was bolted into the strong floor, as shown in Figure 6-11, along with the dimensions involved. The limited capacity of the strong floor's M20 sockets at 105 kN tensile force required the introduction of an extended baseplate (with a lever arm of 800mm instead of 250mm), also shown in Figure 6-11.
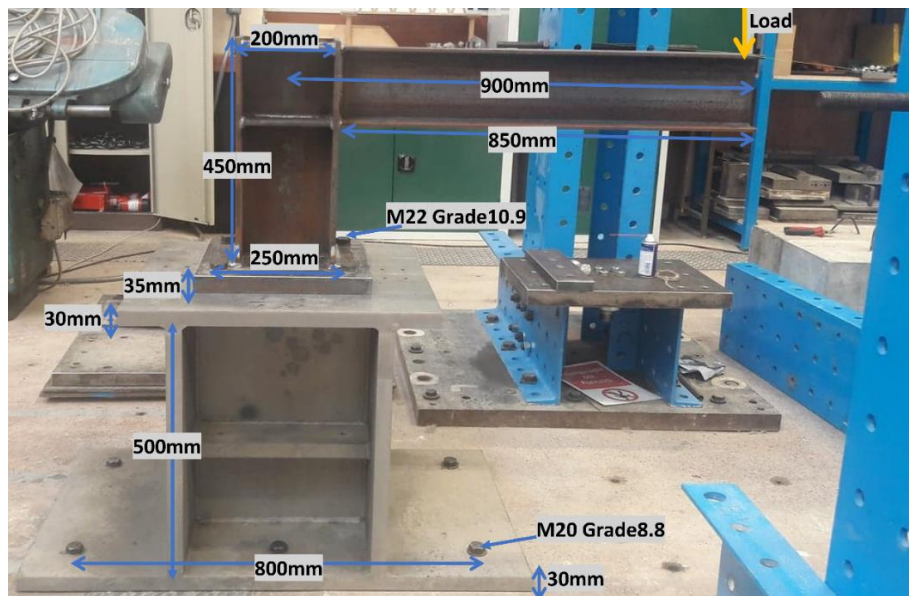
Figure 6-11. With joint specimen in position the base block to provide vertical height and to transfer load actions into the ground floor.

The 800mm lever arm enabled the maximum predicted capacity of 100 kN, to reach the design moment resistance of the joint, to be safely transferred to the floor sockets. According

to the design data for upwards forces (see Appendix 6.1), the maximum designed capacity of the anchoring tensile forces at each socket is 105 kN. Using the relationship of moment is equal to force times length of lever arm, the anchoring force is given by (100 x 900)/800/2 = 56 kN, which does not exceed 105 kN. The lever arm is the distance from the centre of the load to the centre of the column, which was 900mm for the conventional joint, as shown in Figure 6-11, and 850mm for the printed joint, as shown in Figure 6-9. Four M20 steel bolts (grade 8.8) were used to connect the base plate of the base block to the strong floor.

6.4.2. Preparation of the beam-to-column joint

Although the following is for the printed joint, the sensors were first calibrated for the testing of the conventional joint.

The four main steps required to test the printed joint were as follows:

1) Welding the stiffeners

The printed component is of weldable steel, so the steel stiffeners were welded in the workshop in the SoE instead of complicating the printing process. Figure 6-12(a) illustrates the beam-to-column joint and the stiffener plates, before they were welded to the web and the flanges of the component, as presented in Figure 6-8. Figure 6-12(b) shows a section of the column's web between two horizontal stiffeners, all welded together on one side of the column panel, and this was also the case for the other side. The photograph in Figure 6-12(c) is here to indicate the location for web stiffeners towards the tip of the beam. Note that the welding of the stiffeners followed the same weld parameters as used to fabricate the conventional joint.
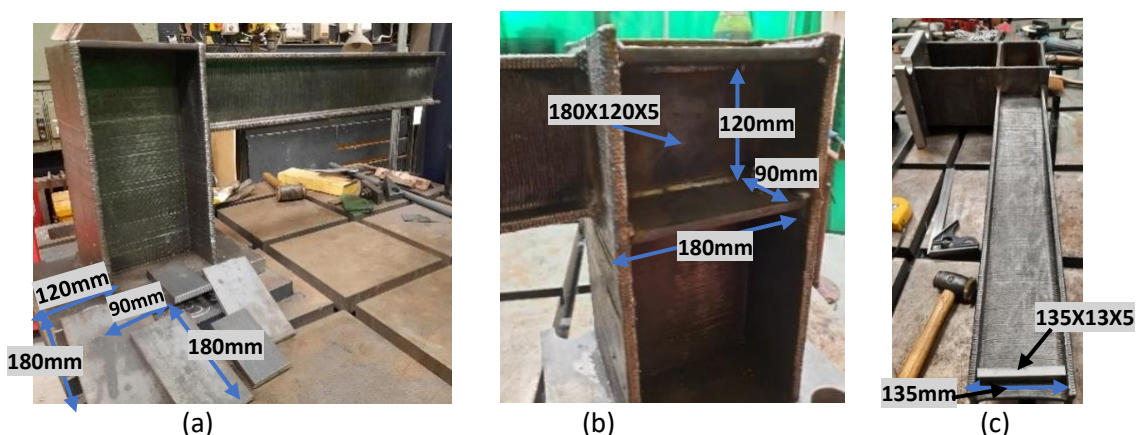
Figure 6-12. (a) Joint with its stiffeners before welding; (b) A 180x90x10 welded stiffeners for the column; (c) a 135x13x5 stiffener to web of beam at location for point end-load, before welding.

2) Drilling four holes in the base plate with the joint, which was originally the base for printing the column section). Figure 6-13 presents details of the preparation of the base plate of size 400x300x30 mm, which was placed on the CNC machine as shown in Figure 6-13(a). Figure 6-13(b) shows with blue marker pen-lines the locations for the drilled holes. Figure 6-13(c) shows the drilled base plate positioned on the designed plate in the testing area, when it was welded in place.

| (a) | (b) | (c) |
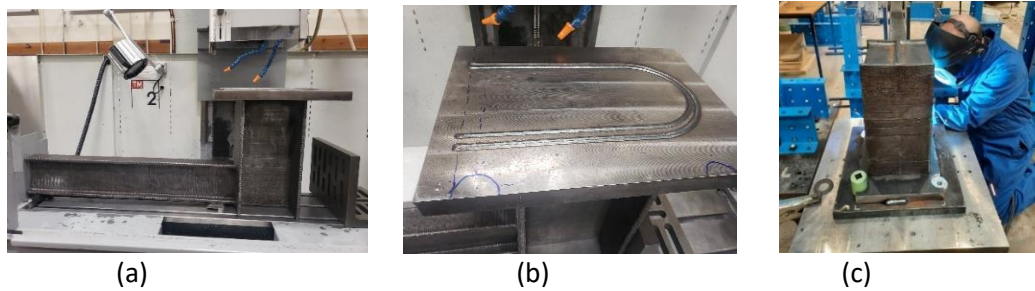
Figure 6-13. (a) Preparation set-up for the joint; (b) Marked holes to be cut-out; (c) Onsite welding after the component was drilled and bolted to the top plate in the base block.

3) Calibration of the sensors

Lucas Accustar electronic inclinometers (serial numbers SIN 1015003 and SIN 43460062) were used to measure the rotational displacement, and LSC Transducers (serial number HS100100/5754, HS50/A and HS50/B) were used to measure the translation displacement. The Linear Displacement Transducers' (LDT) were calibrated by changing their internals setting via the trim factor, using the Cubus software (presented later in section 6.4.3), to match the gauge meter external reading in Figure 6-14 (a). For the LDT sensors, the LDT holder, the gauge meter and the gauge cubes are to be used as shown in Figure 6-14 (a); while the inclinometer was calibrated using an optical measurement tool, as shown in Figure 6-14 (b). Verification of the readings was carried out before the experiments were started,i.e., the readings from the sensors were checked with an external reference before the instruments were glued in position on the printed joint.

| (a) | (b) |
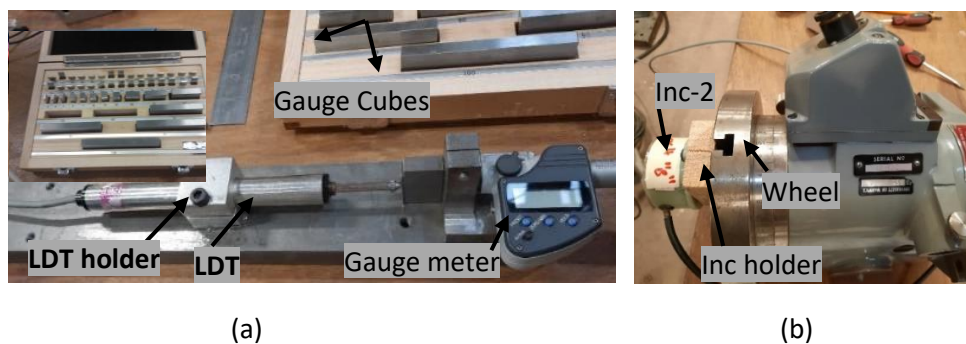
Figure 6-14. Calibration set-up for: (a) LDT; (b) inclinometer

Two ranges of LDTs were used in this experiment: The first LDT, is marked as DT in Figure 6-5 and Figure 6-9, has a gauge length of 100mm, while DT-T and DT-B sensors have a gauge length of 50 mm. The 50 mm LDTs were calibrated in bipolar mode, where the reference point at zero was calibrated to be at 25 mm and full scale for the DT. During the calibration of the LDTs, the measured displacements (on the digital screen of the laptop using the Cubus software) ensured that the length of the gauge cubes matched the gauge meter readings. The outcomes of the calibration process were fitted with a straight line of the form y=mx+c, to investigate whether the sensors were precisely recording the data during the load test.

For the inclinometers, angles of 0°, 10° and 20° were used to calibrate the device. The inclinometer was first fixed vertically to the optical measurement tool at an angle of 0° and then rotated to angles of 10° and 20° respectively. To calibrate the inclinometer, the value of the measured angle on the computer screen had to match the value on the wheel seen adjacent to the inclinometer in Figure 6-14 (b).

4) Attaching the sensors.

As seen in Figure 6-5, two inclinometers were used in this experiment: the first one was attached at the centre of the column while the second one was located at the centreline from the first inclinometer and the closest possible edge to the beam. The distance from the edge of the inclinometer to the end of the transition zone was measured to be 10mm, as shown in Figure 6-15(a).

| (a) | (b) |
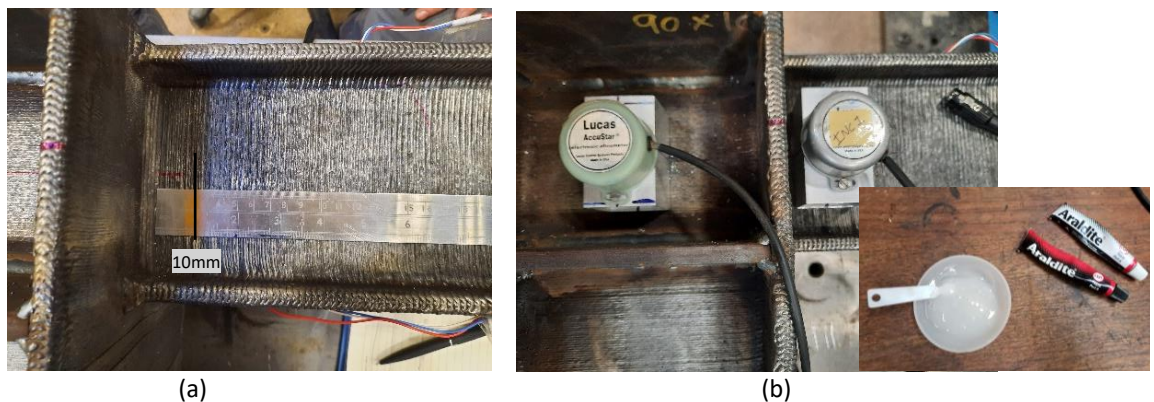
Figure 6-15. (a) Marking the centre of the section for the positioning of the inclinometers; (b) Two inclinometers glued to the beam and column sections using steel adhesives

After preparing the surface of the beam section (see Section 4.1.4.1), YEFLA-2 strain gauges were glued at the centre of the beam and at a distance of 10 mm from the transition region. The positions are shown in Figure 6-16.
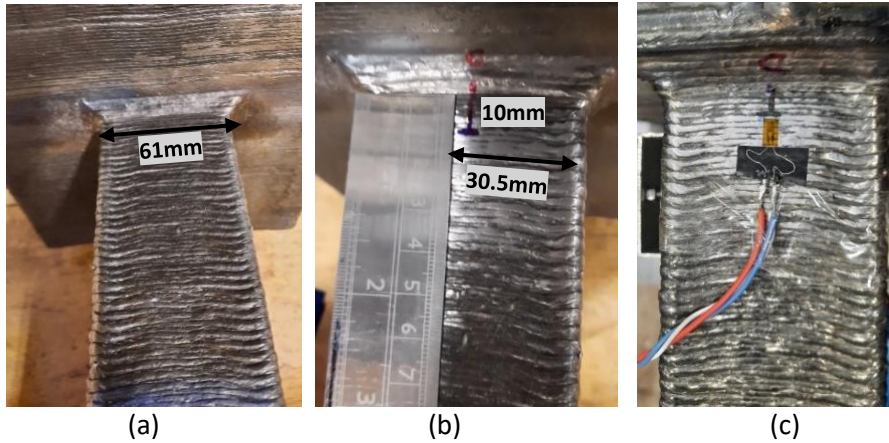
Figure 6-16. Positioning the YEFLA-2 strain gauges on the surface of the flange of the component (a) Measuring the width of the beam; (b) Marking the suggested location of the strain gauge; (c) gluing and wiring the strain gauge

6.4.3. Experimental tools and loading profiles

Figure 6-17(a) shows the overall system and its connections to carry out the experiments. The experimental set-up includes the hydraulic actuator, the specimen, the sensors, the cable connections with the computer and the external hardware boxes (control cubes which synchronise the readings).
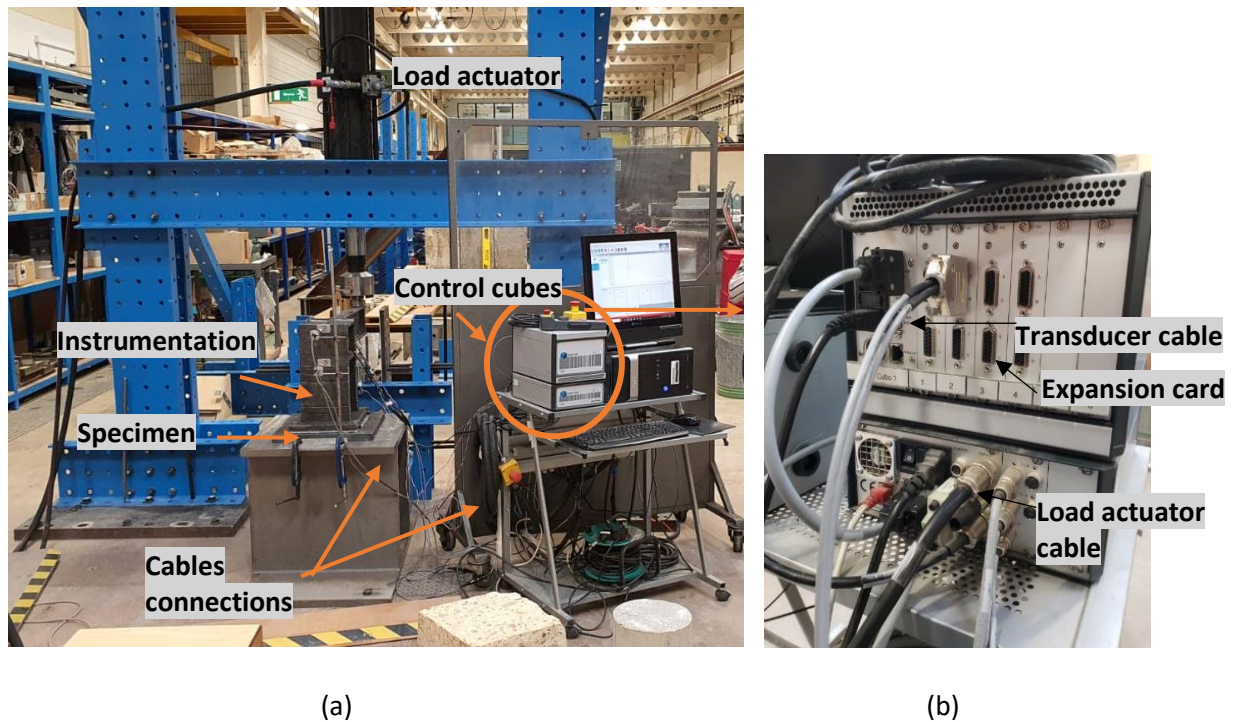
Figure 6-17. (a) Front view of the test-rig and the experimental set-up; (b) Zoomed in view of the control cubes

A CaTS[3] control cube system was used to link the hydraulic load actuator with the different types of transducers (LDTs), inclinometers and strain gauges using two control boxes. The

transducers were connected via signal conditioning circuitry in different expansion cards, as shown in Figure 6-17(b), where the constituents of the control cubes and connections with the load actuator can be seen.

The hydraulic actuator, operating in displacement control mode at a rate of 0.5mm/sec, was used to apply the vertical compressive load at the tip of the cantilever beam. The beam section was designed to ultimately fail with a plastic hinge at the connection with the column under bending, without any elastic or plastic local or lateral-torsional buckling instabilities.

Vertical force and corresponding vertical displacement were recorded by the load cell and a displacement transducer (incorporated within the actuator). The frequency of taking a pair of data points was 1 Hz.

Seven loading profiles were created in sync with the hydraulic load cell so that the change in the readings from the sensors were recorded at the same time as the actuator (see Appendix 6.2). The profiles can be divided into three main categories to measure three different sets of parameters which are for strain, displacement, and inclination angle. The Cubus software was used to configure the different types of transducers, as presented earlier in Table 6-3.

6.5. Moment-Rotation Results and discussion

Following the non-destructive characterisation work reported herein to provide knowledge on the quality of the WAAM-GMAW steel, the joint was characterised for its structural engineering performance by way of a destructive moment–rotation test. Details of the test set-up and test procedure are presented in Section 6.4. The main purpose of testing is to determine the strength and the rotational behaviour of the specimen. Loading under stroke control the displacement at the tip of the beam was increased gradually up to either plastic hinge failure or until the stroke of the actuator reached its limit at 80 mm.

The conventional joint is a UB 152x89x16 section with a web stiffener, and its cross-sectional dimension is the closest to the existing printed sections in the market. The classification for the cross-section of both beam sections is Class 1 in accordance with Table 5.2 in EN 1993-1-1:2004. Based on the nominal measured dimensions the elastic section modulus (W_{el}) as reported in Table 6-4 is 100696 mm^3 and the plastic section modulus (W_{pl}) of the WAAM-GMAW beam section is 1.2 x 10^5 mm^3, whilst the conventional section has elastic and plastic section modulus values of 1.4 x 10^5 mm^3 and 1.6 x 10^5 mm^3, respectively. Table 6-4, also, reports the calculated elastic moment (M_e) and the design plastic moment of resistance of

the two beam sections ($M_{pl, Rd}$). The theoretical calculated plastic moment resistance of the printed beam, with an f_y value of 493Mpa for the calculated mean; 466 Mpa for the characteristic's values, is 57.3 kNm and 60.0kNm repectively, whilst the conventional beam has a plastic moment capacity of 56.6 kNm.

Table 6-4: Theoretical calculation for the moment capacities of the tested joints

Moment (kNm)	UB 152 section S355	Printed section	
		Characteristics S466	Mean
$W_{el}(mm^3)$	1.4 x 10⁵	1.01 x 10⁵	
$W_{pl}(mm^3)$	1.6 x 10⁵	1.2 x 10⁵	
$M_{el, Rd} = W_{el} \times f_y$	50.7	46.9	49.6
$M_{pl,Rd} = W_{pl} \times f_y$	56.6	57.3	60.6

A test run was carried out on the printed beam, which took 2 hours and 30 minutes for the programmed actuator to reach a displacement of 80 mm, at a corresponding vertical load of 86.4 kN (see the black lines in Figure 6-18).
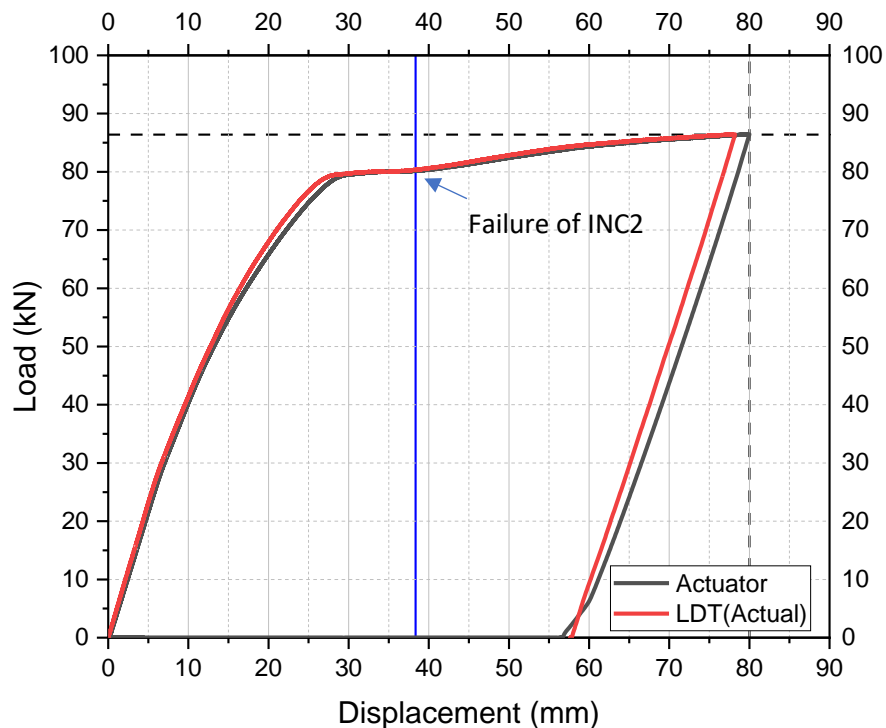
Figure 6-18: Compressive load against vertical displacement from testing WAAM-GMAW joint.

159

Plotted in Figure 6-18, the red curve displays the displacement at distance of 50mm from the tip of the cantilever, recorded by DT see Figure 6-9, where the beam reaches its elastic capacity at a load of 79kN and a displacement of 27mm. The vertical blue line in Figure 6-18 marks when the inclinometer (INC2) fell off at the beam a recorded load of 80kN and a displacement of 38mm.

Figure 6-19 shows the printed joint after the test was stopped and no fracturing of the monolithic steel component could be visually observed. The observed inelastic permanent deformation was a result of exceeding the elastic moment capacity of the cross-section, that is 46.9 kNm. Rotation was only recorded for the first 40 minutes because of failure of the glue connecting inclinometer INC2 to the beam; hence it is missing from the photograph shown in Figure 6-19.

Figure 6-19. Printed beam-to-column joint after its deflection reached 80mm

Figure 6-20 shows the moment-rotation relationship for the conventional joint (of grade S355 steel) and the WAAM-GMAW joint (of characteristics grade S466 and mean grade S493 steel) under monotonic static loading. For the joint deformation in the plane of the beam, the difference between the inner (INC2) and the outer (INC1) inclinometers was used to measure the rotation of the joint. The main response parameters are the rotational stiffness (the moment required to produce a unit rotation in a joint), the moment resistance and the rotational capacity (the angle through which the joint can rotate for a given resistance without failing). Additionally, the strain gauges readings match the predicted behaviour for any given applied load.
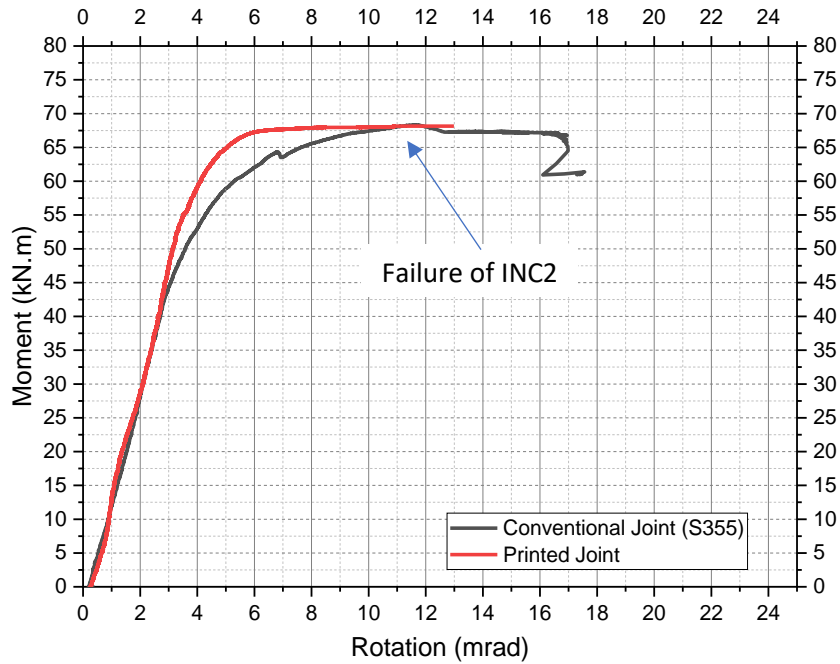
Figure 6-20: Test results for the moment-rotation characteristic curves of the conventional and WAAM-GMAW beam-to-column joints

Figure 6-21 shows the notation for the various variables involved in accordance with EN 1993-1-8:2005.
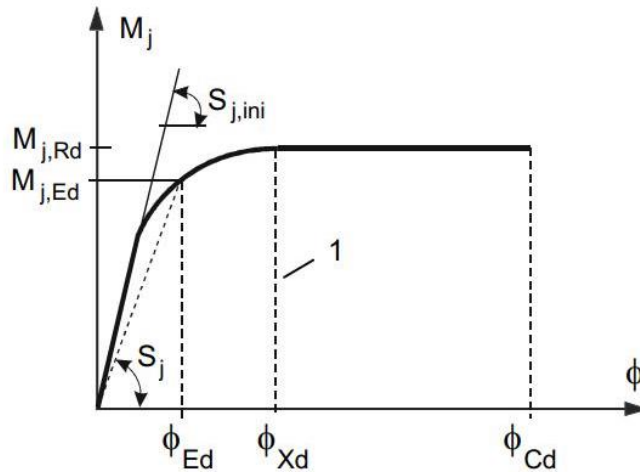
Figure 6-21: Design moment-rotation characteristics (EN1993-1-8, 2005)

Summarised in Table 6-5 are the key test results, with column 1 showing that row 1 of the test results is for the conventional joint and row 2 for welded joint. The initial rotational stiffness of a joint is $S_{j,ini}$, and is reported in column 4. It is determined from the slope of the elastic range of the moment-rotation relationship, $= M_{j,Ed} / \Phi_{j,Ed}$, which are the results in columns 2 and 3). The rotational stiffness, S_j, which is the secant stiffness as indicated in Figure 6-21, listed in column 7, is calculated by dividing the design moment resistance of the

joint, $M_{j,Ed}$ (column 5), by its corresponding rotation of the joint $\Phi_{j,Ed}$ (column 6). Column 8 is the last column in the table, and it records the key parameter of moment of resistance of the joint, $M_{j,Rd}$.

Table 6-5: Summary of moment-rotation test results from joint testing.

Joint	$M_{j,int}$ (kNm)	$\Phi_{j,ini}$ (mrad)	$S_{j,in}$ x10^3 (kNm/rad)	$M_{j,Ed}$ (kN)	$\Phi_{j,Ed}$ (mrad)	S_j x10^3 (kNm/rad)	$M_{j,Rd}$ (kN)
1	2	3	4	5	6	7	8
Conventional (S355)	45.8	2.8	16.1	53	4	13.3	67.6
WAAM-GMAW S466	49.9	2.9	17.1	59.4	4.04	14.7	68.1

Prior to presenting and discussing the moment-rotation test results from the printed joint, its classification, and the type of joint model within a rectilinear framed structure will be presented. Standard BS EN 1993-1-8:2005 for the design of joints lists in Table 5.1 the type of joint model, based on the method of global analysis, which can be either elastic, rigid-plastic or elastic-plastic.

The connection type influences the response of the steelwork structure, which varies due to the distribution of the internal forces, the displacements of the overall structure and the type of failure. In general, the joint should have sufficient strength to transmit the (shear and axial) forces and the moment acting through it, without affecting any other part of the structure. A joint may be classified by their (rotational) stiffness and/or by their strength. The classification by stiffness considers the joint to be either nominally pinned, rigid or semi-rigid. Whereas for the classification by strength the joint is to be either a nominally pinned, full-strength or partial- strength joint.

The characterisation of the welded steel using tensile coupon testing, refer to test results in Table 5-16 in Section 5.5, showed that the steel's ductility requirements satisfied the elastic global analysis to be used in steel structures. 5.1.2 in EN 1993-1-8:2005 provides the elastic global analysis requirements for the design of joints, which are expressed as follows:

– Steel joints should be classified according to their rotational stiffness.
– In the case of a semi-rigid joint, the S_j corresponding to the bending moment $M_{j,Ed}$ should generally be used in the analysis. If $M_{j,Ed}$ does not exceed 2/3$M_{j,Rd}$, $S_{j,ini}$ may be taken in the global analysis of the framed structure.

- For joints connecting H- or I-shaped sections, the value of S_j is calculated using the method illustrated in Figure 6-21.

The main aim of the joint testing programme had been to investigate if the 3D printing strategy had affected the overall behaviour in classifying the type of joint. To proceed with the elastic global analysis, the joint is classified by its stiffness, according to Figure 6-22 from Section 5.2.2.5.(1) of EN 1993-1-8:2005. The joint's design was based on the assumption that the joint would be a rigid, moment-resistant connection. The author will now use the new experimental evidence just reported to check that by 3D printing the joint with new manufacturing technology to check the design approach.

Investigating the rotational response of the printed joint is a key element in this research. By comparing $S_{j,ini}$ with the classification boundaries, the zone into the joint falls can be decided. The classification of the boundaries can be calculated by multiplying the mean modulus of elasticity by the moment of inertia, I, of the cross section by a k factor (referring to the zone), then dividing it by the length of the beam, as presented in Figure 6-22.

Zone 1: rigid, if $S_{j,ini} \geq k_b EI_b / L_b$

where:
$k_b = 8$ for frames where the bracing system reduces the horizontal displacement by at least 80 %
$k_b = 25$ for other frames, provided that in every storey $K_b/K_c \geq 0.1$ [*)]

Zone 2: semi-rigid

All joints in zone 2 should be classified as semi-rigid. Joints in zones 1 or 3 may optionally also be treated as semi-rigid.

Zone 3: nominally pinned, if $S_{j,ini} \leq 0.5 EI_b / L_b$

[*)] For frames where $K_b/K_c < 0.1$ the joints should be classified as semi-rigid.

Key:
K_b is the mean value of I_b/L_b for all the beams at the top of that storey;
K_c is the mean value of I_c/L_c for all the columns in that storey;
I_b is the second moment of area of a beam;
I_c is the second moment of area of a column;
L_b is the span of a beam (centre-to-centre of columns);
L_c is the storey height of a column.

Figure 6-22: Boundaries for the classification of the joints based on their stiffnesses in accordance with 5.2 in EN 1993-1-8:2005.

For the printed beam-to-column joint, the measured mean modulus of elasticity, E, from chapter 5 (see Table 5-16) is 209kN/mm^2; the major-axis second moment of area, I is 7.2 x 10^6 mm^4; and if we assume the beam has a span-to-depth of 20 the span (L_b) is equal to 2800mm for the 140mm depth the I-section. Comparing the joint rotational stiffness with

the measured stiffness in Table 6-5, the joint falls in the rigid zone according to Figure 6-22, as the value of $S_{j,\text{ini}}$, at 16100kNm/rad is greater than the 3010 kNm/rad or 9404kNm/rad whether k_b is equal to 8 or 25, respectively.

The transition zone, which transfers the beam's loading to the column is a key element in addressing the functionality of the joint. It was therefore printed in tapered layers, as highlighted in Section 3.4.4.5. The classification of the joint as 'rigid' can be linked with the X-CT imagining analysis. Table 6-1 reports that beam has a volume fraction of porosity of 0.07% and, even lower, at 0.002% in the transition region. Such a very low (nearly zero) percentage of porosity shows that steel in the transition region and beam responded as designed; that is without porosity.

To enable a rigid-plastic global analysis to be used in the structural design (which does not apply to the WAAM-GAMW steels printed, because they do not satisfy the ductility requirements as discussed in Section 5.4), joints are to possess a sufficient rotational capacity to sustain a plastic hinge. It also has to be classified by its strength to be full-strength. Referring to sections 5.2.3(3) and 6.4.1(3) of EN 1993-1-8:2005, the rotational capacity of the joint does not need to be checked provided that $M_{\text{j,Rd}}$ is at least 1.2 times larger than the $M_{\text{pl,Rd}}$ for the cross section of the connected member. Additionally, the rotation capacity at fracture should exceed 0.0015 radians, to ensure that the paragraph in EN 1993-1-8:2005 is satisfied.

The printed joint can be classified as a full-strength joint (see Section 5.2.3.3 of EN 1993-1-8:2005), because $M_{\text{j,Rd}}$ at 68.1 kNm (refer to Table 6-5) is 1.2 times larger than its $M_{\text{pl,Rd}}$ (57.3 kNm, taken from Table 6-4). This check also satisfies paragraph 6.4.1(3) in EN 1993-1-8:2005 for the joint possessing sufficient rotational capacity.

6.6. Concluding remarks

As the beam-to-column joint is a unique 3D printed structural component, it is essential as part of the PhD work that an understanding of how the chosen printing strategy of the joint affects its overall Moment-Rotation response is gained.

X-CT was used to capture the percentage of porosity and the spatial distribution of the pores in the beam-to-column joint, to learn how the tapered layering strategy at the transition zone impacted the density of the material. A relatively higher density (fromFigure 6-2) and a

low percentage of porosity (from Table 6-1) was found at the transition zone, compared to the column section.

The two mains' limitations in sizing the beam-to-column joint were: the maximum capacity of the load cell (150kN) and the capacity of the tensile forces in each floor socket (105kN for SoE, University of Warwick).

A detailed testing program was described for the preparation of the Moment-Rotation test, summarised as follows:

- Designing the testing rig to carry the hydraulic-load actuator at the tip of the cantilever.
- Welding the stiffeners to the beam-to-column joint, attaching the sensors, and setting up the base plate.
- Calibrating, validating and creating loading profiles for the sensors to synchronise the reading with the load controller.

Investigating the rotational response of the 3D printed beam-to-column joint is key in this research.

The printed material satisfied the ductility requirements for elastic global analysis, so the joint was classified by its stiffness (according to Figure 6-22). By comparing $S_{j,ini}$ with the classification boundaries, the printed beam-to-column joint falls under the 'rigid' zone. The classification of the 'rigid' joint can be linked with the X-CT analysis, which had a very low (or zero) percentage of porosity and showed that the transition zone would fail as designed in pure bending.

7. Conclusions

7.1. Summary of Achievements

The first part of this chapter provides a brief introduction to the research work and a summary of what has been achieved.

Additive Manufacturing (AM) used to print 3D steel components may still be considered as a novel fabrication process method to manufacture components used to construct steel framed building structures. As the literature review to this thesis introduces it has recently become an practical option following research and development work to characterise material properties and structural performance. Presented in this thesis is a contribution in support of this growing evidence of knowledge and understanding for steels printed using Wire Arc Additive Manufacturing (WAAM) with the Gas Metal Arc Welding (GMAW) based process for steel deposition. The justification for using this AM process is that it permits a relatively high rate of weld steel deposition for the manufacture of relatively large monolithic steel components as is required to construct steel framed buildings.

Chapters 3 and 4 present details for the WAAM-GMAW processing of seven components and what destructive and non-destructive test methods were applied to characterise the printed steels. As a reminder, three different WAAM-GMAW processing kits were used, and this is the reason why their printed steels are referred to as 'Autodesk' or 'Steelo' or 'RAMLAB, depending on which company carried out the AM printing.

Following the investigation of mechanical properties in Chapter 5 that confirms specified ductility limits in Eurocode 3 (EN 1993-1-1 and EN 1993-1-14) were satisfied, the WAAM processing was taken to another level by way of printing a monolithic beam-to-column joint weighing 36kg. This structural component was chosen to have thin-walled sections of I-section shape, instead of an optimised geometry for 'form follows forces', because the adopted research approach is to provide a benchmark example and focused on the printing process and printing strategy. The WAAM-GMAW process builds-up a solid structure by laying down welded wire (of 1.2 mm diameter) at a weld temperature that allows the steel to form a solid mass, which inherently can have a degree of porosity. Following a trial of two printing strategies one was chosen to print the beam and column sections, and a transition region with a tapered wall thickness in the beam section was introduced to reinforce the

junction between the I-shaped beam and column sections (of different sizes), where the highest moment (with a shear force) is to be resisted.

The non-destructive test method of X-Ray Computed Tomography (X-CT) was utilised to inspect component or coupon integrity and to identify internal structural features; and this characterization work is for Quality Control. X-CT uses the principles of X-Ray radiography to produce a 3D volume of the interior geometry of a solid object, the resolution depending on the power of the X-CT instrument and the size of the scanned object. As the CT scan data is identified as a voxelized volume, which is a cluster of grey scale voxels that corresponds to the relative densities of features in the internal structure, darker areas in the scan image are for individual pores and the lighter areas are for the solid material that has absorbed more of the X-rays. X-CT test results were used to provide information on the internal structure and to establish volume fraction of porosities. This allowed the research to know what constituents there are in WAAM-GMAW steels (after welding) and enabled there to be a link made between mechanical and structural properties, and the 3D printing process and strategy.

As introduced in the literature review of Chapter 2, AM components can be categorised by either a redesigning or enhancement stage. The plate components that were printed horizontally or vertically belong in the enhancement category. The author notes that the 'Autodesk' horizontally printed plate could be the method for printing in rehabilitation applications, where an additional thickness of steel is needed to increase the local stiffness or resistance. The two 'Steelo' vertically printed plate components could be employed to produce fins attached to main beams (e.g., in a composite floor structural scheme to connect to secondary beams), because by employing an automated welding process it minimises the necessity for a skilled welder. Components consisting of the 'Steelo' rectangular hollow square section, and the 'RAMLAB' two stub column sections and 36 kg beam-to-column joint, are for the redesigning stage in the evolution of AM 3D printing.

Chapter 6 presents the physical testing of the beam-to-column joint to characterise its moment-rotation response. The joint's test results are used to classify the joint by its stiffness in accordance with EN 1993-1-8. The printed steel inside the joint was investigated by X-CT analysis, and the constructed 3D images were examined to build-up a base of understanding for the relationship between porosity, internal fusion, and the layers from employing the chosen printed strategy for the beam and column sections and for the transition region. This

study also investigated how the WAAM-GMAW printing parameters could have affected the overall homogeneity of the joint component.

7.2. Main findings

The section of the chapter is for the main findings from the research, which are presented for each of the chapters in turn.

Literature Review in Chapter 2

The limitations and advantages of different types of metal AM printers have been highlighted. For metals as the printed material, the choice of AM processing is either between a Powder Bed Fusion (PBF) or a Direct Energy Deposition (DED) process. DED was chosen for this PhD work, primarily, because of its capacity to print large-sized components at a higher metal deposition rate. Had the PBF process been chosen, the component size would have been limited by the size of the PBF chamber and the cost would have been higher owing to an inherent processing lower deposition rate and longer times to print the same steel component.

The literature review did expose that there are limitations to using 3D steel components in structural engineering regarding knowing their material properties and having the necessary industry standards and regulations. To transfer the advantages of AM into structural engineering practice it is necessary to build confidence, and to achieve this goal a finding is that research and development work is required to fill in existing gaps in knowledge. The literature review has, therefore, informed the author to develop and carry-out a programme of research that provides new knowledge and understanding to commence a process to address current limitations that are known to hinder exploitation.

WAAM-GMAW component printing in Chapter 3

The main finding from Chapter 3 that, explores the current state-of-the-art in WAAM-GMAW printing, is that printing quality and efficiency is governed by the choice of printing parameters and printing conditions, the latter associated with, e.g.: printing strategy, heat accumulation and dissipation; surface temperature control before the next steel layer is printed. It is observed that the printing process has core stages (e.g., path planning and printing strategy) to be controlled by optimisation of the WAAM-GMAW parameters. From applying three different WAAM-GMAW kits (in the thesis referred to as 'Autodesk', 'Steelo' or 'RAMLAB'), the author has found that the key printing parameters to be controlled in

process optimisation are to achieve: arc stability; homogeneity and continuity of the steel weld bead; spreading of the weld bead (with a width-to-height ratio > 4); cleanliness of the weld.

To print a 2D layer in the horizontal plane there are three types of printing paths, known as linear, contour and hybrid. In this research it has been appropriate to employ the linear path method, and to achieve 'quality' printings with the seven components it was essential to implement the basic principles of multi-pass welding in accordance with the welding standards for steel.

Test methods in Chapter 4

Chapter 4 is for factual information on how the dog bone coupons were prepared from the various WAMM-GMAW steel components. The main conclusion from this chapter is that to provide test results that are reliable and relevant for future comparisons it is necessary to carry-out this preparation using appropriate coupon test standards. In the latter part of the chapter there is an introduction to the non-destructive test method of X-ray Computed Tomography (X-CT). Important information is presented on the preparation requirements (e.g., the tilt angle of the scanned object and defining the scanning parameters) and experimental set-up to effectively run the X-CT scan. The 36 kg beam-to-column joint component was used to clearly demonstrate that the data reduction process of analysing the many individual scan images that create the three-dimensional image is lengthy, and it requires many human manual operations. In this research the Aviso software was used to interrogate the X-CT scans and create 3D images, and to enable the author to establish the volume fraction of porosities within known volumes of the different printed steel components.

Characterization work with steels Chapter 5

By presenting and discussing in this chapter test results for impact, tensile and density mechanical properties, and the X-CT investigations the author was able to compare the mechanical properties of the printed steels with conventional structural steels. By making this comparison with the mechanical properties of structural steels listed in Section 3 Materials of EN 1993-1-1 for mild grades of steel, and, when appropriate, in EN 1993-1-12 for high yield grades of steel, the following has been established:

- The mean modulus of elasticity of the WAAM-GMAW steels satisfied the design requirements set-out in Eurocode 3.

- The stress-strain relationships and characterisation values (such as yield and ultimate strengths and strains) will have variations that are dependent on different weld steels and the level of porosity and other defects in the WAAM-GMAW printed steels.

- Tensile rupture of the printed steel coupons is accompanied with the typical ductile cup-and-cone failure of structural grades of steel.

- The 'Autodesk' printed steel is acceptable as a S355 grade of steel for elastic global analysis only and is a practical steel only for buildings (not for bridges), because the material satisfies the ductility requirements (in BS EN 1993-1-1) of the strength ratio f_u/f_y = 1.15 (subscript 'u' is for ultimate and subscript 'y' is for yield), the elongation at failure > 15%, and strain relationship $\varepsilon_u \geq 15\varepsilon_y$; but the $f_u/f_y < 1.2$ (which does not satisfy plastic analysis).

- The 'Steelo' steel satisfies the ductility requirements of S355 grade of steel for elastic and plastic global analysis for design of buildings or bridges, as the mean of two f_u/f_y ratios is greater than 2; the elongation at failure is larger than 15% and ε_u at 8% is > 15 and, also, 20 times ε_y.

- The 'RAMLAB' steel satisfies the ductility requirements of S460 grade of steel for bridges, buildings and other (highway) structures for elastic global analysis, as the ratio f_u/f_y is higher than 1.1; the elongation at failure is >10% and $\varepsilon_u \geq 15f_y/E$.

Additionally, from the programme of impact testing, the toughness of the WAAM-GMAW steels is found to satisfy the toughness requirement at room temperature given in standard BS EN 1993-1-10.

By using X-CT analyses the following WAAM-GMAW processing lessons were learnt:

- The existence of identifiable interfaces between the five printed layers in the 'Autodesk' horizontal plate shows that the printing parameter of the step-over distance was insufficient for the steel weld beads to properly fuse together.

- There was a processing error when printing the 'Steelo' Wall A and Wall B components owing to having a too high interpass temperature between consecutive weld beads, which was not controlled as it should have been for quality printing.

- By increasing the cooling time for the later printing of the 'Steelo' RHS component it was observed that this processing change was directly reflected by the percentage of

porosity reducing drastically from 4.4% (in Wall A component) to 0.04% (in the RHS component).

- The X-CT analysis for the 'RAMLAB' printed steel (from a stud column component) showed a scattered distribution of pores, with a range varying between 0.5-1%. The presence of porosity was due to a technical problem, which was identified as splattering and vapour condensation on the shielding gas cap of the welding torch. By periodically removing this scrap material there was a significant reduction in printed steel porosity.

When discussing the test results the author made an evaluation by way of linking the volume fraction percentages of porosity to the determined material properties. This had the objective of investigating how localised discontinuities (voiding) may have affected properties, and in particular the strain at rupture. By using this research approach a key overall finding is that the WAAM-GMAW processing creates porosity that is not uniform in both volume fraction and shape. The author recommends that X-CT scanning technologies can be used to provide the necessary quality control linkage between printing an acceptable porosity level and the required mechanical/structural properties of the printed steels. The results for porosities reported in this thesis suggest that porosity volume fractions should not exceed 1% for WAAM-GMAW components in building structures. Note that one reason for this conclusion is that fatigue is not a critical consideration in the design of steel building.

Characterization work with the joint component Chapter 6

By presenting in Chapter 6 the determination of the moment-rotation characteristics for the 'RAMLAB' beam-to-column joint the test results could be used to prove that joint classification is for a 'rigid' joint by using its rotational stiffness in accordance with EN 1993-1-8. Although this was an expected outcome, this important finding demonstrates that this WAAM-GMAW printing had been successful in terms of the objective to manufacture a relatively large monolithic component, that ought to have a joint stiffness classified as rigid. Moreover, this classification of a 'rigid' joint can be linked to the X-CT analysis, which shows there to be a very low (if not zero) percentage of porosity in the transition region that is the potential 'weak link' in the structural performance of the beam-to-column joint.

7.3. Future Work

When this PhD started in January 2018, there was a limited amount of published research into this subject, as highlighted in the literature of this thesis.

Before looking at the possible future applications of this technology, it is worth summarising what progress other groups have made in the last years in pushing this new technology further.

Imperial College London studied a total of 137 coupons that were extracted from steel WAAM printed plates, as reported in their latest publications (Huang et al., 2022). The outcome of the intensive experimental tests showed consistent mechanical properties to the conventionally produced steel plates and satisfied the Eurocode 3 requirements. This outcome support one of the main findings of the thesis.

Similarly, a group from China studied the characteristics of normal and high strength WAAM steel at an ambient and elevated temperature (Fang et al., 2022). The results at ambient temperature also support the thesis findings in showing the component's suitability in meeting the design requirements in the building industry. However, the result at elevated temperatures shows that the mechanical properties meet all the fireproof requirements for high-rise buildings apart from its yield strength. The results at elevated temperature (600∘C for four hours) show the need to change the weld wire composition, as yield strength reaches 347 MPa compared to 700 MPa at ambient temperature.

Ongoing research into the characteristics of WAAM steel in the building industry complement the thesis outcome by showing the WAAM's suitability to fabricate fully dense, or optimised shaped metallic components for building applications.

The findings in this thesis aim to provide a foundational benchmark for the produced material to realise its potential in future steel frames buildings applications. However, many questions remain unanswered for the construction industry, e.g., what wire diameter is most appropriate? What type or types of weld wire can be used (e.g., with the WAAM-GMAW process) in structural engineering applications? What is the required internal composition of the wire? What is the maximum acceptable roughness that won't have an impact on the fatigue tolerance for use in bridge application? And what is the maximum percentage of porosity that won't affect the fatigue tolerance? What is the durability of 3D printed steels material when there are, e.g., exposed to weathering or fire? In structural design what are the required reduction factors to strength properties with increasing nominal thickness (see, e.g., Table 3.1 in EN 1993-1-1:2005)?

The expected benefits from using this technology in construction can be summarised as follows:

- Aesthetics geometries.

- Automated fabrication to minimise health and safety concerns of welders

- Cost saving to bridge maintenance.

- Facilitating access to civil engineering works in remote places.

- Minimising carbon emissions and promoting sustainability.

In the short and medium-term at least, WAAM 3D printing will likely complement rather than replace traditional techniques for fabricating steel structures. Questions to address that require further work are:

- How to make the best use of this innovative manufacturing technology in the short term?
- Is it currently limited to non-key elements in the building industry until its functionality and quality are assured?
- Or could it be a tool for augmenting hot rolled steel beams with 3D printed stiffeners or even end-joint details?
- Or can it be in the armoury methods used in maintenance and repair of existing steel structures?
- How will the quality of printed components be assured; what role might in-process monitoring play?
- Does controlled printing processes help us in assuring the highest quality is achievable, and thereby non-destructive testing, such as by X-CT or ultrasound is no longer necessary for quality control?
- When should the 3D printed surface be ground after printing to reduce roughness and hence the potential for stress concentrations for structures with fatigue loading?
- Will we be witnessing a robot undertaking 3D printing for maintenance and repair of steel bridge?

Plangger et *al.* (Plangger et al., 2019) present results for the mechanical characteristics of an optimised steel component, see Figure 7-1, which was printed directly onto a sub-assembly application for a crane. This project shows the feasibility of taking WAAM technology on-site to carry out in-situ bridge maintenance and repairs, thereby avoiding additional costs, such as from the impact of closing roads or railway lines.

Figure 7-1: Printed element onsite (Plangger et al., 2019)

Are WAAM technologies the way forward to manufactured optimised aesthetic elements? As an illustrative example there is the 6 m (length) by 3.6m (wide) by 2.7 m (height) curved roof structure for the Cucuyo Bar shown in Figure 7-2. This large outdoor steel component was printed by MX3D in The Netherlands, and the bar will be opened in September 2022 (MX3D, 2022a)? Two other examples are shown in 7-3. In Figure 7-3 (a) we see the optimised connection for joining timber elements that is printed by MX3D for TAKENAKA (MX3D, 2022b). The photograph in Figure 7-3 (b) is for the top section a stainless steel diagrid column for the research and development project by Laghi et *al.* (Laghi et al., 2021)) (Laghi et al., 2020).
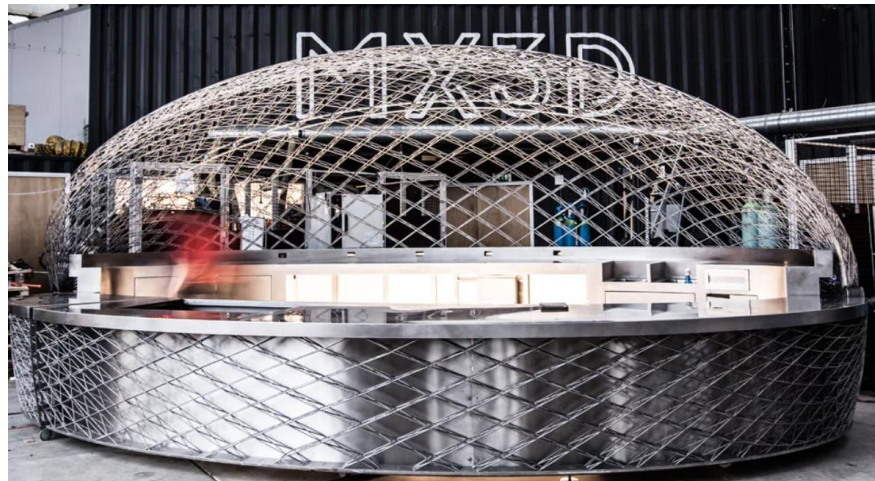
Figure 7-2: 3D printed roof by MX3D
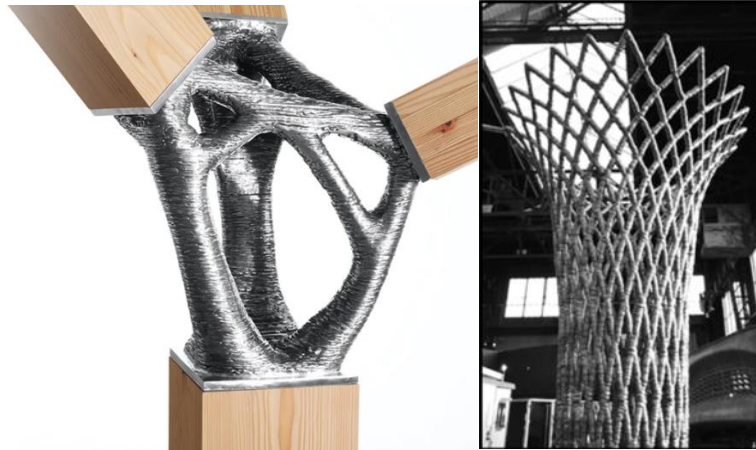
Figure 7-3: (a) Optimised printed connection (MX3D, 2022a); (b) Diagrid column (Laghi et al., 2020)

The main findings presented in this Chapter correspond to the overall vision of international researchers (Kanyilmaz et al., 2021), who are exploring the development of metal 3D printing by increasing its quality and its potential impact on resource efficiency. It is being established be researchers that WAAM can provide the benefits of aesthetics, less metal mass per component and/or structure and with less material waste, which inherently and positively lowers the amount of energy used and reduces carbon emissions to meet the climate emergency call.

8. References

ADDITIVE MANUFACTURING RESEARCH GROUP. *About Additive Manufacturing* [Online]. Loughborough univeristy. Available: http://www.lboro.ac.uk/research/amrg/about/the7categoriesofadditivemanufacturing/directedenergydeposition/ [Accessed 21/04 2018].

APISCOR. 2016. Available: https://www.apis-cor.com/ [Accessed 2021].

ASHLEY, S. 1991. Rapid Prototyping Systems. *Mechanical Engineering,* 113**,** 34.

ASHRAF, M., GIBSON, I. & RASHED, M. G. 2018. *CHALLENGES AND PROSPECTS OF 3D PRINTING IN STRUCTURAL ENGINEERING*.

ASTM, I. L. 2013. Standard Terminology for Additive Manufacturing Technologies. *F2792 – 12a.*

ATKEARNEY 2015. 3D Printing: A Manufacturing Revolution.

AUGUR, H. 2016. *3D Printed Office Building Unveiled in Dubai* [Online]. Creative Commons Attribution 4.0 International License. Available: https://all3dp.com/3d-printed-office-building/ [Accessed 3/5 2018].

BADDOO, N. R. 1996. *Castings in construction*, Steel Construction Institute.

BERMAN, B. 2012. 3-D printing: The new industrial revolution. *Business Horizons,* 55**,** 155-162.

BHAVAR ET AL. 2014. A Review on Powder Bed Fusion Technology of Metal Additive Manufacturing. *4th International conference and exhibition on Additive Manufacturing Technologies-AM-2014.* Bangalore, India.

BHAVAR, V., KATTIRE, P., PATIL, V., KHOT, S., GUJAR, K. & SINGH, R. 2017. A review on powder bed fusion technology of metal additive manufacturing. *Additive Manufacturing Handbook.* CRC Press.

BONESSIO, N., LOMIENTO, G. & VALDEVIT, L. 2017. *Cellular periodic material design for enhanced seismic protection of low-rise buildings*.

BOS, F., WOLFS, R., AHMED, Z. & SALET, T. 2016. Additive manufacturing of concrete in construction: potentials and challenges of 3D concrete printing. *Virtual and Physical Prototyping,* 11**,** 209-225.

BS 2007. Eurocode 3 — Design of steel structures —. *Part 1-12: Additional rules for the extension of EN 1993 up to steel grades S 700.*

BS/EN1991-1-1:2002 Eurocode 1: Actions on structures. *Part 1-1: General actions — Densities, self-weight, imposed loads for buildings.* Brussels.

BS/EN-ISO6892-1:2019 Metallic Materials-tensile Testing, Part 1: Method of Test at Room Temperature

Geneva, Switzerland: International Organization for Standardization.

BSI 2005. Design of steel structures, part 1-1 General rules and rules for buildings. London: British Standard Institute.

BSI 2005 BS EN 1993-1-1:2005 Design of Steel Structures Part 1-1 General Rules and Rules for Buildings. London.

BUCHANAN, C., MATILAINEN, V.-P., SALMINEN, A. & GARDNER, L. 2017. Structural performance of additive manufactured metallic material and cross-sections. *Journal of Constructional Steel Research,* 136**,** 35-48.

BUSWELL, R. A., DE SILVA, W. L., JONES, S. Z. & DIRRENBERGER, J. 2018. 3D printing using concrete extrusion: A roadmap for research. *Cement and Concrete Research,* 112**,** 37-49.

CAMACHO, D. D., CLAYTON, P., O'BRIEN, W., FERRON, R., JUENGER, M., SALAMONE, S. & SEEPERSAD, C. Applications of Additive Manufacturing in the Construction Industry

– A Prospective Review. 2017 2017 Vilnius. Vilnius Gediminas Technical University, Department of Construction Economics & Property, 1-8.

CAMACHO, D. D., CLAYTON, P., O'BRIEN, W. J., SEEPERSAD, C., JUENGER, M., FERRON, R. & SALAMONE, S. 2018. Applications of additive manufacturing in the construction industry–A forward-looking review. *Automation in construction,* 89**,** 110-119.

CANADA RESEARCH CENTER. 2017. *3D Printing infiltrating in which Industry Sectors?* [Online]. ING, Bloomberg. Available: https://canadaresearchcentre.ca/2017/11/11/3d-printing-infiltrating-in-which-industry-sectors/ [Accessed 09/04 2018].

CANESSA, E., FONDA, C., ZENNARO, M. & DEADLINE, N. 2013. Low-cost 3D printing for science, education and sustainable development. *Low-Cost 3D Printing,* 11.

CHAKRABORTY, D., REDDY, B. A. & CHOUDHURY, A. R. 2008. Extruder path generation for curved layer fused deposition modeling. *Computer-Aided Design,* 40**,** 235-243.

CONSTRUCTION. 2013. *Skanska claims first with 3D printed cladding* [Online]. Available: https://constructionmanagermagazine.com/skanska-claims-industry-first-3d-printed-cladding/ [Accessed].

CONSTRUCTIONMARKET. 2021. *Construction Market By Type (Building Construction, Heavy and Civil Engineering Construction, Specialty Trade Contractors, Land Planning and Development), By Building (Residential Building, Non-Residential Building), By Construction Machinery, By End-Use, and By Region Forecast to 2028* [Online].

: Emergen Research. Available: https://www.emergenresearch.com/industry-report/construction-market [Accessed 2022].

COPLEY, D. C., EBERHARD, J. W. & MOHR, G. A. 1994. Computed tomography part I: Introduction and industrial applications. *JOM,* 46**,** 14-26.

CROWLEY, A. 1998. Construction as a manufacturing process: Lessons from the automotive industry. *Computers & Structures,* 67**,** 389-400.

CYBE. 2014. *CyBE Construction* [Online]. Available: https://cybe.eu/service/design-engineering/ [Accessed 29/12 2019].

D-SHAPE. *D-Shape Enterprises L.L.C.-Global Mega-Scale Additive Manufacturing* [Online]. Available: https://dshape.wordpress.com/applications/applications-construction/ [Accessed 29/12/2019].

DECKARD, C. R. 1989. Method and apparatus for producing parts by selective sintering. Google Patents.

DING, D., PAN, Z., CUIURI, D. & LI, H. 2015a. A multi-bead overlapping model for robotic wire and arc additive manufacturing (WAAM). *Robotics and Computer-Integrated Manufacturing,* 31**,** 101-110.

DING, D., PAN, Z., CUIURI, D. & LI, H. 2015b. A practical path planning methodology for wire and arc additive manufacturing of thin-walled structures. *Robotics and Computer-Integrated Manufacturing,* 34**,** 8-19.

DING, D., PAN, Z., CUIURI, D., LI, H. & LARKIN, N. 2016a. Adaptive path planning for wire-feed additive manufacturing using medial axis transformation. *Journal of Cleaner Production,* 133**,** 942-952.

DING, D., PAN, Z., VAN DUIN, S., LI, H. & SHEN, C. 2016b. Fabricating superior NiAl bronze components through wire arc additive manufacturing. *Materials,* 9**,** 652.

DING, D., PAN, Z. S., CUIURI, D. & LI, H. 2014. A tool-path generation strategy for wire and arc additive manufacturing. *The international journal of advanced manufacturing technology,* 73**,** 173-183.

DUDA, T. & RAGHAVAN, L. V. 2016. 3D Metal Printing Technology. *IFAC-PapersOnLine,* 49**,** 103-110.

DUNLAVEY, M. R. 1983. Efficient polygon-filling algorithms for raster displays. *ACM Transactions on Graphics (Tog),* 2**,** 264-273.

DUTCHREVIEW. 2021. *World's first 3D-printed bridge made entirely of steel is opened in Amsterdam* [Online]. Available: https://dutchreview.com/news/worlds-first-3d-printed-bridge-amsterdam/ [Accessed].

DWIVEDI, R. & KOVACEVIC, R. 2004. Automated torch path planning using polygon subdivision for solid freeform fabrication based on welding. *Journal of Manufacturing Systems,* 23**,** 278-291.

EN1993-1-1:2005 Eurocode 3: Design of Steel Structures. *Part 1-1: General rules and rules for buildings* Brussels.

EN1993-1-8 2005. 1-8: 2005. Eurocode 3: design of steel structures–Part 1–8: design of joints. *British Standards Institution, United Kingdom.*

EN1993-1-12:2007 Part 1-12: Additional rules for the extension of EN 1993 up to steel grades S 700 . Brussels: The European Standard-British Standard.

EN10025-1 2004. Hot rolled products of structural steels —. *Part 1: General technical delivery conditions.*

EN10088-1 2014. Stainless Steels.

EN/ISO148-1:2016 2016. Metallic materials - Charpy pendulum impact test - Part 1: Test method (ISO 148-1:2016)

EUDIER, M. 1962. The mechanical properties of sintered low-alloy steels. *Powder Metallurgy,* 5**,** 278-290.

FANG, Q., ZHAO, L., CHEN, C.-X., CAO, Y., SONG, L., PENG, Y. & YIN, F.-X. 2022. 800 MPa Class HSLA Steel Block Part Fabricated by WAAM for Building Applications: Tensile Properties at Ambient and Elevated (600° C) Temperature. *Advances in Materials Science and Engineering,* 2022.

FAROUKI, R., KOENIG, T., TARABANIS, K., KOREIN, J. & BATCHELDER, J. 1995. Path planning with offset curves for layered fabrication processes. *Journal of Manufacturing Systems,* 14**,** 355-368.

FELDKAMP, L. A., DAVIS, L. C. & KRESS, J. W. 1984. Practical cone-beam algorithm. *Josa a,* 1**,** 612-619.

FENG, L. & YUHONG, L. 2014. Study on the Status Quo and Problems of 3D Printed Buildings in China. *Global Journal of Human-Social Science Research*.

FERNANDES, P., ALMEIDA, N. M. & BAPTISTA, J. R. 2021. The Concrete at the 4th Industrial Revolution. *Sustainability and Automation in Smart Constructions.* Springer.

GALJAARD, S., HOFMAN, S., PERRY, N. & REN, S. 2015. *Optimizing Structural Building Elements in Metal by using Additive Manufacturing*.

GAO, W., ZHANG, Y., RAMANUJAN, D., RAMANI, K., CHEN, Y., WILLIAMS, C. B., WANG, C. C. L., SHIN, Y. C., ZHANG, S. & ZAVATTIERI, P. D. 2015. The status, challenges, and future of additive manufacturing in engineering. *Computer-Aided Design,* 69**,** 65-89.

GARDNER, L., KYVELOU, P., HERBERT, G. & BUCHANAN, C. 2020. Testing and initial verification of the world's first metal 3D printed bridge. *Journal of constructional steel research,* 172**,** 106233.

GIBSON, I., KVAN, T. & WAI MING, L. 2002. Rapid prototyping for architectural models. *Rapid prototyping journal,* 8**,** 91-95.

GOSSELIN, C., DUBALLET, R., ROUX, P., GAUDILLIÈRE, N., DIRRENBERGER, J. & MOREL, P. 2016. Large-scale 3D printing of ultra-high performance concrete–a new processing route for architects and builders. *Materials & Design,* 100**,** 102-109.

GUELL IZARD, A., FABIAN ALFONSO, R., MCKNIGHT, G. & VALDEVIT, L. 2017. Optimal design of a cellular material encompassing negative stiffness elements for unique combinations of stiffness and elastic hysteresis. *Materials & Design,* 135**,** 37-50.

HARDIN, R. & BECKERMANN, C. 2013. Effect of porosity on deformation, damage, and fracture of cast steel. *Metallurgical and Materials Transactions A,* 44**,** 5316-5332.

HARDIN, R. A. & BECKERMANN, C. 2007. Effect of porosity on the stiffness of cast steel. *Metallurgical and Materials Transactions A,* 38**,** 2992-3006.

HE, P., DU, W., WANG, L., KIRAN, R. & YANG, M. 2020. Additive Manufacturing and Mechanical Performance of Trifurcated Steel Joints for Architecturally Exposed Steel Structures. *Materials,* 13**,** 1901.

HOPKINSON, N., HAGUE, R. & DICKENS, P. 2006. Rapid manufacturing. *An Industrial Revolution for the Digital Age. Chichister, England: John Wiley and Sons, Ltd*.

HUANG, C., KYVELOU, P., ZHANG, R., BRITTON, T. B. & GARDNER, L. 2022. Mechanical testing and microstructural analysis of wire arc additively manufactured steels. *Materials & Design***,** 110544.

HULL, C. E. 1986. *Apparatus For Production of Three-Dimensional Objects By Stereolithography* 638,905.

ING REPORT 2017. 3D printing: a threat to global trade, Locally printed goods could cut trade by 40%. Economic and Financial Analysis, ING,.

IOWA_S_U. *Toughness* [Online]. IOWA STATE UNIVERSITY: Center for Nondestructive Evaluation. Available: https://www.nde-ed.org/Physics/Materials/Mechanical/Toughness.xhtml [Accessed 16/03 2021].

ISO377 2013. Steel and steel products. *Location and preparation of samples and test pieces for mechanical testing.*

ISO14341 2010. Welding consumables-Wire electrodes and weld deposits for gas shielded metal arc welding of non alloy and fine grain steels-Classification. *4.2 Symbol for strength and elongation of all-weld metal* CEN-European Committee For Standardization.

ISO-14175 2008. Welding consumables – Gases and gas mixtures for fusion welding and allied processes. *BS EN ISO 14175:2008.* London: British Standards Institution.

ISO/ASTM 52900-15 2015. Standard Terminology for Additive Manufacturing-General Principles-Terminology

JEZARD, A. 2018. *One-quarter of Dubai's buildings will be 3D printed by 2025* [Online]. World Economics Forum articles. Available: https://www.weforum.org/agenda/2018/05/25-of-dubai-s-buildings-will-be-3d-printed-by-2025/ [Accessed].

KANARIS, S. 2018. *3D printed offshore crane hook passes test* [Online]. Available: http://www.cranestodaymagazine.com/news/3d-printed-offshore-crane-hook-passes-test-6027847/ [Accessed 21/4 2018].

KANYILMAZ, A., DEMIR, A. G., CHIERICI, M., BERTO, F., GARDNER, L., KANDUKURI, S. Y., KASSABIAN, P., KINOSHITA, T., LAURENTI, A. & PAOLETTI, I. 2021. Role of Metal 3D Printing to Increase Quality and Resource-efficiency in the Construction Sector. *Additive Manufacturing***,** 102541.

KARABEGOVIĆ, I. 2018. THE ROLE OF INDUSTRIAL AND SERVICE ROBOTS IN THE 4th INDUSTRIAL REVOLUTION–" INDUSTRY 4.0". *Acta Technica Corviniensis-Bulletin of Engineering,* 11**,** 11-16.

KEATING, S. 2014. Beyond 3D Printing: The New Dimensions of Additive Fabrication. *Designing for Emerging Technologies: UX for Genomics, Robotics, and the Internet of Things (379-405). O'Reilly Media*.

KHOSHNEVIS, B. & DUTTON, R. J. M. T. 1998. Innovative rapid prototyping process makes large sized, smooth surfaced complex shapes in a wide variety of materials. 13**,** 53-56.

KIETZMANN, J., PITT, L. & BERTHON, P. 2015. Disruptions, decisions, and destinations: Enter the age of 3-D printing and additive manufacturing. *Business Horizons,* 58**,** 209-215.

KOSLOW, T. 2017. *3D Printed House – World's 35 Greatest 3D Printed Structures* [Online]. All3DP. Available: https://all3dp.com/1/3d-printed-house-homes-buildings-3d-printing-construction/ [Accessed 18/02 2018].

KRUTH, J., VANDENBROUCKE, B., VAN VAERENBERGH, J. & MERCELIS, P. 2005. Benchmarking of different SLS/SLM processes as rapid manufacturing techniques. *Laser,* 1**,** 3D.

KRUTH, J. P., BARTSCHER, M., CARMIGNATO, S., SCHMITT, R., DE CHIFFRE, L. & WECKENMANN, A. 2011. Computed tomography for dimensional metrology. *CIRP Annals,* 60**,** 821-842.

LAGHI, V., PALERMO, M., GASPARINI, G. & TROMBETTI, T. 2020. Computational design and manufacturing of a half-scaled 3D-printed stainless steel diagrid column. *Additive Manufacturing,* 36**,** 101505.

LAGHI, V., PALERMO, M., SILVESTRI, S., GASPARINI, G. & TROMBETTI, T. 2021. Experimental behaviour of Wire-and-Arc Additively Manufactured stainless steel rods. *ce/papers,* 4**,** 2387-2392.

LIM, S., BUSWELL, R. A., LE, T. T., AUSTIN, S. A., GIBB, A. G. & THORPE, T. J. A. I. C. 2012. Developments in construction-scale additive manufacturing processes. 21**,** 262-268.

LOPEZ, A., BACELAR, R., PIRES, I., SANTOS, T. G., SOUSA, J. P. & QUINTINO, L. 2018. Non-destructive testing application of radiography and ultrasound for wire and arc additive manufacturing. *Additive Manufacturing,* 21**,** 298-306.

MACRAE, M. 2016. *The 3D Printed Office of the Future* [Online]. ASME. org. Available: https://www.asme.org/engineering-topics/articles/manufacturing-design/3d-printed-office-the-future [Accessed 03/05 2018].

MARKETSANDMARKETS. 2019. *3D Printing Market by Offering (Printer, Material, Software, Service), Process (Binder Jetting, Direct Energy Deposition, Material Extrusion, Material Jetting, Powder Bed Fusion), Application, Vertical, Technology, and Geography - Global Forecast to 2024* [Online]. Available: https://www.marketsandmarkets.com/Market-Reports/3d-printing-market-1276.html [Accessed].

MARTINA, F., DING, J., WILLIAMS, S., CABALLERO, A., PARDAL, G. & QUINTINO, L. 2019. Tandem metal inert gas process for high productivity wire arc additive manufacturing in stainless steel. *Additive Manufacturing,* 25**,** 545-550.

MICHAEL MOLITCH-HOU. 2017. *7 Issues to Look Out for in Metal 3D Printing* [Online]. Available:
https://www.engineering.com/3DPrinting/3DPrintingArticles/ArticleID/15202/7-Issues-to-Look-Out-for-in-Metal-3D-Printing.aspx [Accessed 06/03 2018].

MOAVENZADEH, J. The 4th industrial revolution: Reshaping the future of production. World Economic Forum, 2015.

MOLITCH-HOU, M. 2015. *BETABRAM SET TO 3D PRINT TWO-STORY HOUSE THIS SUMMER* [Online]. Available: https://3dprintingindustry.com/news/betabram-set-to-3d-print-two-story-house-this-summer-50826/ [Accessed 29/12/2019].

MRAZOVIĆ, N., BAUMERS, M., HAGUE, R. & FISCHER, M. 2018. Guiding building professionals in selecting additive manufacturing technologies to produce building components. *Materials Today Communications,* 15**,** 199-202.

MUELLER, C. T. 2016. 3D Printed Structures: Challenges and Opportunities. *STRUCTURE,* 54.

MX3D. 2022a. *Cucuyo Bar* [Online]. Available: https://mx3d.com/industries/design/cucuyo/ [Accessed].

MX3D. 2022b. *WAAM for Architecture & Constrcution* [Online]. Available: https://mx3d.com/industries/architecture-construction/ [Accessed 2022].

NELSON, J. C., XUE, S., BARLOW, J. W., BEAMAN, J. J., MARCUS, H. L. & BOURELL, D. L. 1993. Model of the selective laser sintering of bisphenol-A polycarbonate. *Industrial & Engineering Chemistry Research,* 32**,** 2305-2317.

PAN, Z., DING, D., WU, B., CUIURI, D., LI, H. & NORRISH, J. 2018. Arc welding processes for additive manufacturing: a review. *Transactions on intelligent welding manufacturing***,** 3-24.

PEGNA, J. 1997. Exploratory investigation of solid freeform construction. *Automation in construction,* 5**,** 427-437.

PLANGGER, J., SCHABHÜTTL, P., VUHERER, T. & ENZINGER, N. 2019. CMT additive manufacturing of a high strength steel alloy for application in crane construction. *Metals,* 9**,** 650.

RAJAN, V., SRINIVASAN, V. & TARABANIS, K. A. 2001. The optimal zigzag direction for filling a two-dimensional region. *Rapid Prototyping Journal*.

RAMADANY, M. & BAJJOU, M. S. 2021. Applicability and integration of concrete additive manufacturing in construction industry: A case study. *Proceedings of the Institution of Mechanical Engineers, Part B: Journal of Engineering Manufacture,* 0**,** 0954405420986102.

RAMAKRISHNAN, R., GRIEBEL, B., VOLK, W., GÜNTHER, D. & GÜNTHER, J. 3D printing of inorganic sand moulds for casting applications. Advanced Materials Research, 2014. Trans Tech Publ, 441-449.

ROYLANCE, D. 2001. Stress-strain curves. *Massachusetts Institute of Technology study, Cambridge*.

RYDER, G., ION, B., GREEN, G., HARRISON, D. & WOOD, B. 2002. Rapid design and manufacture tools in architecture. *Automation in construction,* 11**,** 279-290.

SABOURIN, E., HOUSER, S. A. & BØHN, J. H. 1996. Adaptive slicing using stepwise uniform refinement. *Rapid prototyping journal*.

SAKIN, M. & KIROGLU, Y. C. 2017. 3D Printing of Buildings: Construction of the Sustainable Houses of the Future by BIM. *Energy Procedia,* 134**,** 702-711.

SCOTT, C. 2018. *Autodesk Introduces Mobile Additive Manufacturing Toolbox To 3D Print On Location* [Online]. Available: https://3dprint.com/231758/autodesk-introduce-mobile-am-toolbox/ [Accessed 2021].

SEIFI, M., SALEM, A., BEUTH, J., HARRYSSON, O. & LEWANDOWSKI, J. J. 2016. Overview of Materials Qualification Needs for Metal Additive Manufacturing. *JOM,* 68**,** 747-764.

SKILTON, M. & HOVSEPIAN, F. 2018. *The 4th industrial revolution*, Springer.

SMARTECH. 2018. *SmarTech Report Predicts Construction Industry Set to Massively Adopt 3D Printing Technologies, Generating $40 Billion in Revenues by 2027* [Online]. SmarTech Markets Publishing. Available: http://www.globenewswire.com/news-release/2018/01/18/1296555/0/en/SmarTech-Report-Predicts-Construction-Industry-Set-to-Massively-Adopt-3D-Printing-Technologies-Generating-40-Billion-in-Revenues-by-2027.html [Accessed 02/03/2021].

STAMPLER, L. 2015. *A Chinese Company 3D-Printed This Five-Story Apartment Building* [Online]. Time. Available: http://time.com/3674557/3d-printed-apartment-building-winsun/ [Accessed 1/5 2018].

THEGUARDIAN. 2021. *Europe's first fully 3D-printed house gets its first tenants-video* [Online]. Eindhoven University of Technology. Available: https://www.theguardian.com/technology/video/2021/apr/29/europes-first-fully-3d-printed-house-gets-its-first-tenants-video [Accessed 24-10 2021].

VAYRE, B., VIGNAT, F. & VILLENEUVE, F. 2012. Metallic additive manufacturing: state-of-the-art review and prospects. *Mechanics & Industry,* 13**,** 89-96.

WAINWRIGHT, O. 2014. *Work begins on the world's first 3D-printed house* [Online]. Available: https://www.theguardian.com/artanddesign/architecture-design-blog/2014/mar/28/work-begins-on-the-worlds-first-3d-printed-house [Accessed 1/5/2018 2018].

WANG, L., DU, W., HE, P. & YANG, M. 2019a. Topology Optimization and 3D Printing of Three-Branch Joints in Treelike Structures. *Journal of Structural Engineering,* 146**,** 04019167.

WANG, S., WANG, Y., CHEN, C.-S. & ZHU, X. 2013. An adaptive slicing algorithm and data format for functionally graded material objects. *The International Journal of Advanced Manufacturing Technology,* 65**,** 251-258.

WANG, X., WANG, A. & LI, Y. 2019b. A sequential path-planning methodology for wire and arc additive manufacturing based on a water-pouring rule. *The International Journal of Advanced Manufacturing Technology,* 103**,** 3813-3830.

WANGLER, T., LLORET, E., REITER, L., HACK, N., GRAMAZIO, F., KOHLER, M., BERNHARD, M., DILLENBURGER, B., BUCHLI, J. & ROUSSEL, N. 2016. Digital concrete: opportunities and challenges. *RILEM Technical Letters,* 1**,** 67-75.

WEAST, R. C. 1972. *Density of Water(g/mL) vs. Temperature (C).* [Online]. Available: http://jupiter.plymouth.edu/~jsduncan/courses/2012_Spring/Techniques/Exams/DensityOfWater-vs-Temp.pdf [Accessed 15/4 2020].

WILLIAMS, S. W., MARTINA, F., ADDISON, A. C., DING, J., PARDAL, G. & COLEGROVE, P. 2016. Wire+ arc additive manufacturing. *Materials Science and Technology,* 32**,** 641-647.

WU, P., WANG, J. & WANG, X. 2016. A critical review of the use of 3-D printing in the construction industry. *Automation in Construction,* 68**,** 21-31.

XIA, C., PAN, Z., POLDEN, J., LI, H., XU, Y., CHEN, S. & ZHANG, Y. 2020. A review on wire arc additive manufacturing: Monitoring, control and a framework of automated system. *Journal of Manufacturing Systems,* 57**,** 31-45.

XIONG, J., LI, Y., LI, R. & YIN, Z. 2018. Influences of process parameters on surface roughness of multi-layer single-pass thin-walled parts in GMAW-based additive manufacturing. *Journal of Materials Processing Technology,* 252**,** 128-136.

YA, W., HERNÁNDEZ-SÁNCHEZ, J., PATHIRAJ, B. & VELD, A. H. I. T. A study on attenuation of a Nd: YAG laser power by co-axial and off-axial nozzle powder stream during cladding. International Congress on Applications of Lasers & Electro-Optics, 2013. Laser Institute of America, 453-462.

YALCINKAYA, G. 2018. *World's first 3D-printed steel bridge unveiled at Dutch Design Week* [Online]. Available: https://www.dezeen.com/2018/10/22/worlds-first-3d-printed-steel-bridge-completed-mx3d-technology/?li_source=LI&li_medium=bottom_block_1 [Accessed 3/1 2020].

YANG, P. & QIAN, X. 2008. Adaptive slicing of moving least squares surfaces: toward direct manufacturing of point set surfaces. *Journal of Computing and Information Science in Engineering,* 8.

YILI, D., SHENGFU, Y., YUSHENG, S., TIANYING, H. & LICHAO, Z. 2018. Wire and arc additive manufacture of high-building multi-directional pipe joint. *The International Journal of Advanced Manufacturing Technology,* 96**,** 2389-2396.

YUSUF, B. 2015. *5 Reseaons Why 3D Printing Industry will Boom by 2020* [Online]. All3DP. Available: https://all3dp.com/5-reasons-why-3d-printing-industry-will-boom-by-2020/ [Accessed 09/04 2018].

ZENOU, M. & GRAINGER, L. 2018. Additive manufacturing of metallic materials. *Additive Manufacturing.* Elsevier.

ZHANG, Y., WU, L., GUO, X., KANE, S., DENG, Y., JUNG, Y.-G., LEE, J.-H. & ZHANG, J. 2018. Additive manufacturing of metallic materials: a review. *Journal of Materials Engineering and Performance,* 27**,** 1-13.

ZHAO, G., MA, G., FENG, J. & XIAO, W. 2018. Nonplanar slicing and path generation methods for robotic additive manufacturing. *The International Journal of Advanced Manufacturing Technology,* 96**,** 3149-3159.

9. Appendices

Appendix 3.1

Data sheet for the used wire at Autodesk-Birmingham

Union K 40

Classifications	EN 440	AWS A 5.18
	G2Si1 (mod.)	ER70S-G [ER70S-3 (mod.)]

Characteristics and field of use

GMAW solid wire electrode for welding unalloyed and low alloy steels with shielding gas. Especially suited for electrolytically and hot-dip galvanized thin sheets. Used primarily in vehicle and autobody fabrication in conjunction with gas mixtures M12 to M23.

Materials

DC01+ZE - DC04+ZE, S220GD+Z - S350GD+Z

Typical analysis in %

C	Si	Mn
0.10	0.35	1.10

Mechanical properties of the weld metal according to EN 1597-1 (min. values at RT)

Heat-treatment	Shielding gas	Yield strength 0.2% N/mm^2	Tensile strength N/mm^2	Elongation ($L_0=5d_0$) %	Impact values in J CVN
AW	M23	360	440	25	80

Welding position

Polarity = +
Shielding gas (EN 439) **M12 - M23**

Packaging and weights

Diam. (mm)	Spool	kg / pack
0.8	B300	15
0.9	B300	18
1.0	B300	18
1.2	B300	18

233

Appendix 3.2

Data sheet for the used wire at Steelo Manufacturer:

<table>
<tr><td rowspan="4">**INE**</td><td rowspan="4">**DATA SHEET**
DS 004
Rev. 7 dd 11/05/2015
INEFIL</td><td>I.N.E. S.p.A.
Via Facca 10
35013 Cittadella (PADOVA)
ITALY
Tel. : +39 049/9481111   Fax: + 39 049/9400249
Internet: www.ine.it   E mail: ine@ine.it</td></tr>
</table>

CLASSIFICATION

APPROVALS

AWS SPECIFICATIONS	EN SPECIFICATIONS
AWS A 5.18: ER70S-6	EN ISO 14341-A: G 46 4 M21 3Si1
AWS A 5.18M: ER48S-6	EN ISO 14341-A: G 42 2 C1 3Si1
ASME SFA 5.18: ER70S-6	EN ISO 14341-A: G 46 3 M14 3Si1
ASME SFA 5.18M: ER48S-6	

ABS	TÜV	RINA
GL	DNV	
DB	LRS	

ALLOY TYPE

Copper-coated solid wire for welding carbon and C-Mn steels with tensile strength up to 510 MPa.

APPLICATIONS

Copper-coated solid wire designed for welding carbon and carbon-manganese steels with tensile strength up to 510 MPa. Suitable for single pass or multi-pass welding. Applications include tanks, boilers, steel structural works, earthworks and construction works. To be used under the shield of $Ar+CO_2$, $Ar+O_2$ or CO_2.

MATERIALS TO BE WELDED

ASTM		EN		Others	
A139	A131 Gr A, B, D	10113-2 S275	10113-3 S420M	Fe 360	
A210 Gr A1	API 5LX42	10113-2 S355	10113-3 S420ML	Fe 430	
A210 Gr C	API 5LX46	10113-2 S420	10025 S185, S235	Fe 510	
A36	API 5LX52	10113-3 S275M	10025 S275, S355	(steel group 1	EN
A234 Gr WPB	API 5LX60	10113-3 S275ML	10208-1 L210, L240	288/3)	
A334 Gr 1		10113-3 S355M	10208-1 L290, L360		
A106 Gr A, B, C		10113-3 S355ML			

WELDING GUIDELINES

Preheat and PWHT are not required.

TECHNICAL INFORMATION

Gas: CO_2, Mix Ar- CO_2 & Mix Ar- O_2 (EN ISO 14175)
Welding position: all positions

WELDING PARAMETERS

Current	DC + Reverse polarity					
Diameter (mm)	0.8	1.0	1.2	1.6		
Volts (V)	16 ÷ 28	17 ÷ 32	18 ÷ 34	19 ÷ 38		
Intensity (A)	60 ÷ 200	80 ÷ 260	100 ÷ 360	130 ÷ 450		

TYPICAL CHEMICAL COMPOSITION OF WIRE

C %	Mn %	Si %	S %	P %	Cu %	Ni %	Cr %	Mo %	
0.07	1.40	0.80	0.012	0.012	0.15	-	-	-	

TYPICAL MECHANICAL PROPERTIES

GAS		Yield strength	Tensile strength	Elongation on % 5d	Impact energy (Charpy V)				
		Rs	Rm	A 5d	+ 20°C	0°C	-20°C	-30°C	-40°C
		(MPa)	(MPa)	%	(Joule)	(Joule)	(Joule)	(Joule)	(Joule)
M21	as welded	470	560	26	-	-	90	70	60
C1	as welded	440	530	26	-	-	70	-	-
M14	as welded	480	580	28	-	-	80	60	-

PRODUCTS AVAILABLE

Process	Product	Classification AWS	Classification EN
MIG/MAG	INEFIL S2	AWS A 5.18: ER70S-2	EN 14341-A: G2Ti
Solid wire	INEFIL 13.7	AWS A 5.18: ER70S-3	EN 14341-A: G2Si
	INEFIL S4	AWS A 5.18: ER70S-4	EN 14341-A: G3Si1
	INEFIL 19.12	AWS A 5.18: ER70S-6	EN 14341-A: G4Si1
	INEFIL NR	AWS A 5.18: ER70S-6	EN 14341-A: G3Si1
TIG	INETIG S2	AWS A 5.18: ER70S-2	EN 636-A: W2Ti
Rods	INETIG 13.7	AWS A 5.18: ER70S-3	EN 636-A: W2Si
	INETIG	AWS A 5.18: ER70S-6	EN 636-A: W3Si1
SAW	INESUB S2	AWS A 5.17: EM12K	EN 14171-A: S2
Submerged arc	INESUB S2Si	AWS A 5.17: EM12K	EN 14171-A: S2Si
	INESUB S3Si	AWS A 5.17: EH12K	EN 14171-A S3Si
FCAW	INETUB R71T1	AWS A 5.20: E71T-1	EN 17632-A: T 46 2 P M
Cored wire	INETUB R70T1	AWS A 5.20: E70T-1	EN 17632-A: T 42 2 R M
	INETUB R71T1-CO2	AWS A 5.20: E71T-1	EN 17632-A: T 46 2 P C
	INETUB M71TG	AWS A 5.18: E70C-6	EN 17632-A: T 46 2 M M
	INETUB B71T5	AWS A 5.20: E71T-5	EN 17632-A: T 46 4 B M
SMAW	INE 50 B	AWS A 5.1: E7018	EN 2560-A: E 42 4 B
Electrodes	INE 55 B	AWS A 5.1: E7018-1	EN 2560-A: E 42 4 B

Data sheet for the used wire at RAMLAB Manufacturer:

MILD STEEL SOLID WIRE

SupraMig Ultra® HD

MicroGuard™ Ultra

for **HYPERFILL™** process available as HF-version

CLASSIFICATION

AWS A5.18	ER70S-6	A-Nr	1	**Mat-Nr**	1.5130
EN ISO 14341-A	G46 3 C 4Si1 / G50 5 M 4Si1	F-Nr	6		
		9606 FM	1		

GENERAL DESCRIPTION

Solid wire with increased Mn for semiautomatic and robotic applications
Microguard™ Ultra provides superior feeding and arc stability
Ultimate GMAW wire for heavy duty high deposition applicationst
Deep root penetration and improved fatigue life

Very consistent welding performance
Self releasing silicates islands
Minimal spatters
Available in spools and Accutrak®

WELDING POSITIONS [ISO/ASME]

PA/1G PB/2F PC/2G PD/4F PE/4G PF/3Gu PG/3Gd

SHIELDING GASES [ACC. ISO 14175]

M21	Mixed gas Ar+ >15-25% CO_2
C1	Active gas 100% CO_2

APPROVALS

ABS	LR	BV	DNV-GL	TUV	DB	CE	CWB
+	+	+	+	+	+	+	-

CHEMICAL COMPOSITION [W%] TYPICAL WIRE

C	Mn	Si
0.08	1.70	0.85

MECHANICAL PROPERTIES, TYPICAL, ALL WELD METAL

	Shielding gas	Condition	Yield strength [N/mm²]	Tensile strength [N/mm²]	Elongation [%]	Impact ISO-V[J] -20°C	Impact ISO-V[J] -40°C
Typical values	M21	AW	500	650	26	80	80
	C1	AW	490	620	30	60	50

EXAMPLES OF MATERIALS TO BE WELDED

Steel grades	Standard	Type
General structural steels	EN 10025	S185, S235, S275, S355
Ship plates	ASTM A131	Grade A, B, D, AH32 to DH 36
Cast steels	EN 10213-2	GP240R
Pipe material	EN 10208-1	L210, L240, L290, L360
	EN 10208-2	L240NB, L290NB, L360NB, L360QB, L240MB, L290MB, L360MB, L415MB, L415NB
	API 5LX	X42, X46, X52, X60
	EN 10216-1	P235T1, P235T2, P275T1
	EN 10217-1	P275T2, P355N
Boiler & pressure vessel steels	EN 10028-2	P235GH, P265GH, P295GH, P355GH
Fine grained steels	EN 10025 part 3	S275, S355, S420
	EN 10025 part 4	S275M, S275ML, S355M, S355ML, S420M, S420ML

PACKAGING AND AVAILABLE SIZES

Diameter [mm]	1.0	1.2	1.32	1.6
16 kg spool B300	X	X	X	
16 kg spool BS300	X	X	X	
250 kg Accutrak® Drum	X	X	X	X
500 kg Accutrak® Drum	X	X	X	

Other sizes and packaging on request

Supramig® Ultra HD: rev. C-EN09-20/11/20

LINCOLN ELECTRIC

www.lincolnelectric.eu

GMAW

Appendix 5.1

-Density adjustment temperature

Table below to adjust ρ$_w$ for the recorded temperature (T_w) in column 9 in Table 5-1 and Table 5-2 , (Weast, 1972).

	0.0	0.1	0.2	0.3	0.4	0.5	0.6	0.7	0.8	0.9
15	0.999099	0.999084	0.999069	0.999054	0.999038	0.999023	0.999007	0.998991	0.998975	0.998959
16	0.998943	0.998926	0.998910	0.998893	0.998877	0.998860	0.998843	0.998826	0.998809	0.998792
17	0.998774	0.998757	0.998739	0.998722	0.998704	0.998686	0.998668	0.998650	0.998632	0.998613
18	0.998595	0.998576	0.998558	0.998539	0.998520	0.998501	0.998482	0.998463	0.998444	0.998424
19	0.998405	0.998385	0.998365	0.998345	0.998325	0.998305	0.998285	0.998265	0.998244	0.998224
20	0.998203	0.998183	0.998162	0.998141	0.998120	0.998099	0.998078	0.998056	0.998035	0.998013
21	0.997992	0.997970	0.997948	0.997926	0.997904	0.997882	0.997860	0.997837	0.997815	0.997792
22	0.997770	0.997747	0.997724	0.997701	0.997678	0.997655	0.997632	0.997608	0.997585	0.997561
23	0.997538	0.997514	0.997490	0.997466	0.997442	0.997418	0.997394	0.997369	0.997345	0.997320
24	0.997296	0.997271	0.997246	0.997221	0.997196	0.997171	0.997146	0.997120	0.997095	0.997069
25	0.997044	0.997018	0.996992	0.996967	0.996941	0.996914	0.996888	0.996862	0.996836	0.996809
26	0.996783	0.996756	0.996729	0.996703	0.996676	0.996649	0.996621	0.996594	0.996567	0.996540
27	0.996512	0.996485	0.996457	0.996429	0.996401	0.996373	0.996345	0.996317	0.996289	0.996261
28	0.996232	0.996204	0.996175	0.996147	0.996118	0.996089	0.996060	0.996031	0.996002	0.995973
29	0.995944	0.995914	0.995885	0.995855	0.995826	0.995796	0.995766	0.995736	0.995706	0.995676
30	0.995646	0.995616	0.995586	0.995555	0.995525	0.995494	0.995464	0.995433	0.995402	0.995371

Appendix 6.1

- **Design Data for upward forces applied to the floor's sockets**

3.4 Design data for upwards forces applied to floor

Upwards forces are limited by the tensile strength of the holding-down bolts. From Lab. Note No.1, maximum upwards force at Serviceability Limit State is 105 kN per socket.

Appendix 6.2

- **A detailed summary for the different types of transducers profiles used to configure the profiles using the Cubus software**

Transducer Name	Transducer	Polarity	Polarity mode	Bridge	Gauge resistance (Ohm)	Gauge Factor	Bridge excitation (Volt)	Sensitivity mV/V	Calibration type
SG-Top	Symmetric	Inverted	Bipolar	Quarter Bridge	120	2.13	2.5	-	Standard
SG-Bottom	Symmetric	Inverted	Bipolar	Quarter Bridge	120	2.13		-	Standard
DT-A	Asymmetric	Normal	Bipolar	Full Bridge	350	-	10	3	2-Point Calibration
HS-50A-Top	Asymmetric	Inverted	Bipolar	Full Bridge	350	-	10	1.8	2-Point Calibration
HS-50B-Bottom	Asymmetric	Inverted	Bipolar	Full Bridge	350	-	10	1.8	2-Point Calibration
Inc-1	Asymmetric	Normal	Bipolar	Half Bridge	120	-	9	260	2-Point Calibration
Inc-4	Asymmetric	Normal	Bipolar	Half Bridge	120	-	9	260	2-Point Calibration

189